THE UNIVERSITY *of* ADELAIDE

A Laser Based Sensor for Airborne Methane Detection

BY

Joshua Pease

A thesis submitted towards the degree of

Doctor of Philosophy

August 2019

at the

School of Physical Sciences

Department of Physics

Abstract

Mitigating climate change and its detrimental impact to the Earth is a critical issue facing modern science. To reduce greenhouse gas emissions there is growing pressure to transition from coal-based energy sources to cleaner alternatives. Natural gas is considered the fossil fuel of choice to facilitate this transition and maintain energy production. However, natural gas predominantly consists of methane (CH_4) - a greenhouse gas with a global warming potential 25 times greater than carbon dioxide (CO_2). If the total methane emissions throughout the production, storage and transport exceeds 3% the benefits of natural gas from a global warming perspective are nullified.

Thus, there are financial and environmental incentives to minimise fugitive leaks across the global network of natural gas pipelines. Methane sensors mounted in aircraft provide a means of wide-area scanning with a high spatial resolution and sensitivity for leak detection and repair. Current airborne systems use high complexity sensors and prohibitively long average times: increasing the operating costs and reducing the spatial resolution. There is thus a commercial need for a compact sensor with a high single-shot measurement sensitivity for airborne methane detection.

In this thesis I describe the development of an Integrated Path Differential Absorption (IPDA) LIDAR system optimised for methane sensing from a fixed-wing light aircraft. A new dual-pulsed Q-switched Er:YAG laser source capable of producing injection-seeded pulses at the 'online' and 'offline' methane absorption wavelengths is developed. It uses a novel adaptation of the Pound-Drever-Hall (PDH) frequency stabilisation technique to simultaneously 'lock' two low-power diode lasers to a Q-switched Er:YAG resonator for reliable injection-seeding. The high control bandwidth of this system will enable stable wavelength control in a high-vibration aircraft. The online and offline pulses have a temporal separation of 2.3 µs, which to our knowledge is the smallest reported in any dual-wavelength Q-switched laser, thus maximising system commonality and reducing potential sources of error.

I also present the design and construction of custom low-noise, high-bandwidth photodetectors for measuring the return LIDAR signal. These are used in conjunction with a commercial telescope to demonstrate a ground-based measurement of methane through a 300 m atmospheric column above Adelaide, Australia. The concentration was measured to be 1.979 ± 0.003 ppm with a single-shot sensitivity of 0.124 ppm. To our

knowledge the sensitivity reported in this thesis is the highest achieved by a methane IPDA LIDAR system.

Declarations

I certify that this work contains no material which has been accepted for the award of any other degree or diploma in my name, in any university or other tertiary institution and, to the best of my knowledge and belief, contains no material previously published or written by another person, except where due reference has been made in the text. In addition, I certify that no part of this work will, in the future, be used in a submission in my name, for any other degree or diploma in any university or other tertiary institution without the prior approval of the University of Adelaide and where applicable, any partner institution responsible for the joint-award of this degree.

I acknowledge that copyright of published works contained within this thesis resides with the copyright holder(s) of those works.

I also give permission for the digital version of my thesis to be made available on the web, via the Universitys digital research repository, the Library Search and also through web search engines, unless permission has been granted by the University to restrict access for a period of time.

I acknowledge the support I have received for my research through the provision of an Australian Government Research Training Program Scholarship.

Signed:

Date: 30/08/2019

Supervisors: Prof. David Ottaway
Prof. Peter Veitch

Acknowledgements

Firstly I would like to thank my supervisors David Ottaway and Peter Veitch for their advice and guidance. You have both given me a fantastic opportunity to work on this project and I am grateful for all you have taught me.

I would also like to thank Richard White, without your technical advice throughout the early stages of my candidature I would have broken twice the equipment and learnt half as much.

Throughout my PhD I have had the pleasure of meeting a fantastic group of students and staff who are always willing to offer advice and support. To Alexei Ciobanu, Andrew Malouf, Ashby Hilton, Ben Sparkes, Blair Middlemiss, Bob Chivell, Chris Perella, Craig Ingram, Deeksha Beniwal, Huy Cao, Jarrah Mik, Jonathan Hedger, Lachlan Harris, Miftar Ganija, Myles Clark, Nathaniel Bawden, Nathaniel Wilson, Ori Henderson-Sapir, Phillip Light, Sarah Scholten, Sarah Watzdorf and Sebastian Ng - thank-you all for your assistance and best wishes for whatever the future holds.

Last but not least I would like to thank my family, my parents Leanne and Carl Pease and my sister Emily. I am forever grateful for all of your love and support, you have allowed me to pursue my dreams and I wouldn't be in this position without you. Finally, to my partner and best friend Natalie, I wouldn't have gotten through the last three years without your constant emotional support. Thank-you for always being there for me, I love you.

Contents

List of Figures

List of Tables

List of Acronyms

AC	Alternating Current
ADC	Analog-to-Digital Converter
AOM	Acousto-Optic Modulator
ASD	Amplitude Spectral Density
ASE	Amplified Spontaneous Emission
BFP	Back Focal Plane
BJT	Bi-Polar Junction Transistor
BPF	Band-Pass Filter
BW	Bandwidth
CPFS	Co-Planar Folded Zig-Zag Slab
CRDS	Cavity Ring-Down Spectroscopy
CW	Constant Wave
DAQ	Data Acquisition
dBFS	Decibel Full-Scale
DBR	Distributed Bragg Reflector
DC	Direct Current
DFB	Distributed Feedback
ECDL	External Cavity Diode Laser
EDFL	Erbium Doped Fiber Laser
EOM	Electro-Optic Modulator
EPA	Environmental Protection Agency
ETU	Energy Transfer Upconversion
FET	Field Effect Transistor
FM	Frequency Modulation
FOV	Field of View
FPGA	Field Programmable Gate Array
FSR	Free Spectral Range
FTIR	Fourier-Transform Infrared Spectroscopy
FWHM	Full Width Half Maximum
GFF	Geometric Form Factor

GOSAT	Greenhouse Gases Observing Satellite
HF	High Frequency
HR	High Reflectivity
HV	High Voltage
HWP	Half Wave Plate
InGaAs	Indium Gallium Arsenide
InGaAsP	Indium Gallium Arsenide Phosphate
IPDA	Integrated Path Differential Absorption LIDAR
LF	Low Frequency
LFGL	Low Frequency Gain Limit
LDAR	Leak Detection and Repair
LIDAR	Light Detection and Ranging
LO	Local Oscillator
LPF	Low-Pass Filter
MERLIN	Methane Remote Sensing LIDAR Mission
MF	Matched Filtering
MPA	Mean Population Approximation
MOPA	Master Oscillator Power Amplifier
ND	Neutral Density
NOAA	National Oceanic and Atmospheric Administration
NPRO	Non-Planar Ring Oscillator
OA	Optical Axis
OC	Output Coupling
OD	Optical Density
ODE	Ordinary Differential Equation
OGI	Optical Gas Imaging
OPG	Optical Parametric Generation
OPLL	Optical Phase Locked Loop
OSA	Optical Spectrum Analyser
PBS	Polarising Beam Splitter
PC	Pockels Cell
PCB	Printed Circuit Board
PD	Photodetector
PDH	Pound Drever Hall
PI	Proportional-Integral
PLL	Phase Locked Loop
PRF	Pulse Repetition Frequency
PSD	Power Spectral Density
PZT	Piezo-electric Transducer

QWP	Quarter-Wave Plate
RBW	Resolution Bandwidth
RF	Radio Frequency
RMS	Root Mean Square
RTP	Rubidium Titanyl Phosphate
SA	Spectrum Analyser
SC	Schmidt-Cassegrain
SD	Shunt Diode
SNR	Signal-to-Noise Ratio
TDC	Time-to-Digital Converter
TEA	Transversely Excited Atmospheric
TFP	Thin Film Polariser
TIA	Transimpedance Amplifier
TIR	Total Internal Reflection
TTL	Transistor Transistor Logic
VBG	Volume Bragg Grating
VBW	Video Bandwidth
VCO	Voltage Controlled Oscillator
YAG	Yttrium Aluminium Garnet

Chapter 1

Introduction

Global average temperatures have risen by 1.25°C over the past century and the key contributor to this is the increase in atmospheric greenhouse gases and the associated increase in radiative forcing [1]. Methane (CH_4) is an important greenhouse gas because although its concentration in the atmosphere is small in comparison to carbon dioxide (CO_2) its potency as a greenhouse gas is twenty-five times higher [2]. Despite this, its relatively short atmospheric lifetime of ten years [3] means that reducing anthropogenic methane emissions may reduce some short term climate change effects.

Estimates of the atmospheric methane levels published by MacFarling *et al.* [4] show a significant increase in methane levels starting at the turn of the 19th century. This observation is consistent with global methane level mapping conducted by the National Oceanic and Atmospheric Administration (NOAA) [5] and the analysis by Petit *et al* [6].

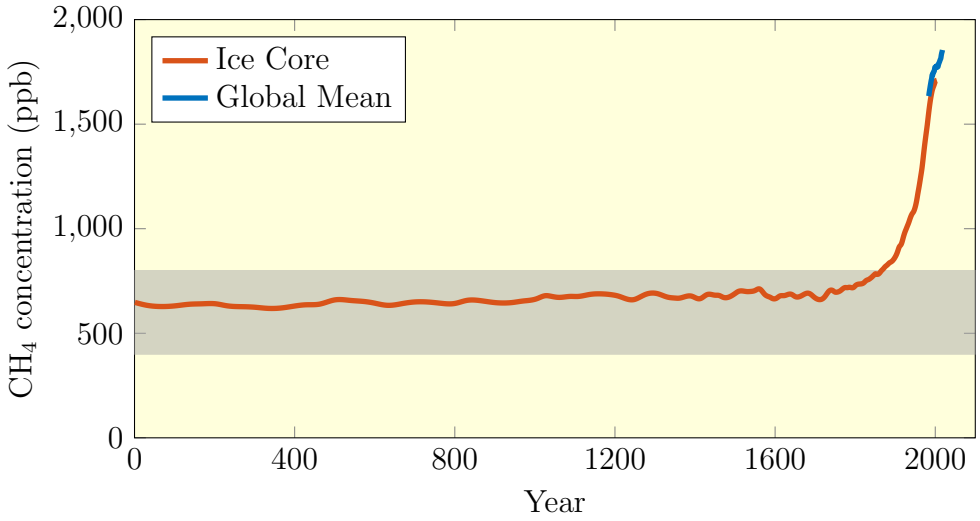

Figure 1.1: Analysis of atmospheric methane levels from air bubbles trapped in ice, the shaded grey area shows the range of methane levels from 2,000 to 400,000 years before the present (from Petit *et al.* [6]).

If greenhouse gas concentrations continue to increase there will be broad implications for the human race including detrimental effects to human health [7], a reduction of global crop production [8] and a reduced habitability of coastal regions [9] which are populated by approximately 20% of the global population [10]. Hence, there is growing pressure to phase-out coal-based electricity generation and transition to low-greenhouse-gas alternatives whilst maintaining energy production.

Natural gas is considered the fossil fuel of choice for many Western countries as they transition to renewable sources [11–13], primarily because it has a lower carbon footprint compared to coal or oil [14]. However, according to a recent study by Alvarez *et al.*, if the total methane emissions throughout the production and distribution process is greater than 3.2% the benefits of natural gas are nullified [15]. Howarth *et al.* [16] found that the natural gas system in the United States has a 20-50% greater carbon footprint in comparison to coal, due to significant leaks in the storage, transport and distribution networks.

Thus there is direct need for a method to monitor fugitive methane emissions in the transmission and storage of natural gas with a high spatial resolution and sensitivity. We propose to develop a methane sensor capable of mitigating both the environmental and financial impacts of anthropogenic methane leaks by rapidly mapping the thousands of kilometres of gas pipelines distributed worldwide.

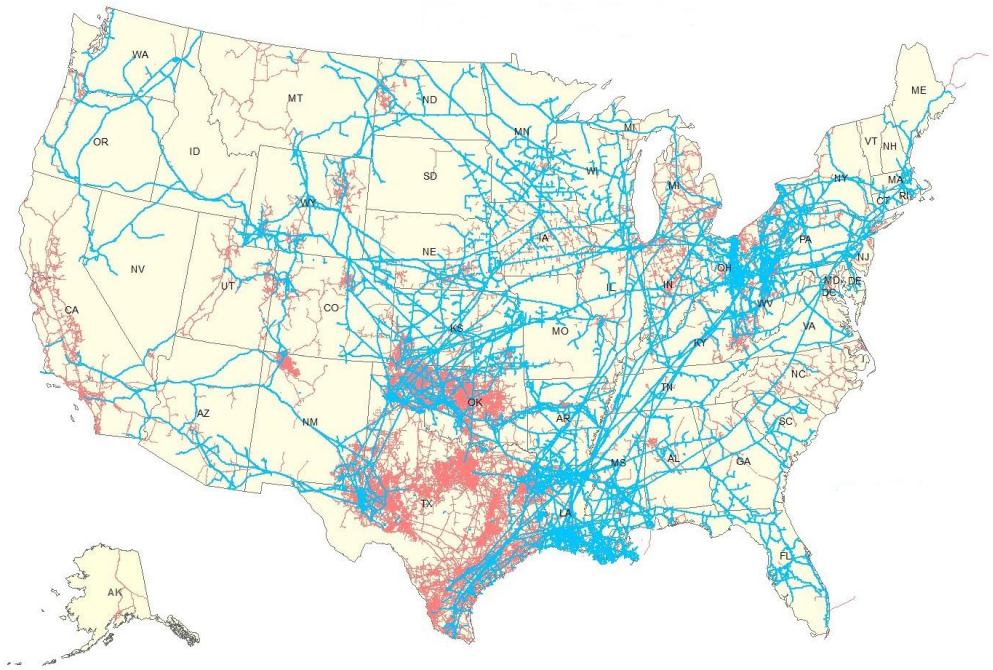

Figure 1.2: A map of both the intrastate and interstate natural gas supply network in the United States as of 2013 [17].

1.1 Methane Absorption Spectra

Local methane sensing has been receiving increasing attention in both industry and academia, with studies establishing a range of techniques including those based upon semiconductors [18], carbon nanotubes [19] and acoustic methods [20]. In comparison, methane sensing using optical techniques have the potential for high-sensitivity long-range measurements [21]. There exists a range of optical sensing techniques, discussed in further detail in Section 1.2, all of which exploit the spectroscopic properties of the trace gas. In the design of these systems it is critical to know the dominant absorption lines of the target gas and other atmospheric constituents.

Many of the fundamental absorption lines of methane are centred around 3.3 µm as illustrated in Figure 1.3. The high Optical Density (OD) of methane in this wavelength band makes it suitable for passive imaging techniques as there is a high contrast in comparison to the background. However, for active techniques which rely on measuring the absolute absorption, operating in this region will lead to very weak return signals; reducing the overall system sensitivity. Furthermore, unless the system is capable of spectral scanning, the high absorption of other atmospheric constituents within this band limits the ability to differentiate between absorption lines.

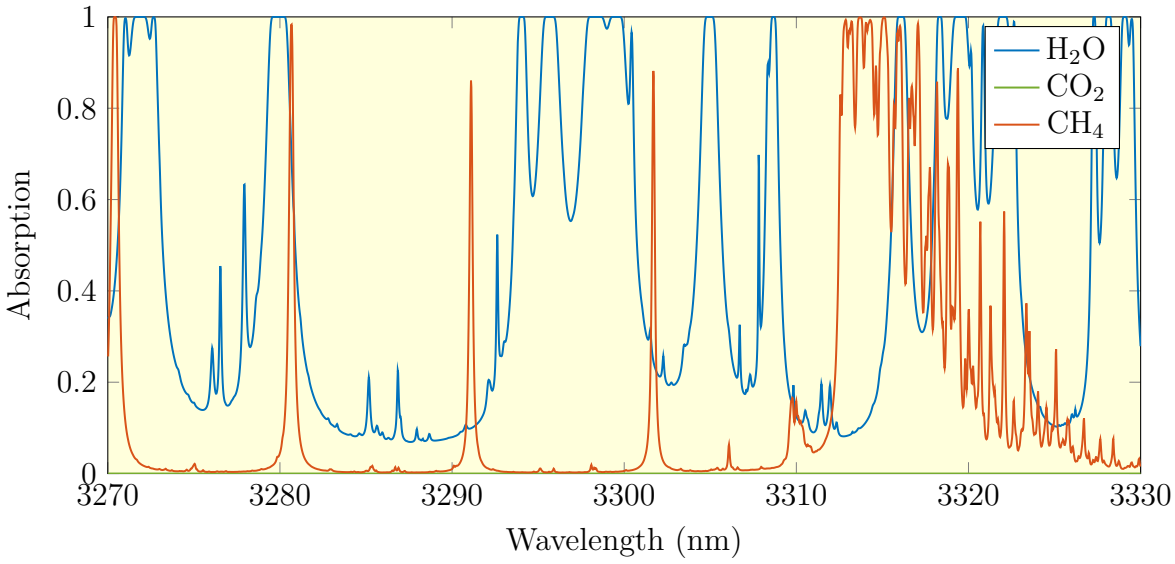

Figure 1.3: Dominant absorption lines of atmospheric constituents in the mid-infrared calculated via the HITRAN 2012 database through a 1 km path.

Other weaker absorption lines of methane are centred around the 1.6 µm wavelength band as illustrated in Figure 1.4. The reduced OD in this region makes it more suitable for long-range active measurement techniques. Furthermore, this wavelength band is sparsely populated by other absorption features, allowing easier differentiation between methane and other trace gases.

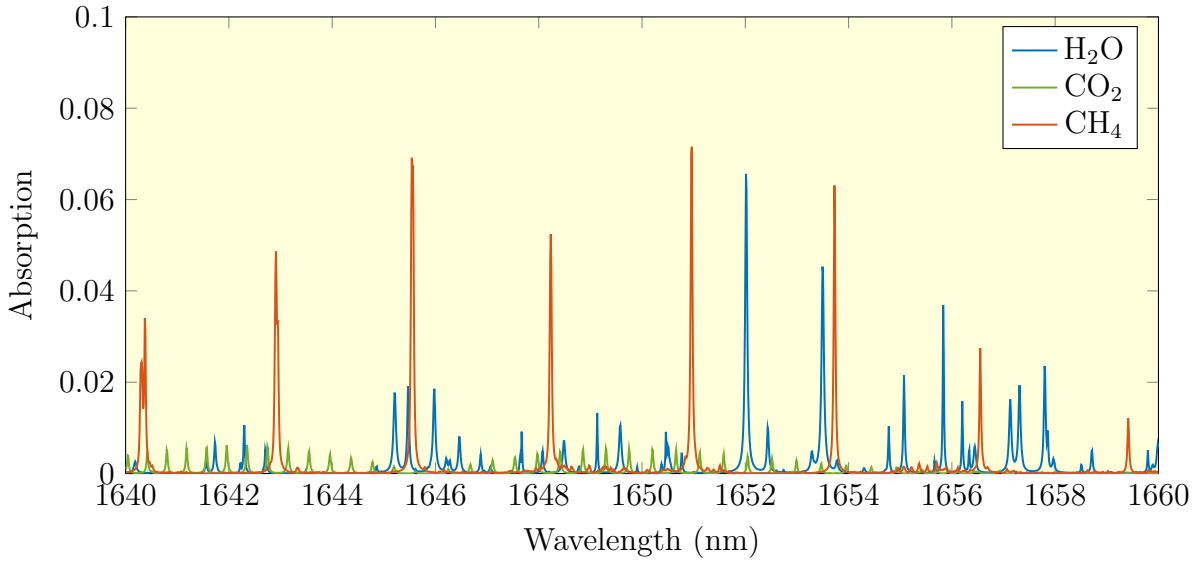

Figure 1.4: Dominant absorption lines of atmospheric constituents in the near-infrared calculated via the HITRAN 2012 database through a 1 km path.

1.2 Optical Sensing of Methane

There are a variety of methane measurement platforms that span a range of spatial and temporal scales; from the large scale monitoring of global methane levels to instantaneous small scale measurements at a local source. These techniques all have various limitations, and as such, are often used in complement with one another to build a complete description of methane emissions. In this section, three separate sensing platforms are reviewed and the limitations of each are discussed.

1.2.1 Ground Based Sensors

A number of methods, including both dynamic and static flux chamber techniques, have been used to quantify methane emission rates from a known source [22–24]. These require a tracer gas to be injected near the leak source, where an array of chambers downwind measure both the tracer gas and methane at distances of up to 100 m away [25]. For accurate estimates of emission rates adjacent chambers must be spaced less than 7 m apart [26], which when combined with the low sampling rate, means that a measurement of a single source can take upwards of two days [27].

To complement this technique research groups are assessing mobile techniques to measure emissions from off-site locations using spectroscopic technologies such as Cavity Ring-Down Spectroscopy (CRDS) [28, 29] and Fourier-Transform Infrared spectroscopy (FTIR) [30, 31]. These techniques allow broader area mapping, however, measurement accuracy is limited by the local wind conditions [32] and occasionally vehicle emissions [33].

In recent years, the improvement of commercially available analytical instruments has enabled a new range of measurement techniques including vertical radial plume mapping [34], inverse plume modelling [35] and Optical Gas Imaging (OGI) [36]. Recently the United States Environmental Protection Agency (EPA) has required the use of OGI to monitor methane leaks in the oil and gas industry [37]. This passive technique uses high cost hyperspectral cameras (≈$100k USD [38]) to image a narrow spectral region in the mid-infrared where methane heavily attenuates the solar background light. Simulations have shown this technique has a detection rate of 90% at a distance of only ten metres and under ideal atmospheric conditions has a sensitivity of only 10,000 ppm [39].

Commonly this technology is used to complement off-site mobile techniques to help pinpoint the emission source [40]. An active adaptation of this technology is the backscatter absorption technique [41, 42] which uses an infrared laser to illuminate plumes before imaging, improving both the sensitivity and range. These direct onsite measurement techniques are rarely used more than monthly as it is resource intensive to train and send staff to widely distributed sites [43].

1.2.2 Satellite Based Sensors

A significant limitation in the current models of methane sinks and sources is the imprecise global map of atmospheric CH_4. Ground based technologies are insufficient as the network is too coarse for adequate mapping [44]. To overcome these shortcomings satellite based measurements are used as they allow global coverage with multiple measurements per instrument. Both the Scanning Imaging Absorption Spectrometer for Atmospheric Chartography (SCIAMACHY) [45] and the Greenhouse Gases Observing Satellite (GOSAT) [46] implement a passive measurement technique that monitors the spectra of sunlight backscattered from the surface of the Earth to look for methane signatures. However, these instruments cannot measure in high-latitude regions or during the night [47] and suffer from low sensitivity in the lower troposphere [48].

The nadir-viewing Atmospheric Infrared Sounder (AIRS) [49] and the limb-scanning Microwave Limb Sounder [50] have been providing vertically-resolved methane concentrations by implementing microwave limb sounding. This microwave radiometry technique remotely measures methane and other atmospheric constituents by observing gigahertz thermal emission as the instrument field-of-view is scanned [51]. However, these systems require significant calibration to remove instrument effects [52] and are commonly limited by thermally induced errors in the antenna [53, 54].

Moving forward, the Methane Remote Sensing LIDAR Mission (MERLIN) is looking to overcome many of these limitations by implementing the Integrated Path Differential Absorption LIDAR (IPDA) technique [55, 56]. Set to launch in 2021, this will

allow continuous mapping of global methane levels with a target sensitivity of 8 ppb. However, with a low horizontal resolution of 50 km it is unable to pinpoint sources of spurious methane leaks.

1.2.3 Aircraft Based Sensors

Aircraft based systems offer a compromise between the high spatial accuracy achievable by ground monitoring and the large area coverage of satellite sensors. A study by Kemp *et al.* [57] found that airborne sensors are the most cost-effective platform for Leak Detection and Repair (LDAR) in the natural gas sector. This study also showed that in principal a low-cost LDAR program can rely on highly sophisticated and expensive technology as long as rapid large area coverage is available. Commercially available airborne sensors appear to follow this logic, with many based on the high-cost OGI technique or highly-complex IPDA technique. A comparison of these airborne methane sensor systems is given in Table 1.1.

Type	Altitude (m)	Sensitivity (ppb)	Avg. Time (s)	Ref.
OGI	1,000	440	-	[58]
OGI	4,000	90	-	[59]
OGI	50	100	-	[60]
OGI	1,000	400	-	[61, 62]
FTIR	65	1,000	60	[63]
IPDA	10,000	21.4	1	[64–66]
IPDA	2,000	14	10	[67–69]
IPDA	800	62.5	-	[70]

Table 1.1: Comparison of airborne methane sensors.

Many of the commercially available sensors such as the Mako [58], AVIRIS [59], HyperCam Methane [60] and HyTES [61, 62] systems use a form of OGI known as hyperspectral imaging to resolve methane plumes. A hyperspectral camera acquires spectrally resolved images of gas plumes, allowing differentiation between methane and other hydrocarbons in the 0.5-15 µm wavelength band [71]. Despite the obvious advantages of broad spectral monitoring, these passive instruments struggle to resolve weak gas plumes as the image contrast is dependent on the ground composition and significant signal processing is often required to correct for natural variances in the landscape [72].

The BOREAL Gasfinder [63] is a low-cost, low-footprint alternative platform capable of mounting underneath a helicopter. A measurement cell mounted underneath the aircraft is probed by a low-power laser diode giving real-time FTIR spectroscopy measurements of methane plumes. Unlike the hyperspectral cameras, this technique is not sensitive to the ground conditions. However, it is only capable of measuring the

gas concentration at the aircraft altitude, which when combined with a low-sampling rate, means that it is often difficult to pinpoint the source of the leak.

Riris *et al.* [64–66] and Amediek *et al.* [67–69] have both reported airborne systems which implement the IPDA technique. Both systems use Optical Parametric Generation (OPG) to generate wavelengths capable of probing the 1.6 µm absorption lines; increasing the footprint, complexity and energy requirements. Furthermore, the spatial resolution of these systems is limited by the prohibitively long average times required. *Ball Aerospace* [70] reported an airborne IPDA sensor which uses an erbium doped yttrium aluminium garnet (Er:YAG) laser to directly lase at a 1.6 µm absorption line. Whilst direct lasing will reduce both system complexity and energy requirements, these advantages are yet to be fully realised as a second time synchronised Er:YAG laser source is required. The details of such systems are discussed in Section 1.4.

Active methane sensing using the IPDA technique is regarded as a promising candidate to overcome the shortcomings of passive techniques [73]. However, due to limitations in the laser systems these advantages have not yet been realised in an airborne system.

1.3 Light Detection and Ranging (LIDAR)

LIDAR is a remote sensing technique that measures the distance to a target by probing the target with a pulsed laser. Since this method was first demonstrated in 1963 by the National Centre for Atmospheric Research [74] it has become a common technique for mapping large areas in 3D space [75]. Extending this concept further, the presence of a trace gas can be measured by tuning the laser wavelength to a suitable absorption line and monitoring the decrease in the return laser energy. The wavelength of the laser must be carefully chosen to ensure it does not coincide with absorption lines of other atmospheric constituents.

There are two common LIDAR configurations used in gas sensing: monostatic LIDAR where the laser and detector are co-located and single-pass bistatic LIDAR where the laser and detector are spatially separated [76]. By co-locating all components monostatic systems are a comparatively portable system, allowing broad area-mapping by mounting onto a mobile platform such as a car or aircraft. The return signals measured in these systems are due to reflection by a distant hard-target such as the ground or alternatively from aerosol backscatter. The measurement sensitivity of these systems is ultimately limited by the inability to distinguish between changes in return pulse energy due to a varied concentration of the trace gas from natural variations in the landscape. Single-pass bistatic systems, by contrast, do not rely on a reflection of a pulse but are not portable.

By spatially separating the laser and receiver the bistatic system overcomes this

limitation, as in theory, the only fluctuation in measured laser energy should be due to changes in gas concentration. However, these systems lack the portability of monostatic systems, limiting their usefulness in the broad-area mapping of methane leaks.

1.3.1 Differential Absorption LIDAR (DIAL)

Differential Absorption LIDAR (DIAL) is commonly used to overcome the limitations of single-wavelength LIDAR [77–79]. A DIAL system requires a laser source that emits at two different wavelengths: one tuned to an absorption line of the target gas (the 'online' wavelength λ_{on}), the other tuned off of this absorption feature (the 'offline' wavelength λ_{off}). In the presence of the gas the atmospheric backscattered pulses at λ_{on} and λ_{off} will have different energies, allowing the concentration of the trace gas to be calculated. This technique has been used to successfully measure carbon dioxide [80–86], water [87–91], nitrous oxide [92–95] and methane [96–98].

The advantage of this technique is that it is self-calibrating [99] as the online and offline pulses have common optics and paths, removing all instrumental and environmental constants [100]. Care must be taken when selecting the wavelengths to ensure they avoid the absorption of other atmospheric constituents [101, 102], minimise errors due to the temperature dependence of absorption lines [103, 104] and coincide with an online OD that is neither too high nor too low [105].

The IPDA LIDAR technique, represented in Figure 1.5, is an adaptation of DIAL which uses surface reflection to determine the column-averaged gas concentration.

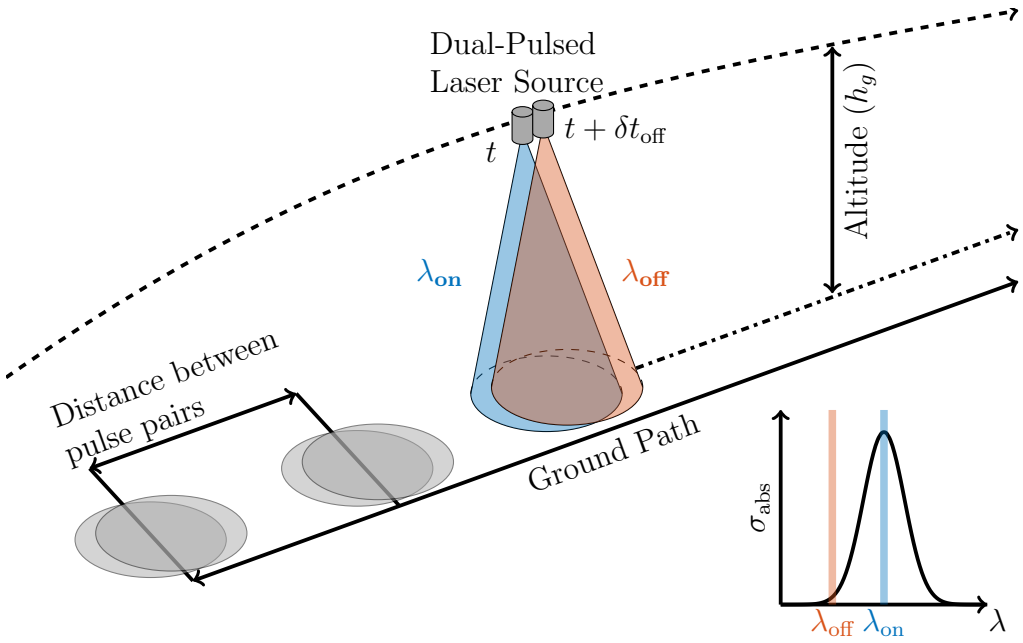

Figure 1.5: Schematic of an airborne IPDA LIDAR system; a source at altitude h_g emits two laser pulses tuned on and off of a gas absorption line separated by δt_{off}.

By reflecting from a hard-target the return signal is larger than that obtained by aerosol backscatter, allowing higher measurement sensitivity [106]. In addition to wavelength selectivity, the IPDA laser source must be capable of producing high-energy pulses to maximise the return energy, minimising the temporal separation of the pulses δt_{off} to ensure maximum overlap of the on- and off-line footprints [107] and operating at a high Pulse Repetition Frequency (PRF) to improve the spatial resolution.

1.4 Published Laser Systems

Light sources used for methane LIDAR are compared in Table 1.2.

Type	E_p	Δt_p	δt_{off}	PRF	λ_{on}	Ref.
OPG	60 µJ	3 ns	160 µs	6.3 kHz	1651 nm	[64–66]
OPG	10 mJ	20 ns	500 µs	50 Hz	1645 nm	[67–69]
OPG	220 µJ	60 ns	-	5 kHz	1651 nm	[96]
OPG	30 mJ	12 ns	-	10 Hz	3300 nm	[97]
Raman	3 mJ	-	4 s	10 Hz	1666 nm	[98]
Raman		30 mW CW			1650 nm	[108]
Diode		10 mW CW			1650 nm	[109]
Er:YAG (x2)	800 µJ	-	600 ns	10 kHz	1645 nm	[70]
Er:YAG	2 mJ	100 ns	250 µs	2 kHz	1645 nm	[110, 111]

Table 1.2: Comparison of laser sources used in methane DIAL where E_p is the pulse energy and Δt_p is the pulse width.

The most common technique is to use OPG to frequency down-convert light from a neodymium-doped yttrium aluminium garnet (Nd:YAG) laser. This adds significant complexity and results in large pulse separation, thus reducing the overlap between the online and offline footprints. Amediek *et al.* [67–69] reported systematic errors depending on the arrival sequence of the online and offline pulses. These findings are attributed to geometric differences between these pulses, further exacerbating the poor common-mode rejection of noise.

Ikuta [98] Raman shifted a Ti:Sapphire laser to produce light at 1666 nm. While this provides a compact light source, the sensitivity of this system is severely limited by the long separation of the online and offline pulses.

CW lasers for methane detection have also been reported, but these lasers are unsuitable for long-range LIDAR. Vujkovic-Cvijin *et al.* [108] achieved CW lasing at 1650 nm by amplifying a diode laser with a Raman fibre amplifier. Alternatively, CW lasing can be achieved by using laser diodes as reported by Iseki *et al.* [109], however the low-power of CW systems significantly limits their operating range.

As proposed over forty years ago by White and Schleusener [112], direct lasing at the methane absorption line of 1645.55 nm can be achieved using Er:YAG sources. *Ball*

Aerospace [70] use two Er:YAG lasers that are wavelength stabilised using temperature controlled Volume Bragg Gratings (VBG) to produce light at the online and offline wavelengths of 1645.55 nm and 1645.40 nm respectively. High-speed digital electronics are used to synchronise the pulse arrival, resulting in a temporal offset of 600 ns. Whilst in principle this should ensure high common-mode rejection, differences between the mode shape and beam alignment of the two sources may ultimately limit system sensitivity. Furthermore, by using two sources the potential improvements in system complexity, footprint and energy requirements achievable by direct lasing are not realised.

Fibertek Inc. [110, 111] attempted to overcome these limitations by using a single Er:YAG laser to produce both the online and offline pulses. Injection-seeding technique is used to achieve wavelength control. While this technique enables lasing near methane line-centre at 1645.52 nm, the temporal offset is limited to 250 µs by the control systems required to ensure reliable injection-seeding, severely limiting the potential sensitivity of an airborne IPDA system.

1.5 Thesis Outline

This thesis reports the development of a IPDA LIDAR system for sensing anthropogenic methane sources with a high sensitivity and spatial resolution. It includes the development of a dual-pulsed, Q-switched Er:YAG laser that can be reliably injection-seeded to produce pulses tuned onto and off the methane absorption line plotted in Figure 1.6. This compact laser source overcomes the limitations of other methane DIAL transmitters, enabling it to be mounted in a light aircraft for broad-area mapping at a low altitude.

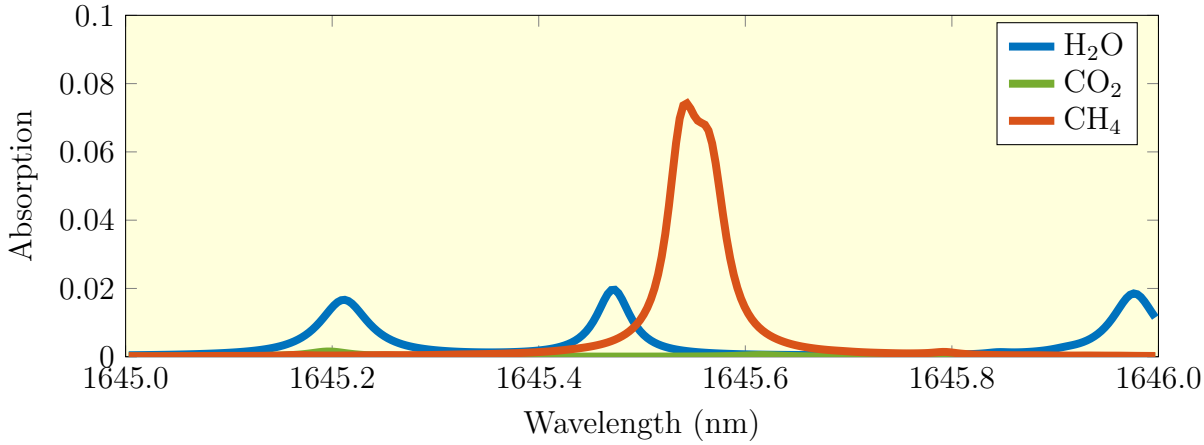

Figure 1.6: Dominant absorption lines of methane and other atmospheric constituents near the Er:YAG emission line calculated via the HITRAN 2012 database for an aerial observer at an altitude of 1 km.

We use a single Q-switched Er:YAG laser to generate high energy (1 mJ) short duration (100 ns) pulses. Wavelength tuning is achieved using the injection-seeding technique with a high-bandwidth control system to ensure reliable injection-seeding for operation in a high-vibration aircraft. The online wavelength will be tuned onto the 1645.55 nm absorption line and to avoid nearby absorption lines the offline wavelength will be between 1645.30 and 1645.40 nm.

We will use a novel throttled Q-switch technique to produce two pulses from a single pump interval with a separation of 2 µs. This small separation maximises the spatial overlap of these pulses, which reduces error caused by variations in the scattering surface.

We implement a receiver that provides a high single-shot sensitivity, mitigating the need for averaging and hence improving the spatial resolution. For this thesis, we use a commercial telescope capable of imaging the pulse footprint at the ground to a photodetector. This photodetector must have a large active diameter (>1 mm), high-bandwidth (>10 MHz), high-gain (>10,000) and low-noise.

Directly generating both pulses from a single Er:YAG laser increases system efficiency and reduces complexity in comparison to OPG sources. The reduced weight and volume of our system facilitates mounting in a small aircraft, thus reducing the operating costs while still offering an improved measurement sensitivity. This would offer increased incentives for natural gas providers to routinely inspect their infrastructure, reducing global methane emissions and improving profits.

In Chapter 2 the injection-seeded Er:YAG slave laser is characterised, and issues with the injection-seeding performance of this system are discussed. In Chapter 3 we introduce a numerical model capable of predicting, and thus enabling us to overcome, the limitations of the injection-seeded Er:YAG slave laser. Chapter 4 describes the control systems used to ensure reliable injection-seeding of two pulses at the methane online and offline wavelengths with a temporal separation of 2.3 µs. Finally, in Chapter 5, I describe the design and construction of a low-noise LIDAR detection system optimised for long-range methane sensing. I demonstrate that this system can measure the background concentration of methane through a 300 m atmospheric column with a world-leading measurement sensitivity.

Chapter 2

A Q-Switched Er:YAG Laser for Remote Methane Sensing

2.1 Introduction

For airborne methane DIAL we require a laser capable of producing pulses with an energy of 1 mJ and width of 100 ns at a Pulse Repetition Frequency (PRF) of 1 kHz. The laser must also be capable of producing two pulses with a small temporal separation and wavelength tunability around a methane absorption line. To meet these specifications a free-space Q-switched Er:YAG laser was constructed by Myles Clark of the University of Adelaide in a PhD project that preceded the research presented in this thesis.

This laser is capable of producing Q-switched pulses at the erbium line-centre wavelength of $\lambda = 1645.15$ nm which met the pulse-energy and pulse-width requirements. Myles investigated the feasibility of a technique known as injection-seeding to tune the wavelength onto the nearby methane absorption line of $\lambda = 1645.55$ nm. This technique allows the control of the spectral properties of a high-power 'slave' laser by injection of a low-power 'master' laser. Despite extensive research and development reliable injection-seeding of every pulse in a train was not realised during his candidature.

Building upon the foundations laid by Myles Clark my preliminary research focused on understanding and overcoming the limitations of the injection-seeded slave laser. In this chapter I present a complete description and characterisation of the laser system and highlight the unreliable injection-seeding performance. All measurements presented in this chapter, unless explicitly stated otherwise, were undertaken by myself.

A description and characterisation of the slave laser is given in Section 2.2. In Section 2.3 we describe the injection-seeding technique and the optics used to efficiently couple the master laser light into the slave laser resonator. The pulse properties used as a metric for the quality of injection-seeding are also discussed. A characterisation

of the master lasers used in this project is given in Section 2.4. The electronics used to produce two Q-switched pulses with a small temporal separation is described in Section 2.5. This chapter concludes with an analysis of the poor injection-seeding performance of the Er:YAG laser in Section 2.6. A solution to the injection-seeding limitations is outlined in Chapter 3.

2.2 The Slave Laser

A diagram of the ring-resonator designed and constructed by Myles Clark is shown in Figure 2.1. Our research group have used the ring-resonator geometry to produce injection-seeded Q-switched pulses from an Nd:YAG laser [113–115]. This will be crucial for tuning the laser wavelength onto a methane absorption line.

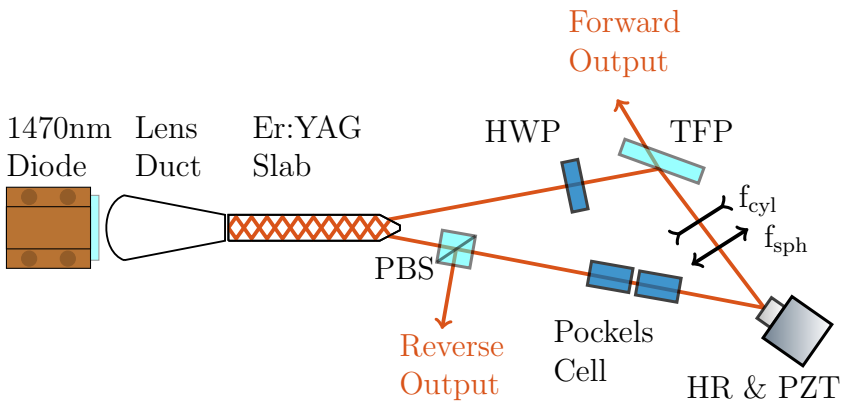

Figure 2.1: A schematic of the Q-switched laser ring resonator highlighting key components including the Thin-Film Polariser (TFP), Polarising Beam Splitter (PBS), Half-Wave Plate (HWP) and a High-Reflectivity (HR) mirror mounted on a Piezo-electric Transducer (PZT). Note the lenses have focal lengths of $f_{\text{sph}} = 100\,\text{mm}$ and $f_{\text{cyl}} = -200\,\text{mm}$.

To achieve lasing near the methane absorption line $\lambda = 1645.55\,\text{nm}$ we use Er:YAG as a gain medium. This consists of yttrium aluminium garnet (YAG, $Y_3Al_5O_{12}$) in which some of the trivalent aluminium ions are replaced with the laser active erbium ions (Er^{3+}). The high thermal conductivity of YAG offers improved cooling and allows scaling to high average power operation.

The Er:YAG crystal uses the Co-Planar Folded Zig-Zag Slab (CPFS) geometry end-pumped with a 1470 nm diode bar. The CPFS geometry is described in Section 2.2.1 and the end-pumping scheme is described in Section 2.2.2. Q-switched pulses are generated using a Rubidium Titanyl Phosphate (RTP) Pockels Cell (PC) as described in Section 2.2.3. A characterisation of the Q-switched lasing performance is given in Section 2.2.4. A mathematical analysis of the fundamental laser mode is described in Appendix B.

2.2.1 The CPFS Gain Medium

The slave laser uses the CPFS geometry pioneered by Richards and McInnes [116] for side-pumped Nd:YAG lasers. The entrance and exit faces are cut at Brewster angle to minimise loss, thus ensuring the light is π-polarised within the gain medium. The laser mode propagates along the slab via Total-Internal Reflection (TIR), thus removing the need for optical coatings. This zig-zag path increases the overlap of the laser mode with the pumped region, facilitating an efficient lasing performance [117].

The dimensions of the CPFS gain medium used in the slave laser is shown in Figure 2.2. To increase the pump absorption through the short slab length of 35.6 mm the YAG crystal is doped with 0.5% erbium ions. This higher concentration will increase the detrimental energy-transfer upconversion effect, discussed in further detail in Chapter 3, but will ensure sufficient pump absorption for high-average power lasing. The narrow slab width increases the pump intensity and hence the available gain. In this geometry the laser mode completes 16 TIR bounces per-side and one on the back face for a total of 33 TIR bounces.

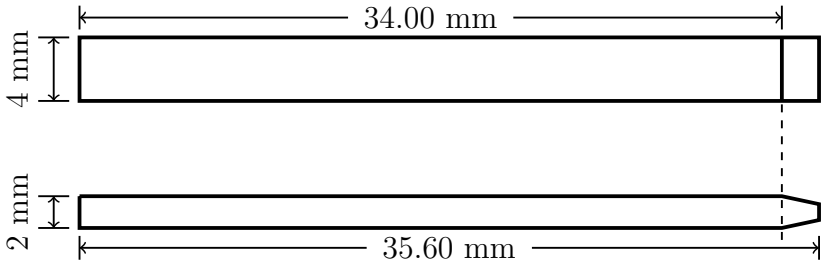

Figure 2.2: Scale diagram of the CPFS geometry used in the slave laser.

To extract excess heat from the slab it is conductively cooled by mounting between two copper blocks. Internal water channels are machined into both blocks to allow cooling with an external water cooler. Layers of indium are positioned between the slab and the copper to minimise stress and facilitate efficient heat transfer. The water chiller was operated at a temperature of 16°C to collapse the degenerate energy levels within the ground state manifold and increase the available gain [118]. Reducing the water temperature further will cause condensation to form on the crystal once it reaches the 'dew-point'. Er:YAG laser systems have been presented in literature that operate at cryogenic temperatures [119, 120] to increase the Stokes efficiency and minimise thermal stress. However, the increased complexity and size of these cryogenic systems limit their applicability in airborne operation.

2.2.2 Pump Source

In Er:YAG ions can be excited from the ground-state to the upper lasing level via 'resonant pumping' at either 1470 or 1532 nm. Direct excitation to the upper lasing level ensures a high quantum efficiency, minimising both thermally induced lensing and birefringence to facilitate efficient operation at a range of output power levels [121]. The absorption cross-section (σ_{abs}) of Er:YAG within this wavelength band is plotted in Figure 2.3.

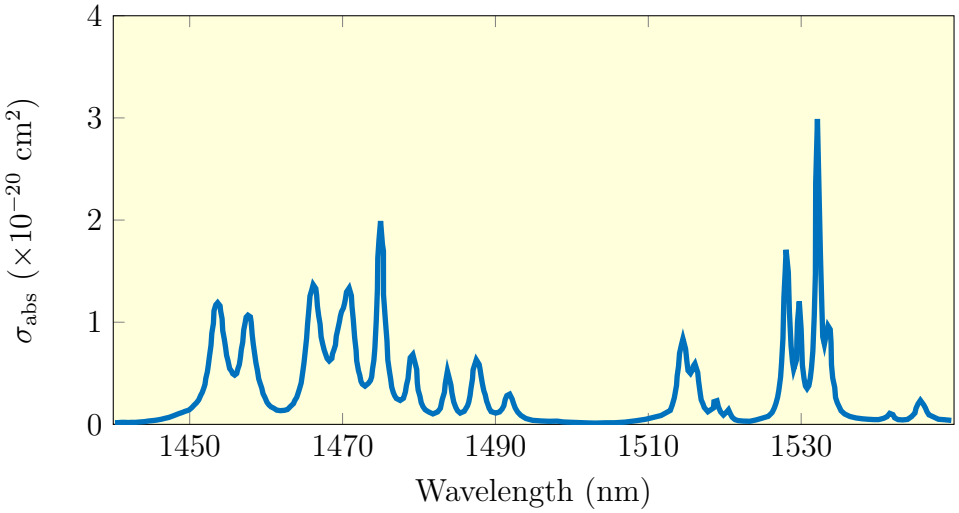

Figure 2.3: Absorption spectrum of Er:YAG at 300 K from Kudryashov *et al.* [122].

Two approaches, differing by the choice of pump-source, are commonly used to pump these absorption lines. The first is using Indium Gallium Arsenide Phosphide (InGaAsP) diode lasers operating at either 1470 or 1532 nm [123, 124]. By using compact laser diodes this approach has the attraction of simplicity, but is complicated by the low-brightness and broad-emission ($\approx$ 10 nm) of commercially available sources [125]. Thus imposing constraints on the crystal geometry, dopant levels and resonator design to maximise absorption and mode-matching in an end-pumped configuration. To efficiently pump the narrow 1532 nm absorption line, the laser diode must be stabilised by a volume Bragg grating [126].

Advancements in erbium-doped fiber lasers (EDFLs) have enabled the second approach, referred to as the hybrid fiber-bulk laser scheme, whereby a Er,Yb fiber laser operating at 1532 nm is used as the pump source [127–129]. The added complexity of this approach is offset by the advantages of these narrow-linewidth, high beam-quality sources which can access the narrow absorption line at 1532 nm. Thus simplifying the constraints on the resonator design and facilitating the potential for power scaling.

For compactness we employ the former approach; pumping with a 20 W 1470 nm diode (M3N-1470.20-20C) manufactured by *DILAS Diodenlaser*. The output is emitted

from a 10mm long horizontal bar consisting of 19 Indium Gallium Arsenide (InGaAs) emitters with a spectral width <12 nm. The vertical fast-axis is collimated using a microlens design to reduce the divergence to <8 mRad whilst the horizontal slow-axis has a divergence < 8°. The slow-axis is coupled into the slab using a lens-duct, this simple component overcomes the challenges of transforming a highly divergent pump source into a low-area for efficient end-pumping. In comparison to other pump-coupling options this is both cheap and easy to align whilst ensuring a homogenised output [130].

To remove excess heat from the diode it is mounted to a water cooled copper block. The temperature of the diode, and hence its emission wavelength, can be tuned by changing the water temperature. To facilitate heat transfer and minimise stress a layer of indium is placed between the copper block and the diode. The optical Power Spectral Density (PSD) was measured using a HP70004a Optical Spectrum Analyser (OSA) and is plotted in Figure 2.4. We observe a broad spectral emission with a peak at the absorption line of 1470 nm.

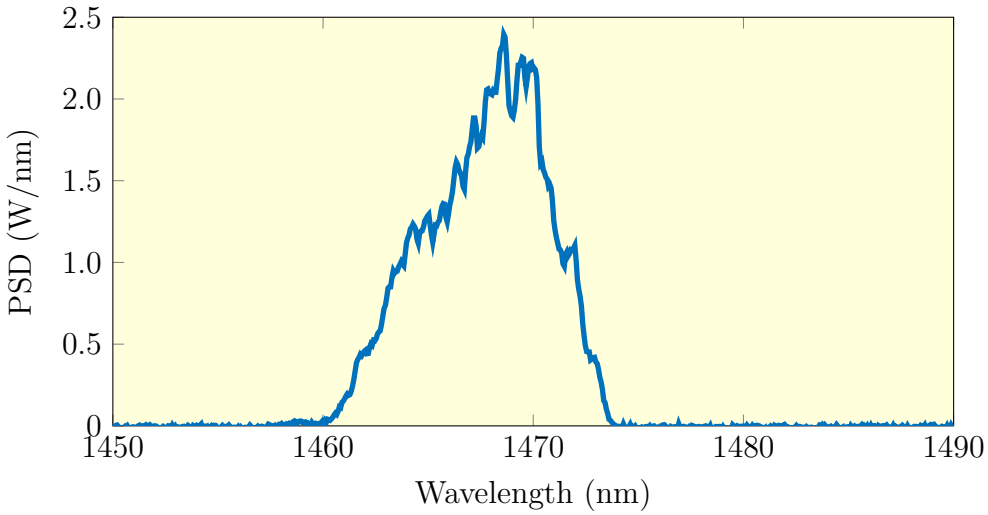

Figure 2.4: Measured optical spectrum of the pump diode at an output power of 20 W and a water temperature of 21°C.

2.2.3 Q-switched Operation

The polarisation dependent reflection and transmission of the TFP (PBS) combined with the PC forms the Q-switch for the counter-clockwise (clockwise) propagating eigenmode. Although the Brewster-angled faces of the slab are not critical for Q-switching they do provide high-loss to vertically polarised (σ) light. Hence, we only consider the eigenmode which is horizontally polarised (π) leaving the slab. Consider first the counter-clockwise propagating eigenmode with polarisation states illustrated below in Figure 2.5.

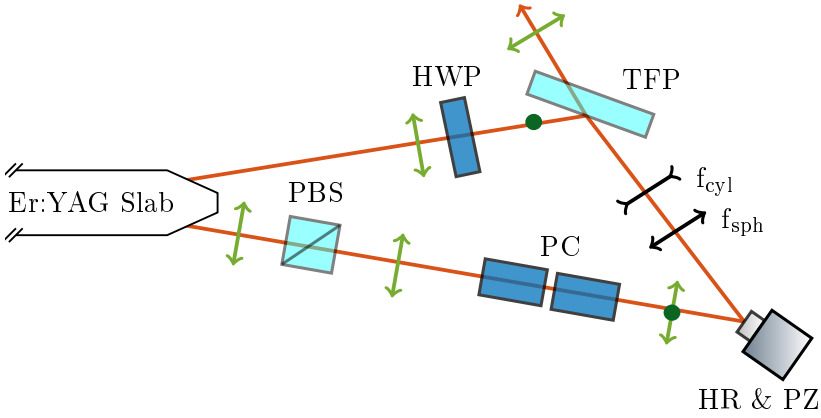

Figure 2.5: Schematic of the Q-switched laser mode highlighting the horizontal and vertical polarisation states of the counter-clockwise propagating eigenmode.

In the counter-clockwise propagating case the π-polarised light transmitted through the Brewster face is completely transmitted through the PBS and is then incident on the PC. The voltage applied to the PC determines the polarisation state of light incident on the TFP, thus determining the fraction that is reflected and transmitted. When no voltage is applied ($V_{PC} = 0$) the polarisation state is unchanged and the output-coupling (OC) is 100% (low-Q), when the half-wave voltage ($V_{PC} = V_{\lambda/2}$) is applied the output-coupling is 0% (high-Q) and for an intermediate voltage ($0 < V_{PC} < V_{\lambda/2}$) we will observe a partial output-coupling. Thus, the choice of voltage provides a means of dynamically tuning the output-coupling. Similarly, consider the clockwise propagating eigenmode with polarisation states illustrated below in Figure 2.6.

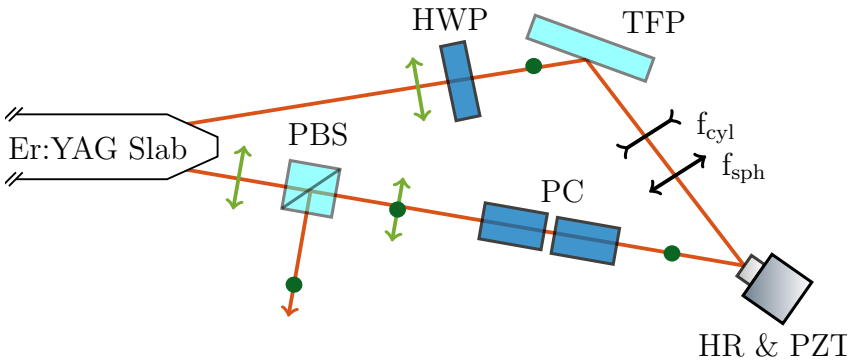

Figure 2.6: Schematic of the Q-switched laser mode highlighting the horizontal and vertical polarisation states of the clockwise propagating eigenmode.

In the clockwise propagating case the π-polarised light rotated to σ-polarised by HWP where it is completely reflected off of TFP and is then incident on the PC. The voltage applied to the PC determines the polarisation state of light incident on the PBS, thus determining the fraction that is reflected and transmitted. Similar to the counter-clockwise case when no voltage is applied ($V_{PC} = 0$) the polarisation state is unchanged

and the output-coupling is 100% (low-Q), when the half-wave voltage ($V_{PC} = V_{\lambda/2}$) is applied the output-coupling is 0% (high-Q) and for an intermediate voltage ($0 < V_{PC} < V_{\lambda/2}$) we will observe a partial output-coupling. A mathematical analysis of this output-coupling mechanism is described in Appendix C and is commonly used throughout this Chapter to calibrate the PC voltage directly to an output-coupling reflectivity.

2.2.4 Lasing Performance

The ring resonator was initially operated in Q-switched mode at a PRF of 1 kHz, however, it was observed that pulses were occasionally skipped. This indicates that a significant fraction of the available gain is extracted per pulse, causing the following pulse to be missed. By reducing the PRF to 100 Hz we observed a stable pulse train at a range of output-couplings. A plot of the pulse energy and pulse Full-Width Half Maximum (FWHM) as a function of the output-coupler reflectivity is shown in Figure 2.7.

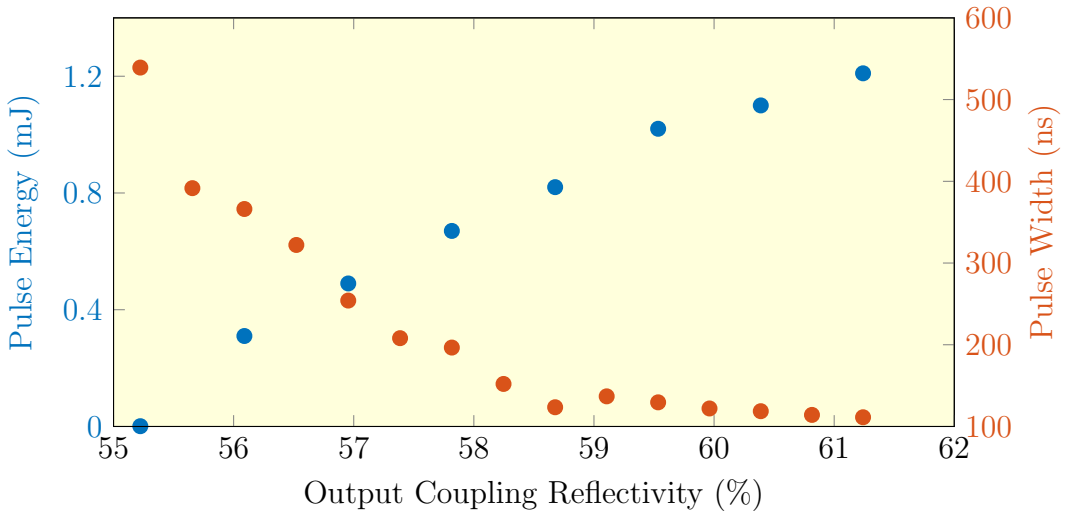

Figure 2.7: A measurement of the Q-switched laser pulse energy and FWHM at a PRF of 100 Hz and a pump power of 20 W

At an output-coupler reflectivity of 61.2%, corresponding to a PC voltage of 2.05 kV, we measure a pulse energy of 1.2 mJ and a FWHM of 105 ns. A trace of this Q-switched pulse, recorded on a 1 GHz oscilloscope (*Tektronix* MDO3104), is plotted in Figure 2.8. A pulse develops approximately 1.6 µs after the Q-switch is engaged. We observe a high-frequency beating between the longitudinal modes within the resonator superimposed on the pulse. A Fourier analysis of this data shows this has a frequency of 638 MHz - corresponding to the Free-Spectral Range (FSR) of the cavity.

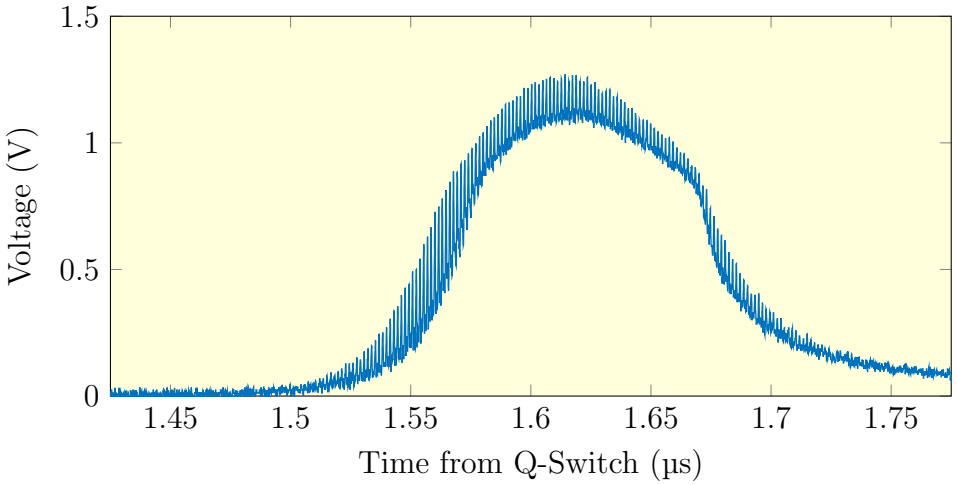

Figure 2.8: A Q-switched pulse generated from the laser with the PC set to 2.05 kV.

The optical spectrum of the Q-switched laser is shown at a range of pulse energies in Figure 2.9. This was measured using the HP70004a OSA with a Resolution Bandwidth (RBW) of 0.08 nm, a Video Bandwidth (VBW) of 10 Hz and a sensitivity of -90 dBm. We observe lasing at the erbium gain-centre wavelength of $\lambda = 1645.15$ nm with evidence of spectral broadening at higher pulse energies.

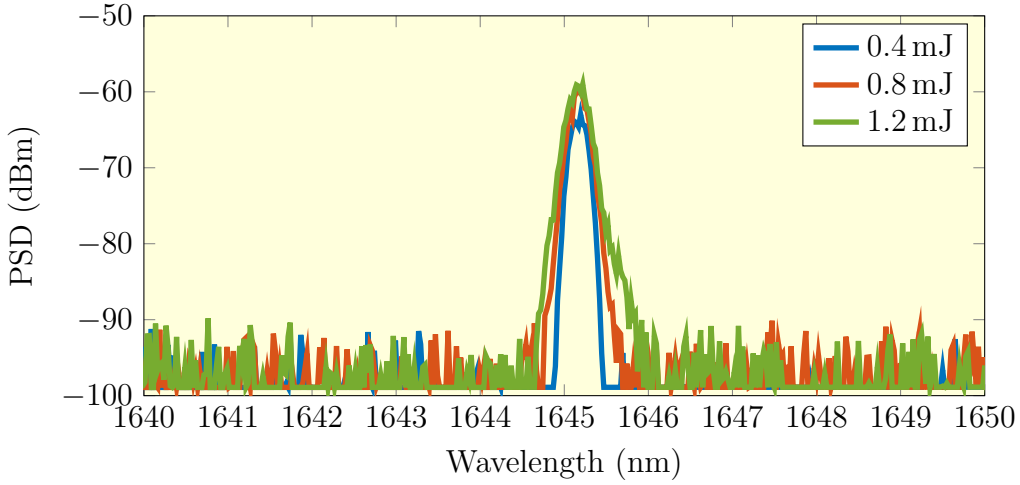

Figure 2.9: Measured optical spectra of the free-running slave laser.

2.3 Injection Seeding

Injection-seeding is a technique used to control the spectral properties of a high-power 'slave' laser via injection of a low-power 'master' laser [131]. This has advantages over other methods which implement intra-cavity wavelength control elements such as gratings, prisms, birefringent filters and etalons which tend to introduce relatively

high-loss - reducing the efficiency of the laser. These elements often have low damage thresholds, further limiting their applicability in high-power laser systems.

In a Q-switched laser system there must be 'seed' source from which a pulse develops, in the absence of externally injected light this is provided by the natural spontaneous emission that occurs within the laser gain medium. Light injected from an external master laser acts to compete as an alternative seed source. If the injected seed is large enough and its wavelength is resonant with a longitudinal mode of the slave laser then a pulse will develop from the master laser, depleting the available gain before the natural pulse develops. In this case, the pulse will mimic the properties of the master laser. We propose to use this technique to control the wavelength of both the online and offline pulses for use in methane DIAL.

2.3.1 The Injection Arm

The intra-cavity PBS of the slave laser is an available injection port for the master laser, the optics used to efficiently couple the master laser is illustrated in Figure 2.10. Light from the fiber-coupled master is collimated and passed through a HWP that is orientated to maximise the reflection off the intra-cavity PBS. Light leaving the master laser passes through a lens ($f_1 = 200\,\text{mm}$) which focuses the beam into an Acousto-Optic Modulator (AOM) which induces a 40 MHz frequency shift which is useful for heterodyne measurements discussed later in Section 2.3.2. The lenses f_2 and f_3 are used as a telescope to mode match the master laser to the slave resonator. Following this a free-space isolator ensures the master laser is protected from the reverse wave pulse from the slave laser resonator.

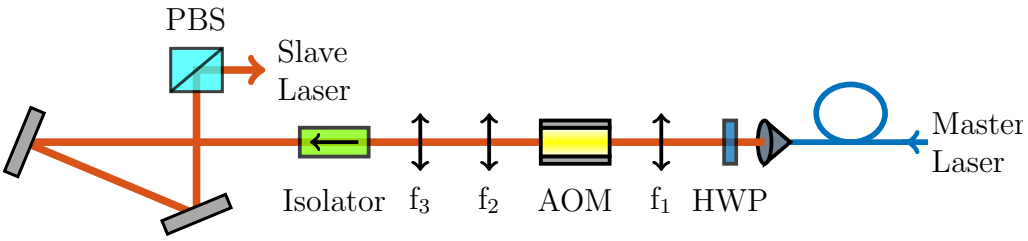

Figure 2.10: A schematic of the injection seeding arm.

To facilitate efficient injection seeding the master and slave must be adequately mode-matched. By imaging the slave laser mode at multiple points using an InGaAs camera (*Goodrich* SU320KTS-1.7RT) and applying a fitting algorithm, a $1/e^2$ half-width in both the horizontal (ω_x) and vertical (ω_y) plane was extracted. Using this, the lenses $f_2 = 200\,\text{mm}$ and $f_3 = 150\,\text{mm}$ were positioned to optimise the modal overlap. The measured mode of both the slave and the master, as well as the corresponding M^2 fit, is plotted in Figure 2.11.

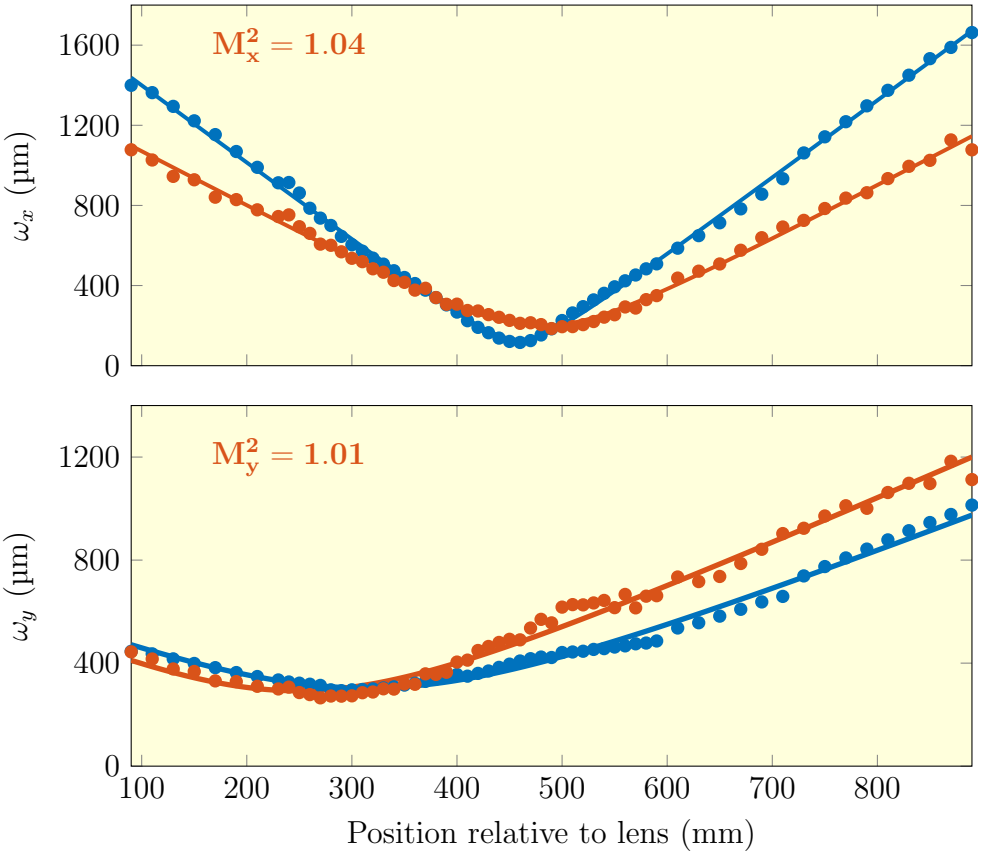

Figure 2.11: Measured beam widths and M^2 fit of the master and slave lasers in the horizontal and vertical planes. The M^2 values presented are for the slave laser output mode.

Evidently there is a high degree of overlap, mathematically, the quality of mode matching can be quantified with the overlap integral.

$$\eta = \frac{\left|\int E_1^* E_2 \mathrm{dA}\right|^2}{\int |E_1|^2 \,\mathrm{dA} \int |E_2|^2 \,\mathrm{dA}} \tag{2.1}$$

Where E_1 and E_2 are the complex electric fields of the slave laser and master laser respectively. This calculation is complicated by the astigmatic nature of both the slave and master mode, however, we can extend the common description of stigmatic Gaussian beams to describe simple astigmatic beams. The Gaussian beam can be decomposed into two independent stigmatic beam representations - one in each plane of symmetry [132]. This allows the complex electric field to be described using the following expression [133].

$$E(\mathbf{r}, z) = E_0(z) \exp\left[-i\left(\phi_{ac} + k\left(\frac{x^2}{2q_x(z)} + \frac{y^2}{2q_y(z)}\right)\right) - \phi_g(z)\right] \tag{2.2}$$

Where k is the wavenumber, $q_{x,y}$ is the complex beam parameter in the horizontal/vertical plane, ϕ_{ac} is the accumulated phase relative to a common reference point

and ϕ_g is the gouy phase, for simplicity this is approximated as the average between the two planes and is given by.

$$\phi_g(z) = \frac{1}{2}\left[\arctan\left(\frac{z - z_{0x}}{z_{Rx}}\right) + \arctan\left(\frac{z - z_{0y}}{z_{Ry}}\right)\right] \tag{2.3}$$

Where $z_{0x,y}$ is the waist position in the horizontal/vertical plane and $z_{Rx,y}$ is the Rayleigh range in the horizontal/vertical plane. Combining Equations 2.1, 2.2 and 2.3 the overlap integral is calculated to be $\eta = 0.88$ - suggesting a high degree of overlap between the master and slave modes.

2.3.2 Quantifying Injection Seeding

There are three pulse properties we use to determine whether injection-seeding occurred: the reduction in build-up time, the frequency of a heterodyne beat and the suppression of the reverse wave. All three metrics are discussed in further detail in the following sections.

Heterodyne Beat Metric

When successfully injection-seeded the frequency of the slave laser output will closely match that of the injected master laser. The heterodyne detection technique devised by Fee *et al.* [134] is a convenient tool to determine the relative frequency of the master and slave laser. For simplicity and ease of alignment we use an all-fiber configuration as illustrated in Figure 2.12.

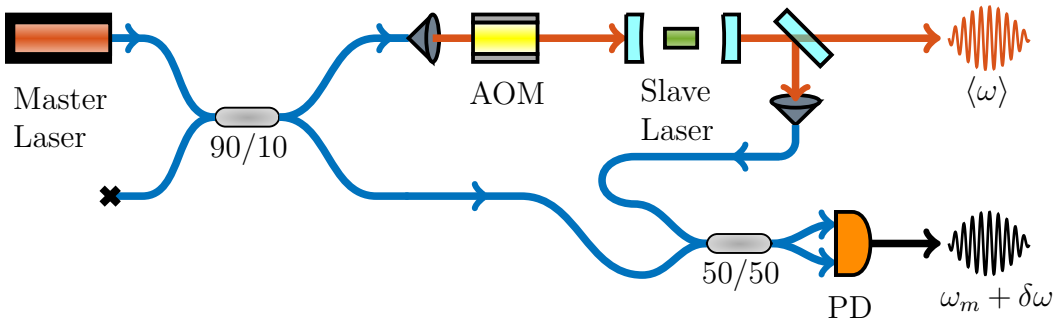

Figure 2.12: Schematic of the optical heterodyne system for measuring the frequency jitter of the injection-seeded laser on a pulse-to-pulse basis.

The master laser is split using a fiber-splitter, a large fraction (90%) is frequency shifted by $\omega_m = 40\,\text{MHz}$ using an AOM before it is injected into the slave resonator. We define the slave laser to have an average output frequency $\langle\omega\rangle$, which is instantaneously offset from the master laser frequency ω_0 by $\delta\omega$. This frequency offset is measured by coupling a small-fraction of the pulsed output into fiber and combining it with the

unshifted master laser using a 50/50 fiber-splitter, resulting in a beat-note which is measured on the *Newport* 1817-FC fiber-coupled balanced photodetector (PD). Its power spectrum is then calculated using a Fourier transform.

Build-Up Time Metric

The pulse build-up time is defined as the time taken for a pulse to develop after the Q-switch is engaged. When the slave laser is successfully injection-seeded it will exhibit a reduction in the build-up time in comparison to the corresponding unseeded build-up time. This occurs because the pulse will develop from the regenerative amplification of a pre-populated mode rather than from spontaneous emission.

A theoretical analysis of injection-seeding presented by Barnes *et al.* [135] states that a pulse is considered 'seeded' if it is over before the pulse which evolves naturally from spontaneous emission can extract a significant amount of energy. By defining the unseeded build-up time as τ_n, the seeded build-up time as τ_s and the pulse width as τ_p we represent this criteria schematically in Figure 2.13.

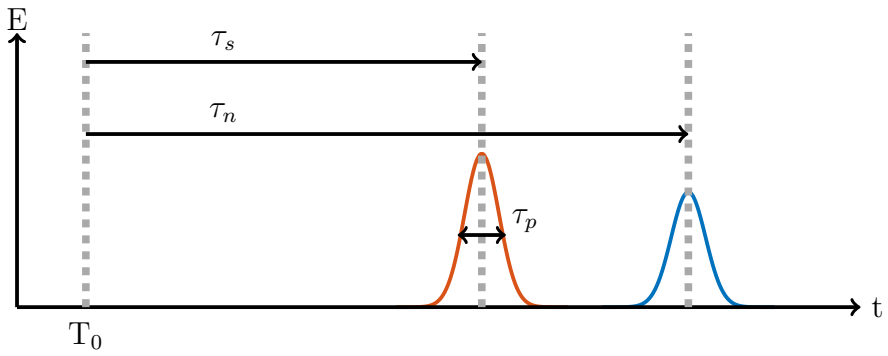

Figure 2.13: A schematic of the build-up time metric used to quantify injection-seeding, highlighting the build-up time reduction of the seeded pulse in comparison to the unseeded pulse. The Q-switch is engaged at time T_0.

Alternatively, this criteria can be represented mathematically.

$$\tau_s < \tau_n - \tau_p \tag{2.4}$$

Reliable injection-seeded laser systems have been described in literature which adjust the cavity length to maintain a minimum average build-up time [136–138].

Reverse Wave Suppression Metric

In a ring resonator there exists two counter propagating modes which compete for gain, we denote these as the forward (counter-clockwise) and reverse (clockwise) waves. In the absence of directional dependent components both modes will experience the same round-trip gain, hence pulses of similar energy and build-up time will be produced

in both directions. When successfully injection-seeding one direction, in this case the forward wave, a significant fraction of the gain will be extracted before the reverse wave has developed. Thus the reverse wave should be significantly suppressed in comparison to the forward wave.

This metric has been implemented by Ertel *et al.* [139] to quantify the efficiency of an injection-seeded Ti:Sapphire laser system. By measuring the ratio of the pulse energy in the forward E_{fwrd} and reverse E_{rvrs} directions they define the seeding efficiency as.

$$\eta_{seed} = 1 - \frac{E_{\text{rvrs}}}{E_{\text{fwrd}}} \tag{2.5}$$

We measured the reverse-wave using the *Thorlabs* DET01CFC fiber-coupled photodetector positioned at the unused port of the 90/10 fiber-splitter illustrated in Figure 2.12.

2.4 Master Laser Characterisation

For efficient injection seeding a narrow linewidth and highly stable master laser is critical, additionally, we require a laser that is tunable around the 1.6 µm wavelength band and insensitive to mechanical vibrations. There are a variety of commercially available sources including External Cavity Diode Lasers (ECDL) [140], Distributed Bragg Reflector (DBR) lasers [141, 142] and Distributed Feedback (DFB) diode lasers [143] which may be suited for this application.

Two master lasers were considered during this project; a DFB diode laser from *Sacher Lasertechnik* (DFB-1644-003) and an ECDL from *Yenista Optics* (T100-1620AR) - their optical properties are given in Table 2.1.

	DFB-1644-003	T100-1620AR
Type	DFB	ECDL
Power	3 mW	4 mW
Centre-Wavelength	1644 nm	1620 nm
Tuning Range	3 nm	100 nm
Side-mode Suppression	-	100 dB
Linewidth	10 MHz	150 kHz
Modulation Band	DC to 100 MHz	50 Hz to 50 MHz

Table 2.1: Specified optical properties of the master lasers used for injection-seeding.

In this section we will characterise the optical spectra and frequency noise of both master lasers to determine which is more suitable for injection-seeding.

2.4.1 Master Laser Optical Spectrum

The measured optical spectra of both master lasers is plotted in figure 2.14. This was recorded using the HP70004a OSA with a VBW of 20 kHz, a RBW of 0.08 nm and a noise floor of -60 dBc.

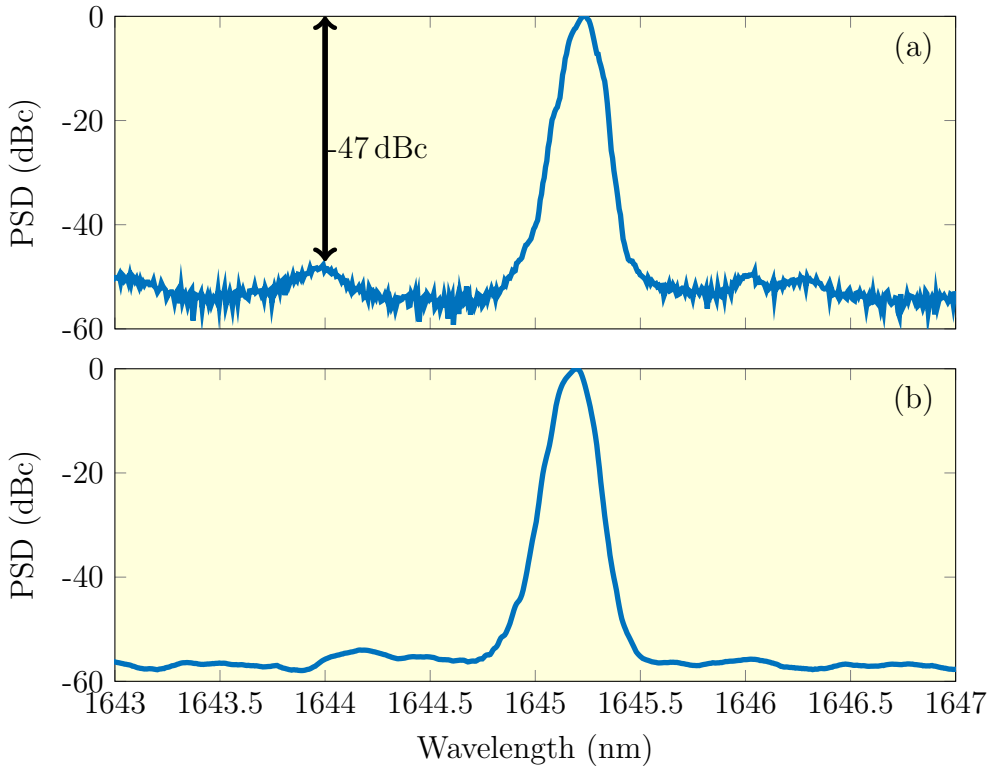

Figure 2.14: Measured optical spectra of (a) the DFB and (b) the ECDL master laser.

Both lasers can tune around the methane absorption line $\lambda_{on} = 1645.55$ nm as required. The DFB exhibits background Amplified Spontaneous Emission (ASE) which is 49 dB to 56 dB lower than the primary mode and a side-mode suppression of -47 dBc. Both the ASE and side-mode suppression of the ECDL are limited by the measurement noise floor.

2.4.2 Master Laser Frequency Noise

The Pound-Drever-Hall (PDH) technique provides a direct means of measuring the frequency noise of a semiconductor laser, a detailed discussion of this technique is given in Appendix D. By generating an error signal with a slope denoted D_s (V/Hz) voltage noise at the error point can be directly calibrated to a frequency noise. In comparison to other measurement techniques, such as FM spectroscopy in which the 3 dB point of a Fabry-Perot cavity resonance dip is used as a frequency discriminator, PDH provides a well-defined discriminator signal with high-linearity.

The frequency noise measurement system is illustrated in Figure 2.15. The Fabry-Perot cavity used in this system (*Thorlabs* SA210-14A) has a FSR of 10 GHz and the rear mirror is mounted on a PZT. A mode-matching lens $f_+ = 100$ mm is introduced to couple efficiently into the cavity. The polarisation of the reflected light is rotated by a Quarter-Wave Plate (QWP) and is then incident on a PD (*Thorlabs* DET01CFC). The corresponding electrical signal is demodulated with the Local Oscillator (LO), generating an error signal at V_{out}.

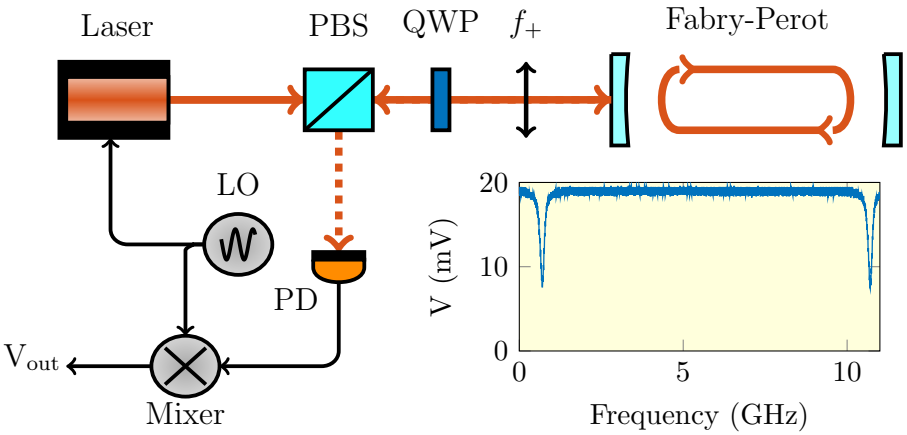

Figure 2.15: A schematic of the frequency noise measurement system. The inset graph illustrates the output signal as the cavity is scanned across multiple resonance dips, this is used to calibrate the frequency axis.

The error signal generated using this system, plotted in Figure 2.16, exhibits a well-defined linear region centred at zero.

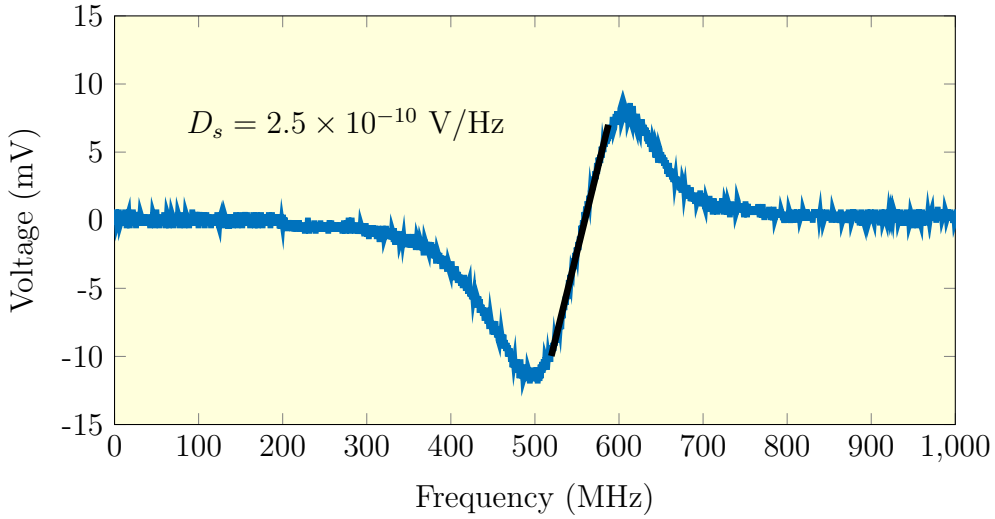

Figure 2.16: The error signal generated from the Fabry-Perot cavity used to calibrate voltage noise to master-laser frequency noise. The linear fit and corresponding slope are also illustrated.

Using the *Agilent* 89410A spectrum analyser we calculate the voltage noise power spectral density and convert this to a frequency noise power spectral density $S_\nu(f)$ with units of $\mathrm{Hz}/\sqrt{\mathrm{Hz}}$. No active servo control is used to keep the laser on resonance, instead we rely on the laser sitting on resonance over the measurement time. The measured frequency noise of the DFB master laser is plotted in Figure 2.17.

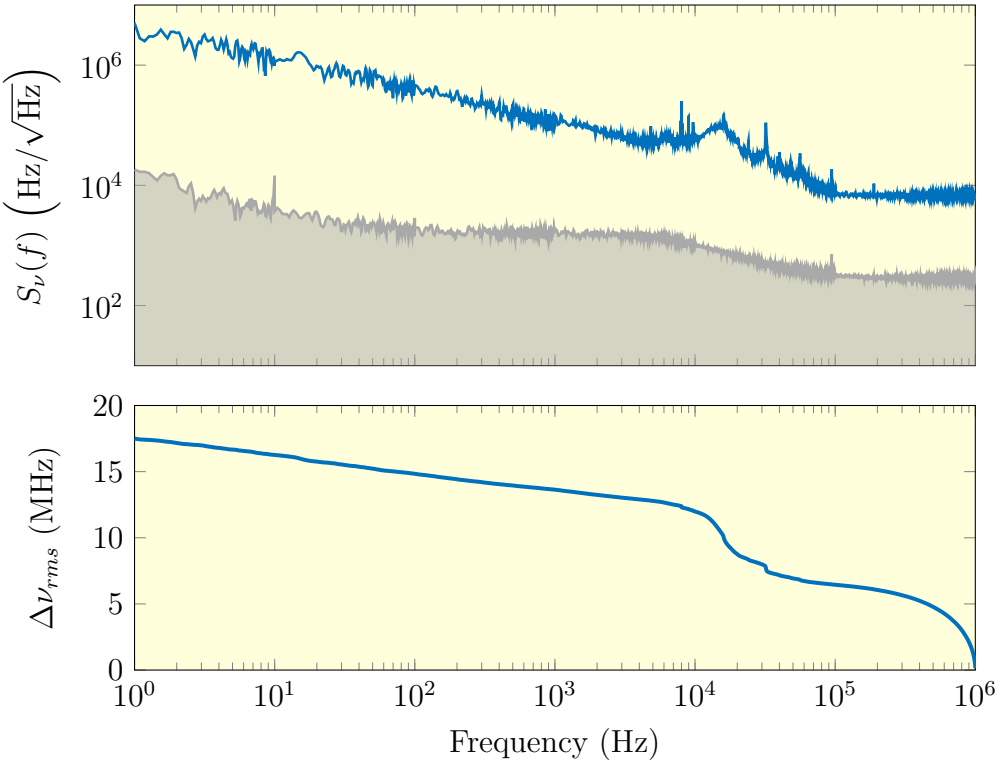

Figure 2.17: Frequency noise of the DFB laser measured using the PDH technique as the laser sits on resonance, the grey shaded area is the noise floor of the measurement.

We observe broadband frequency noise which is dominated by a $1/f$ component, this is consistent with experimental studies [144, 145] which attribute this to current noise on the diode driver. This noise can be reduced by decreasing the drive current, however, the Schawlow-Townes-Henry theory [146] states that this will cause the high-frequency Gaussian white noise component to increase.

The measured frequency noise of the ECDL master laser is plotted in Figure 2.18. The RMS frequency noise indicates that it is dominated by low-frequency spurious components. From discussions with the manufacturer the low-frequency noise peaks are attributed to cooling fans on the mainframe whilst the peak at 16 kHz and its higher harmonics are due to electrical noise. Since the frequency noise of the ECDL is significantly lower than the DFB it is used as the master laser in preliminary injection-seeding characterisation.

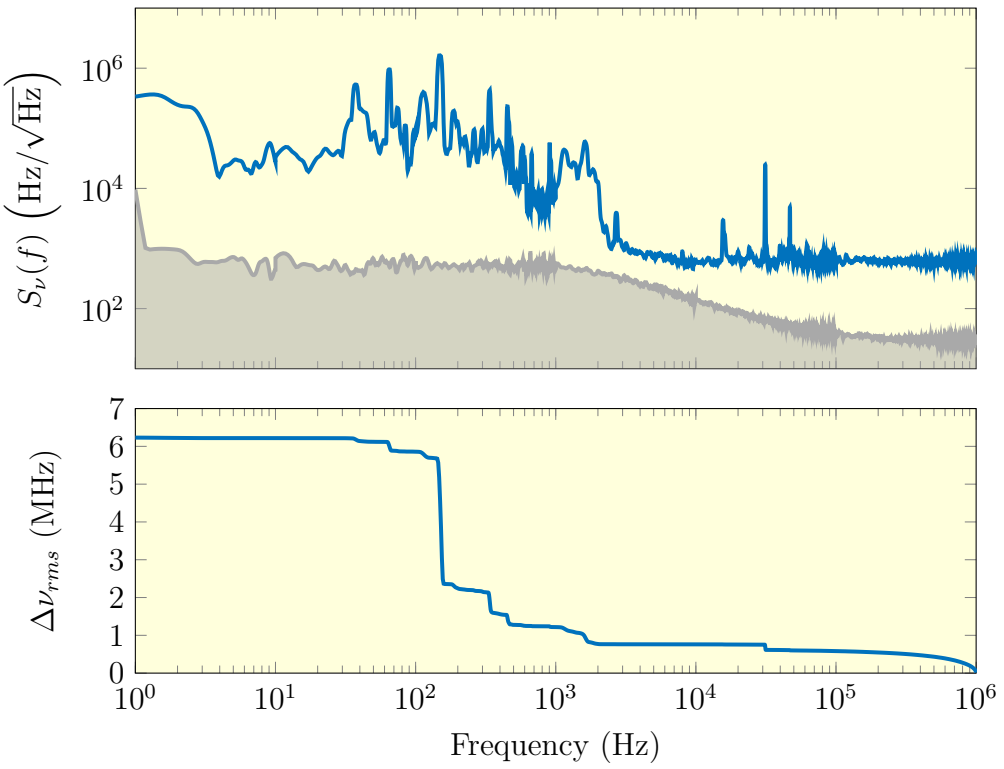

Figure 2.18: Frequency noise of the ECDL measured using the PDH technique as the laser sits on resonance, the grey shaded area is the noise floor of the measurement.

2.5 Dual Pulsed Operation

For airborne IPDA methane sensing we require a Q-switching technique capable of producing two pulses of two separate wavelengths with a small temporal separation. Although techniques for producing two controllable pulses from a Q-switched laser were described as early as 1969 [147] few systems have extended this for dual-wavelength operation. A comparison of these systems is listed in Table 2.2.

	[148]	[149]	[150]	[151]
Gain Medium	$Cr:BeAl_2O_4$	Cr:LiSAF	Ho:Tm:YLF	Ho:YLF
λ_{on}	727 nm	896.2 nm	tunable	2051.01 nm
λ_{off}	732 nm	898.2 nm	2051.25 nm	2051.25 nm
Pulse Energy	50 mJ (x2)	30 mJ (x2)	90/45 mJ	42/12 mJ
Pulse Width	250 ns	28 ns	200/350 ns	33/74 ns
PRF	10 Hz	1 Hz	10 Hz	303.5 Hz
Pump-Source	Flash lamp	Flash lamp	Diode	Fiber laser
Q-Switch	AOM	PC	-	AOM
Δt_{off}	55 µs	82 µs	150 µs	250 µs

Table 2.2: A comparison of published dual-pulsed, dual-wavelength laser systems.

Bruneau *et al.* [148] described an alexandrite laser for water vapour sensing that achieved wavelength selectivity using a birefringent filter and a PC. Intra-cavity etalons allow only two resonator modes to lase, these two modes correspond to the online and offline wavelengths. Selectivity of these adjacent modes is achieved by inducing a voltage dependent phase difference using the birefringent filter and PC. An AOM is then used to Q-switch twice, giving a pulse separation of 55 µs chosen to maximize the output laser energy.

Chang-Shui *et al.* [149] report a flash-lamp pumped Cr:LiSAF laser that achieves wavelength selectivity by switching between two separate resonator arms using a PC and a TFP. Four separate prisms are located within each arm to tune the gain to λ_{on} and λ_{off}. During optical pumping the quarter-wave voltage is applied to the PC to produce high-loss, by switching this to the half-wave voltage the loss is decreased and a pulse is generated from one resonator arm. Following this, the PC is switched to zero volts generating a pulse from the other arm with an offset of 82 µs. This time separation is chosen to ensure the energies of both pulses are equal.

Refaat *et al.* [150] report a Ho:Tm:YLF Q-switched laser for airborne CO_2 sensing based upon a system developed by Yu *et al.* [152]. The slow energy transfer between the Tm and Ho energy levels [153] is exploited to efficiently utilise the pump energy - producing two high-energy pulses from a single pump pulse. The pulse delay is set to 150 µs to maximize the energy extraction and wavelength selectivity was achieved by injection-seeding both pulses at separate wavelengths.

Gibert *et al.* [151] describe a Ho:YLF laser which does not exploit this energy transfer processes. Instead, two low-energy pulses are amplified using a Master Oscillator Power Amplifier (MOPA) configuration to scale the pulse-energy for space-borne CO_2 sensing. The pulse delay of 250 µs is limited by the control systems used to achieve injection-seeding of both the online and offline pulses, the details of this system are discussed further in Chapter 4.

The temporal separation of these dual-pulsed systems does not meet the requirements of our airborne IPDA system. In this section we describe a Q-switch design capable of producing two pulses separated by 2 µs; Section 2.5.1 describes the timing of the dual-pulse sequence and Section 2.5.2 describes the Q-switch driver.

2.5.1 Q-Switch Timing

The proposed sequence of the dual-pulse Q-switch is illustrated in Figure 4.34. At time T_0 the trigger arrives and activates the High-Voltage (HV) driver, applying a voltage HV_1 to the pockels cell. This reduces the output-coupling from 100% to OC_1, allowing a pulse to develop with a build-up time τ_1. Shortly after the falling edge of the pulse the PC is disengaged at time T_1, returning the PC voltage to 0 V. This delay is set by

a digital delay generator.

At time T_2 the HV driver is re-engaged, applying a higher voltage HV_2 to the PC. This produces a smaller output-coupling OC_2 allowing a pulse to develop despite the gain extracted by the previous pulse. In the case where the temporal offset between the two switching events is small ($T_2 - T_1$) the pulse delay is largely determined by the second pulse build-up time τ_2, which has been measured to be less than 2 µs. Following the second pulse the PC is disengaged at time T_3, returning the slave laser to a low-Q state in preparation for the following pulse-pair.

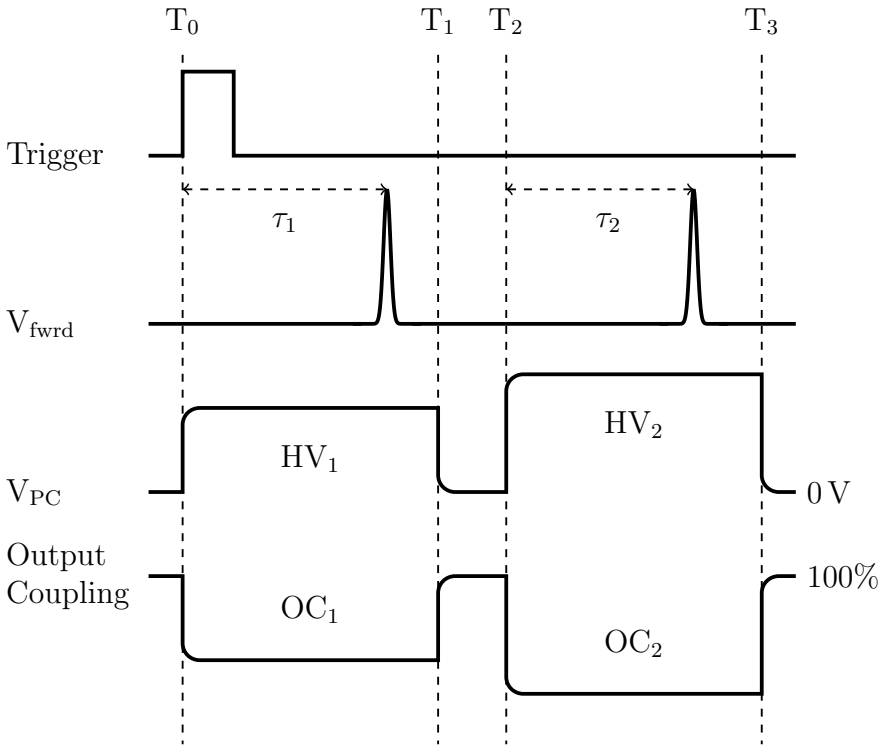

Figure 2.19: The proposed timing of the voltage applied to the pockels cell to produce two pulses with a small time separation.

2.5.2 Q-Switch Driver

To quickly charge, discharge and recharge the pockels cell to high voltages we use the circuit designed and constructed by Neville Wild, illustrated in Figure 2.20. Two high-voltage supplies, labelled HV_1 and HV_2, are connected to the PC via high-voltage switches controlled by digital logic inputs SW_1 and SW_2. The high-voltage supplies used are the 6A12-P4-I5 and 6A12-N4-I5 from Advanced Energy, capable of producing 0 to +6 kV and 0 to -6 kV respectively. To rapidly switch between the high-voltage supplies and ground we use two high-speed high-voltage double-pole switches (PHVSW-005V) from *Willamette*. The outputs of these switches are connected to the PC via 35 cm of RG316 cable.

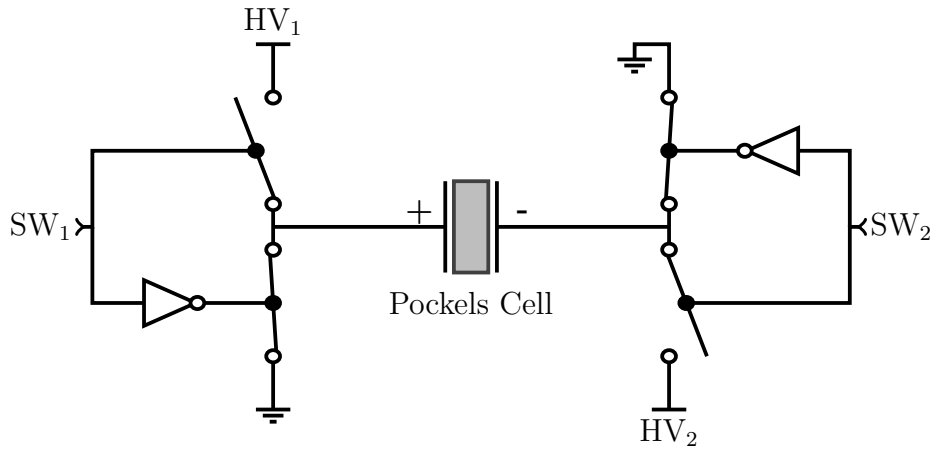

Figure 2.20: A schematic of the high-voltage switching circuit.

When SW_1 is engaged a positive voltage is applied to the cathode and the anode remains grounded whilst when SW_2 is engaged a negative voltage is applied to the anode and the cathode remains grounded. Thus ensuring that the electric field applied across the PC remains in the same direction. With this circuit configuration we were able to achieve a low switching delay ($T_2 - T_1 \approx 100\,\text{ns}$), ensuring high commonality between the online and offline pulses.

2.6 Preliminary Injection-Seeding Results

In this section we present a characterisation of the injection-seeded Er:YAG slave laser to determine the feasibility of reliably tuning the wavelength onto a methane absorption line. When injection-seeded there should be a clear relationship between the slave laser build-up time, heterodyne beat-frequency and reverse-wave suppression. Potentially enabling a servo to be implemented to ensure reliable injection-seeding. Although the data presented in this section does not exhibit the properties expected of an injection-seeded laser it forms the basis of a theoretical and experimental analysis presented in Chapter 3. This ultimately enabled a control system which ensured reliable injection-seeding to be implemented, as discussed further in Chapter 4.

The slave laser, operating at a PRF of 100 Hz, was injection-seeded with the Yenista ECDL tuned to erbium line-centre $\lambda = 1645.15\,\text{nm}$. The forward-wave, reverse-wave and beat-note are captured using the GaGe CSE1642 Data Acquisition (DAQ) system; a 125 MHz, 200 MS/s, 16-bit, 4-channel oscilloscope capable of continuous data collection. This device is selected for its low digitisation noise specifications and is used extensively to capture large data sets throughout this thesis.

Typical profiles of the unseeded and injection-seeded slave laser outputs are shown in Figure 2.21.

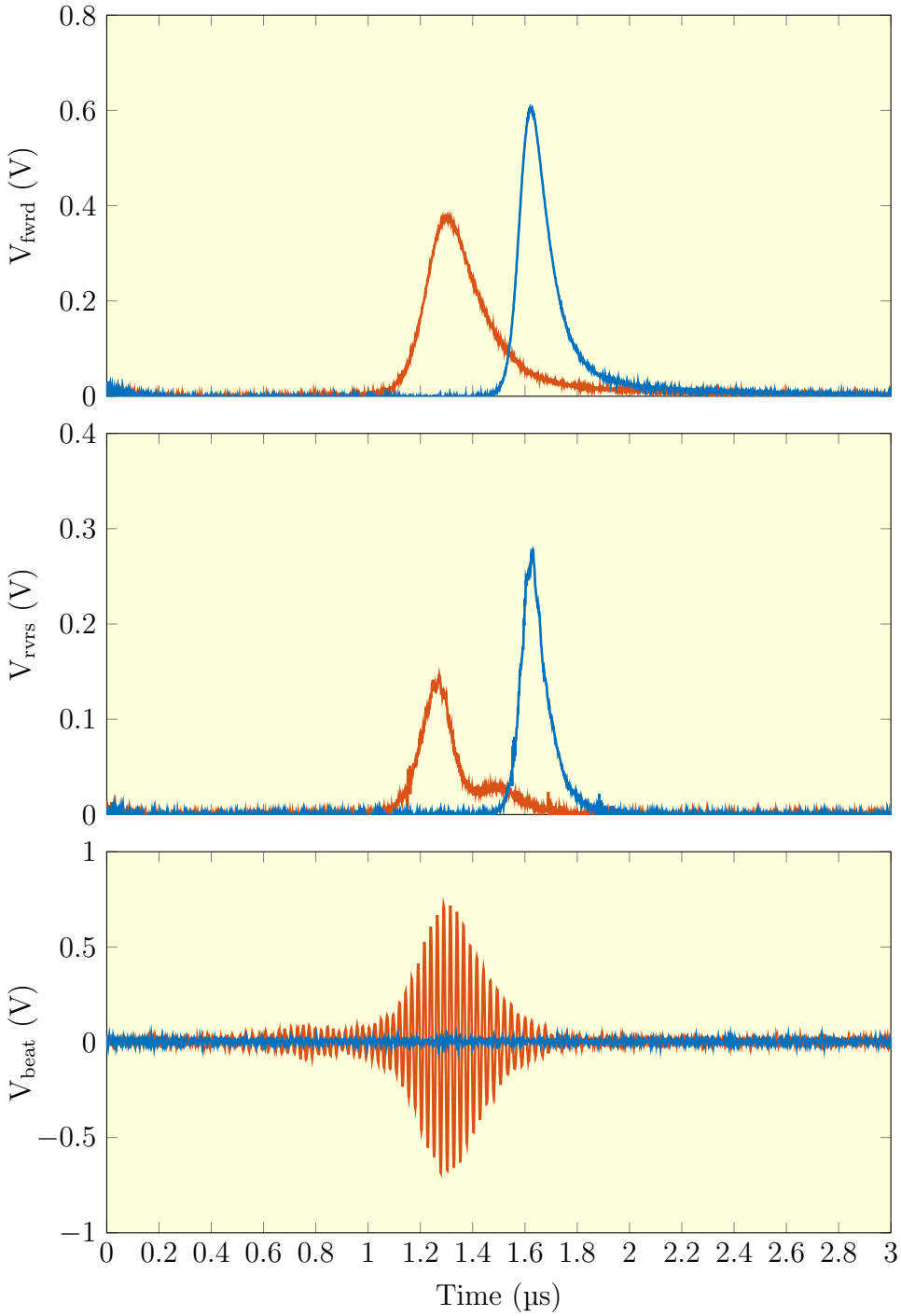

Figure 2.21: An example of the measured forward wave, reverse wave and beat signal of the free-running and injection-seeded slave laser.

The seeded forward-wave exhibits a reduction in build-up time but not a significant increase in the pulse energy. This is consistent with the incomplete suppression of the corresponding reverse-wave, indicating the slave laser is poorly seeded. Occasionally the slave laser produced two-pulses from a single Q-switch event when injection-seeded, an example of this is shown in Figure 2.22.

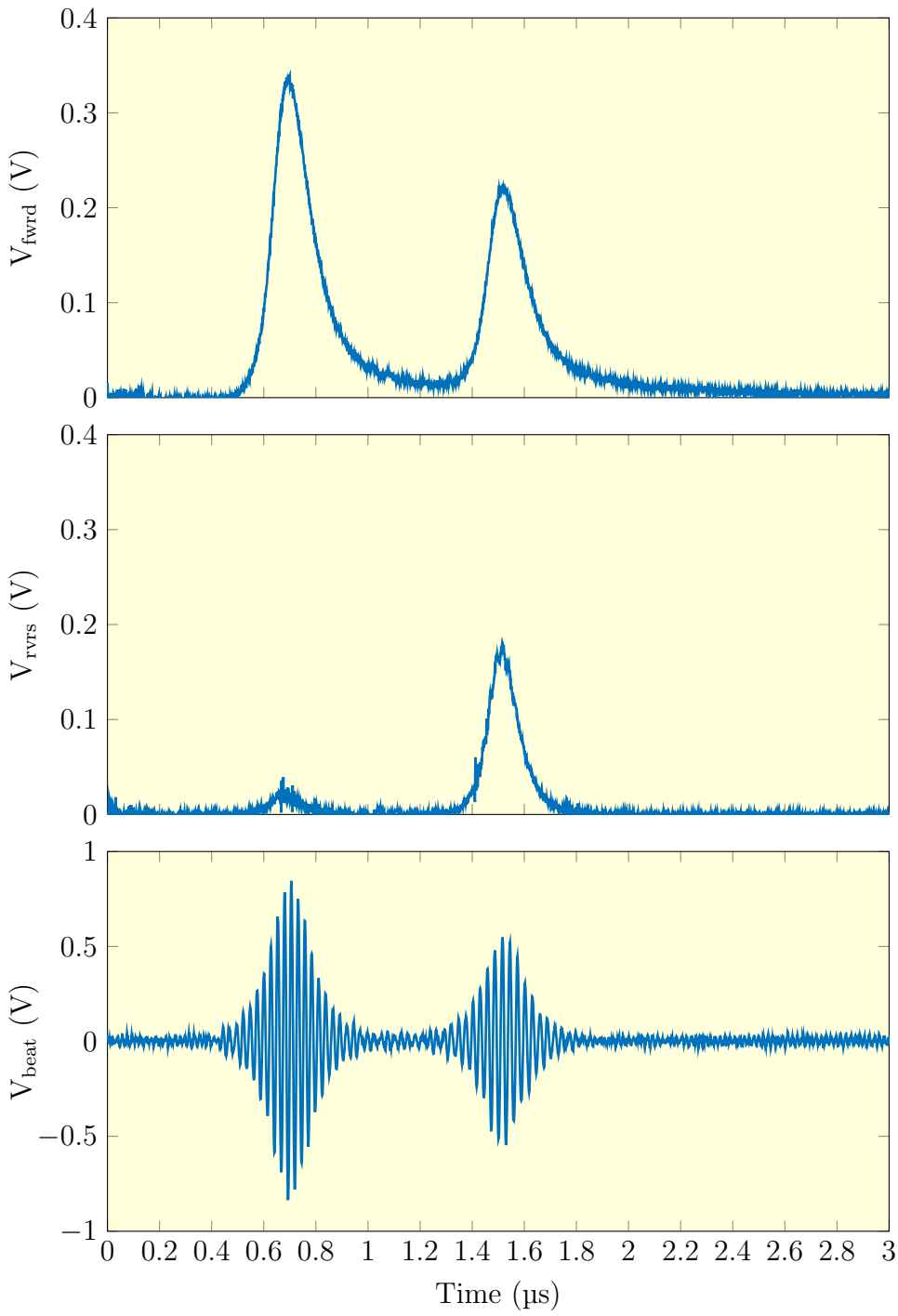

Figure 2.22: An example of the measured forward wave, reverse wave and beat signal of the injection-seeded slave laser that exhibited uncontrolled dual pulsing.

Compared to the free-running build-up time of ≈1.5 µs the first pulse exhibits a significant reduction in build-up time and complete suppression of the reverse-wave, suggesting it is well seeded. A second uncontrolled pulse develops later at 1.5 µs with no reduction in build-up time nor evidence of reverse-wave suppression. Whilst we require the slave laser to produce two pulses this sporadic behaviour was uncontrollable and

is not be suitable for stable differential absorption measurements of methane.

We examined the seeding reliability by applying a 12.5 mHz ramp to the PZT to sweep the slave cavity length through resonance. Both the build-up time and beat frequency of 10,000 consecutive pulses were measured on the GaGe digitiser. A voltage threshold of 500 mV was applied to the beat-note to filter any background signals which may occur off of resonance. The total sweep is plotted in Figure 2.23.

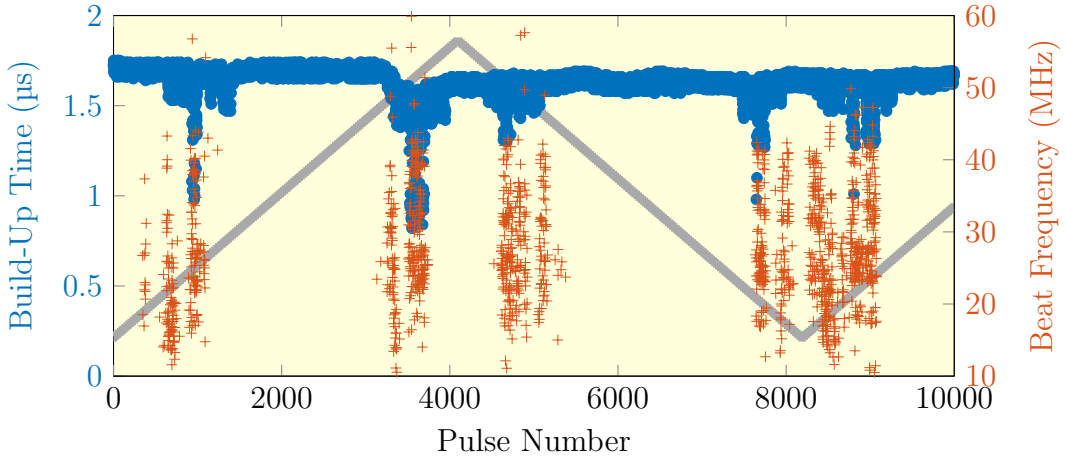

Figure 2.23: A plot showing the build-up time and beat-frequency of the injection-seeded slave laser as it is swept through resonance. The grey line represents the voltage applied to the PZT and is arbitrarily scaled to fit within the plot.

We clearly resolve regions where a significant reduction in build-up time has occurred, this is examined further by only plotting a resonance region in Figure 2.24. With few pulses exhibiting the build-up time reduction required to consider them 'seeded', this plot highlights the unreliable seeding efficiency of the slave laser.

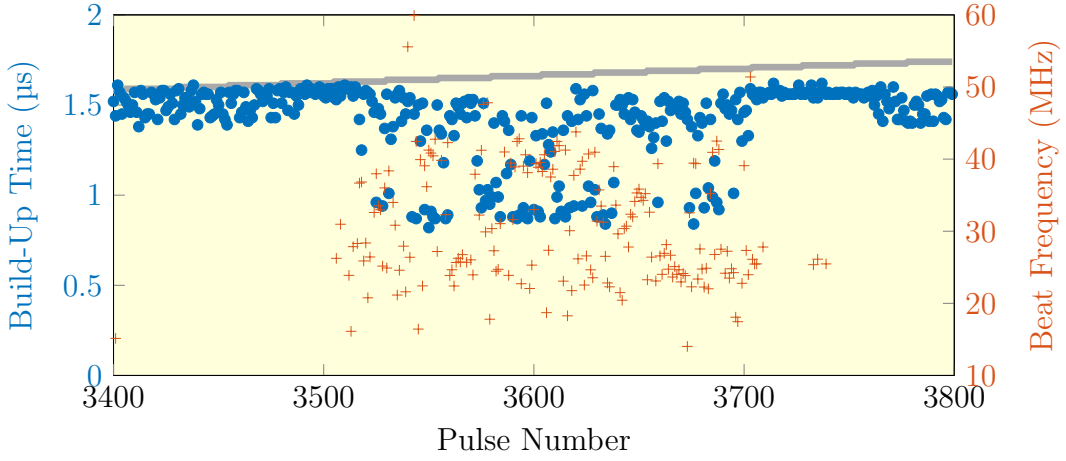

Figure 2.24: A plot showing the build-up time and beat-frequency of the injection-seeded slave laser in a resonance region. The grey line represents the voltage applied to the PZT and is arbitrarily scaled to fit within the plot.

The injection-seeding was further investigated by plotting the relationship between the build-up times and the corresponding beat frequencies of the seeded pulses measured in the cavity scan in Figure 2.25. This plot shows that a small fraction of pulses exhibit a reduction in build-up time. Additionally, there is minimal apparent structure between the build-up time and corresponding beat frequency - further indication of poor injection-seeding.

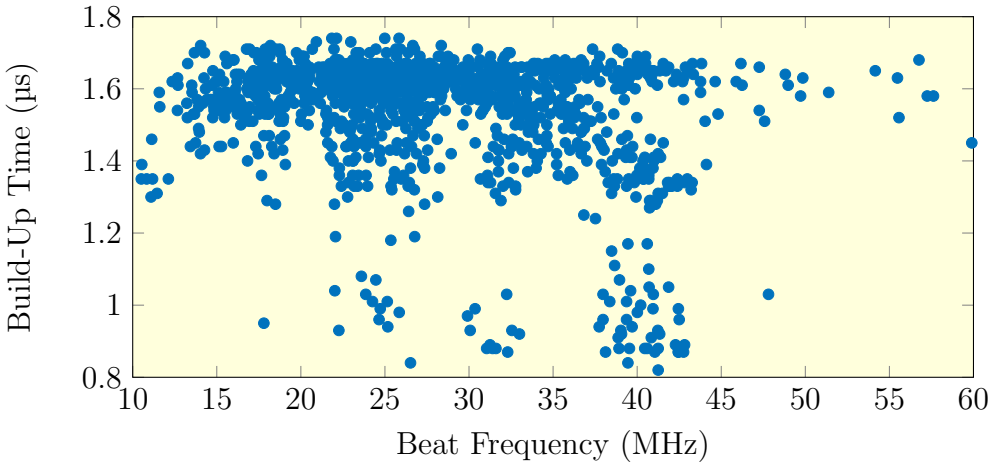

Figure 2.25: Relationship between the build-up time and beat frequency of the injection-seeded slave laser.

2.7 Conclusion

This chapter described the characterisation of an injection-seeded Er:YAG laser developed by Myles Clark as part of a preceding PhD thesis. The slave laser was capable of producing Q-switched pulses with an energy of 1.2 mJ, a width of 100 ns at a PRF of 100 Hz which was limited by a lack of available pump power. The optics used to couple the master laser into the slave cavity were introduced and the degree of modal overlap was calculated. Using the build-up time, beat frequency and reverse wave suppression of the injection-seeded slave laser the poor injection-seeding behaviour was characterised. Unreliable injection-seeding and uncontrollable dual-pulsing will both need to be removed to facilitate wavelength tunability for methane sensing.

Chapter 3

A Study of Injection-Seeding

3.1 Introduction

Since single-mode operation of a Q-switched laser system was first demonstrated in 1969 [154], the injection-seeding technique has become ubiquitous in systems spanning the infrared [155, 156] to the ultra-violet [157, 158]. Despite this, very few theoretical analyses of the injection-seeding process have been presented in literature. Lachambre *et al.* [159] described the analysis of a Transversely Excited Atmospheric (TEA) CO_2 laser based upon a field propagation model which has since been further extended to other laser materials [160]. Tashiro *et al.* [161] later reported this model was inaccurate in reliably describing high-peak power laser systems.

Rather than applying a field propagation model we instead explored the development of an injection-seeded numerical model based upon energy level population density rate equations. Whilst a similar approach has been implemented by Ganiel *et al.* [162] to describe a pulsed dye laser, to our knowledge this is the first describing injection-seeding in an Er:YAG system. Inconsistencies between this model and experiment lead to a study of the temporal response of the Pockels Cell. A novel technique to stabilise the Q-switch is introduced, resulting in good agreement with theoretical predictions and significantly improved seeding behaviour.

The development of this model is described in Section 3.2 which is divided into three sub-sections. Section 3.2.1 introduces a steady-state model to solve for the gain-medium population densities; in Section 3.2.2 we adapt this to solve for photon-densities and in Section 3.2.3 we introduce a term to describe injection-seeding. The results of a Pockels Cell response measurement are given in Section 3.3 and a means of stabilising this response, with updated experimental results, is described in Section 3.4. This chapter concludes in Section 3.5 with a characterisation of the improved injection-seeding results of the Er:YAG laser.

3.2 A Numerical Model for Injection Seeding

The population dynamics of the energy levels in a gain medium are described by a set of rate equations. These Ordinary Differential Equations (ODEs) incorporate absorption, emission, energy transfer and non-radiative decay processes.

The energy level transitions in Er^{3+} that are associated with 1.6 µm operation are illustrated in Figure 3.1. Neglecting higher order processes, four manifolds are required to adequately describe the system [163–165], with the sub-level populations within each manifold approximated by a Boltzmann distribution.

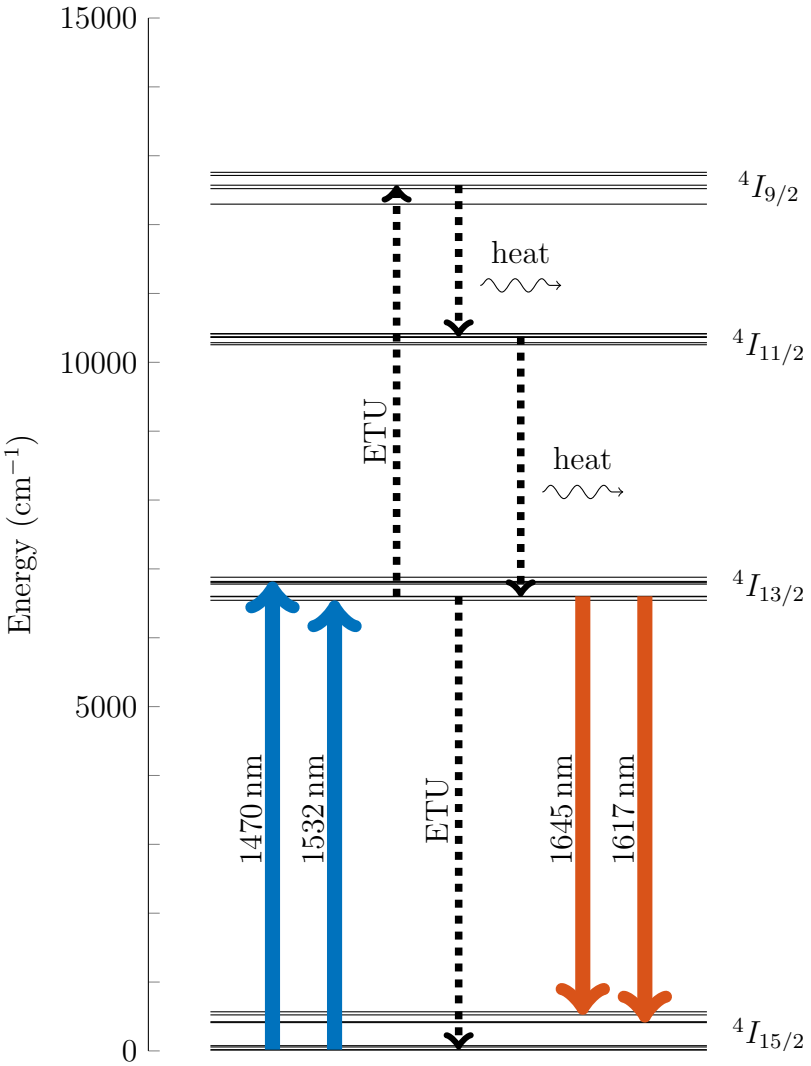

Figure 3.1: Diagram of the four lowest energy level manifolds in Er:YAG. The energy levels are sourced from [163] & [164] and all transitions are sourced from [165].

For resonantly-pumped Er^{3+} doped lasers operating in the 1.6 µm region both the absorption and emission transitions occur between the $^4I_{15/2}$ (N_1) and $^4I_{13/2}$ (N_2) manifolds. The $^4I_{9/2}$ (N_4) level is populated via Energy-Transfer Upconversion (ETU) - a parasitic process whereby two erbium atoms in the $^4I_{13/2}$ manifold interact to excite

one to the $^4I_{9/2}$ manifold and de-excite one to the $^4I_{15/2}$ manifold. As the energy gap for these transitions are not identical this process is phonon assisted to ensure energy conservation [166]. The $^4I_{11/2}$ (N_3) level is populated from the $^4I_{9/2}$ level via non-radiative decay, which then undergoes further non-radiative decay to the $^4I_{13/2}$ level.

3.2.1 Steady State Pumping Model

Many numerical models that aim to predict the performance of end-pumped quasi-three-level laser systems under steady-state pumping conditions have been presented in literature [167–171]. The model published by R. J. Beach [170] provides simple analytical expressions for the laser output power. Auge *et al.* [171] extended that model to account for the non-negligible re-absorption losses and the axial variation in pump intensity that occurs in longitudinally pumped systems. However, these numerical models are unable to predict time-dependent lasing behaviour which is critical in evaluating injection-seeding. A complete model of the laser system would require a set of equations that describe the time-dependent axial population densities of the i^{th} manifold $N_i(z,t)$. Whilst spatial-temporal numerical models of end-pumped Er:YAG laser systems have been presented in literature [172] they are significantly more complex and computationally intensive.

Instead we follow the approach outlined by White *et al.* [173] and N. Chang [169], in which the spatially-averaged population densities $\hat{N}_i(t)$ are calculated. This approximation, referred to as the Mean Population Approximation (MPA), is valid when the pump light intensity does not vary significantly with z - as would be required in a quasi-three-level gain medium to avoid re-absorption losses.

The rate equations for the four lowest energy levels of Er:YAG under steady-state pumping conditions are given below where all symbols are defined and discussed below.

$$\frac{dN_1}{dt} = N_2 w_{21} + N_3 w_{31} + N_4 w_{41} + \frac{P_p \eta_{eff}}{h\nu_p V_p}\left[1 - \exp\left(-\sigma_p l_s \Delta N_p\right)\right] + C_{up} N_2^2 \tag{3.1}$$

$$\frac{dN_2}{dt} = N_3 w_{32} + N_4 w_{42} - N_2 w_{21} - \frac{P_p \eta_{eff}}{h\nu_p V_p}\left[1 - \exp\left(-\sigma_p l_s \Delta N_p\right)\right] - 2C_{up} N_2^2 \tag{3.2}$$

$$\frac{dN_3}{dt} = N_4 w_{43} - N_3 w_{32} - N_3 w_{31} \tag{3.3}$$

$$\frac{dN_4}{dt} = -N_4 w_{43} - N_4 w_{42} - N_4 w_{41} + C_{up} N_2^2 \tag{3.4}$$

The pump source is defined to have an output power P_p and is launched into the gain medium with an efficiency η_{eff} where it is assumed to uniformly fill a volume V_p within the slab of length l_s. The pump absorption is assumed to occur between a single pair of sub-levels with populations determined by the corresponding Boltzmann factor f_i. The absorption of pump light is dependent on the absolute cross-section σ_p and the

population inversion density ΔN_p, given by.

$$\Delta N_p = f_{2p} N_2 - f_{1p} N_1 \tag{3.5}$$

The ETU process is described by the upconversion coefficient C_{up}, this parameter has been documented at room temperature for a range of Er^{3+} concentrations with measurements yielding a value of $C_{up} = 2 \times 10^{-17}\,\mathrm{cm}^3/\mathrm{s/at.\%}$ [174]. As this parameter increases linearly with Er^{3+} concentration, lower dopant levels are typically used to limit the effect of the ETU process.

The decay rate of ions from the i^{th} to the j^{th} energy level is described the parameter w_{ij}. The values of all decay rates are given in Table 3.1; the rates w_{32} and w_{43} are dominated by non-radiative processes and are significantly larger than the radiative rates [175].

w_{21}	w_{31}	w_{32}	w_{41}	w_{42}	w_{43}
136 [176]	118 [177]	9,000 [178]	51 [179]	57 [179]	123,000 [180]

Table 3.1: Er:YAG room-temperature decay rates (s^{-1}).

A numerical model was used to validate this rate equation model and explore the dynamics of the laser gain medium during steady-state pumping. The MATLAB model used the inbuilt function *ODE45* [181] to solve equations 3.1 - 3.4 over a time span of 10 ms. It is assumed that at the start of the simulation all Er^{3+} atoms are in the ground-state (i.e. $N_1\,(t=0) = N_{Er}, N_{2-4}\,(t=0) = 0$).

The Boltzmann factors and the associated cross-sections for the pump transition at wavelength λ_p and lasing transition at wavelength λ_l are given in Table 3.2 and all other free parameters used in the steady-state pumping simulation are given in Table 3.3. Although this sub-section focuses on the dynamics of optical pumping we have introduced the lasing cross-sections as they are later used to further validate the rate equation model.

λ_p (nm)	σ_p (cm^2)	f_{1p}	f_{2p}
1470	4.2×10^{-20}	0.264	0.089
1532	5.2×10^{-20}	0.276	0.241
λ_l (nm)	σ_l (cm^2)	f_{1l}	f_{2l}
1617	3.4×10^{-20}	0.036	0.209
1645	3.1×10^{-20}	0.022	0.209

Table 3.2: Cross-sections and Boltzmann factors of the available pump and lasing transitions in Er:YAG at 300 K [182]. Note that the temperature dependence of these parameters is not accounted for in this model.

Parameter	Value	Note
Lasing wavelength	$\lambda_l = 1645\,\text{nm}$	
Pump wavelength	$\lambda_p = 1470\,\text{nm}$	
Pump horizontal diameter	$d_{px} = 2\,\text{mm}$	
Pump vertical diameter	$d_{py} = 1.7\,\text{mm}$	
Pump power	$P_p = 20\,\text{W}$	
Pump launch efficiency	$\eta_{eff} = 75\%$	
Output coupler reflectivity	$R_{oc} = 64\%$	
Round-trip loss	$L_{cav} = 9\%$	
Erbium concentration	$N_{Er} = 7 \times 10^{-19}\,\text{cm}^{-3}$	0.5% at. Er doping
Upconversion coefficient	$C_{up} = 1 \times 10^{-17}\,\text{cm}^3/\text{s}$	0.5% at. Er doping
Er:YAG crystal length	$l_s = 33\,\text{mm}$	slab back face to nose
Mode path-length	$l_p = 93.3\,\text{mm}$	$l_p = 2\sqrt{2}l_s$
Steady state time-span	$t_{ss} = 10\,\text{ms}$	

Table 3.3: Experimental parameters used in the steady-state pumping numerical model.

The predicted spatially averaged populations densities for the four lowest energy manifolds is shown in Figure 3.2.

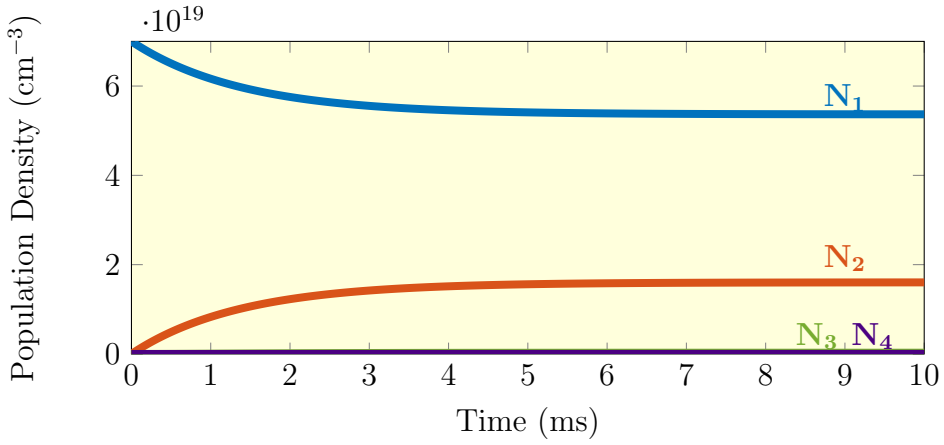

Figure 3.2: Predicted population densities of the four lowest energy manifolds in Er:YAG.

As expected, ions are excited from the ground-state to the upper lasing level until steady-state is reached after approximately 10 ms. The populations of the higher energy levels are negligible due to the fast decay rates of these states relative to that of the N_2 manifold.

The round-trip gain G at the start of the pumping was then calculated using the population densities

$$G = R_{oc} L_{cav} \exp\left(\sigma_l \left(f_{2l} N_2 - f_{1l} N_1\right) l_p\right) \tag{3.6}$$

where R_{oc} is the laser output-coupling, L_{cav} is the cavity round-trip loss and σ_l is

the absolute lasing cross-section. This parameter is critical as, unlike the population densities, it can be easily compared to experimental observations. The predicted round-trip gain is plotted in Figure 3.3

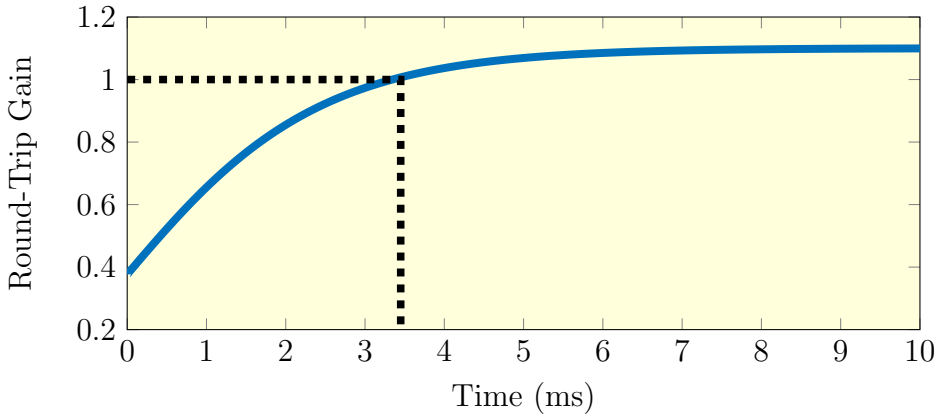

Figure 3.3: Predicted slave laser round-trip gain

Thus, the laser reaches threshold after pumping for 3.5 ms and saturates at a gain $G = 1.1$. For pulse repetition rates greater than 300 Hz the available energy will be coupled to the energy extracted by the previous pulse. At a pulse repetition rate of 1 kHz we have experimentally observed unstable pulse-to-pulse energies as illustrated in Figure 3.4. Evidently, missed pulses occur as the previous pulse extracts a significant fraction of the stored energy, leaving the laser sub-threshold for the following pulse.

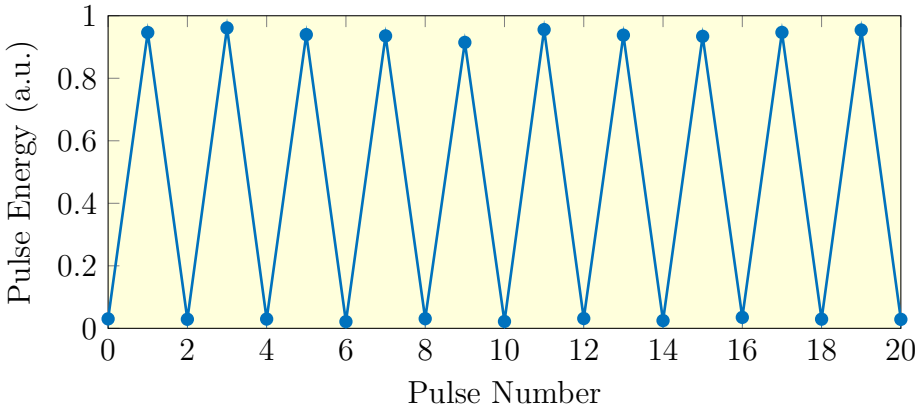

Figure 3.4: Measured pulse-to-pulse energy of the Q-switched laser output operating at a repetition rate of 1 kHz highlighting that a missed pulse will consistently follow a high-energy pulse.

The gain and the available lasing energy is limited by the bleaching of ground-state erbium ions by the pump diode. This process, known as pump-bleaching, can be mitigated by increasing the doping concentration of erbium ions. However, this will also increase the rate of ETU and laser re-absorption - both of which act to reduce

the laser efficiency. Recent advancements in erbium-doped fiber lasers have enabled high-power pump sources capable of accessing the narrow absorption line at 1532 nm, allowing the repetition rate [183] and pulse energy [184] to be increased significantly. Although not considered in the scope of this project, this may be crucial in overcoming the limitations of diode pumping predicted in this section.

The steady-state model predicts the physical processes that occur within the laser gain medium when pumped with a Constant-Wave (CW) source. However, for direct comparison to experimental data, we require a model which simulates pulsed laser output parameters such as pulse build-up time, pulse-width and peak-power. As such, we use the steady-state model described in this sub-section as the basis of a Q-switched numerical model.

3.2.2 Q-Switched Model

Upon engagement of the Q-switch a laser pulse will quickly develop from spontaneous emission. The differential equations describing this behaviour were first derived by Wagner *et al.* [185]. During the pulse evolution there is a change in the internal photon density ϕ which is coupled to the population density via the following expression [186]:

$$\frac{d\phi}{dt} = \left[\frac{\sigma_l \left(f_{2l} N_2 - f_{1l} N_1\right) l_p}{t_r} - \frac{1}{t_c}\right] \phi \tag{3.7}$$

where t_r is the resonator round-trip time and t_c is the cavity lifetime, given by.

$$t_c = -\frac{t_r}{\ln\left(R_{oc}\left(1 - L_{cav}\right)\right)} \tag{3.8}$$

For a ring-resonator with no directional dependent components both the clockwise and counter-clockwise laser modes experience the same round-trip gain, and thus a pulse will develop in both directions. To account for this, we define a photon density in the clockwise ϕ_+ and counter-clockwise directions ϕ_-.

In the absence of an external seed, the Q-switched laser pulse develops from spontaneous emission. Unlike the laser radiation, the spontaneous emission is not confined spatially or spectrally by the laser resonator. Hence, a significant portion of the spontaneously emitted photons do not contribute to the buildup of the laser pulse. This effect can be described by the spontaneous emission coupling factor k_{se}. An accurate calculation of this term requires integrating the atom-field coupling across all optical modes of the resonator [187–189]. To avoid unnecessary complexity, we instead consider three simple factors which describe how spontaneously emitted photons couple into the laser cavity.

1) Spatial Overlap - For a Gaussian laser mode the far field divergence solid angle Ω is.

$$\Omega = \frac{\lambda^2}{\pi\omega_0^2} \tag{3.9}$$

As the emission direction of the photons are random, the fraction of spontaneously emitted photons that couple with the Gaussian mode is.

$$k_g = \frac{\Omega}{4\pi} = \left(\frac{\lambda}{2\pi\omega_0}\right)^2 \tag{3.10}$$

2) Modal Overlap - Spontaneously emitted photons with frequencies not matched to the longitudinal cavity modes do not contribute to pulse buildup. The fraction of spontaneously emitted photons with a frequency within the resonator mode is given by,

$$k_m = \frac{\Delta_s}{\Delta_\nu} = \frac{1}{F} \tag{3.11}$$

where Δ_s is the spectral width of a longitudinal mode, Δ_ν is the mode spacing and F is the cavity finesse.

3) Spectral Overlap - Above threshold the laser spectral output narrows around the maximum gain of the laser medium. Spontaneously emitted photons which fall outside of this narrow spectra cannot contribute to lasing [190]. We describe this with the spectral overlap factor,

$$k_s = \frac{\Delta_l}{\Delta_f} \tag{3.12}$$

where Δ_l and Δ_f are the spectral widths of the laser and spontaneous emission respectively. Combining equations 3.10, 3.11 and 3.12 gives the total spontaneous emission coupling factor.

$$k_{se} \approx \left(\frac{\lambda}{2\pi\omega_0}\right)^2 \frac{1}{F}\frac{\Delta_l}{\Delta_f} \tag{3.13}$$

The rate at which spontaneously emitted photons couple into the cavity is also dependent on the number of atoms in the upper lasing sub-level (i.e. $N_2 f_{2l}$). The rate at which those atoms decay and the fraction that decay into the lower sub-level associated with lasing at λ_l which is described by the branching ratio β_{ij}. By combining these terms equation 3.7 is adapted to describe the photon densities in a ring-resonator which develop due to spontaneous emission.

$$\frac{d\phi_\pm}{dt} = \left[\frac{\sigma_l\left(f_{2l}N_2 - f_{1l}N_1\right)l_p}{t_r} - \frac{1}{t_c}\right]\phi_\pm + N_2 f_{2l} w_{21}\beta_{21}k_{se} \tag{3.14}$$

During the evolution of the Q-switched pulse the population densities of the lasing

manifolds will change due to re-absorption and gain extraction. These processes can be accounted for by adapting equations 3.1 & 3.2. Note that equations 3.3 & 3.4 remain unchanged as there is no interaction between the laser photons and the higher energy levels.

$$\begin{aligned}\frac{dN_1}{dt} =& N_2 w_{21} + N_3 w_{31} + N_4 w_{41} + \frac{P_p \eta_{eff}}{h\nu_p V_p}\left[1 - \exp\left(-\sigma_p l_s \Delta N_p\right)\right] + C_{up} N_2^2 \\ &+ Bc\sigma_l\left(\phi_+ + \phi_-\right)\Delta N_l + \frac{\left(\phi_+ + \phi_-\right) c_{yag}}{l_p}\left[1 - \exp\left(-\sigma_l l_p \Delta N_l\right)\right] \qquad (3.15)\\ \frac{dN_2}{dt} =& N_3 w_{32} + N_4 w_{42} - N_2 w_{21} - \frac{P_p \eta_{eff}}{h\nu_p V_p}\left[1 - \exp\left(-\sigma_p l_s \Delta N_p\right)\right] - 2C_{up} N_2^2 \\ &- Bc\sigma_l\left(\phi_+ + \phi_-\right)\Delta N_l - \frac{\left(\phi_+ + \phi_-\right) c_{yag}}{l_p}\left[1 - \exp\left(-\sigma_l l_p \Delta N_l\right)\right] \qquad (3.16)\end{aligned}$$

The first term introduced describes the gain extraction, as described in equation 3.14, where c is the speed of light in a vacuum and the factor B was introduced by Ottaway *et al.* [191] used here to account for the laser mode overlapping with itself in the zig-zag gain medium. The gain extraction is dependent on the cross-section σ_l and the population inversion density.

$$\Delta N_l = f_{2l} N_2 - f_{1l} N_1 \qquad (3.17)$$

The second term introduced accounts for re-absorption of the laser light that occurs due to the quasi-three level nature of the gain medium. This is analogous to the pump absorption introduced in the steady-state model, where again the mean population approximation has been applied. We define c_{yag} as the speed of light within the gain-medium.

All parameters introduced in the Q-switched model are given in Table 3.4.

Parameter	Value	Note
Laser horizontal diameter	$d_{lx} = 800\,\mu\text{m}$	See Appendix B
Laser vertical diameter	$d_{ly} = 500\,\mu\text{m}$	See Appendix B
Mode waist size	$\omega_0 = 325\,\mu\text{m}$	Astigmatic average
Mode spectral width	$\Delta_s = 5\,\text{MHz}$	
Mode spacing	$\Delta_\nu = 638\,\text{MHz}$	
Laser spectral width	$\Delta_l = 0.1\,\text{nm}$	See Figure 2.9
Spont. Emiss. spectral width	$\Delta_f = 5\,\text{nm}$	from [192]
Round-trip time	$t_r = 1.56\,\text{ns}$	$t_r = 1/\Delta_\nu$
Mode overlap factor	$B = 2$	zig-zag ring cavity
Branching ratio	$\beta_{21} = 0.12$	from [193]

Table 3.4: Experimental parameters used in the Q-switched numerical model.

Equations 3.3-3.4 & 3.14-3.16 were solved using the ODE solver in MATLAB. The initial conditions of the population densities are provided by the final population densities calculated in the steady-state model (i.e. $N_i(0) = N_i(t_{ss})$) and it is assumed that the initial photon density is zero ($\phi_{\pm}(0) = 0$). The predicted forward wave photon density and population inversion density are plotted in Figure 3.5.

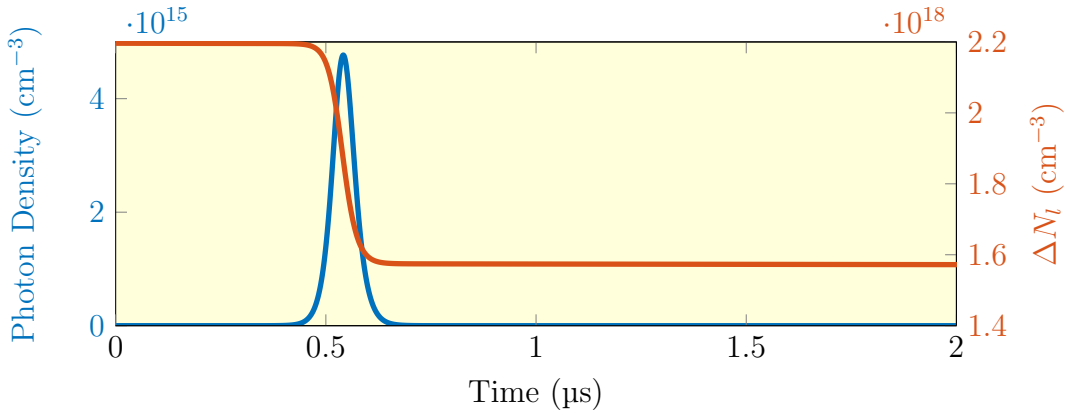

Figure 3.5: Predicted forward wave photon density and population inversion density during the evolution of a Q-switched pulse. The predicted reverse wave photon density ϕ_- is identical as expected

This model shows a pulse developing, during this time gain extraction occurs and the population inversion density is reduced which is consistent with the expected laser dynamics. For direct comparison with experimental results, we convert the photon density to the output power using equation 3.18 where ν_l is the photon frequency and A_l is the cross-sectional area of the laser mode. The predicted forward wave peak power is directly compared to experimental observations in Figure 3.6.

$$P_{\pm,out} = \phi_{\pm} h \nu_l A_l c_{yag} \ln(1/R_{oc}) \tag{3.18}$$

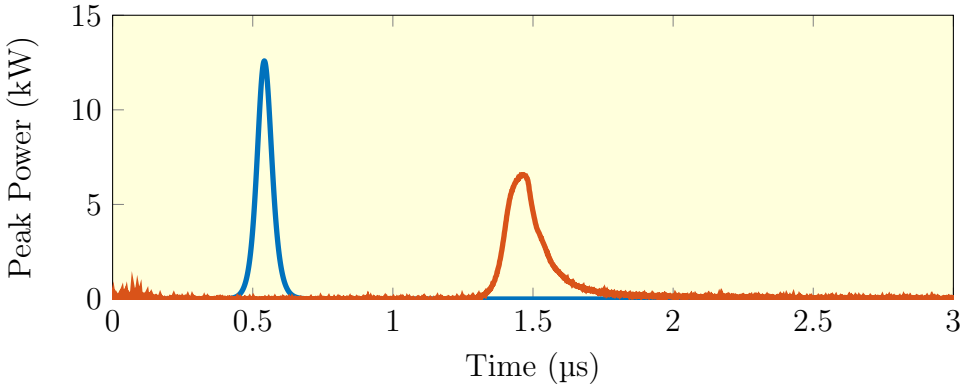

Figure 3.6: Predicted and measured output power of the free-running slave laser.

While the simulated pulse width and energy are comparable to experimental observations, there is a significant discrepancy in the build-up time - a key metric of injection-seeding. An experimental analysis into the possible cause of this discrepancy is described in Section 3.3, for completeness however we will first introduce a term into the numerical model describing injection-seeding.

3.2.3 Injection Seeded Model

In an injection-seeded laser the Q-switch pulse develops from 'seed' photons that are injected from an external master laser. To include this process in the numerical model, we introduce a term into the forward-wave photon density ODE (equation 3.14) describing the master laser contribution to the intra-cavity photon density. We assume that the master laser has a power P_m and the laser mode is well matched to that of the slave laser - filling a volume V_l within the gain medium. The resultant ODE for the counter-clockwise photon density is given in the equation below.

$$\frac{d\phi_+}{dt} = \left[\frac{\sigma_l \left(f_{2l} N_2 - f_{1l} N_1\right) l_p}{t_r} - \frac{1}{t_c}\right] \phi_+ + N_2 f_{2l} w_{21} \beta_{21} k_{se} + \frac{P_m \left(1 - R_{oc}\right)}{h \nu_l V_l} \tag{3.19}$$

We have also assumed that the seed spectral width is narrow compared to the laser spectral width Δ_l and it is operating close to line-centre of the gain spectra. If the master laser is detuned from line-centre or non-resonant with a longitudinal mode of the slave cavity the round-trip gain is reduced. Thus reducing the probability that the pulse develops from the external 'seed'. Unless explicitly stated otherwise, all experimental and theoretical seeding data presented in this chapter is at the erbium line-centre wavelength of 1645.15 nm. Figure 3.7 compares the unseeded and seeded predictions for a master laser power of $P_m = 1\,\mathrm{mW}$.

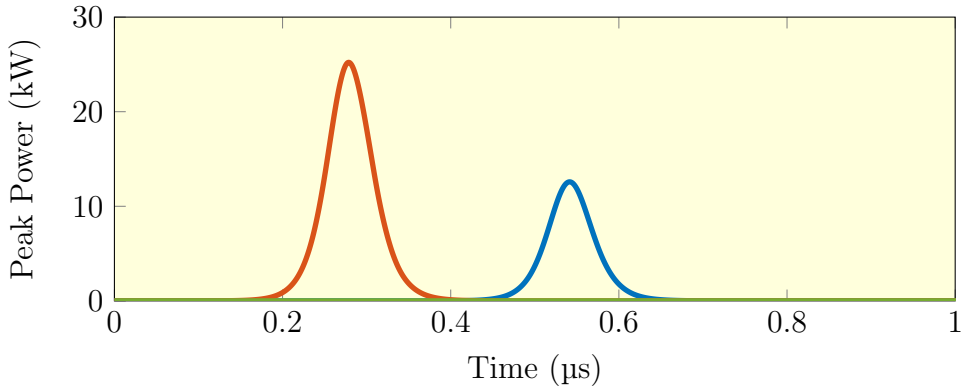

Figure 3.7: Predictions of the unseeded slave laser output power compared to the seeded forward-wave output. Note the seeded reverse wave is also plotted.

This shows a significant reduction in build-up time as expected - suggesting that the slave output is developing from the seed rather than spontaneous emission. This is confirmed by the doubling in pulse energy and the complete suppression of the reverse wave. The model thus suggests we should be observing efficient seeding behaviour in our current system with no evidence of dual pulsing or the minimal build-up time reduction presented in Chapter 2. This inconsistency between the prediction and experiment motivated a complete examination of the laser system to determine the cause of this unexpected behaviour.

3.3 Pockels Cell Temporal Stability

The Pockels Cell was characterised in both the steady-state and time-dependent domain using the system illustrated in Figure 3.8.

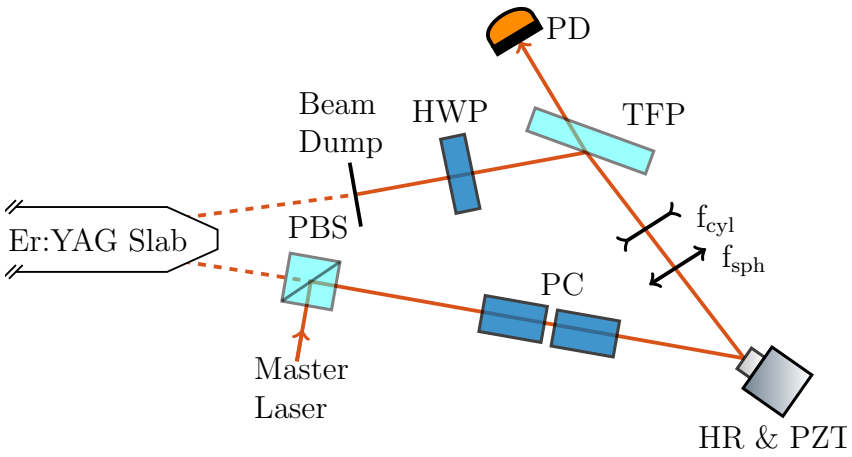

Figure 3.8: A schematic of the polarisation-controlled output-coupling characterisation system.

The PC is located within the laser to ensure any intra-cavity effects such as misalignment are accounted for. The master laser light is injected via the PBS and in the absence of a PC voltage completely reflects at the TFP. As a DC voltage is applied to the PC, denoted V_{PC}, the polarisation of the injected light is rotated and transmitted through the TFP. The power of this light is measured using a *Newport* 1811-FS PD. A beam-dump is used to block the light reflected by the TFP, thus ensuring it does not contribute to the intensity on the following round-trip. The voltage required to maximize the transmitted power was 3.5 kV which corresponds to the half-wave voltage of the PC.

The measured transmittance of the σ-polarised master light was used to calculate the expected reflectivity of the π-polarised laser beam. The results are compared to the output coupling predicted using Jones Matrices (detailed in Appendix C) as plotted

in Figure 3.9. When no voltage is applied to the PC the laser will be in a high-loss state as expected. As this voltage is increased the reflectivity increases and the laser operates in a lower-loss state.

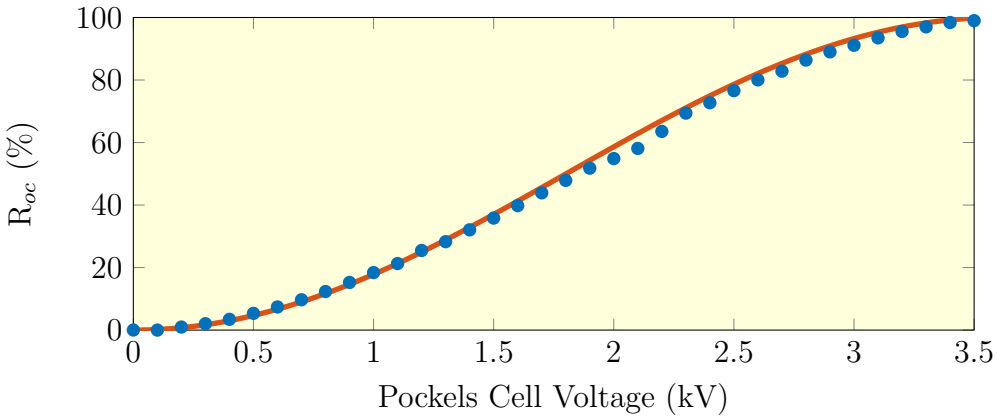

Figure 3.9: Comparison of measured and predicted output-coupler reflectivity as a function of the Pockels Cell voltage.

A plot of the PC temporal response when driven by a voltage of 2.2 kV is illustrated in Figure 3.10. This response exhibits a slower than expected rise time within the first 50 ns, followed by an oscillation with a period of approximately 1 µs.

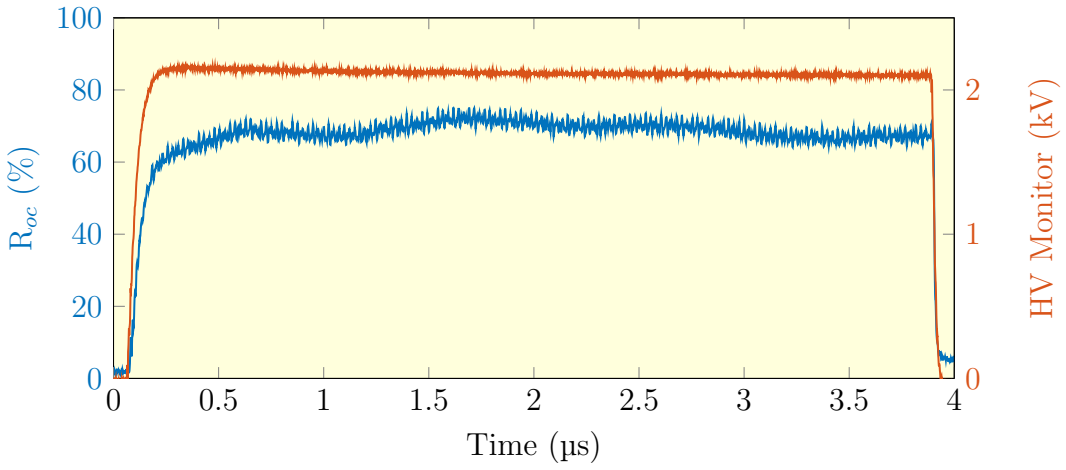

Figure 3.10: Plot of the temporal response of the output-coupler reflectivity when driven with a voltage of 2.2 kV. The HV monitor is the electrical signal sent to the PC.

To investigate the effect of this response on the Q-switching the time-dependent output-coupler reflectivity is introduced into the numerical model. In this updated model the output coupling is replaced by the time-dependent component $R_{oc}(t)$ and equations 3.3-3.4 & 3.14-3.16 were solved as before. The predicted and measured pulses are plotted in Figure 3.11.

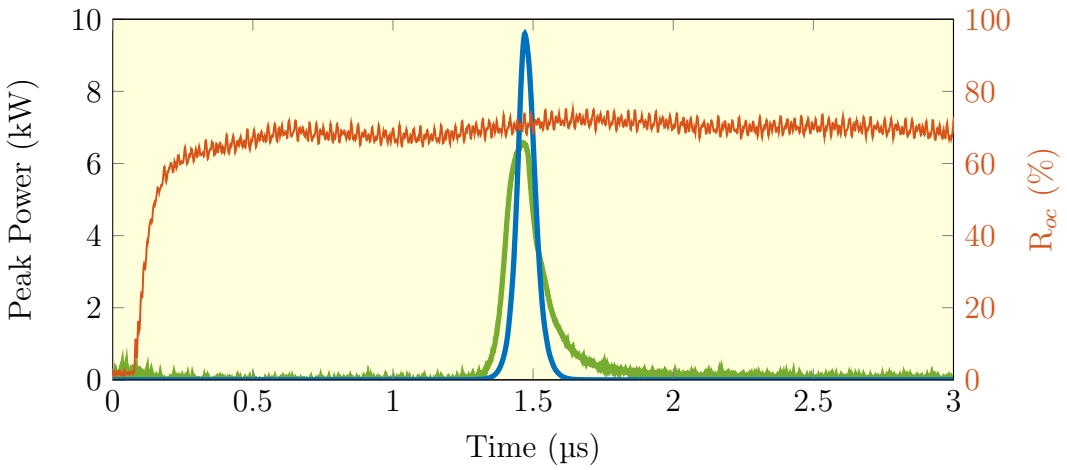

Figure 3.11: Predicted and measured forward-wave pulse in the unseeded case when slow Q-switching is introduced into the model.

Thus, it appears that the PC oscillations are increasing the pulse build-up time, which will decrease the pulse energy and peak power due to the additional losses. The results for the injection-seeded laser are plotted in Figure 3.12.

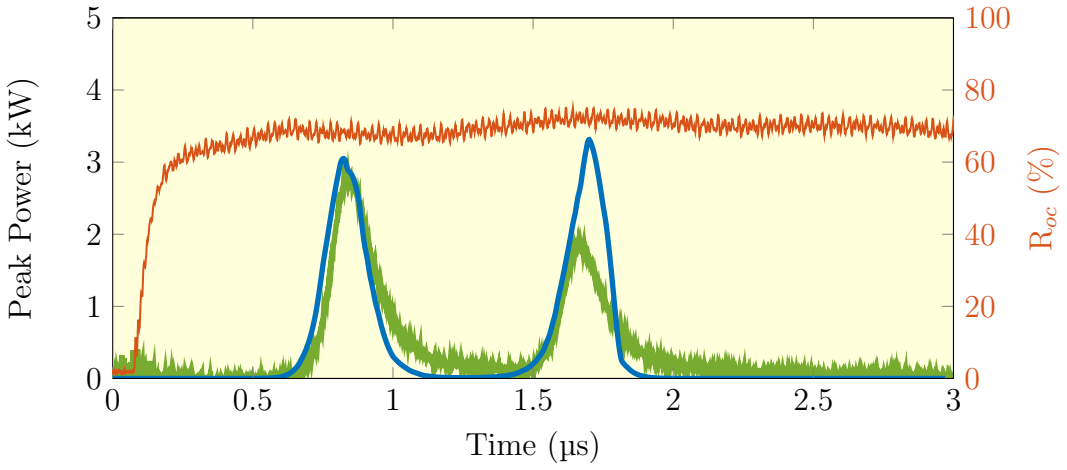

Figure 3.12: Predicted and measured forward wave pulses for the seeded laser when slow Q-switching is introduced into the model.

In addition to a decreased pulse build-up time, we also observe dual pulsing. It is clear that the first pulse arrives when the resonator is in a higher-loss state and thus does not extract all the available gain. The residual gain is extracted by the second pulse when the cavity loss decreases on a peak in the output-coupling oscillation. While the DIAL system requires double pulses, relying on imperfect Q-switching to produce the second could compromise system reliability.

3.4 Preloaded Q-Switch

During the testing of the PC we observed that the optical output-coupling oscillation was reduced at a lower applied voltage. To exploit this an intra-cavity QWP was introduced as shown in Figure 3.13. By setting the optical axis of the QWP to 45° the polarisation at the PC is circular. Hence, with no applied voltage the resonator operates at an output-coupling of 50%, which significantly reduces the voltage required to reach threshold.

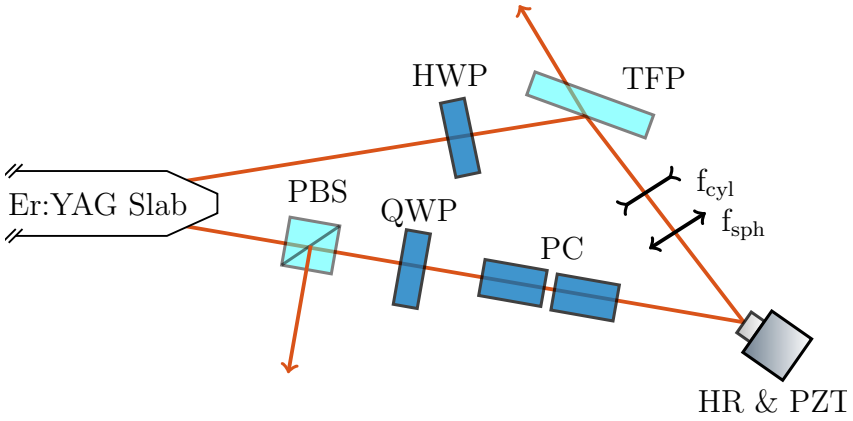

Figure 3.13: A schematic of the slave cavity with an intra-cavity QWP.

To examine the effect of this intra-cavity QWP we repeat the output-coupling characterisation detailed in Section 3.3. A plot of the output-coupling reflectivity as a function of the PC voltage is shown in Figure 3.14.

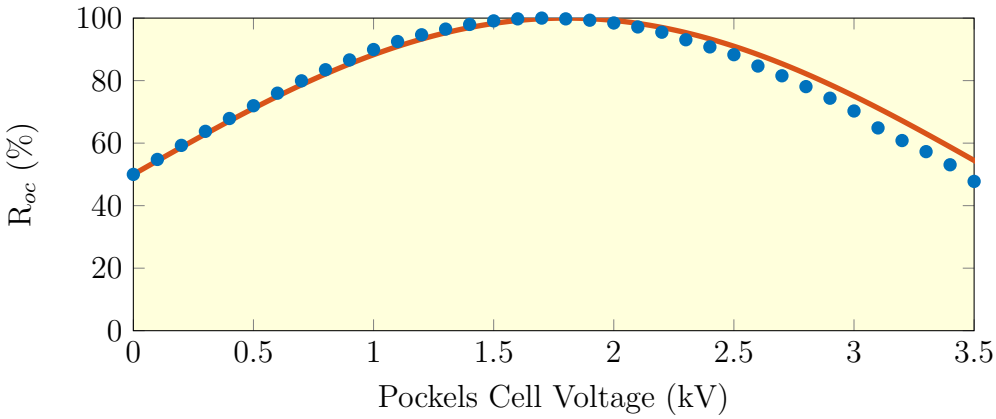

Figure 3.14: Comparison of measured and predicted output-coupler reflectivity as a function of the Pockels Cell voltage when an intra-cavity QWP is introduced.

As expected, the output-coupler reflectivity is at 50% when no voltage is applied to the PC, and the increases as the applied voltage increases. With this configuration the output-coupling used in Section 3.3 can be achieved with a voltage of only 330 V.

The difference in the temporal response between the initial output-coupling system operating at $V_{PC} = 2.2\,kV$ and the preloaded output-coupling system operating at $V_{PC} = 330\,V$ is shown in Figure 3.15. The intra-cavity QWP has thus significantly reduced the oscillations in R_{oc} while still allowing the same output-coupling reflectivity to be reached.

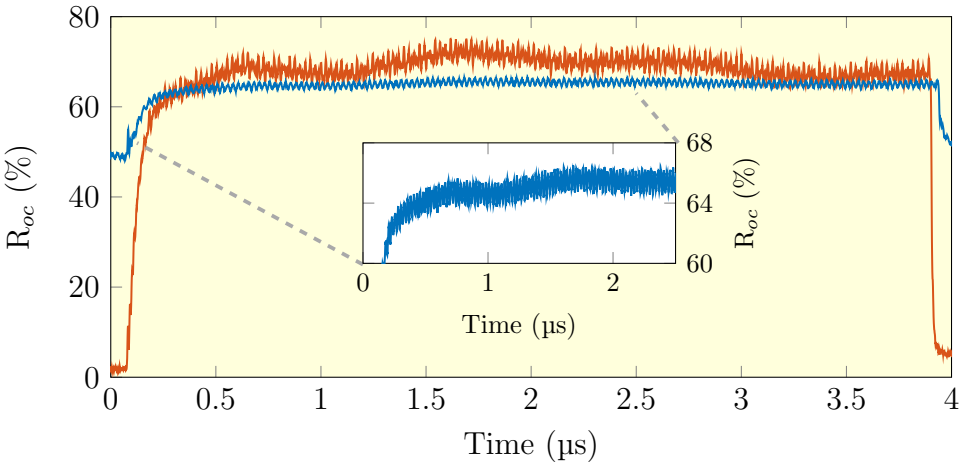

Figure 3.15: Comparison of the temporal response both without and with the intra-cavity QWP. The inset graph highlights that the oscillations are still present on the preloaded Q-switch but are significantly reduced as a fraction of the total output-coupling.

3.5 Injection-Seeding Re-Characterisation

To investigate the effect of the intra-cavity QWP on injection-seeding we measured the build-up time and heterodyne beat-frequency using the system outlined in Section 2.3. The slave laser, operating at a PRF of 100 Hz, was injection-seeded with the *Yenista* ECDL tuned to erbium line-centre $\lambda = 1645.15\,nm$. An example of the seeded forward-wave pulse and heterodyne beat signal measured using the GaGe digitiser is plotted in Figure 3.16. Note the beat-note voltage exceeded the measurement range and is hence clipped at $\pm 1\,V$, this range was increased to resolve the complete beat-note in subsequent measurements.

In comparison to the injection-seeding results presented in Section 2.6 we now observe a significant reduction in the build-up time for both the unseeded and injection-seeded pulses. Due to the improved Q-switching stability there is a clear increase in the injection-seeded pulse energy with no evidence of the unexpected dual pulsing behaviour. This measurement closely resembles the predicted injection-seeding behaviour presented in Section 3.2.3.

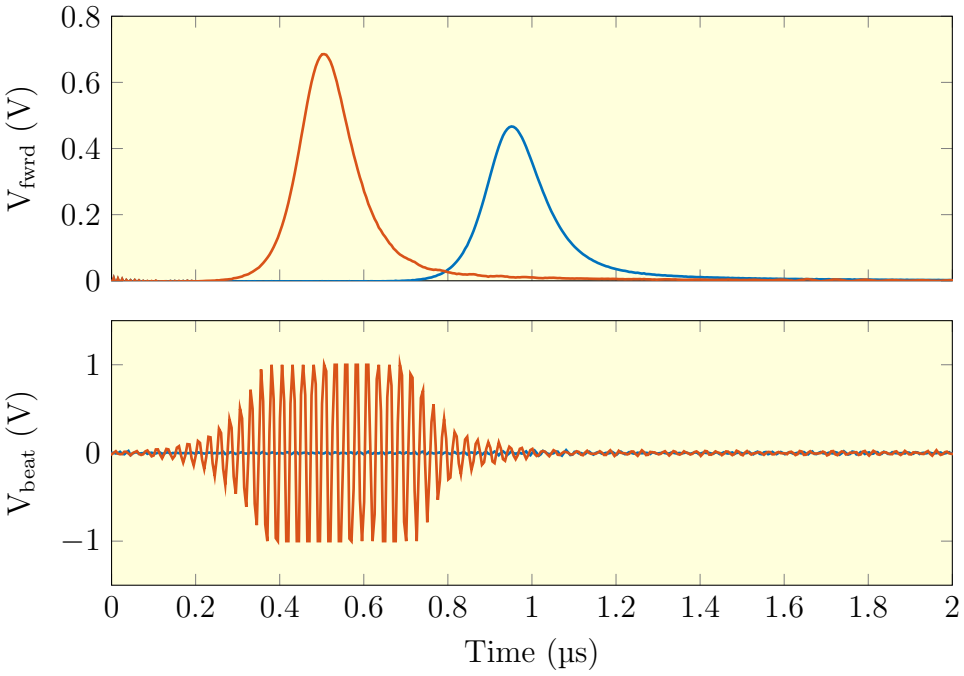

Figure 3.16: Comparison of the unseeded and seeded measured slave laser output with the preloaded Q-switch topology.

We examined the seeding reliability by applying a 12.5 mHz ramp to the PZT to sweep the slave cavity length through resonance. Both the build-up time and beat frequency of 8,000 consecutive pulses were then measured on the GaGe digitiser. A voltage threshold of 500 mV was applied to the beat-note to filter any background signals which may occur off of resonance. The total sweep is plotted in Figure 3.17.

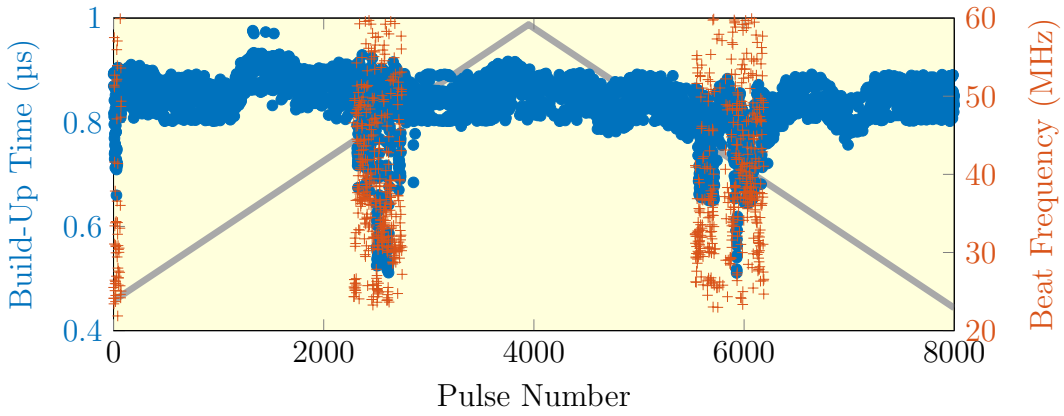

Figure 3.17: A plot showing the build-up time and beat-frequency of the injection-seeded slave laser with the preloaded Q-switch topology as it is swept through resonance. The grey line represents the voltage applied to the PZT and is arbitrarily scaled to fit within the plot.

We clearly resolve regions where a significant reduction in build-up time has occurred. One of these regions is examined further in Figure 3.18. In comparison to the

resonance scan presented in Chapter 2 we observe more structure in the build-up time as the slave laser approaches and leaves resonance. However, the frequency noise of the master laser limits the seeding reliability in this region.

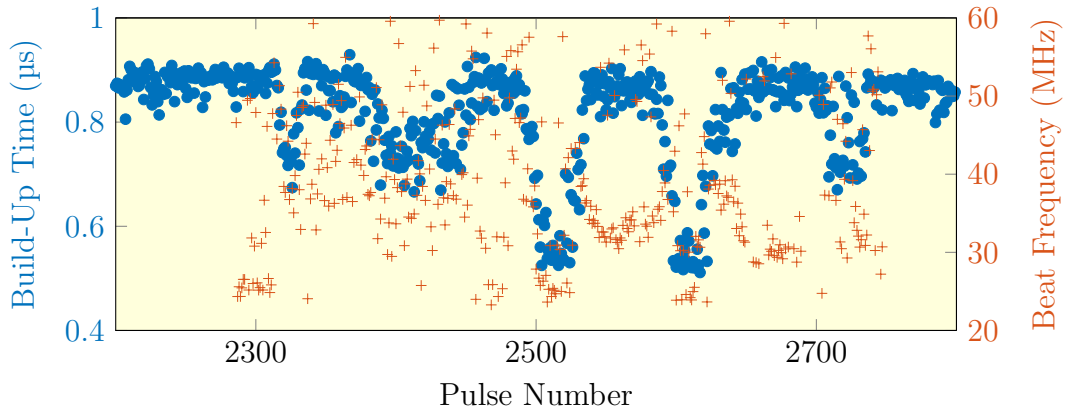

Figure 3.18: A plot showing the build-up time and beat-frequency of the injection-seeded slave laser with the preloaded Q-switch topology on resonance.

The injection-seeding was further investigated by manually adjusting the voltage applied to the PZT to enable consistent seeding and recording all pulses as the slave laser drifted through and around resonance. The relationship between the build-up times and the corresponding beat-frequencies of the seeded pulses is shown in Figure 3.19. Note that the build-up time is reduced in this measurement as the laser was operating with a lower output-coupling.

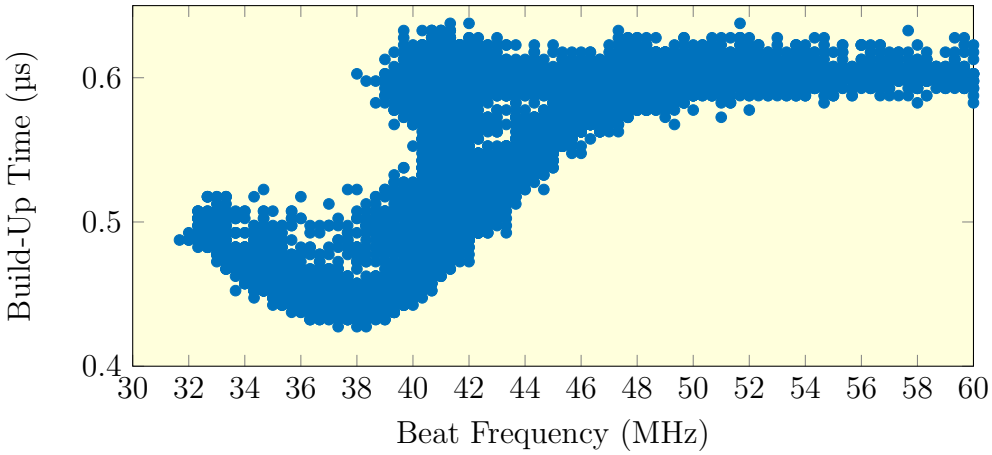

Figure 3.19: The relationship between the build-up time and beat frequency of the injection-seeded preloaded Q-switch slave laser. Note this is not symmetric about the minima as the low-frequency beat signals are heavily attenuated by a passive band-pass filter with a centre frequency of 39 MHz.

This plot shows a relationship between the build-up time and beat frequency, with seeding occurring if the frequency of the master and slave are not detuned by more than

5MHz. Additionally, the minimum build-up time occurs for a beat frequency of 38 MHz, which is offset from the 40 MHz AOM frequency due to an effect known as 'cavity mode pulling', which has been observed in other injection-seeded laser systems [194]. A theoretical model by Bowers and Moody [195] predicted that this effect occurs in systems where the round-trip time is significantly shorter than the build-up time, as in our system.

The frequency change during the evolution of the seeded pulses was investigated by applying a technique described by White *et al.* [196] - represented schematically in Figure 3.20.

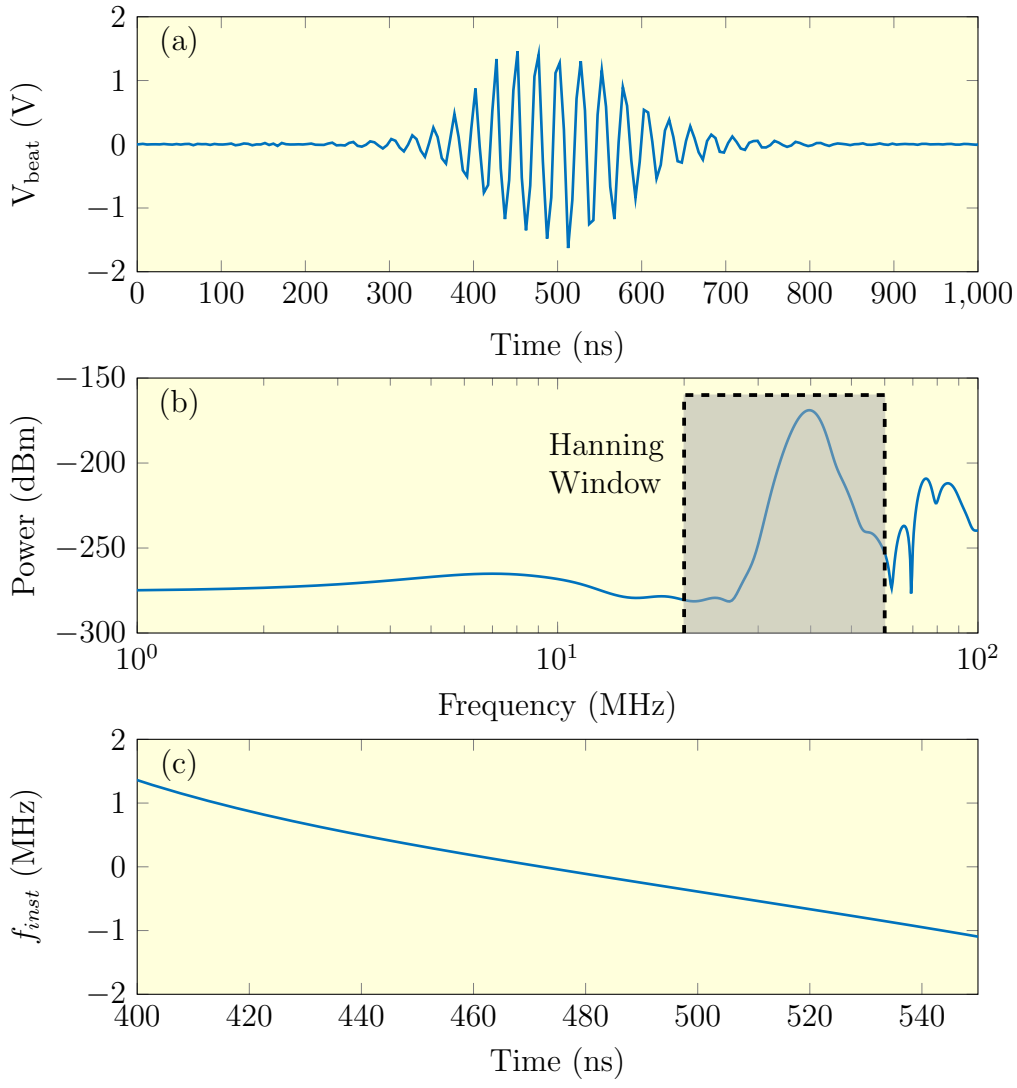

Figure 3.20: Schematic representation of the frequency chirp Fourier analysis procedure. (a) The measured beat note between the frequency shifted seed light and the slave laser pulsed output. (b) The power spectrum of the beat note highlighting the Hanning window applied to the main frequency component. (c) Applying the inverse Fourier transform yields the instantaneous frequency f_{inst} of the pulse relative to average beat frequency $\langle f_{beat} \rangle$.

A typical beat-note and its Fourier transform are shown in Figure 3.20a and 3.20b. Filtering the Fourier transform using a Hanning window and calculating its inverse Fourier transform yields the band-pass-filtered time evolution of the magnitude E(t) and phase $\phi(t)$. The instantaneous frequency of the beat-note $f_{\text{inst}}(t)$ relative to the average beat-frequency $\langle f_{beat} \rangle$ was then calculated using the following equation [197].

$$f_{\text{inst}}(t) = \frac{1}{2\pi}\frac{d\phi}{dt} - \langle f_{beat} \rangle \tag{3.20}$$

The typical instantaneous frequency is plotted in Figure 3.20c. We measure the variation in $f_{\text{inst}}(t)$ by applying a linear-fit to the profile and extracting the frequency chirp rate

$$f_{chirp} = \frac{\Delta f_{\text{inst}}}{\Delta t} \tag{3.21}$$

where Δt is the time period over which the linear-fit is applied, in this case the FWHM of the pulse. The dependence of $\langle f_{beat} \rangle$ and f_{chirp} on the pulse build-up time, for all pulses that had a Fourier peak > 40 dB above the background, is plotted in Figure 3.21

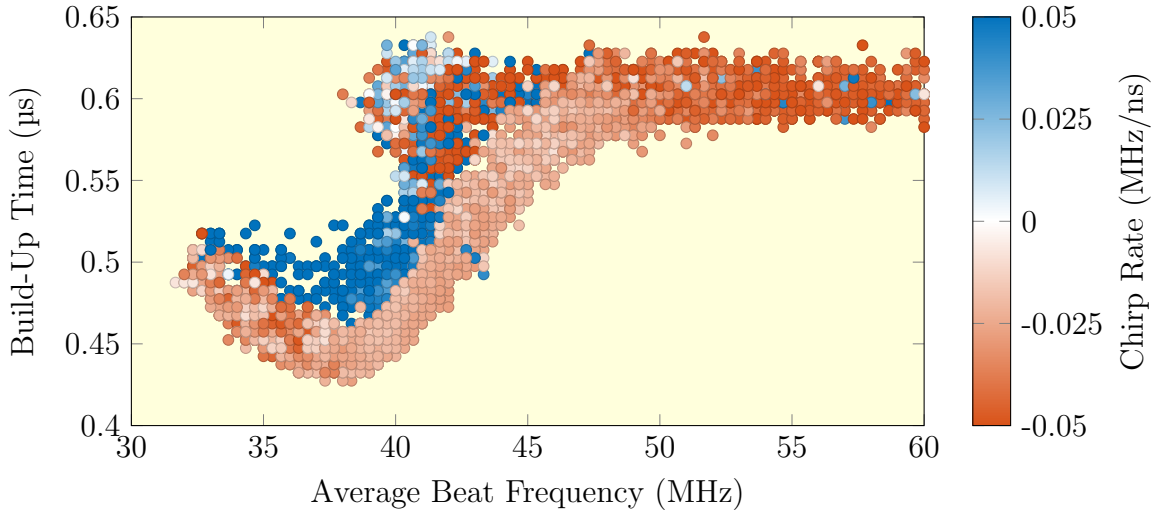

Figure 3.21: The relationship between the build-up time, beat frequency and frequency chirp of the injection-seeded laser.

It thus appears that there were two classes of pulses; those which were slightly down-chirped and those which were heavily up-chirped. The down-chirp is attributed to a heating of the gain-medium caused by ground state phonons. Associated with each photon emitted from the excited state is a phonon redistribution in the ground state [198] - heating the crystal and causing an increase in the refractive index. This can be related to the instantaneous frequency via the following [199].

$$f_{\text{inst}}(t) = -\frac{l}{\lambda_0}\frac{dn(t)}{dt} \tag{3.22}$$

Hence, for $dn/dt > 0$ a natural down-chirp is expected.

It is also apparent that pulses which had the smallest build-up time for a given beat frequency generally exhibited a small down-chirp of $f_{chirp} = -0.02\,\text{MHz/ns}$. Thus, we use the frequency chirp as a metric for injection-seeding and filter all pulses which do not exhibit a small-down chirp as shown in Figure 3.22. This results in a significantly clearer relationship between the build-up time and corresponding beat frequency.

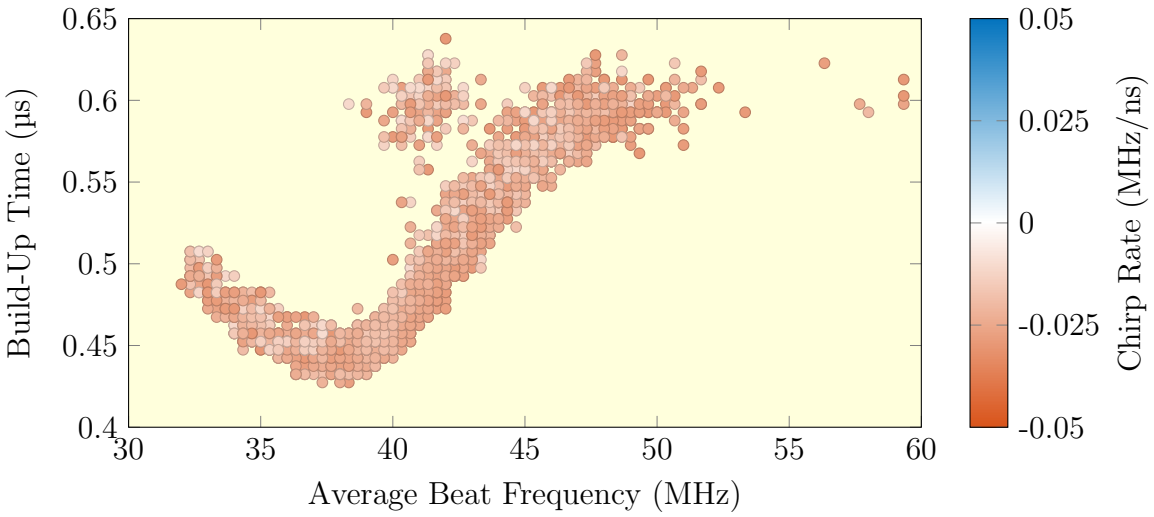

Figure 3.22: The relationship between the build-up time, beat frequency and frequency chirp of the injection-seeded laser. Signal processing has been used to remove all pulses with a frequency chirp greater than $-0.01\,\text{MHz/ns}$ and less than $-0.03\,\text{MHz/ns}$.

An effective servo could be designed to operate at the minima of this curve, ensuring consistent injection-seeding. Whilst active control systems which maintain a minimum build-up time have been presented in literature [200] to our knowledge the pulse frequency chirp has not been used as an injection-seeding metric in a control system. Although real-time Fourier analysis may be cumbersome on a general purpose computer, advancements in Field Programmable Gate Arrays (FPGAs) [201] and Time-to-Digital Converters (TDCs) [202] have made real-time frequency analysis feasible - enabling the possibility of a completely digital servo system based upon build-up time, beat-frequency and frequency chirp. The limitations of such a servo system and possible alternative solutions are discussed further in Chapter 4.

3.6 Conclusion

The numerical model of our injection-seeded laser system uncovered significant discrepancies between experiment and theory caused by oscillations in the Pockels Cell. An intra-cavity QWP was introduced to mute these oscillations and produce better agreement with theory. Injection-seeded pulses were created on erbium line-centre at a

PRF of 100 Hz, by measuring both the build-up time and beat frequency of each pulse we observed significant structure as the slave cavity was swept through resonance. A clear relationship between these two parameters was observed when they were plotted. This was examined further by calculating the frequency chirp of the pulse, which acted as a third metric for injection seeding enabling the structure of the resonance feature to be further improved.

Chapter 4

Systems for Reliable Dual Wavelength Injection-Seeding

4.1 Introduction

Injection-seeding of a high-power slave laser with light from a single-frequency master laser is a powerful technique for spectral control of the high-power laser. However, injection-seeding will only occur if the frequency of the master and slave lasers are close. To ensure stable injection-seeding a servo that minimises this frequency detuning is thus required.

Airborne platforms can have large amplitude vibrations that disturb the resonant frequency of the slave cavity. Measurements of the in-flight acceleration undertaken by Richard White and Sarah Watzdorf of the University of Adelaide are shown in Figure 4.1. Resonant modes at frequencies exceeding 1 kHz are clearly resolved. We require an injection-seeding servo system with a control bandwidth greater than 1 kHz.

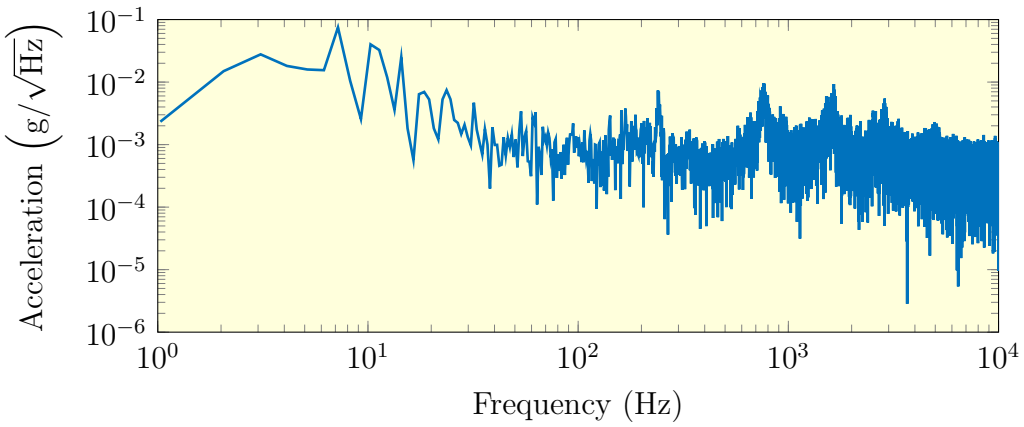

Figure 4.1: Acceleration amplitude spectral density measured in the vertical direction during flight for a Cessna 404 Titan. A ASXL335 digital accelerometer was used.

A variety of servo control systems have been reported. Servo systems that maintain injection-seeding by minimising the pulse build-up time have been presented in literature [136–138]. However, the servo-bandwidth is limited to less than the repetition rate of the laser when using this technique. Since significant accelerations are observed at frequencies >100 Hz this method may not be suitable for injection-seeding of our airborne laser.

The 'ramp-and-fire' technique devised by Henderson *et al.* [203] is commonly used to injection-seed Q-switched laser systems. This method entails scanning the slave cavity length using a PZT until resonant build-up of the injected light is detected, at which point the Q-switch is opened. A disadvantage of this technique is that it introduces pulse-to-pulse timing jitter, which may limit the accuracy of a DIAL system as it requires close co-location of the online and offline pulses.

Two published Er:YAG systems have demonstrated successful injection-seeding using the ramp-and-fire technique. Ye *et al.* [204–206] report a Er:YAG ring-resonator laser capable of producing 10mJ pulses at a PRF of 200 Hz when injection-seeded at 1645.287 nm by a 710 mW Non-Planar Ring Oscillator (NPRO). Yao *et al.* [207,208] report a bow-tie Er:YAG resonator capable of producing 3 mJ pulses at a PRF of 100 Hz when injection-seeded at 1645.24 nm by a 500 mW NPRO.

The Pound-Drever-Hall (PDH) or RF-reflection-locking [209] frequency stabilisation technique is commonly used to injection-lock a single-frequency laser to a cavity or a CW slave resonator. Wulfmeyer *et al.* [210] first reported the application of the PDH technique to a Q-switched laser: a thulium-doped Lu:YAG producing 2 mJ pulses at 2 µm. In this system Q-switching was achieved using an AOM located within a standing wave cavity.

Gibert *et al.* [151] later described a PDH locked Ho:YLF ring-cavity laser capable of producing 12 mJ pulses at a PRF of 2 kHz and wavelength of 2 µm, using an intracavity AOM Q-switch. These implementations of the PDH technique suffer from the high losses in the low-Q state of the slave laser, limiting the subsequent error slope [211] and hence the sensitivity of the system to frequency noise.

Ostermeyer *et al.* [212–214] attempted to overcome these limitations by implementing an adapted PDH technique to an Nd:YAG ring-cavity laser, in which the resonator is in a high-Q state between pump pulses. During this time, the PDH technique is applied to obtain lock. When the pump diode is pulsed a 'sample-and-hold' circuit is used to hold the laser at the lock point during the low-Q state. Using this scheme the authors were able to obtain 20 mJ pulses at a PRF of 400 Hz and pulse-to-pulse frequency reproducibility of sub-megahertz. However, the servo-bandwidth obtainable using this technique is severely limited by the duration in which the cavity is kept in low-Q mode [215], which in this instance was 200 µs.

Fibertek Inc. [110,111] reported an Er:YAG ring-resonator laser capable of produc-

ing 2 mJ pulses at a PRF of 2 kHz injection-seeded using the PDH technique. Resonance was monitored via the transmission through an intra-cavity PBS whilst the cavity is in a low-Q state. As such, the error signal generated is due to interference between only two round-trips of the master laser and is sinusoidal in shape. The authors report reliable injection-seeding near methane line-centre at 1645.52 nm and, by switching onto a second master laser, the capability for methane DIAL measurements. To ensure successful injection-seeding of the second master laser the PDH servo has to re-acquire lock, which takes upwards of 100 µs. This large temporal separation between the online and offline wavelength would severely limit the sensitivity of an airborne DIAL system that relied on ground scattering for a return signal.

In this chapter we investigate the feasibility of a 'sub-threshold' transmission PDH seed architecture that overcomes the low-Q and low-bandwidth limitations of previous Q-switched servo schemes. An outline of this chapter is as follows. Section 4.2 describes the slave resonator, PDH electronics and the corresponding PDH error signal. The development of a custom photodetector capable of monitoring the cavity resonance whilst surviving the high-energy pulses is outlined in Section 4.2.1. The design of high-bandwidth servo-systems for seeding using either a DFB or an ECDL master laser is outlined in Section 4.3.

The reliability of injection-seeding is assessed using the build-up time, heterodyne beat signal and optical spectrum in Section 4.4. This is divided into Sub-Sections 4.4.1 and 4.4.2 which describe injection-seeding with the DFB and ECDL master lasers respectively. While both master lasers enable successful seeding at erbium line-centre ($\lambda = 1645.15$ nm) it was found that only the narrow linewidth ECDL ensures consistent seeding at methane line-centre ($\lambda = 1645.55$ nm).

To enable rapid switching between online and offline master lasers while maintaining injection-seeding, I developed an Optical Phase Locked Loop (OPLL) scheme that locks the offline master laser an integer number of slave laser free-spectral ranges from the online master laser, as outlined in Section 4.5.

This chapter concludes in Section 4.6 with a characterisation of the dual-pulsed injection-seeded laser system, highlighting the wavelength tunability of both the online and offline laser pulses. For the readers reference a full-page diagram of the complete reliable injection-seeded system is provided in Figure 4.36 on page 89.

4.2 Slave Laser PDH System

A schematic of the injection-seeded Q-switched slave laser is shown in Figure 4.2. The QWP was introduced into the resonator in Chapter 3 to overcome instability in the Pockels Cell by 'pre-loading' the Q-switch. This also increases the Q of the resonator as only 50% of the π-polarised light from the gain medium is out-coupled each round-

trip. Thus, injected light from the master laser is regeneratively amplified, creating a sub-threshold pre-lase.

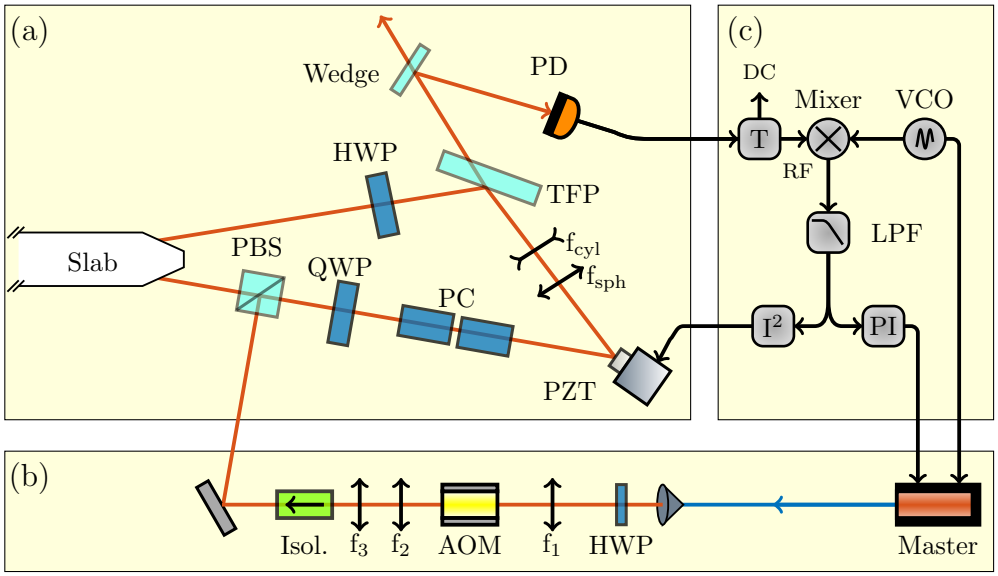

Figure 4.2: Schematic of the PDH injection-seeding scheme highlighting (a) the pumped Er:YAG ring-laser with the pre-loaded Q-switch topology, (b) the master laser injection-arm and (c) the PDH locking electronics including a Bias-Tee (T), Voltage-Controlled Oscillator (VCO), Low-Pass Filter (LPF), Proportional-Integral (PI) controller and double-integrator (I^2) controller.

The transmission of the ECDL master laser injected into the sub-threshold slave resonator was measured as a PZT scanned the cavity length through multiple free spectral ranges, as shown in Figure 4.3. We observe transmission peaks with a narrow resonance width $\Delta_s = 8\,\text{MHz}$ separated by a free spectral range of $\Delta_\nu = 638\,\text{MHz}$ corresponding to a finesse $F = 79.8$.

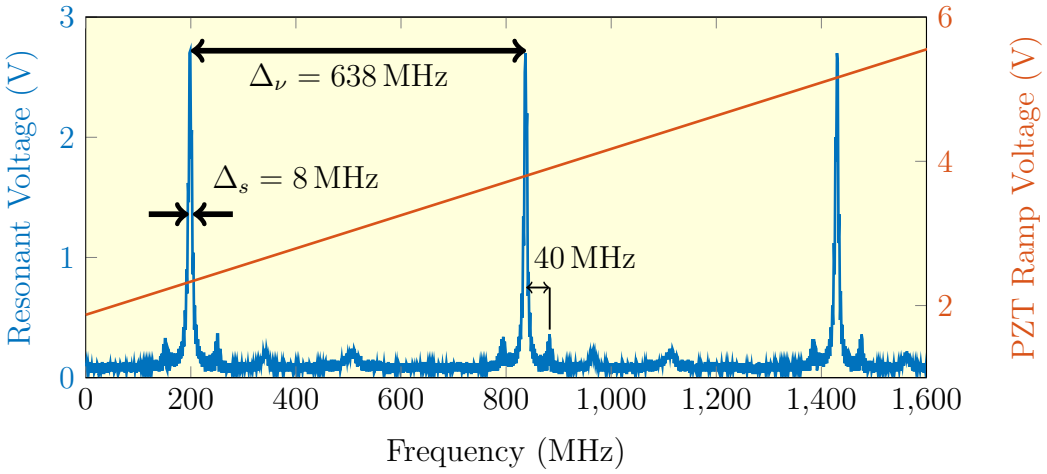

Figure 4.3: Resonance scan of the sub-threshold slave laser measured on a Newport 1811-FS photodetector.

The RF phase-modulation sidebands required for PDH servo-control are imposed on the master laser by modulating the drive current at 40 MHz using a *Mini-Circuits* ZOS-75+ VCO. These sidebands are transmitted through the slave resonator, creating amplitude modulation sidebands if the frequency of the carrier is displaced from the line-centre frequency of the slave resonator. These sidebands are measured using a high-bandwidth photodetector (PD). The PDH error signal is produced by demodulating the PD output to baseband using a *Mini-Circuits* ZFM-3-S+ mixer, the output of which is Low-Pass Filtered (LPF) with a *Mini-Circuits* SLP-1.9+. This signal is processed as described in Section 4.3 and used to control the frequency of the slave laser at low-frequencies and the frequency of the master laser at high-frequencies.

4.2.1 A Photodetector for PDH Seeding

If successfully injection-seeded, the slave resonator will produce a forward-wave pulse that is matched in wavelength, beam-pointing and polarisation to the master laser. Hence, standard optical techniques cannot be used to separate the high-peak-power pulse (≈10 kW) from the regeneratively amplified master laser transmission (≈10 mW). To monitor the PDH modulation signal the photodetector must have a large dynamic range (>120 dB) whilst also maintaining a high-bandwidth (>40 MHz). To our knowledge there are no commercially available photodetectors capable of achieving these specifications.

Whilst high-bandwidth, high-dynamic-range photodetectors have been reported in literature, they either lack the bandwidth [216] or dynamic range [217–219] required. The dynamic range can be increased by implementing a logarithmic amplification stage using a non-linear device such as a Field-Effect Transistor (FET) [220–222], however, this produces non-linear signals that are not suitable for PDH. Alternatively, a low dynamic range photodetector can be used by recognising that the forward-wave pulse can saturate the photodetector provided that the saturation response time does not limit the servo bandwidth. We decided to investigate the feasibility of a custom 'saturating' photodetector with the following specifications.

- High-bandwidth (BW>40 MHz) to resolve the PDH modulation signal.
- High-gain and low-noise to improve sensitivity
- Large area photodiode ($\phi > 1$ mm) to limit peak intensity
- Quick recovery time following an overdriven pulse

The Transimpedance Amplifier (TIA) configuration is commonly used in the design of high-bandwidth photodetectors. However, when large area photodiodes are used their large capacitance ($C_{pd} > 100$ pF) typically limits the photodetector bandwidth.

In this case, a technique known as bootstrapping can be used to reduce the apparent input capacitance and hence enhance the bandwidth [223]. A bootstrapped TIA based upon work presented by Zhou *et al.* [224, 225] is illustrated in Figure 4.4. The principle of this technique is that a follower amplifier acts to keep the voltage difference across the photodiode fixed, reducing the effective photodiode capacitance. In practice, the photodiode capacitance is replaced by the significantly smaller capacitance of the follower amplifier. Whilst we did not require this photodetector to be DC coupled, it proved to be simpler than implementing a resonant tank design.

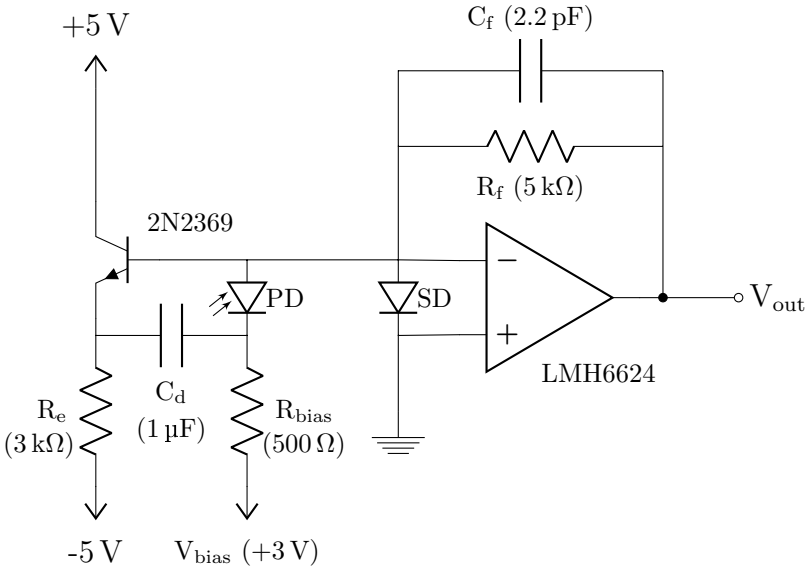

Figure 4.4: The bootstrapped transimpedance amplifier circuit diagram.

To limit the peak intensity we propose to use the large-area *Thorlabs* FGA21 photodiode; this has an active area of $3.1\,\mathrm{mm}^2$ and a capacitance $C_{pd} = 100\,\mathrm{pF}$. This is reverse biased at a voltage V_{bias} which is coupled to the photodiode through R_{bias}.

The bootstrap is implemented using the *Multicomp* 2N2369 Bi-Polar Junction Transistor (BJT), forming a high-bandwidth, low-capacitance emitter follower stage. The resistor capacitor pair (R_e & C_d) correctly biases the emitter follower and couples the AC signal across to the photodiode. This acts as the input stage for the transimpedance amplifier formed using the LMH6624 operational amplifier, selected for its low-noise, high-bandwidth specifications.

The feedback resistor R_f and capacitor C_f are set to $5\,\mathrm{k\Omega}$ and $2.2\,\mathrm{pF}$ respectively to ensure a sufficiently high transimpedance gain with a nominally flat frequency response. The 1N4148W Shunt Diode (SD) is used to protect the op-amp input pins from high-current surges; this low-capacitance device is able to short currents exceeding 1 A.

To ensure the required bandwidth enhancement was achieved, simulations were undertaken in the open-source analog electronic circuit simulator SPICE [226, 227]. The predicted transimpedance gain of both the bootstrapped and standard TIA configu-

rations is plotted in Figure 4.5. This simulation shows a significant bandwidth enhancement to 60 MHz can be achieved by implementing the bootstrapped TIA, which is sufficient for the PDH servo system.

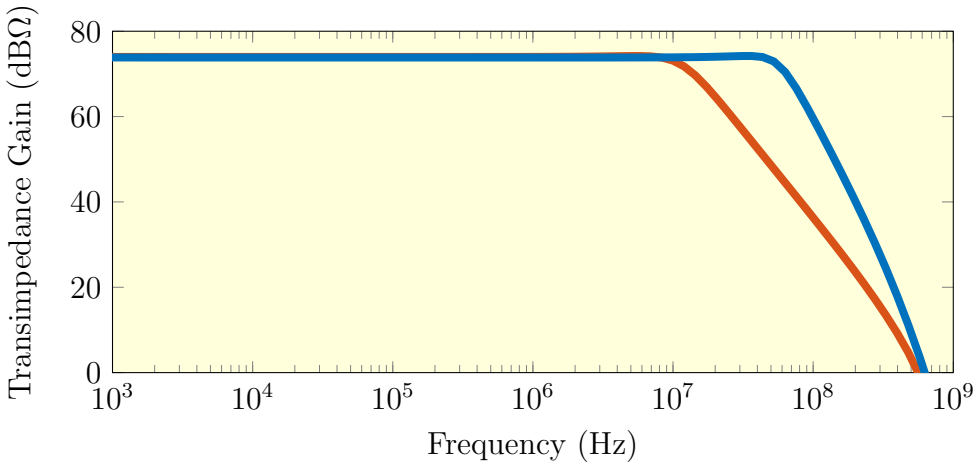

Figure 4.5: Predicted transimpedance gain of the bootstrapped and standard TIA configurations with $R_f = 5\,k\Omega$, $C_f = 2.2\,pF$, $R_e = 3\,k\Omega$, $R_b = 500\,\Omega$ and $C_d = 1\,\mu F$.

A Printed Circuit Board (PCB) was designed and constructed using the simulation parameters; an outline of the circuit design principles is given in Appendix E. To confirm the bandwidth of the circuit, we measured the output voltage noise of the photodetector, as the voltage noise of a TIA will exhibit significant roll-off past the 3 dB bandwidth (see Chapter 5 for more details).

The voltage noise was measured using the *Agilent* 89410A and *Agilent* N9320A spectrum analysers. The measured noise spectrum is plotted in Figure 4.6, and indicates a TIA bandwidth of approximately 60 MHz, as expected.

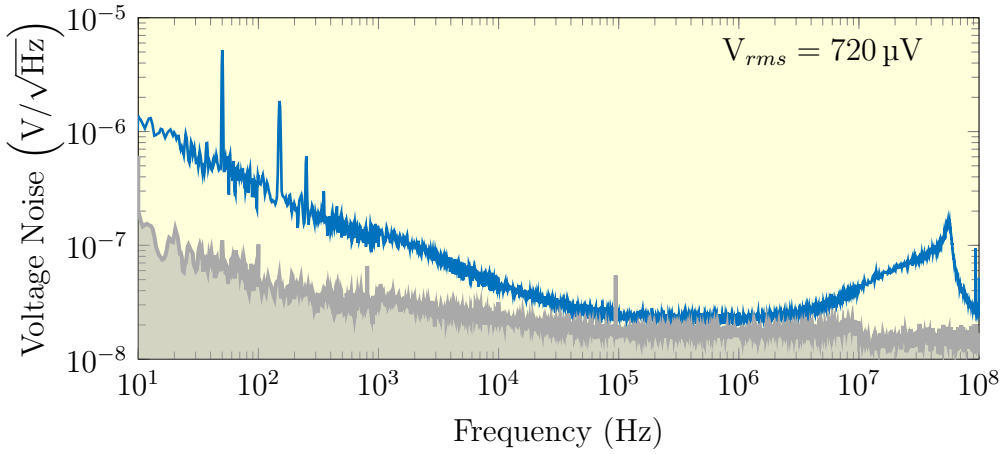

Figure 4.6: Measured voltage noise of the bootstrapped TIA photodetector, the shaded grey area represents the measurement noise floor.

The photodetector must also exhibit a quick response when overdriven to minimise the 'dead-time' where the cavity resonance cannot be monitored and enable high-bandwidth control. Hence, we measured the photodetector recovery time by saturating the photodetector with the pulsed slave laser. We define the recovery time as the time required for the photodetector to return to within 5% of the initial output DC voltage. The measured recovery time is illustrated below in Figure 4.7.

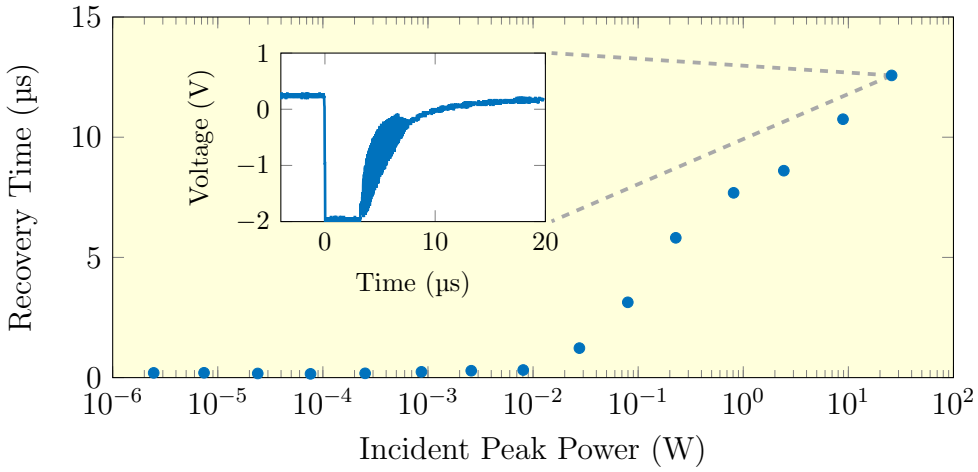

Figure 4.7: Overdrive response time of the bootstrapped photodetector to a range of peak power pulses, the inset graph illustrates the voltage output of the photodetector when heavily overdriven.

We observe two separate response regimes; below a 10 mW peak power, the recovery time is sub-microsecond, and above this power the recovery time increases significantly. The increased recovery time is dominated by an exponential decay (see inset figure) which we believe is caused by the capacitive discharge of the shunt diode. Based on these results, the optical attenuation before the photodetector is set so that the recovery time is approximately 10 µs. To our knowledge this 'dead-time' is significantly lower than that achieved in other published Q-switched PDH systems, thus enabling higher bandwidth control.

The required attenuation is sufficiently low to generate a low-noise PDH error signal from the master laser resonance with a steady state pump of 20 W and a PC voltage of 0 V. As plotted in Figure 4.8 this error signal exhibits a steep linear region with a slope $D_s = 4.0{\times}10^{-9}$ V/Hz. The width of the linear region is approximately $\Delta_{\mathrm{PDH}} = \pm 3$ MHz about laser gain centre, as would be expected from the linewidth measured in Figure 4.3. Thus, we expect a maximum frequency difference between light from the master laser and that in the Q-switch pulse of a few megahertz, which is significantly less than the width of the methane absorption line.

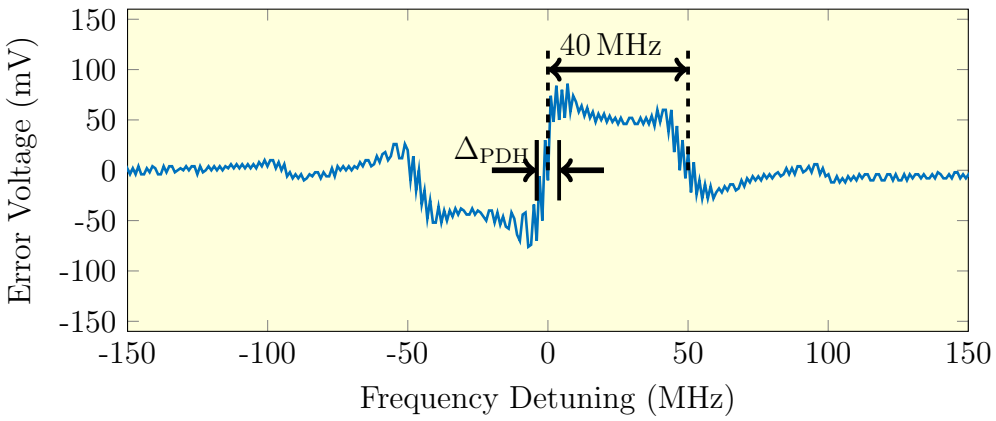

Figure 4.8: Measured PDH error signal generated from sub-threshold slave cavity.

4.3 PDH Control System

A schematic of the servo control system is shown in Figure 4.9. The frequency discriminator described in Section 4.2 generates an error signal with slope D_s which is applied to two separate PI controllers; a high-dynamic-range, low-bandwidth controller with transfer function $PI_{LF}(f)$ which compensates for the low-frequency noise and a high-bandwidth controller with transfer function $PI_{HF}(f)$ to suppress the broadband noise. We achieve low-frequency stabilisation using the slave cavity PZT and high-frequency stabilisation by acting on the master laser current, which have transfer functions $A_{PZT}(f)$ and $A_{ML}(f)$ respectively.

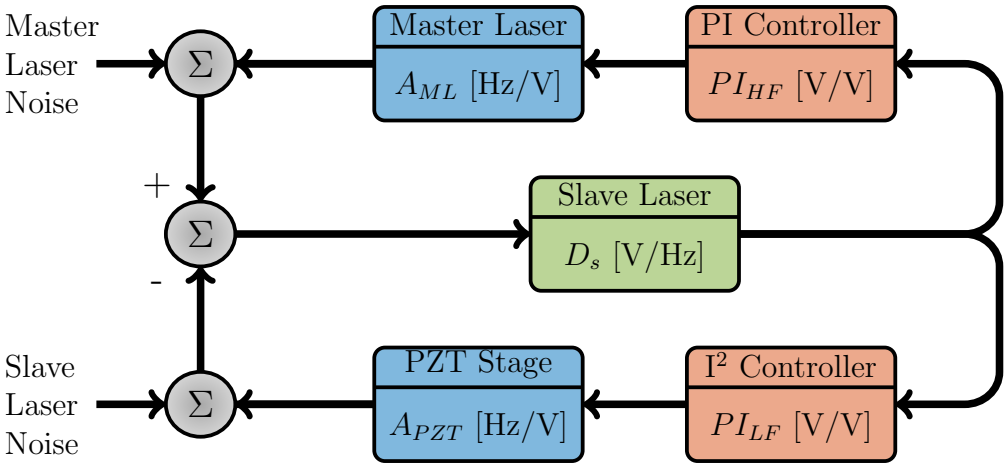

Figure 4.9: Equivalent block diagram of the PDH locking scheme highlighting; the discriminator, the PI controllers and the frequency actuators.

The servo reduces fluctuation in the frequency difference between the master and slave lasers by the loop-gain $G(f)$:

$$G(f) = G_{LF}(f) + G_{HF}(f) \tag{4.1}$$

where $G_{LF}(f)$ and $G_{HF}(f)$ represent the low-frequency and high-frequency control loops, given by.

$$G_{LF}(f) = D_s \times PI_{\mathrm{LF}}(f) \times A_{\mathrm{PZT}}(f) \tag{4.2}$$

$$G_{HF}(f) = D_s \times PI_{\mathrm{HF}}(f) \times A_{\mathrm{ML}}(f) \tag{4.3}$$

The following criteria must be met for stable control:

1. At the 'cross-over frequency' f_c where $|G_{LF}(f)| = |G_{HF}(f)|$ the slopes must differ by less that 40 dB/decade. For good stability, a difference of 20 dB/decade, which will result in a phase lag $\Delta\phi = 90°$, is preferred [228].

2. At the '0 dB frequency' f_{BW} for which $|G(f_{BW})| = 1$, the phase lag must be less than 180° [229]. Alternatively, this can be quantified using the phase margin.

$$\phi_{pm} = 180° - |\angle G(f_{BW})| > 0° \tag{4.4}$$

The closed-loop reduction in frequency difference is given by [230].

$$S(f) = \frac{1}{1 + G(f)} \tag{4.5}$$

The closed-loop error noise can be calculated by multiplying the open-loop noise and $S(f)$, as examined further in Sections 4.3.3 and 4.3.4.

4.3.1 Master Laser Actuation

Current modulation provides a convenient means of direct Frequency Modulation (FM) in semiconductor lasers. A change in current affects both the temperature and carrier density in the active region, altering the refractive index and hence the resonant axial mode frequency of the laser. Ideally, the current-to-frequency transfer function should exhibit high gain with a flat phase response to facilitate broadband feedback with minimal intensity modulation. Multiple techniques have been used to determine this transfer function, these include the use of birefringent optical filters [231] or Mach-Zender interferometers [232].

Alternatively, both the PDH and FM spectroscopy techniques provide a direct means of measuring the current-to-frequency transfer function of a semiconductor laser by using a Fabry-Perot cavity as a frequency discriminator. The PDH technique provides a high-linearity error signal used to calibrate voltage changes at the error point to a frequency change. As discussed previously in Chapter 2, this has distinct advan-

tages over the FM spectroscopy technique which uses the 3 dB point of the Fabry-Perot reflection dip.

We measure the frequency actuation using the system illustrated in Figure 4.10. This is adapted from the master laser frequency noise measurement introduced in Chapter 2 and hence key components are not redefined. The transfer function is recorded by directly modulating the injection current at V_{in} and recording the frequency change at the error point V_{out} as the laser sits on resonance without active servo control.

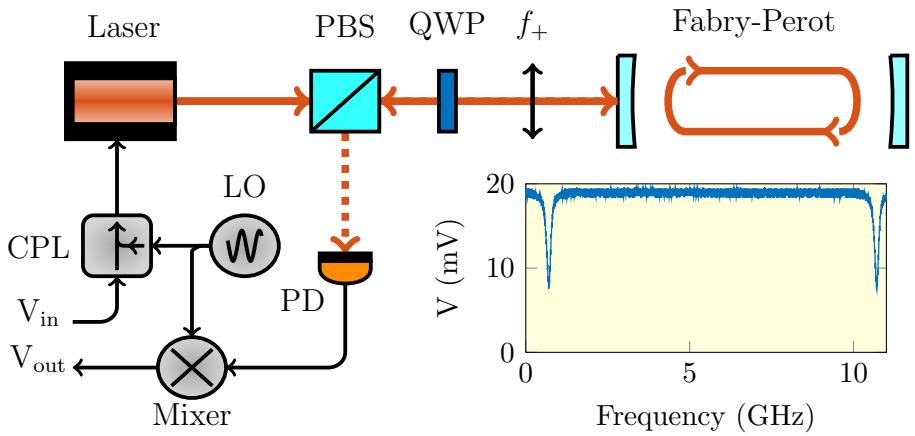

Figure 4.10: A schematic of the current to frequency transfer function measurement system. For the ECDL a coupler (CPL) is introduced to combine the 40MHz LO signal and the input modulation signal, this was not required for the DFB laser as the module has two separate modulation ports. The inset graph illustrates the output signal as the cavity is scanned across multiple resonance dips.

The frequency actuation of the ECDL master laser, recorded using the *Agilent* 89410A spectrum analyser, is plotted in Figure 4.11.

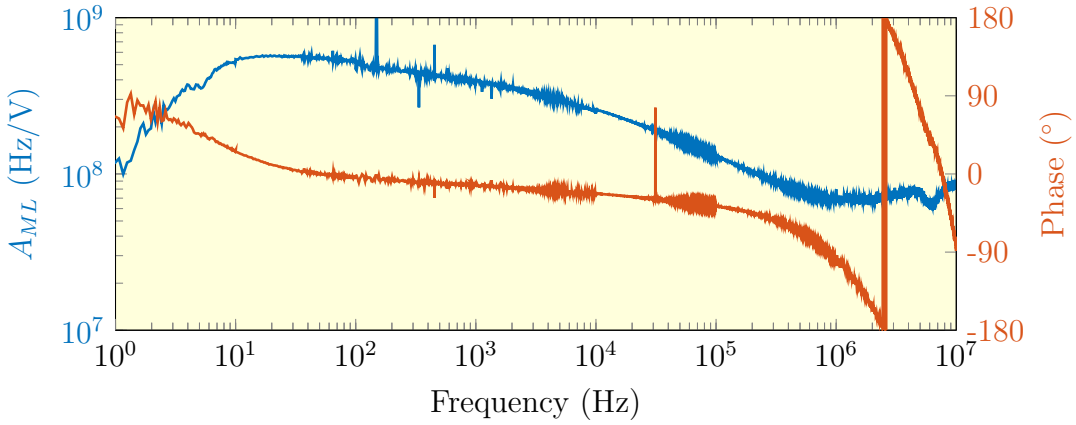

Figure 4.11: Measured frequency actuation of the ECDL master laser.

This exhibits a low-frequency cut-off in actuation below 50 Hz as specified by the manufacturer. Above 50 Hz there is a gradual decline in actuation; this is consistent

with experimental and theoretical results [233, 234] which attribute this to thermal effects within the diode structure. This roll-off flattens at approximately 1 MHz, where the dominant actuation changes from thermal to carrier effects in the diode structure.

The frequency actuation of the DFB master laser, recorded using the Agilent 89410A spectrum analyser, is plotted in Figure 4.12. This exhibits an approximately flat response in the low-frequency regime allowing DC frequency modulation. A notch is clearly resolved at 10 kHz, we believe this is introduced by the manufacturer to reduce the increased frequency noise in this band. Above this frequency, we observe a gradual decline in actuation up to 10 MHz.

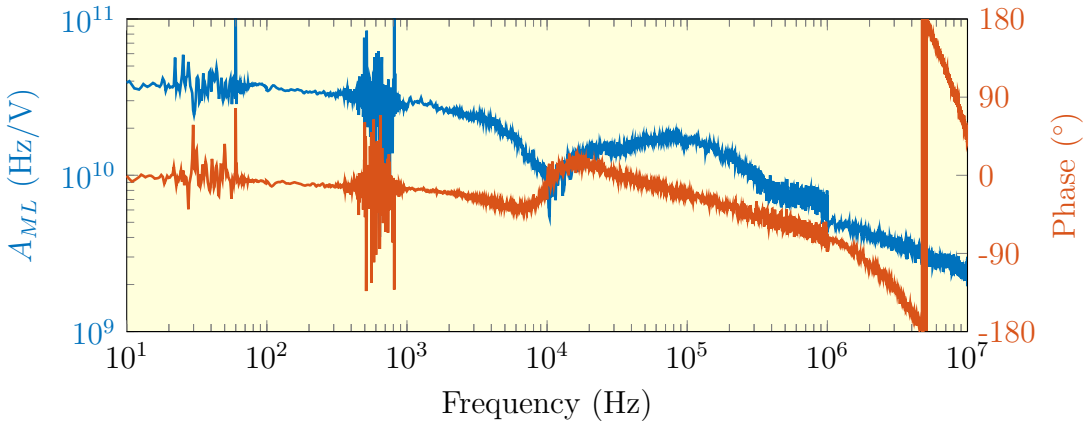

Figure 4.12: Measured frequency actuation of the DFB master laser.

4.3.2 Piezo Actuation

The transfer function of the piezo actuation, A_{PZT}, was estimated from the slave cavity resonance scan, described in Section 4.2, and an electrical transfer function of the PZT and its driver. The result is plotted in 4.13.

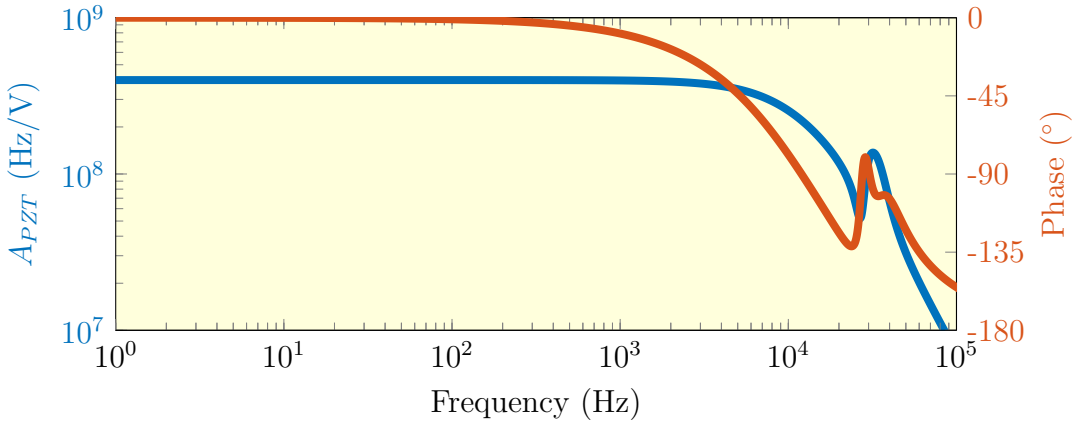

Figure 4.13: Amplitude and phase transfer function of the slave cavity PZT and driver.

The transfer function exhibits phase roll-off above a frequency of 1 kHz and an electrical resonance at 30 kHz - suggesting an achievable low-frequency control bandwidth of approximately 1 kHz. This transfer function estimate does not include the mechanical resonances of the PZT actuator, which would further limit the bandwidth. Specially designed PZT systems have been presented in literature to suppress resonant features and enhance the control bandwidth [235, 236]. However, such designs were not required as the PZT actuator was only used for low-frequency control.

4.3.3 ECDL Servo Design

Since the ECDL actuation drops rapidly below 50 Hz and we wish to maximise the low-frequency loop-gain, the PI controllers must be carefully designed to ensure stability at the cross-over frequency. Thus, the low-frequency (PZT) controller has a unity-gain frequency of 500 Hz, below which the gain increases as a double-integrator with a slope of 40 dB/decade to maximize the suppression of low-frequency noise through the PZT stage. The high-frequency (ECDL) PI controller has a proportional gain of -10 dB and a corner frequency of 300 kHz. To ensure the low-frequency loop-gain dominates below the cross-over frequency the gain is clamped at 30 dB and is hence proportional from DC to 3 kHz, this is commonly referred to as a Low-Frequency Gain Limit (LFGL).

The predicted loop-gains G_{LF} and G_{HF} are shown in Figure 4.14.

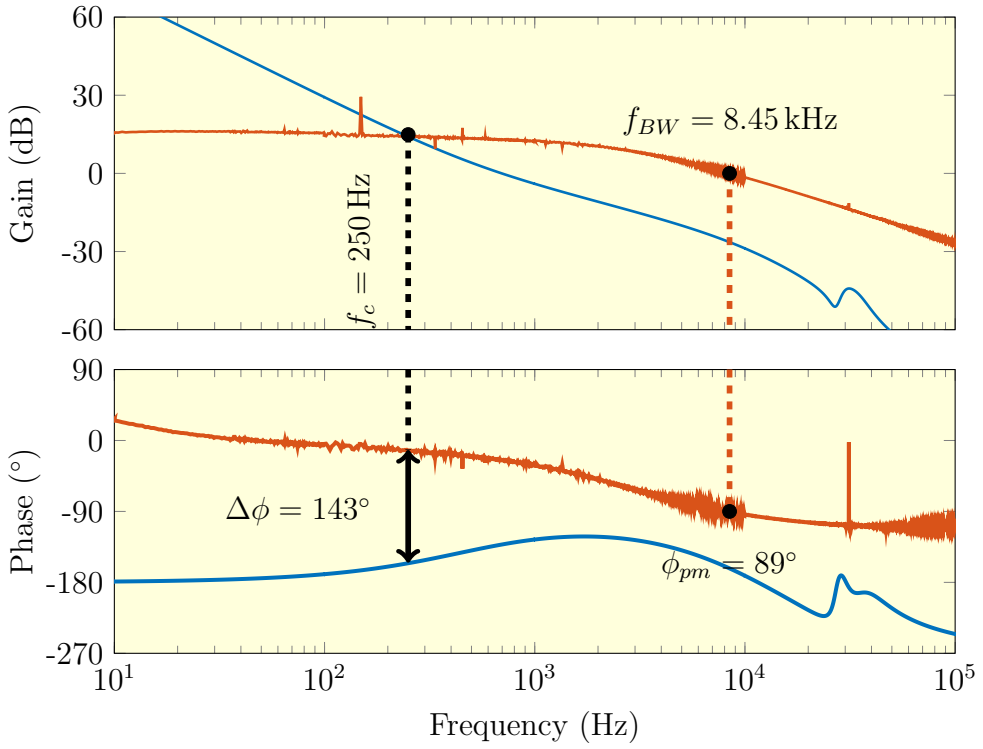

Figure 4.14: Predicted low-frequency (G_{LF}) and high-frequency (G_{HF}) loop-gains for the ECDL servo lock.

This loop-gain model shows a cross-over frequency $f_c = 250\,\text{Hz}$ with a phase difference $\Delta\phi = 143°$, and a 0 dB frequency $f_{BW} = 8.5\,\text{kHz}$ with a phase margin $\phi_{pm} = 89°$.

The lock to the slave laser was implemented using the *Liquid Instruments* Moku:Lab and the *Newport* LB1005 as the low-frequency and high-frequency controllers respectively. The residual closed-loop frequency noise at the error point were measured using the *Agilent* 89410A spectrum analyser. We compare this to the master laser noise measured in Section 2.4.2 and the predicted residual noise in Figure 4.15. We observe this control system suppresses the low-frequency master laser noise with a measured control bandwidth of approximately 7.35 kHz as expected.

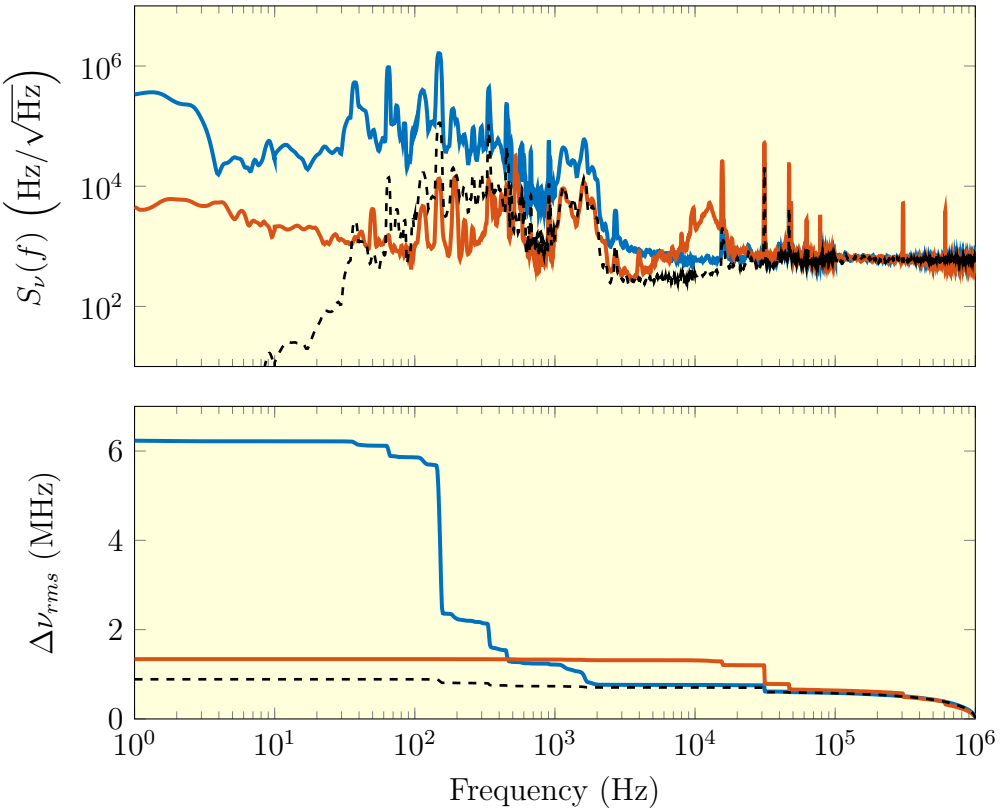

Figure 4.15: Measured frequency noise density of the unlocked and locked ECDL laser, the dashed line represents the predicted frequency noise density. The RMS frequency noise highlights the noise suppression achieved by implementing this control system.

The predicted and measured closed-loop frequency noise agree above 1 kHz. However, the measured frequency-noise shows a significant servo hump at 10 kHz, suggesting the predicted phase margin $\phi_{pm} = 89°$ may be an over estimate. There is also a servo hump near the cross-over frequency, indicating that the phase difference of $\Delta\phi = 143°$ is too large. At frequencies below 50 Hz, the measured closed-loop frequency noise is significantly larger than that predicted. We attribute this discrepancy to the low-frequency slave laser noise which was not accounted for during the measurement of the

master laser noise.

The plotted RMS frequency noise shows that the control system significantly suppresses the low-frequency noise: reducing it from 6 MHz to approximately 1 MHz. Although the model did not account for frequency noise contribution from the slave laser, it appears its contribution to the RMS noise is perhaps negligible.

4.3.4 DFB Servo Design

The DC coupling and wider bandwidth of the DFB actuator simplifies the design of the servo loop. The high-frequency (DFB) controller has a proportional gain of 8 dB and a corner frequency of 1MHz. In this control scheme, the frequency corrections are exclusively sent to the master laser current, eliminating the need for an intra-cavity PZT. The predicted loop-gain is plotted in Figure 4.16.

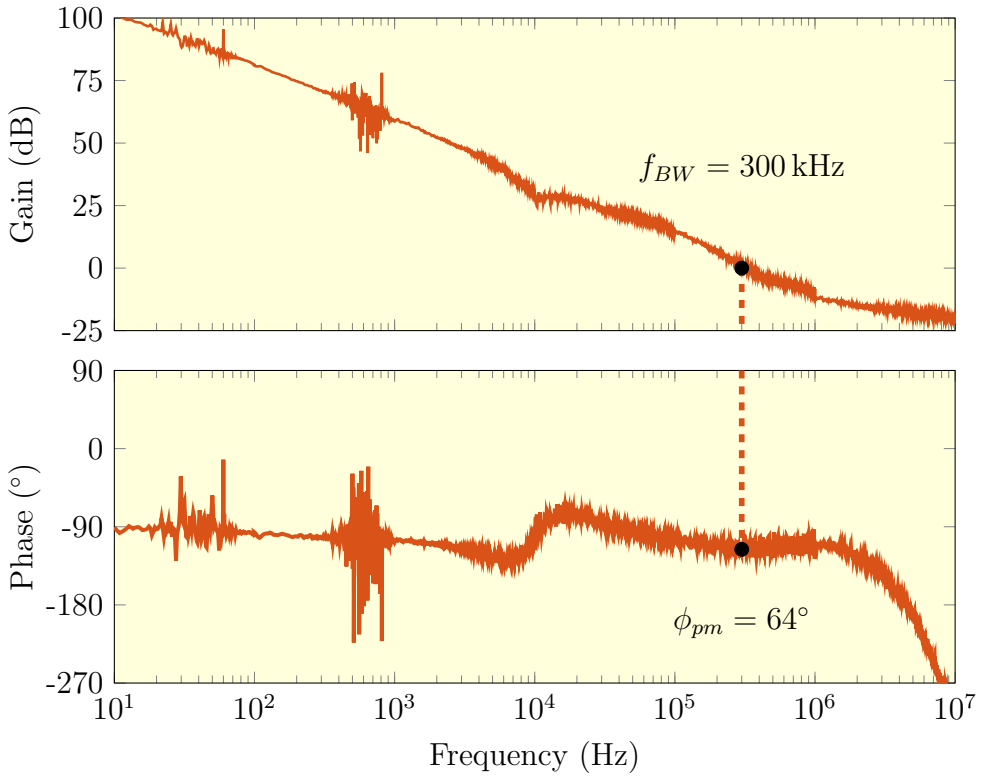

Figure 4.16: Predicted loop-gain of the DFB servo lock where error corrections are exclusively fed-back to the master laser current.

This loop-gain model shows a 0 dB frequency $f_{BW} = 300\,\text{kHz}$ with a phase margin $\phi_{pm} = 64°$. The lock was implemented *Newport* LB1005 PI controller. The residual frequency noise at the error point was measured using the *Agilent* 89410A spectrum analyser as before. We compare this to the master laser noise measured in Section 2.4.2 and the predicted residual noise in Figure 4.17. We observe this control system suppresses the broadband frequency noise of the DFB master laser. The control band-

width is estimated to be approximately 300 kHz based upon the intersection between the open-loop and closed-loop noise spectra, as predicted by the loop-gain model.

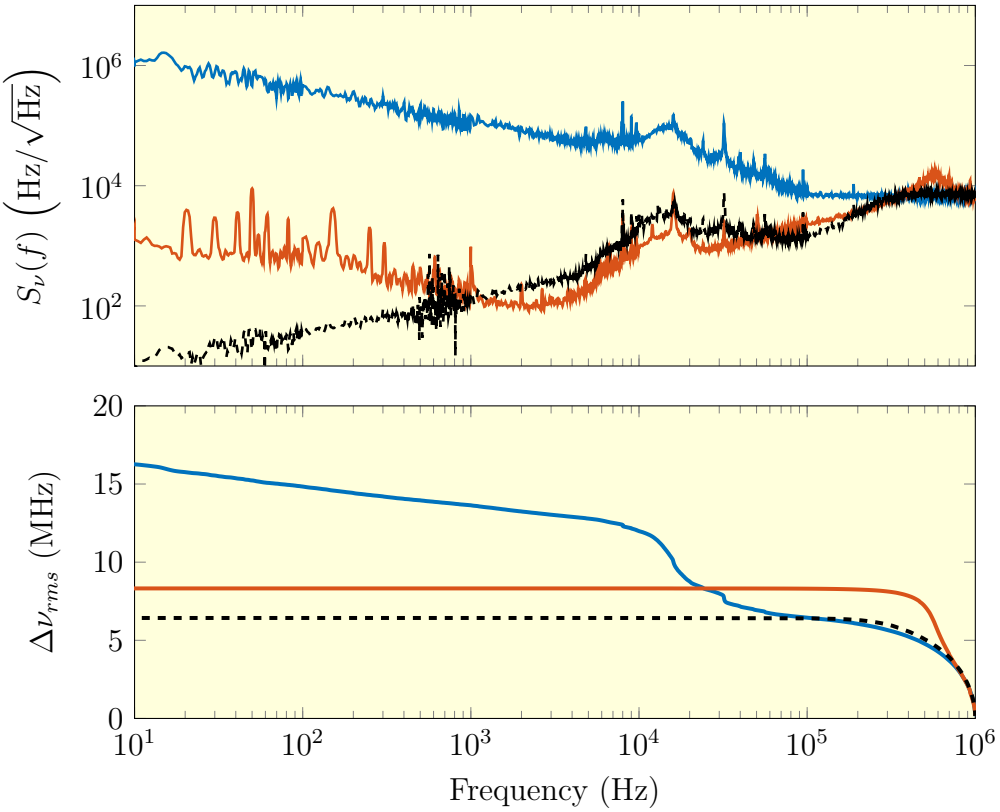

Figure 4.17: Measured frequency noise density of the unlocked and locked DFB laser, the dashed line represents the predicted frequency noise density. The RMS frequency noise highlights the noise suppression achieved by implementing this servo.

Once again, we observe reasonable agreement between the predicted and measured closed-loop noise above 1 kHz and below 1 kHz the loop-gain model suggests the DFB noise should be further reduced. The measured residual noise exhibits narrow peaks between 10 Hz and 100 Hz which may be evidence of resonant mechanical modes within the slave laser.

The plotted RMS frequency noise shows this high-bandwidth control has reduced the broadband noise of the DFB master laser from 16 MHz to approximately 8 MHz. This is significantly broader than the suppressed linewidth of the ECDL servo described in Section 4.3.3 and may limit the seeding efficiency, as examined in further detail in Section 4.4.1. Alternative control schemes may be necessary to further reduce this linewidth, commonly feedback to an Electro-Optic Modulator (EOM) is used to suppress the high-density frequency noise present above 1 MHz [237, 238]. Although this was not considered during this project, it may be applicable in future servo design iterations.

4.4 Reliable Single Pulse Injection-Seeding Characterisation

We have observed that the transmission PDH control scheme enables the master laser and a longitudinal mode of the slave laser to be locked tightly together. To ensure successive injection-seeded pulses we also require this servo to maintain lock following saturation by the forward wave pulse. We characterise the low-frequency temporal response of the lock by monitoring the DC output of the bias-tee (*Mini-circuits* ZFBT-4R2G+) positioned after the PDH photodetector (refer to Figure 4.2). A plot of the response of the PDH servo to consecutive saturating pulses is shown in Figure 4.18.

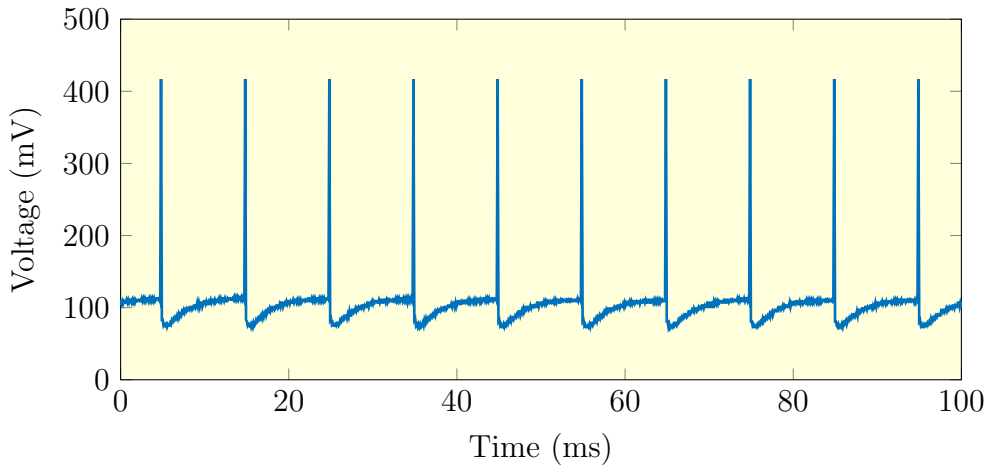

Figure 4.18: Response of the PDH servo to many saturating pulses when injection-seeded with the ECDL master laser.

At time $t = 0\,\text{ms}$ the lock is engaged and we observe an increased DC voltage level at the photodetector due to resonant amplification of the injected light within the slave cavity. Soon after the Q-switch is opened and the forward wave pulse saturates the photodetector. This pulse extracts a significant portion of the available gain, reducing the population inversion and the amplification of the injected power. Hence, we observe a decrease in the pre-lase power.

Following this, the transmission steadily increases as the gain medium is optically pumped and it appears to reach a steady-state level in approximately 10 ms. This behaviour is consistent with the optical pumping dynamics predicted in Chapter 3. We can infer that the lock is successfully maintained as the photodetector voltage reaches the same level as that maintained before the Q-switched pulse. This behaviour is also reproducible over consecutive pulses, suggesting this technique is suitable for reliable injection-seeding at a pulse repetition frequency of 100 Hz.

To quantify the quality of injection-seeding, we apply the build-up time criteria discussed in Section 2.3.2. Recall that we consider the pulse to be 'seeded' if it is

over before the pulse that evolves naturally from spontaneous emission can extract a significant amount of energy. By defining the natural build-up time τ_n, the pulse FWHM τ_p and seeded build-up time τ_s this criteria can be expressed as:

$$\tau_s < \tau_n - \tau_p \tag{4.6}$$

A set of injection-seeded pulses were recorded on the GaGe digitisation system for an observation time of 90 s, after which the lock was disengaged and a final 10 s of data was recorded to determine the natural build-up time and pulse width. In parallel, we recorded the heterodyne beat signal and we measure the optical spectrum of the slave laser using the HP70004a OSA with a resolution bandwidth of 0.08 nm, a video bandwidth of 10 Hz and a sensitivity of -90 dBm.

4.4.1 Injection-Seeding with the DFB Laser

The properties of the pulses produced by the slave laser when injection-seeded by the DFB master laser at the erbium line-centre wavelength of $\lambda = 1645.15$ nm are plotted in Figure 4.19.

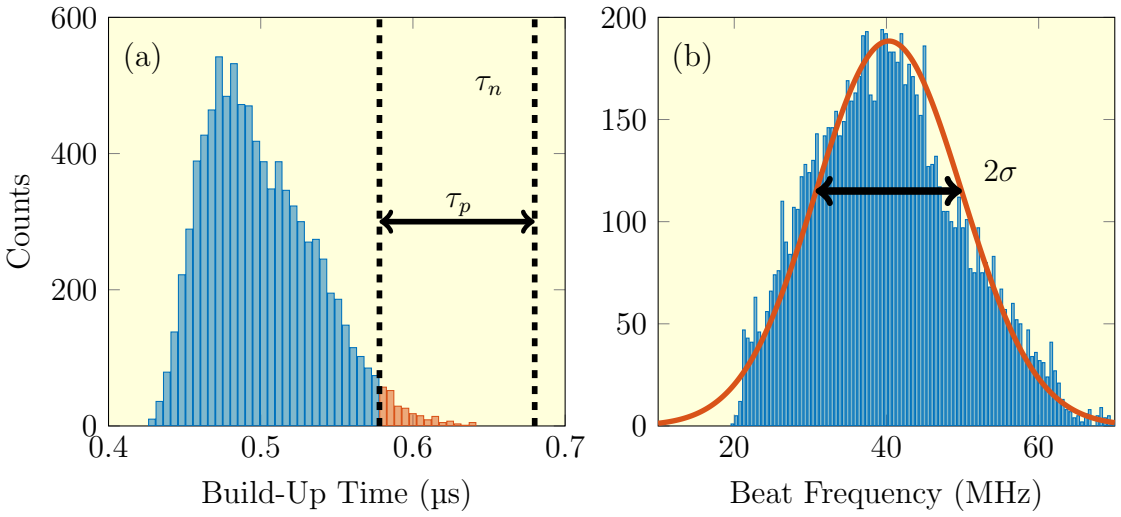

Figure 4.19: Pulse properties of the Er:YAG laser seeded using the DFB master laser operating at λ =1645.15 nm. (a) Histogram of the measured build-up time distribution with a bin size of 5 ns, highlighting the high proportion of pulses which are seeded compared to those which are unseeded. (b) Histogram of the heterodyne frequency for beat signals with an amplitude > 0.15 V. The distribution has a bin size of 0.5 MHz and the solid line represents the fitted Gaussian distribution.

We observe a distribution of build-up times centred around 500 ns. Based on the build-up time criterion 97.3% of the pulses were seeded. Furthermore, 99.9% of the pulses collected produced heterodyne beat signals with an amplitude greater than 150 mV. These heterodyne beats shows a broad distribution centred at 40.3 MHz with

a standard deviation of 9.62 MHz. The high seeding efficiency is further highlighted by the spectral output plotted in Figure 4.20. This exhibits a narrower output centred at the master laser wavelength of $\lambda = 1645.15$ nm, suggesting less longitudinal modes are running.

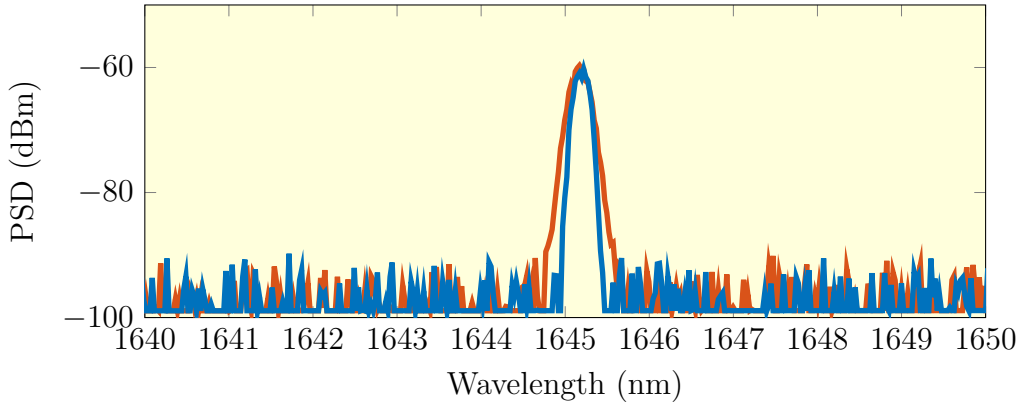

Figure 4.20: Measured spectra of the Er:YAG laser injection-seeded using the DFB master laser operating at λ =1645.15 nm compared to the free-running spectral output.

The properties of the pulses produced by the slave laser when injection-seeded by the DFB master laser on the methane wavelength of $\lambda = 1645.55$ nm are plotted in Figure 4.21.

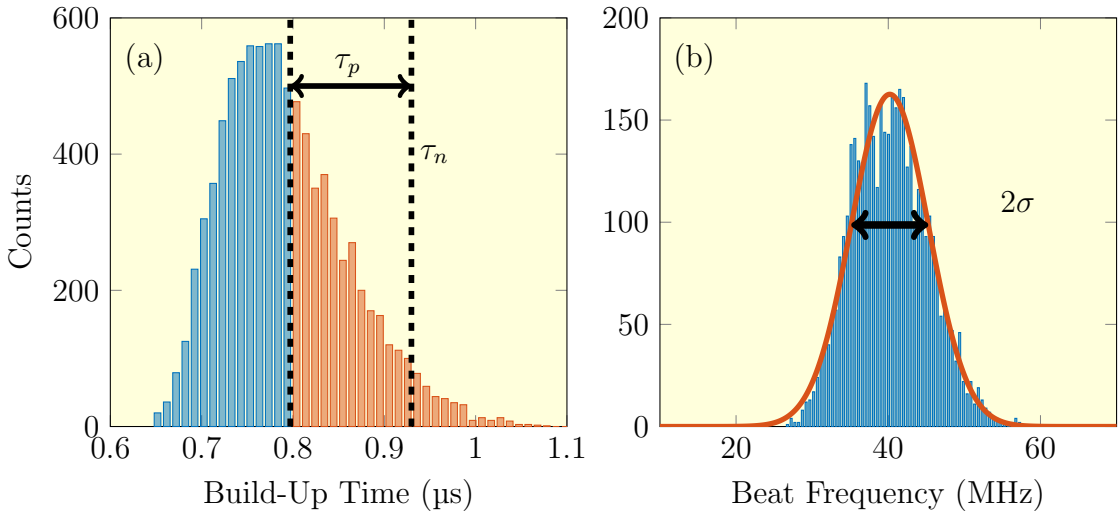

Figure 4.21: Pulse properties of the Er:YAG laser seeded using the DFB master laser operating at λ =1645.55 nm. (a) Histogram of the measured build-up time distribution with a bin size of 5 ns, highlighting the high proportion of pulses which are seeded compared to those which are unseeded. (b) Histogram of the heterodyne frequency for beat signals with an amplitude > 0.15 V. The distribution has a bin size of 0.5 MHz and the solid line represents the fitted Gaussian distribution.

Only 59.3% of the pulses satisfy the build-up time criterion and 46.5% of the pulses collected produced heterodyne beat signals with an amplitude greater than 150 mV.

These heterodyne beats exhibit a normal distribution centred at 40.2 MHz with a standard deviation of 5.06 MHz. In comparison to the erbium line-centre seeding data it is evident that less pulses are considered seeded - suggesting that the pulse is commonly developing from spontaneous emission. Theoretical studies have noted that the conditions for injection-seeded off line-centre are stricter as the injected field observes a lower round-trip gain [239].

This can be overcome by increasing the power of the master laser injected into the slave laser longitudinal mode. To successfully seed other injection-seeded Er:YAG laser system have required a master laser power of 500 mW [204–208]. Alternatively, a narrower linewidth source would ensure more of the injected power contributes to pulse build-up and improves the seeding efficiency. We believe that the broad-linewidth of the DFB master laser limits its effectiveness at injection-seeding off line-centre.

The slave laser spectral output, plotted below in Figure 4.22, further highlights the poor seeding efficiency. This measurement represents the average spectral output of multiple pulses because the measurement time of the OSA is much greater than the repetition rate of the laser. We observe evidence of pulses lasing at both the master wavelength and line-centre, which is further indication of inconsistent injection-seeding.

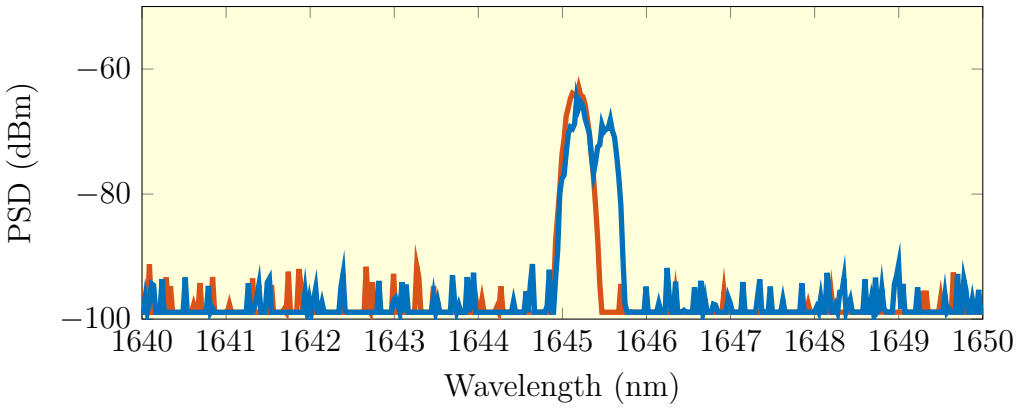

Figure 4.22: Measured spectra of the Er:YAG laser injection-seeded using the DFB master laser operating at λ =1645.55 nm compared to the free-running spectral output.

4.4.2 Injection-Seeding with the ECDL

The properties of all pulses produced by the slave laser when injection-seeded by the ECDL master laser at the erbium line-centre wavelength of $\lambda = 1645.15$ nm are plotted in Figure 4.23. We observe that all pulses were seeded according to the build-up time criteria, with a narrow distribution of build-up times centred at 630 ns, which is significantly reduced in comparison to the free-running build-up time. All heterodyne beat signals measured had an amplitude exceeding 150 mV, these beats exhibit a normal distribution centred at 37.13 MHz with a standard deviation of 0.375 MHz.

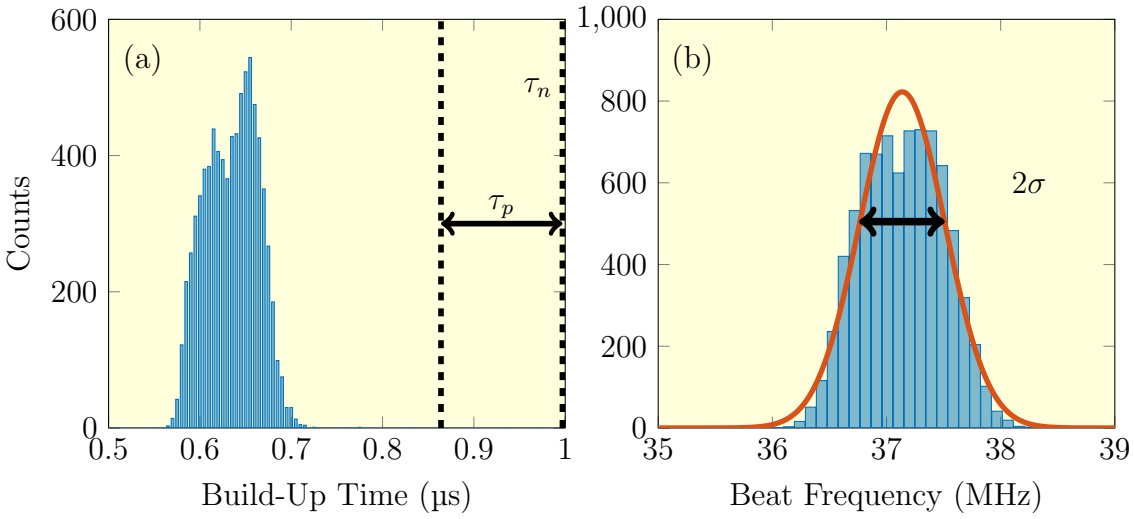

Figure 4.23: Pulse properties of the Er:YAG laser seeded using the ECDL master laser operating at λ =1645.15 nm. (a) Histogram of the measured build-up time distribution with a bin size of 5 ns, suggesting that all pulses were seeded. (b) Histogram of the heterodyne frequency distribution with a bin size of 0.1 MHz, the solid line represents the fitted Gaussian distribution.

An alternative means of illustrating the improved seeding performance is achieved by repeating the frequency chirp analysis outlined in Chapter 3. The relationship between the pulse build-up time, beat frequency and chirp rate is plotted in Figure 4.24. This exhibits a tight grouping of both the beat-frequency and build-up time, which is indicative of successful injection-seeding. Furthermore, all pulses are down-chirped with an average value of $f_{chirp} = -0.01$ MHz/ns.

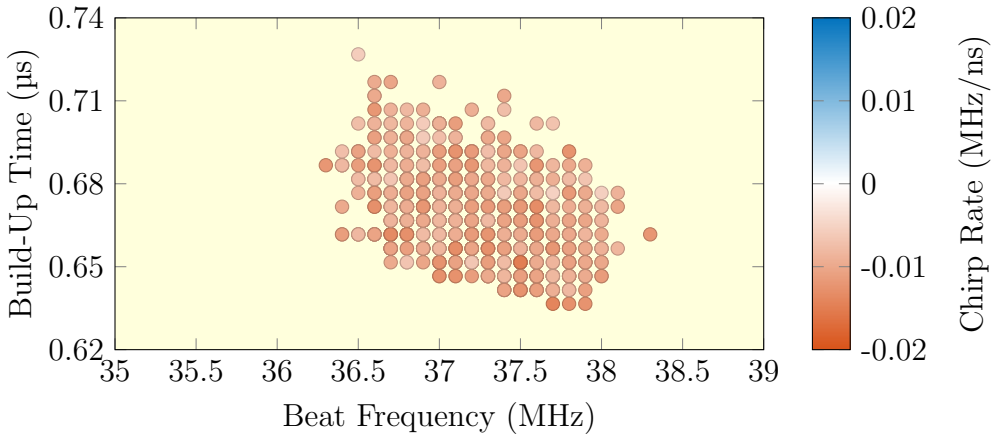

Figure 4.24: The relationship between the build-up time, beat frequency and frequency chirp of the slave laser injection-seeded at λ = 1645.15 nm using the ECDL.

Injection-seeding at the methane wavelength of λ = 1645.55 nm was attempted using the ECDL master laser. All corresponding pulse properties are plotted in Figure

4.25. Once again, we observe a significant reduction in build-up time suggesting that all pulses are seeded based upon the build-up time criterion. The two distinct peaks in the histogram are attributed to a change in slave laser output power that occurred during the observation time. All heterodyne beat signals measured had an amplitude exceeding 150 mV. These exhibit a normal distribution centred at 37.02 MHz with a standard deviation of 0.435 MHz, which is larger than for seeding at $\lambda = 1645.15$ nm but still much less than for the DFB master laser.

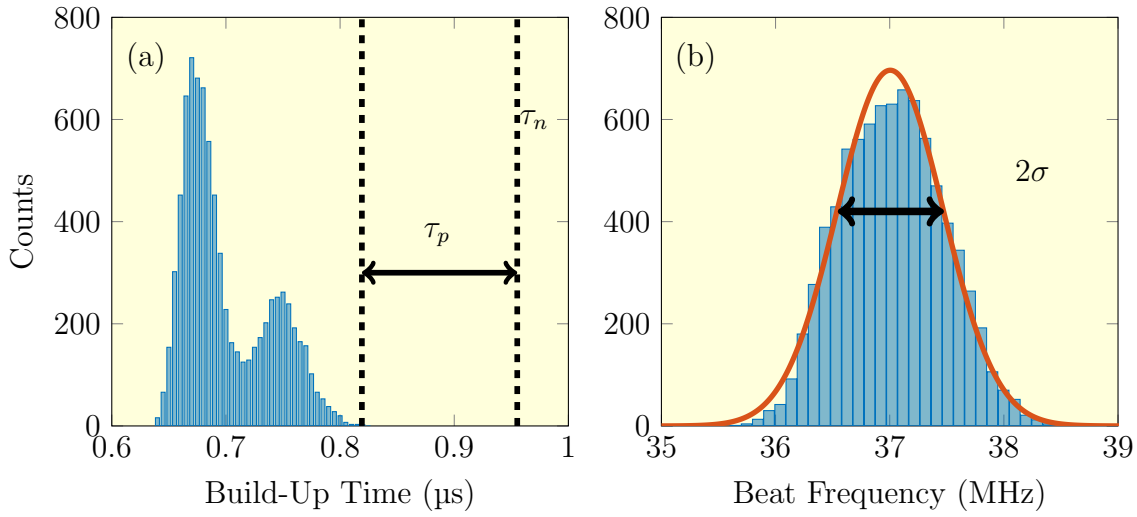

Figure 4.25: Pulse properties of the Er:YAG laser seeded using the ECDL master laser operating at λ =1645.55 nm. (a) Histogram of the measured build-up time distribution with a bin size of 5 ns, suggesting that all pulses were seeded. (b) Histogram of the heterodyne frequency distribution with a bin size of 0.1 MHz, the solid line represents the fitted Gaussian distribution.

The spectral output of the injection-seeded and free-running slave laser are plotted in Figure 4.26.

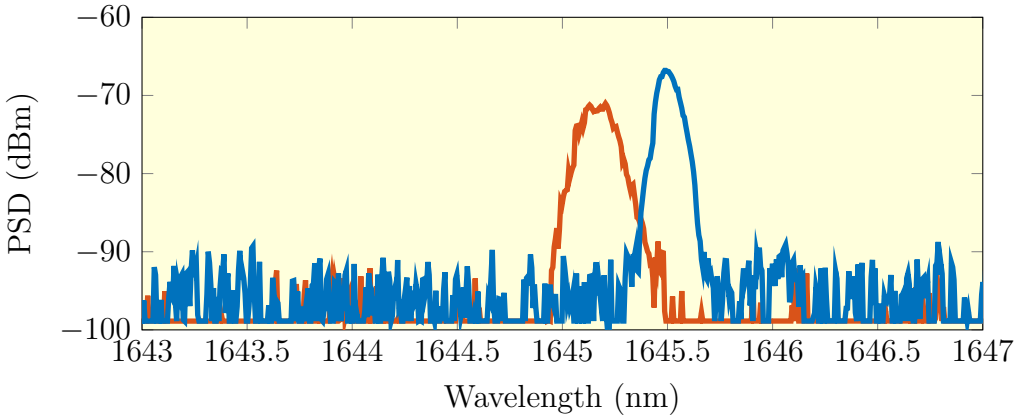

Figure 4.26: Measured spectra of the Er:YAG laser injection-seeded using the ECDL master laser operating at λ =1645.55 nm compared to the free-running spectral output.

We observe reliable seeding at the master wavelength of $\lambda = 1645.55\,\text{nm}$ suggesting more robust injection-seeding is capable using the ECDL master laser.

4.5 An Optical Phase Locked Loop

A Phase Locked Loop (PLL) is a feedback system that enables an oscillator to be phase synchronised to a reference oscillator with a tunable offset frequency. Since this technique was first demonstrated in 1965 [240] it has been applied in numerous fields including microwave photonics [241,242], spectroscopy [243] and astronomy [244]. The optical counterpart, known as the Optical Phase Locked Loop (OPLL) has been applied by Gibert *et al.* [245] for an injection-seeded CO_2 DIAL system and by Hamilton *et al.* [246–248] for a water-vapour DIAL system.

We propose to use an OPLL to lock the online laser with a frequency offset of an integer number of free-spectral ranges. This will ensure that both master lasers are continuously locked to the slave cavity, allowing spectral control of both the online and offline pulse. The online and offline wavelengths for the methane DIAL are compared to the dominant absorption lines near $\lambda = 1645\,\text{nm}$ in Figure 4.27.

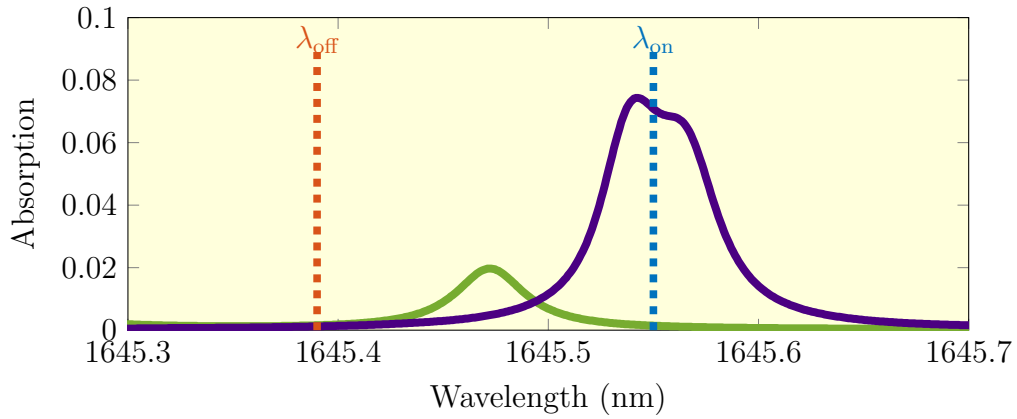

Figure 4.27: The absorption lines of CH_4 and H_2O near the Er:YAG emission line calculated using the HITRAN 2012 database for an observer at a range of 1 km. The proposed online and offline wavelengths are illustrated by the dashed lines.

To ensure a high measurement sensitivity, an offline wavelength $\lambda_{off} = 1645.39\,\text{nm}$ was carefully chosen to avoid the nearby water absorption line. This corresponds to a 15.95 GHz frequency offset (or alternatively a $N = 25$ FSR spacing) from the online wavelength of $\lambda_{on} = 1645.55\,\text{nm}$. Crucially this frequency offset does not exceed the capabilities of commercially available RF electronics.

OPLL systems operating near this frequency offset using commercially available electronics have been presented in literature [249–251]. We follow a similar approach in our system, which is illustrated schematically in the Figure 4.28. Both lasers are

combined onto a 12.5 GHz bandwidth InGaAs photodetector (*Newport* 818-BB-35F). Following this, an amplifier is used to compensate for the reduced gain of the photodetector, increasing heterodyne beat power to -12 dBm. This power level is within the recommended operating range of the $N = 8$ frequency dividers (*Analog Devices* HMC494) which reduce the heterodyne beat to 250 MHz. A $N = 80$ frequency divider (*ON Semiconductor* MC12080) then reduces the beat to 3.125 MHz and high frequency harmonics are filtered using a LPF. By dividing down to the MHz regime we can use the *RIGOL* DG1022 waveform generator, this can output a low-phase noise sine wave (-108dBc/Hz at 10kHz) with a tunable centre frequency. The resultant heterodyne beat is compared with a frequency reference via a mixer, generating a phase error signal which can be fed-back to the laser through a PI gain stage.

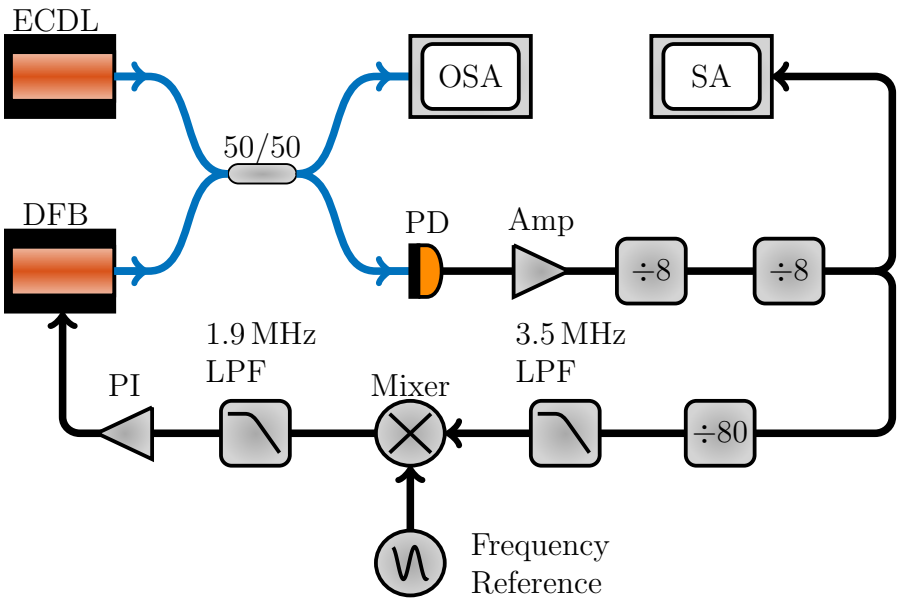

Figure 4.28: A schematic of the OPLL system, a Spectrum Analyser (SA) monitors the heterodyne beat signal.

To suppress relative phase noise ϕ_n, this system requires the laser to be capable of broadband feedback. The only available candidate for this is the DFB, which as noted previously has a broad linewidth. Additionally, to phase lock the two laser sources, the loop bandwidth must exceed the sum of the laser linewidths. For broad linewidth sources this imposes severe limitations on the OPLL design to ensure minimal phase delay in the system [252, 253]. In the case where this requirement is not met then the amount of residual phase noise $\langle\phi_n\rangle$ is determined by the ratio of the laser linewidth to the OPLL bandwidth [254]. If $\langle\phi_n\rangle$ is too large then it may throw the loop out of lock, causing the phase to slip multiple cycles [255].

Typically this issue is overcome by using a large amount of frequency division as this averages out any high-frequency noise present within the loop, improving the stability

of the OPLL by lowering the probability of phase slipping. However, as the loop cannot measure high-frequency changes in phase it cannot correct for them, limiting the maximum achievable bandwidth.

The OPLL used a PI stage with a proportional gain of +20 dB and an integral corner of 100 kHz, which is classified as a Type II loop [256]. This was optimised by monitoring the spectral purity of the 250 MHz heterodyne beat on a *RIGOL* DSA710 spectrum analyser, an example of which is plotted in Figure 4.29.

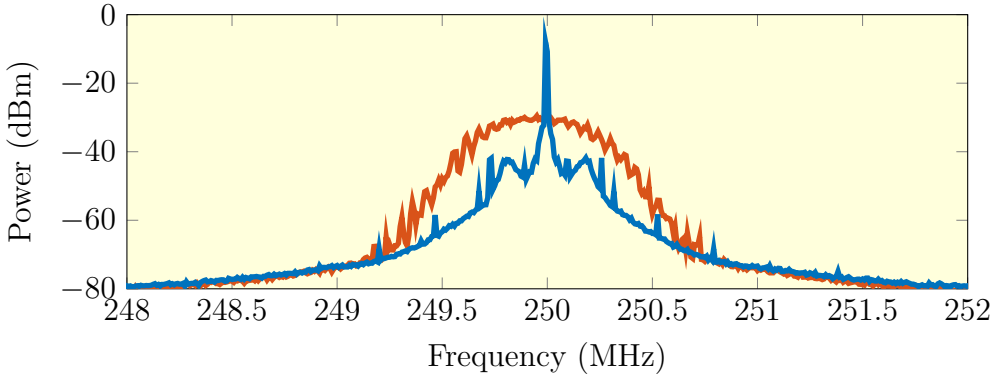

Figure 4.29: Spectrum of the unlocked and locked heterodyne signals divided by $N = 64$, measured with a RBW = 1 kHz, VBW = 1 kHz and $N_{avg} = 25$.

This spectrum exhibits a large reduction in the linewidth and increase in power at the beat frequency, which is indicative of a successful lock. The peaks on either side of the beat frequency are a measure of the loop bandwidth, suggesting a loop bandwidth of $f_{BW} = 200$ kHz.

The tunability of the frequency offset, to ensure it is at an integer number of free-spectral ranges, was tested by continuously tuning the frequency reference. As illustrated in Figure 4.30 the centre-frequency can be tuned with minimal observable difference in the lock performance.

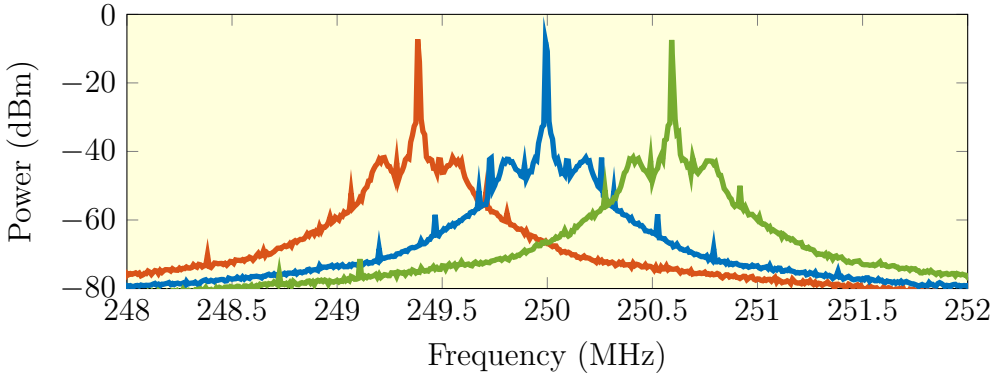

Figure 4.30: Spectra of the locked heterodyne signals as the frequency offset is tuned, measured with a RBW = 1 kHz, VBW = 1 kHz and $N_{avg} = 25$.

4.6 Dual-Pulse Injection-Seeded System

We described in the previous section, a technique for simultaneously locking both the online and offline master lasers to the slave cavity. In this section we will describe how both master lasers are coupled into the slave cavity to produce two injection-seeded pulses separated by 2.5 µs.

4.6.1 Master Wavelength Switching

For dual-pulse injection-seeding we require a means of quickly switching between the online and offline master lasers and minimising the temporal separation of the resulting online and offline pulses. We chose to use an AOM switch (*Brimrose* OS-2-1-1645-100/FFE-100-BT-F1-X/RM PM) capable of switching two fibre-coupled inputs into one output, using a Transistor-Transistor Logic (TTL) signal. It has a specified propagation delay time of 1 µs, a switching time of 200 ns, an insertion loss of <3 dB and 60 dB isolation between the input channels.

Characterisation of both switch inputs in the temporal domain was undertaken using the ECDL master laser connected to one input and a fiber-coupled photodetector (*Thorlabs* DET01CFC) connected to the output. The results are plotted in Figure 4.31. We measured an insertion loss of -4.58 dB on channel 1 and -7.90 dB on channel 2, both of which are higher then specified. The propagation delay relative to the input TTL signal was measured to be 1.8 µs for channel 1, and 0.8 µs to begin connecting channel 2 but an extra 1 µs to complete the switching. The offset of these propagation delay times leads to a 1 µs window where both master lasers will be coupled into the slave cavity but since the pulse build-up time is less than 1 µs the first pulse should seed on the channel 1 master laser.

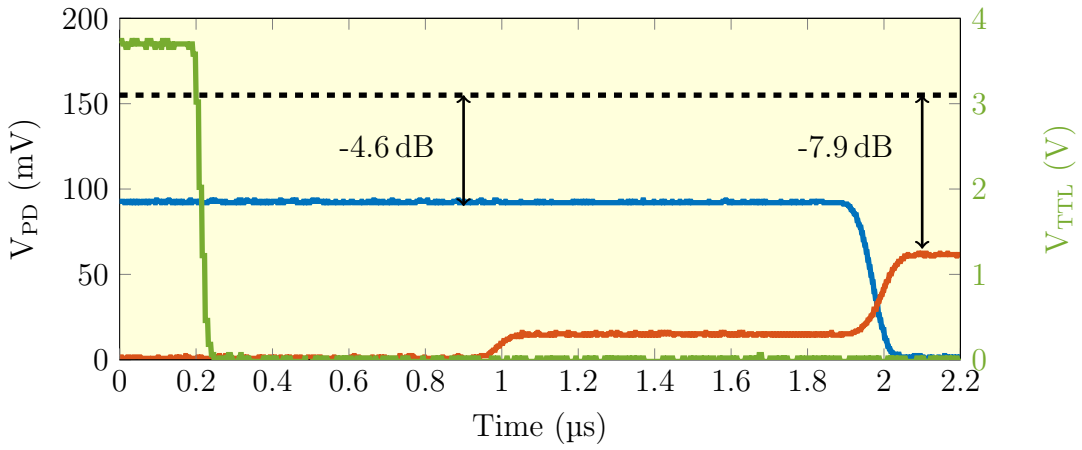

Figure 4.31: Characterisation of the AOM switch showing the response of channel 1 and channel 2 to the TTL input signal, the dashed black line represents the input power level and is used to measure the insertion loss.

The timing diagram is plotted in Figure 4.32. Initially, the channel 1 master laser is connected to the output while pumping, providing an error signal for the PDH locking servo described in Section 4.3. At time $t = 0\,\mu s$ the voltage on the PC is increased, increasing the slave laser Q and enabling an injection-seeded pulse to develop from the online master laser. The TTL signal is switched low, triggered by the rising edge of the PC voltage to account for the propagation delay of the AOM switch.

At time $t = 2.5\,\mu s$ the PC is switched to a low-Q state to dump any remaining λ_{on} photons. At about this time the switching of the channel 2 master laser to the output is complete and the slave laser Q is further increased, enabling a pulse to develop from the offline master laser which is locked to the slave cavity using the OPLL system described in Section 4.5.

Once the offline pulse has been produced, the TTL signal is switched high to re-inject the online master laser into the cavity, enabling the PDH lock to be maintained. This timing diagram suggests we can achieve a pulse separation of $\approx 2.5\,\mu s$.

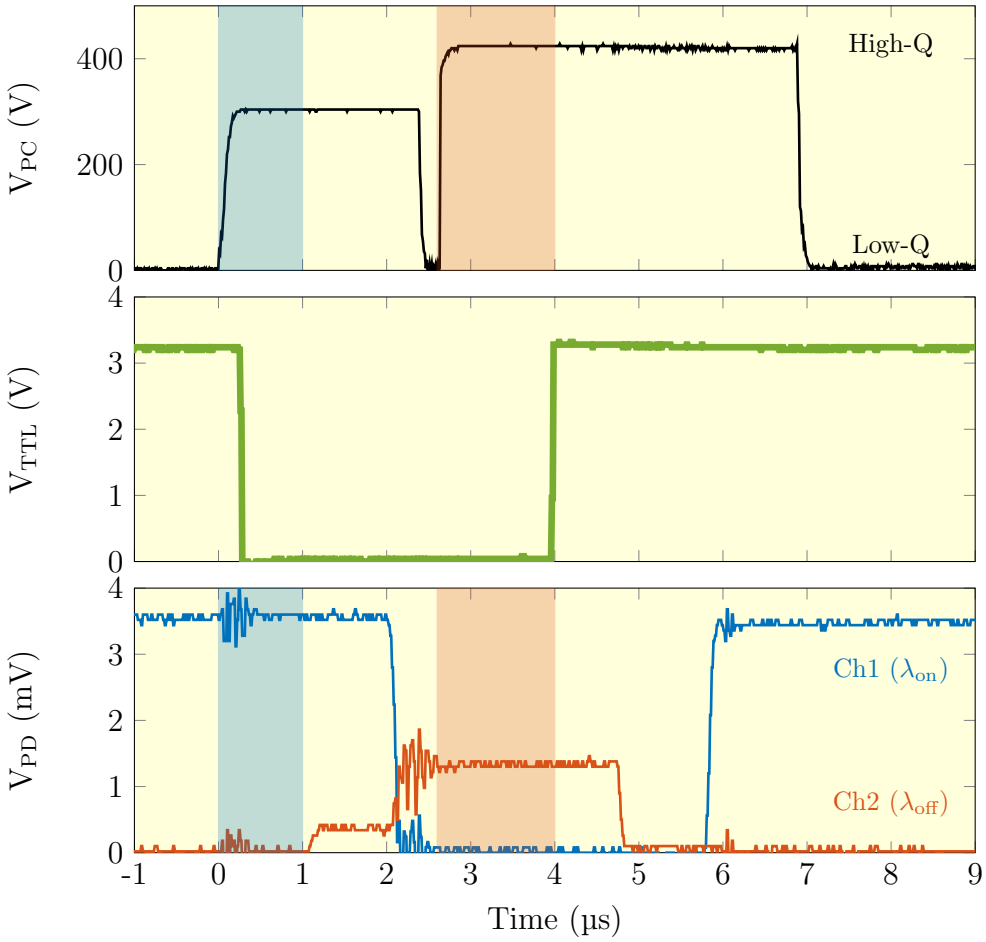

Figure 4.32: Timing of the TTL voltage signal, Q-switch and master laser switching. The shaded areas represent the arrival times of the online and offline seeded pulses. A digital delay generator (*Stanford Research Systems* DG645) is used to adjust the timing of the TTL signal triggered by the PC voltage rising edge.

4.6.2 Dual-Pulse Characterisation

The PDH lock and OPLL were engaged and the slave laser was operated in the dual-pulsed configuration with a PC voltage of 310 V and 450 V for the first and second pulse respectively. The OPLL frequency offset was tuned to produce the largest reduction in build-up time of the offline pulse. This occurred for a frequency offset of 3.11474 MHz, corresponding to a 15.947 GHz offset after accounting for the total frequency division. We recorded forward-wave pulses and heterodyne beat signals for 2500 consecutive pulse-pairs using the GaGe data-acquisition system. An example of one is plotted in Figure 4.33. We observe two pulses separated by a time of 2.3 µs both of which have a corresponding heterodyne beat signal.

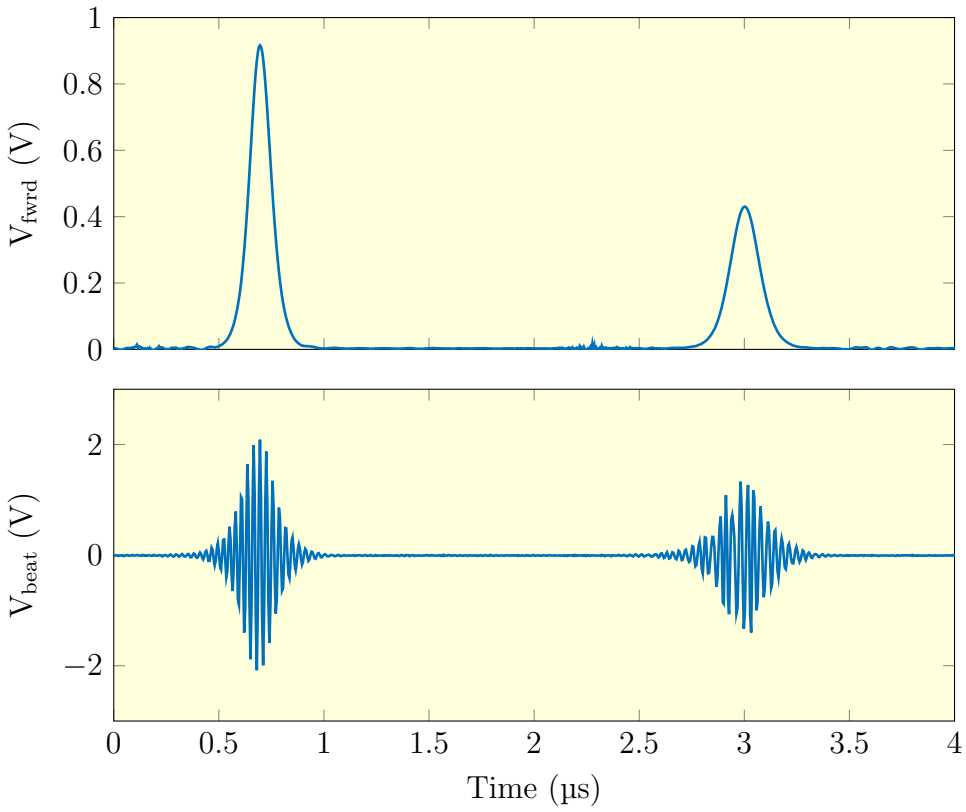

Figure 4.33: Time-trace of the dual-pulsed injection-seeded slave laser forward wave and heterodyne beat signals, the first pulse is locked online at $\lambda = 1645.55$ nm while the second pulse is locked offline at $\lambda = 1645.39$ nm.

Histograms of pulse build-up time and beat frequency are plotted in Figure 4.34. As expected, the online pulses build-up faster and have a narrower range of beat-frequencies, as the ECDL master laser has a narrower linewidth than the offline DFB master laser. These results are consistent with the single-pulse injection-seeding data presented in Sections 4.4.1 & 4.4.2 and suggests the online and offline pulses are being injection-seeded by the corresponding master lasers.

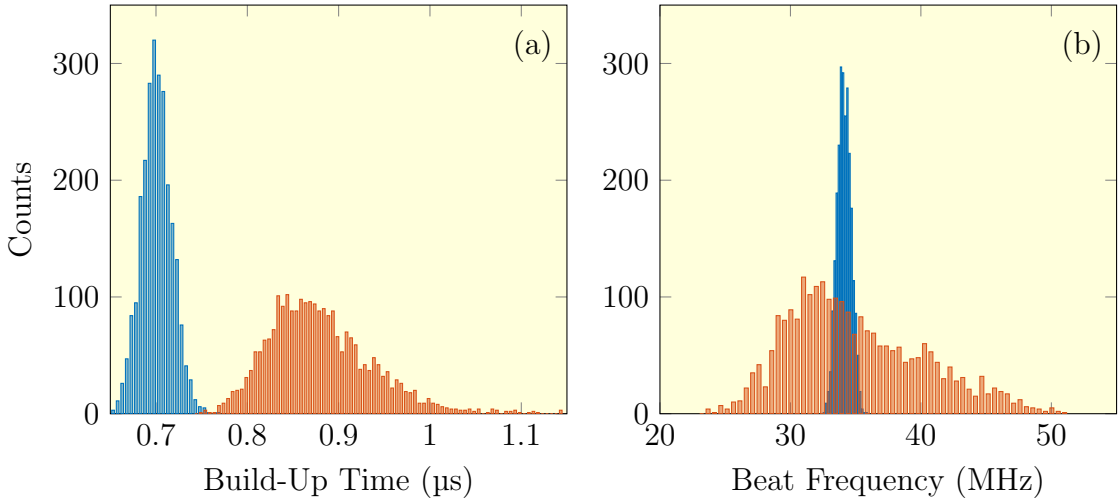

Figure 4.34: Properties of the online and offline pulses of the dual-pulsed injection-seeded Er:YAG system. (a) Histogram of the measured build-up time distribution with a bin size of 5 ns. (b) Histogram of the heterodyne frequency distribution with a bin size of 0.1 MHz.

Lastly we measure the optical spectra of the dual-pulsed slave laser and compare it the combined spectra of the online and offline master lasers as plotted in Figure 4.35. We can clearly resolve two separate spectral peaks which coincide with the online and offline master wavelengths, further confirming both pulses are successfully injection-seeded.

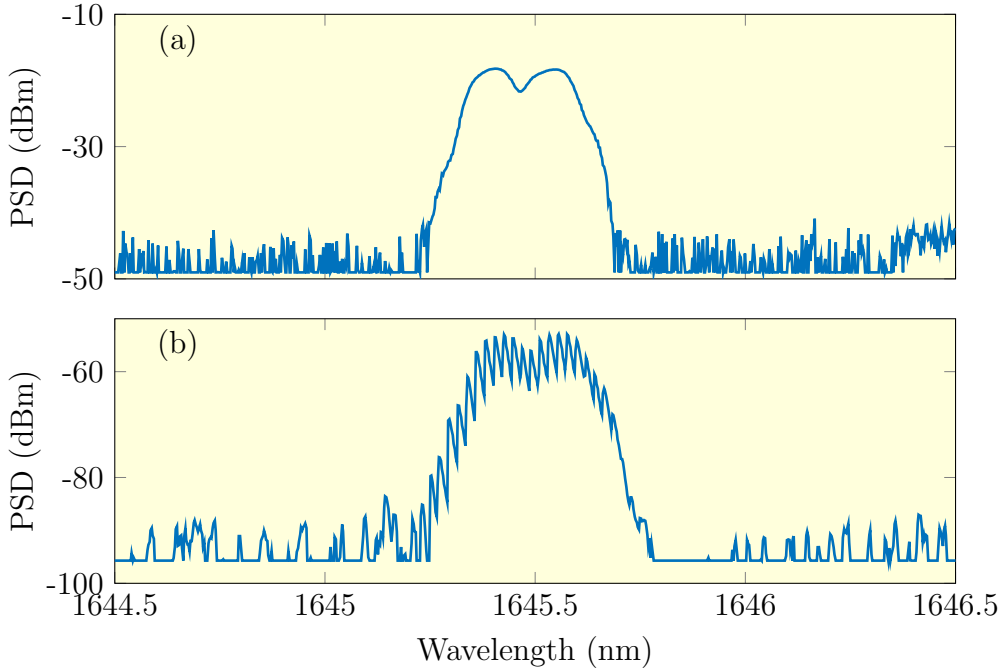

Figure 4.35: Measured optical spectra of (a) the online and offline master lasers & (b) the dual-pulsed injection-seeded slave laser measured using the HP70004a OSA.

4.7 Conclusion

In this chapter we have described the development of a dual-pulsed injection-seeded laser capable of producing two pulses; one tuned onto a methane absorption line of $\lambda_{\text{on}} = 1645.55\,\text{nm}$ and the other tuned off to $\lambda_{\text{off}} = 1645.39\,\text{nm}$. This was achieved by implementing a PDH injection-locking scheme which enabled high-bandwidth locking of a low-power master laser to a Q-switched slave cavity capable of producing 1.2 mJ, 105 ns pulses at a PRF of 100Hz. Crucially, a custom 60 MHz bandwidth photodetector was designed and constructed which was capable of resolving the PDH sidebands whilst recovering in 10 µs after a high peak-power pulse.

To lock the master laser to a resonant mode of the slave cavity we implemented a hybrid control scheme whereby low-frequency corrections are achieved using a PZT actuator in the slave laser whilst high-frequency corrections are achieved by acting on the master laser current. Using this scheme we locked both the ECDL and DFB master lasers with a measured control bandwidth of 7.35 kHz and 300 kHz respectively, both of which are consistent with the servo model presented in this chapter.

Reliable single pulse injection-seeding was attempted using both master lasers at the erbium line-centre wavelength of 1645.15 nm and the methane line-centre wavelength of 1645.55 nm. Whilst both were able to reliably injection-seed at the erbium line-centre wavelength, only the narrow-linewidth ECDL master laser was able to reliably injection-seed at the methane line-centre wavelength. Hence, this source is used as the online master laser.

We then implemented an OPLL to lock the DFB master laser 15.947 GHz from the ECDL master laser. This frequency separation corresponds to an integer number ($N = 25$) of slave cavity FSRs and enables both the online and offline master lasers to be simultaneously locked to the slave cavity. A high-order of frequency division ($N_{\text{div}} = 5120$) was used to divide the heterodyne beat signal of the two lasers down to the MHz frequency regime, allowing an easily tunable waveform generator to be used to precisely adjust the frequency offset.

To quickly switch between the online and offline master lasers we used an AOM switch, unfortunately this device showed an unforeseen delay in the switching response which caused a 1 µs period in which both the online and offline master lasers were injected into the slave resonator. By carefully delaying the timing of the optical switch relative to the Q-switch we were able to circumvent this limitation and produce two injection-seeded pulses separated by 2.3 µs. To our knowledge this is the smallest temporal separation of two separate wavelength pulses produced from a single source and will enable high sensitivity DIAL measurements of methane.

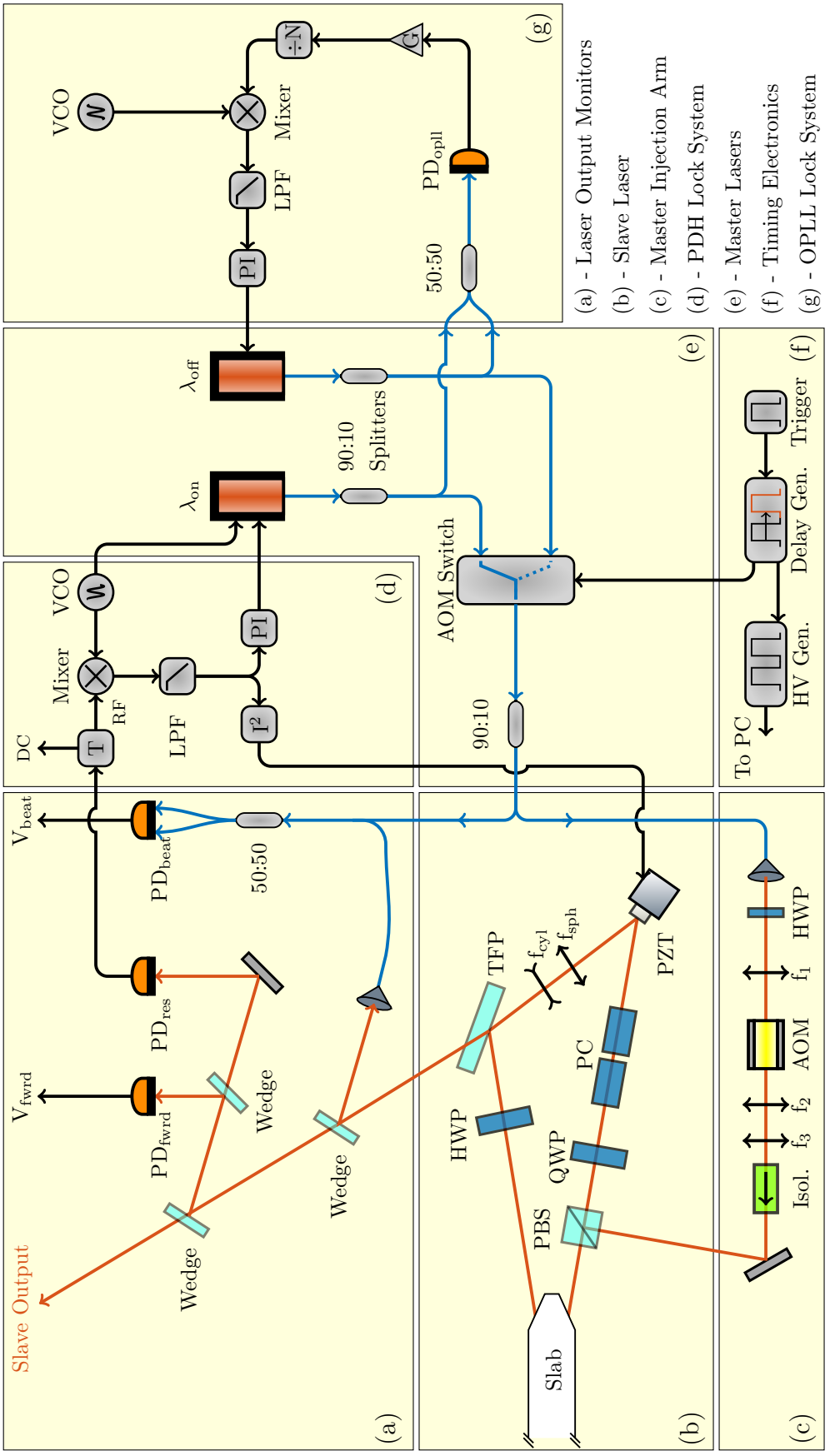

Figure 4.36: Schematic of the dual-pulse injection-seeded Er:YAG laser system.

Chapter 5

A High-Sensitivity IPDA LIDAR Detection System

5.1 Introduction

Integrated Path Differential Absorption (IPDA) LIDAR is a powerful remote sensing technique for monitoring leaks from methane pipelines. In order to better predict the location of low-leak sources and constrain the emission budget of natural gas providers a high sensitivity is required. We quantify the measurement sensitivity using the Signal-to-Noise Ratio (SNR). In this chapter we describe the design of an IPDA LIDAR receiver system which aims to minimise the statistical error on the methane concentration, or alternatively maximise the SNR. Using the atmospheric sensing capabilities of our laboratory, a ground-based LIDAR test system is demonstrated to measure the background concentration of methane at a range of 300 m.

A block diagram of the IPDA LIDAR system described in this chapter is illustrated in Figure 5.1.

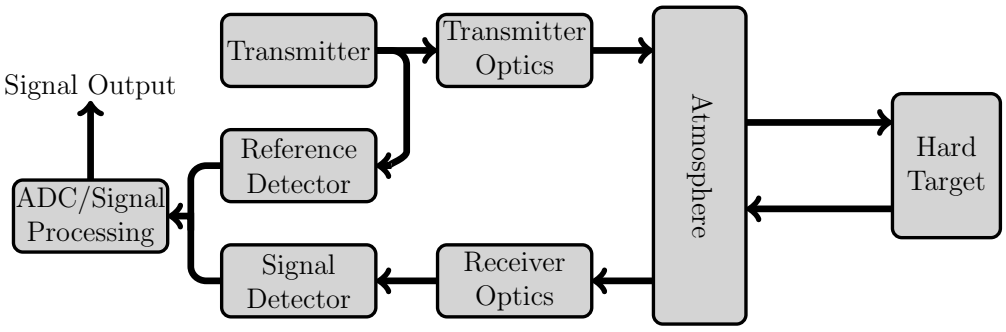

Figure 5.1: A block diagram of the complete IPDA LIDAR test system.

The properties of the dual-wavelength transmitter are described in Section 5.2. To resolve the transmitted and returned LIDAR pulses we developed matching low-noise 'reference' and 'signal' photodetectors, detailed in Section 5.3. In Sub-Section 5.3.1

we review available photodetector components, Sub-Sections 5.3.2 & 5.3.3 describe mathematical models of photodetector stability and noise, finally Sub-Section 5.3.4 details the measured noise of the photodetector. In-lab measurements, detailed in Section 5.4, enabled the photodetector contribution to system noise to be characterised under ideal conditions. This Section also describes the signal processing techniques used to reduce the measurement noise.

In Section 5.5 we describe the transmitting optics which ensure eye-safe operation and the receiving optics used to efficiently focus the back-scattered return signal onto the photodetector. A sensitivity model that uses the instrument parameters of the transmitter/detection system is introduced in Section 5.6 to predict the methane measurement sensitivity under realistic conditions. This chapter concludes in Section 5.7 with a ground-based IPDA LIDAR measurement of the background concentration of methane over the city of Adelaide, Australia on 02/04/2019 at 10:45AM. The concentration was measured to be 1.979 ppm with a standard deviation of 0.124 ppm.

5.2 The Transmitter System

The IPDA LIDAR transmitter, described in Chapters 2-4, consists of a 1.2 mJ, 105 ns, 100 Hz Er:YAG laser injection-seeded by two CW lasers to produce two pulses at λ_{on} =1645.55 nm and λ_{off} =1645.39 nm separated temporally by 2.3 µs. The absorption cross-sections of dominant atmospheric constituents near these wavelengths is plotted in Figure 5.2.

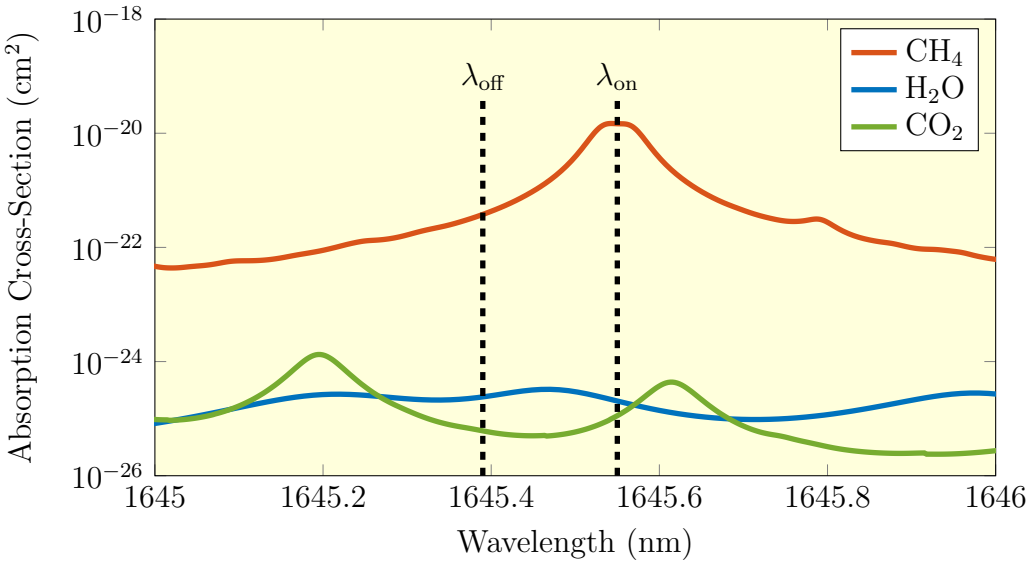

Figure 5.2: Absorption cross-section of dominant atmospheric constituents near 1645 nm at a temperature of 296 K from the HITRAN 2008 database [257]. The online and offline wavelengths of the IPDA LIDAR transmitter are also illustrated.

The methane absorption cross-sections are $\sigma_{on} = 1.47 \times 10^{-20}\,\text{cm}^2$ and $\sigma_{off} = 3.79 \times 10^{-22}\,\text{cm}^2$ [257]. Clearly, the online absorption is predominantly due to methane whilst the offline wavelength absorption is orders of magnitude weaker. Absorption of interfering molecules can be neglected as their cross-sections are approximately equal at the online and offline wavelengths [258].

5.3 Signal & Reference Photodetectors

To maximise the sensitivity of the DIAL system the photodetectors must have a wide bandwidth and low noise. Typically this is achieved using a reverse-biased photodiode with a wideband transimpedance amplifier (TIA), as shown in Figure 5.3.

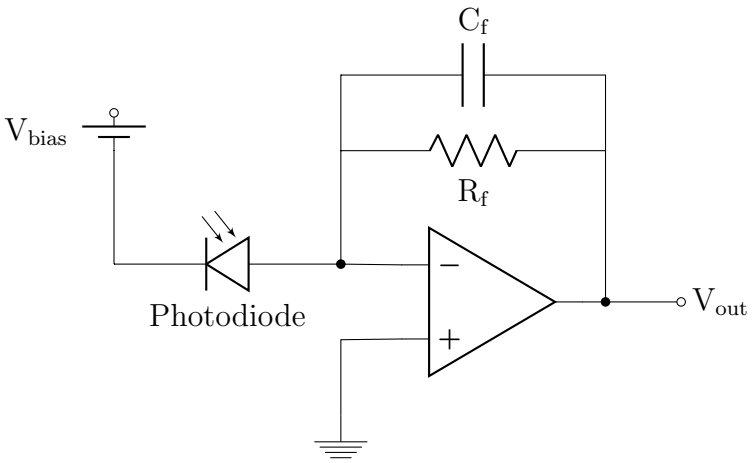

Figure 5.3: A typical photodiode and transimpedance amplifier circuit schematic where V_{bias} is the reverse-bias voltage, R_f is the feedback resistor and C_f is the feedback capacitor.

This is the most straightforward implementation of a transimpedance amplifier. However, there are significant design challenges in the form of trade-offs between bandwidth, noise, gain, power dissipation and stability. Rigorous mathematical models of the TIA have been presented in literature [259, 260] and as such a complete mathematical derivation is not necessary. Instead, a summarised model will be presented that will allow the gain, bandwidth and noise of the photodetector to be optimised for an airborne LIDAR system.

5.3.1 TIA Photodetector Components

We considered three amplifiers produced by *Texas Instruments*: the OPA657, OPA847 and LMH6624, all of which have high bandwidth, low current noise and low voltage noise. We also considered a range of commercially available Indium Gallium Arsenide (InGaAs) photodiodes that exhibit responsivity in the 1.6 µm wavelength band [261];

the FGA10 and FGA21 from *Thorlabs Inc.* and the G12180-020A from *Hamamatsu*. A comparison of all components is given below in Table 5.1.

Parameter	Symbol	OPA657	OPA847	LMH6624
Input Type	-	FET	BJT	BJT
Package	-	SOIC	SOIC	SOIC
Supply Voltage (V)	V_s	±5	±5	±5
Input Bias Current (µA)	I_{bias}	2×10^{-6}	-19	13
Gain-Bandwidth (GHz)	G_{BW}	1.6	3.9	1.5
DC Open Loop Gain (dB)	A_{DC}	70	98	81
Input Capacitance (pF)	C_{in}	5.2	1.7	1.7
Voltage Noise (nV/$\sqrt{\text{Hz}}$)	$\tilde{v}_{amp}$	4.8	0.85	0.69
Current Noise (fA/$\sqrt{\text{Hz}}$)	$\tilde{i}_{amp}$	1.3	2500	2600
Parameter	Symbol	FGA10	FGA21	G12180-020A
Active Area Diameter (mm)	⌀	1	2	2
Wavelength Range (nm)	λ_{range}	900-1700	800-1700	900-1700
Dark Current (nA)	I_d	1.1	50	7.5
Noise Equivalent Power (pW/$\sqrt{\text{Hz}}$)	NEP	0.25	0.60	0.75
Photodiode Capacitance (pF)	C_{pd}	80	100	250
Responsivity (A/W)	$\Re$	1.05	1.04	1.10
Rise Time (ns)	-	10	25	-

Table 5.1: Comparison of commercially available operational amplifiers and photodiodes suitable for use in a high-bandwidth, low-noise transimpedance amplifier.

Evidently the OPA657 has significantly lower current noise, as is typical of Field-Effect Transistor (FET) amplifiers, and also minimal bias current. Critically, FET amplifiers also have a larger specified voltage noise, which ultimately dominates the total output noise as discussed later. In comparison to FET amplifiers, the Bi-Polar Junction Transistor (BJT) amplifiers have a reduced voltage noise. We use the OPA847 in early circuit design iterations as it has an increased gain-bandwidth.

The receiver field-of-view is maximised, thereby loosening restrictions on the focusing optics and increasing the return signal strength, by using larger area photodiodes. However, there are trade-offs with both the photodiode capacitance (C_{pd}) and dark current I_d that can limit the bandwidth and noise of the TIA. We use the *Hamamatsu* G12180-020A photodiode as it has much less dark current than the FGA21.

5.3.2 TIA Photodetector Stability Model

To model the TIA we introduce an equivalent circuit shown below in Figure 5.4. In this equivalent circuit the photodiode is replaced by a current source I_{in} in parallel with a diode capacitance C_{pd}.

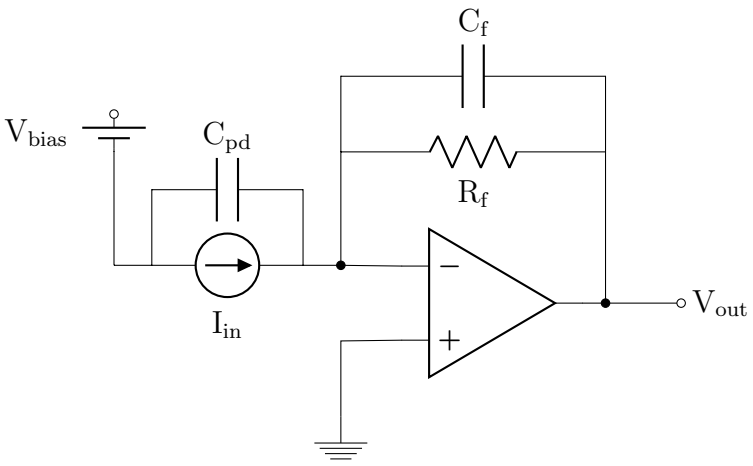

Figure 5.4: The equivalent transimpedance amplifier circuit.

The open-loop gain A_{OL} is dependent on the operational amplifier and is given by [262]:

$$A_{OL}(f) = \frac{A_{DC}}{\left(1 + j\frac{f}{f_{BW}}\right)\left(1 + j\frac{f}{f_{pole}}\right)} \tag{5.1}$$

where A_{DC} is the DC open-loop gain, f_{BW} is the open-loop bandwidth and f_{pole} is a high frequency pole. The feedback to the amplifier input H_{FB} is given by:

$$H_{FB}(f) = \frac{Z_{in}}{Z_f + Z_{in}} \tag{5.2}$$

where Z_f is the impedance of the feedback components and Z_{in} is the input impedance. Thus, the closed-loop gain of the amplifier A_{CL} is given by:

$$A_{CL}(f) = \frac{A_{OL}}{1 + A_{OL}H_{FB}} = \frac{A_{OL}}{1 + A_{Loop}} \tag{5.3}$$

where $A_{Loop} = A_{OL}H_{FB}$. The phase margin at 0 dB loop-gain is given by [229]:

$$\phi_{pm} = 180^\circ - |\angle(A_{Loop} = 0\,\text{dB})| \tag{5.4}$$

For good stability and minimum noise peaking we require $\phi_{pm} \approx 90^\circ$. The transimpedance gain, Z_0, which describes how an input current is amplified to a voltage at the transimpedance amplifier output, is given by:

$$Z_0(f) = \frac{A_{CL} \times Z_f}{1 + Z_f/Z_{in}} \tag{5.5}$$

For stable measurements of the LIDAR return signal we require the transimpedance gain to have a 3 dB bandwidth exceeding 10 MHz and exhibit minimal gain-peaking. To optimise this we plot the loop-gain and transimpedance gain with $C_f = 0$ pF in Figure 5.5. The loop-gain intersects unity-gain at a frequency of 18 MHz with a corresponding

phase margin of 0°. This causes peaking in the transimpedance gain which will lead to significant instability and noise.

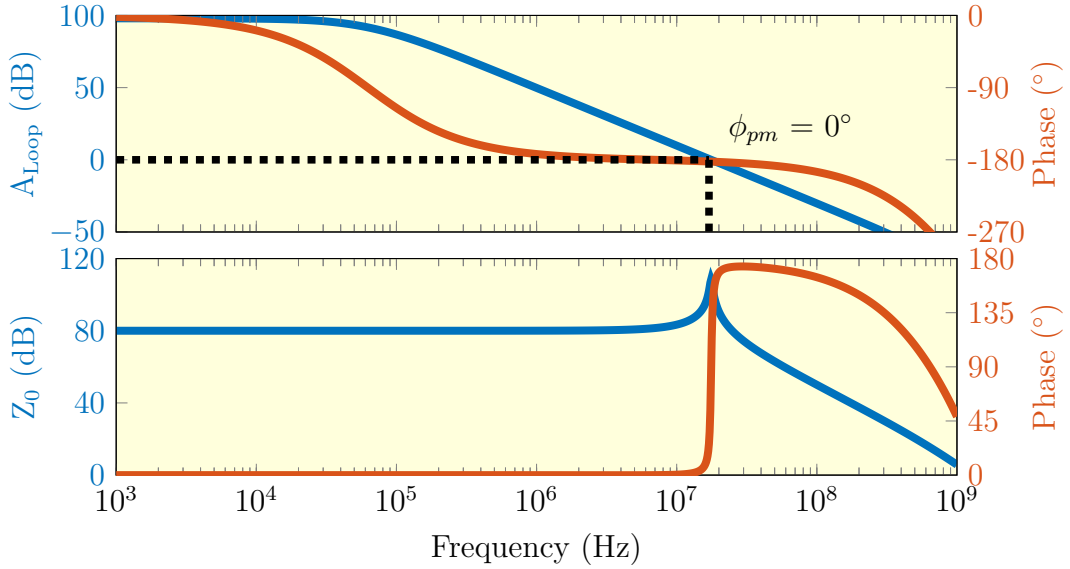

Figure 5.5: Predicted loop-gain and transimpedance gain of a TIA photodetector formed using the OPA847 op-amp and G12180-020A photodiode for $R_f = 10\,k\Omega$ and $C_f = 0\,pF$.

To improve the phase margin we add a feedback capacitor $C_f = 1.5\,pF$ which introduces an additive phase shift to compensate for the input photodiode capacitance, as plotted in Figure 5.6.

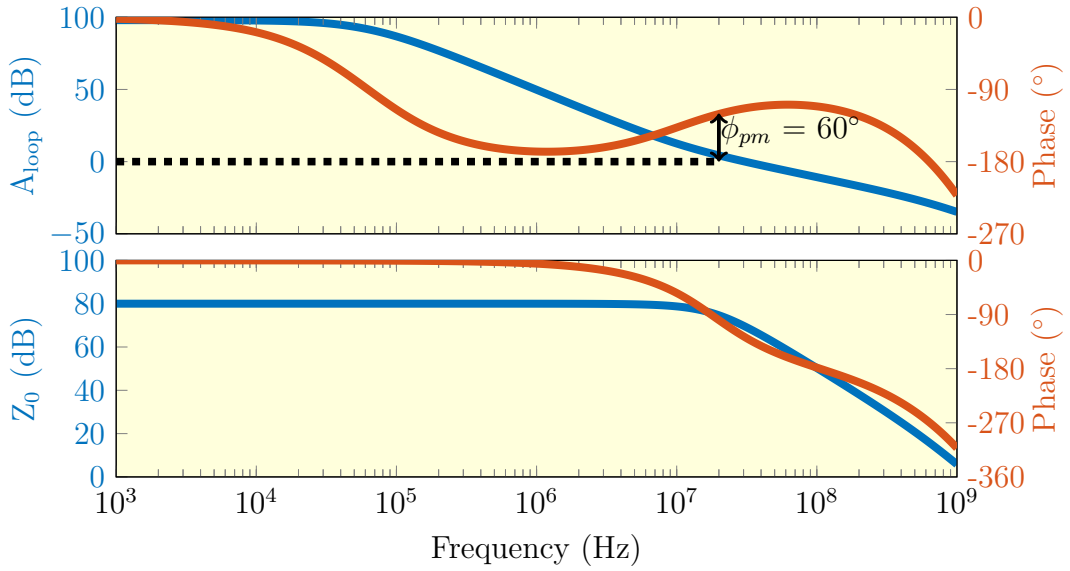

Figure 5.6: Predicted loop-gain and transimpedance gain of a TIA photodetector formed using the OPA847 op-amp and G12180-020A photodiode for $R_f = 10\,k\Omega$ and $C_f = 1.5\,pF$.

The addition of the feedback capacitor increases the phase margin to 60° and minimises transimpedance gain peaking. The corresponding 3 dB bandwidth is 18 MHz, which exceeds the bandwidth required to resolve the transmitted pulse.

5.3.3 TIA Photodetector Noise Model

The availability of detailed noise spectral density characteristics for commercially available operational amplifiers allows for accurate noise analysis under a variety of circuit configurations. A simple but adequate noise model of the transimpedance amplifier is illustrated in Figure 5.7.

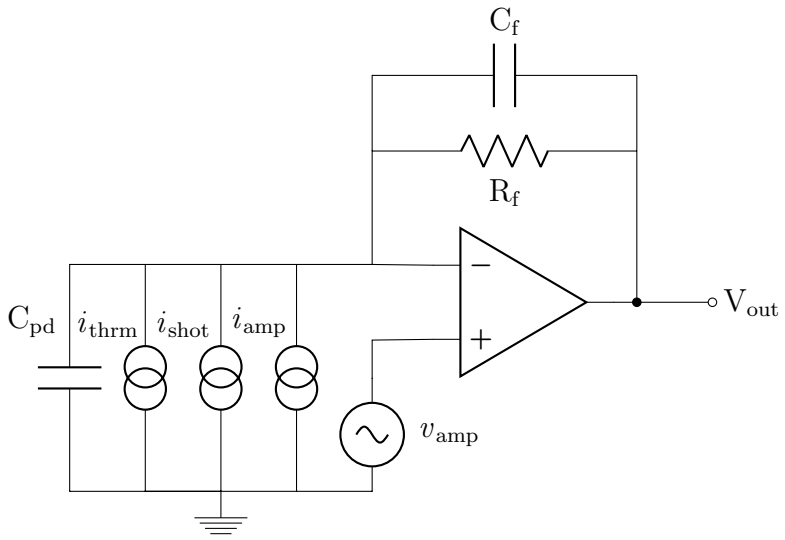

Figure 5.7: Noise model of the TIA photodetector [262].

We consider three sources of current noise; thermal, shot and amplifier noise, all of which are treated identically. These noise sources appear in parallel with the signal current and thus are scaled by the transimpedance gain Z_0. The only noise source that is treated differently is the amplifiers voltage noise v_{amp}. Since the amplifier amplifies differential signals this noise source can be put into either input. For simplicity we put it into the non-inverting input where it will be amplified by the closed loop gain.

The thermal noise $i_{\text{thrm}} = \sqrt{4kT\mathrm{R_f}}$ is dependent on the feedback resistor $\mathrm{R_f}$ and temperature T. Whilst the shot noise $i_{\text{shot}} = \sqrt{2q\mathrm{I_d}}$ is dependent on the photodiode dark current $\mathrm{I_d}$ and electron charge q.

We plot all predicted noise sources in Figure 5.8 using the operational amplifier and photodiode parameters listed in Table 5.1. The low-frequency noise is dominated by op-amp current noise and the high-frequency noise is dominated by op-amp voltage noise. Crucially, this high-frequency voltage noise is damped by the feedback capacitor. If not properly compensated this peaking would limit the detector noise.

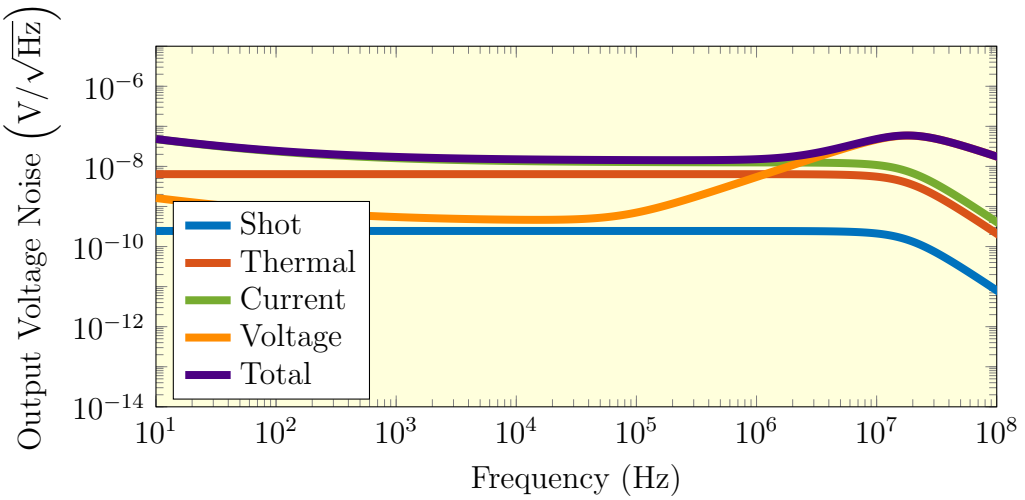

Figure 5.8: Predicted output voltage noise of the TIA photodetector formed using the OPA847 op-amp and G12180-020A photodiode for $R_f = 10\,k\Omega$ and $C_f = 1.5\,pF$.

By integrating the voltage noise spectral density we can calculate the predicted RMS voltage noise of this photodetector to be $v_{pd} = 400\,\mu V$.

5.3.4 TIA Photodetector Noise Measurements

Three TIA photodetectors that used the G12180-020A PD and the amplifiers listed in Table 5.1 were constructed using the Printed Circuit Board (PCB) design principles discussed in Appendix E. The output voltage noise spectra was measured using the *Agilent* 89410A and *Agilent* N9320A spectrum analysers. The measured dark noise for the OPA847 is plotted in Figure 5.9.

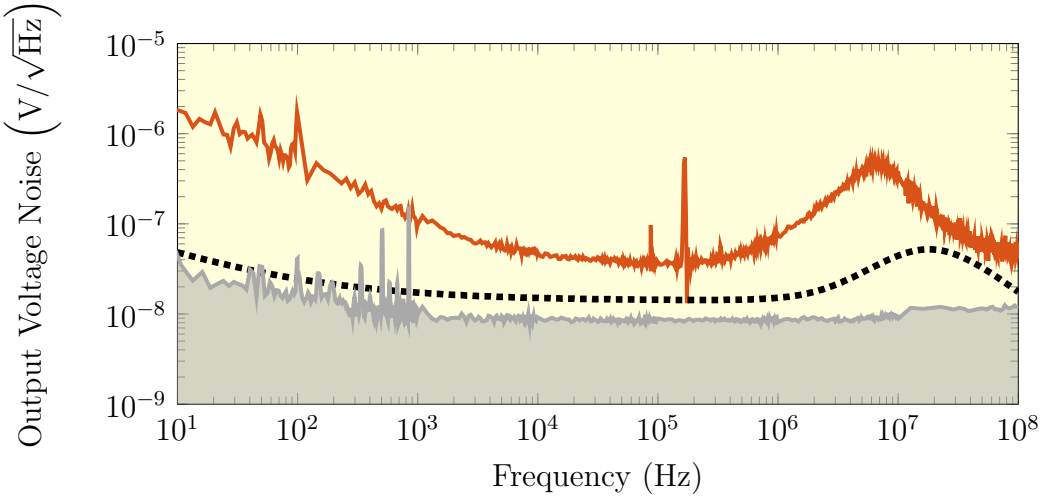

Figure 5.9: Measured output voltage noise of the OPA847 TIA photodetector compared to the predicted noise spectra, illustrated by the dotted lines.

We observe disagreement with the predicted output noise across the complete frequency range, significantly increasing the total RMS voltage noise. The frequency offset between the locations of the voltage peaking may be caused by an increased input capacitance, this has been noted in other investigations into using the OPA847 in a TIA [263]. This measurement suggests that despite the improved noise and bandwidth specifications of the OPA847 it will not be suitable for the LIDAR receiver system.

The measured dark noise for the OPA657 and the LMH6624 are plotted in Figures 5.10 and 5.11.

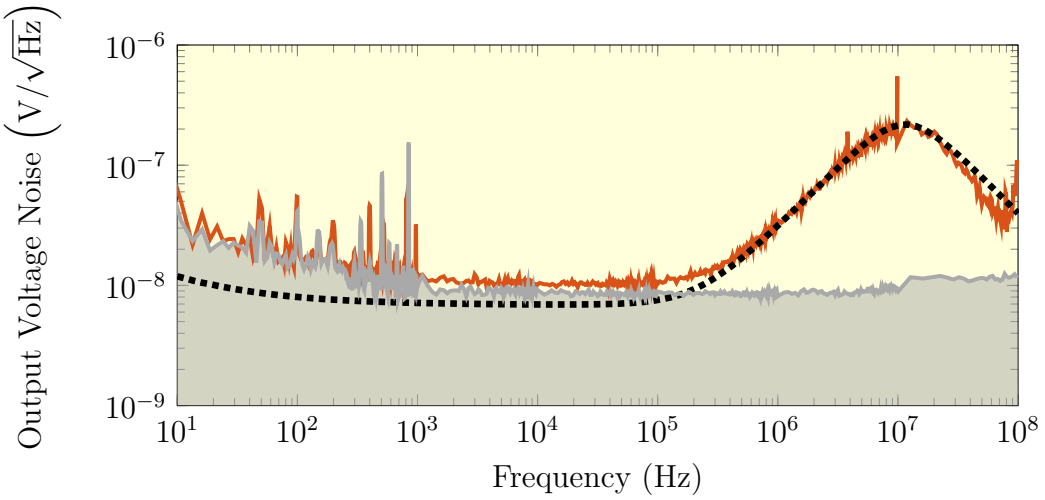

Figure 5.10: Measured output voltage noise of the OPA657 TIA photodetector compared to the predicted noise spectra, illustrated by the dotted lines.

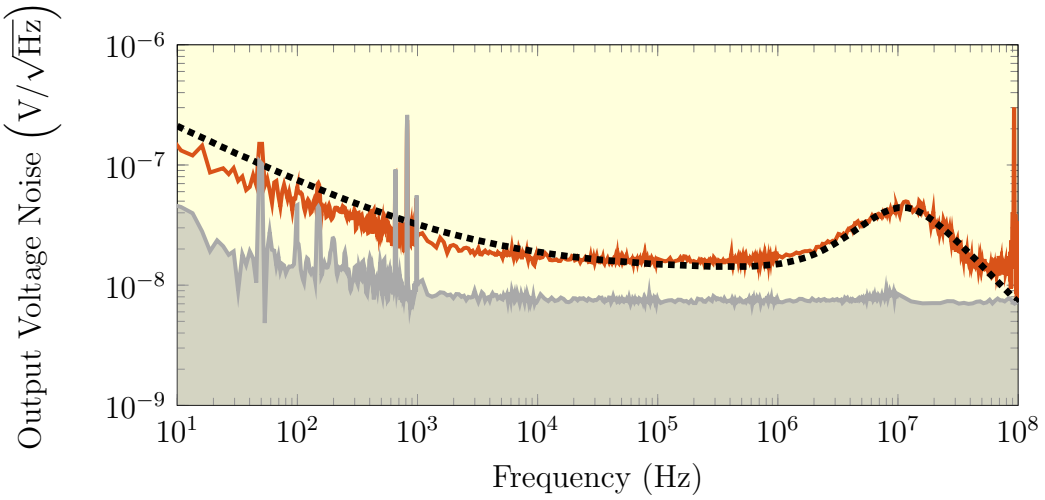

Figure 5.11: Measured output voltage noise of the LMH6624 TIA photodetector compared to the predicted noise spectra, illustrated by the dotted lines.

In both measurements the output voltage noise is in excellent agreement with theory across the entire frequency span. Due to the increased voltage noise of the FET input

OPA657 we observe significantly higher noise at 10MHz, this ultimately limits the RMS voltage noise to $v_{\mathrm{pd}} = 1.2\,\mathrm{mV}$. In comparison, the LMH6624 op-amp has lower noise in this frequency range and has an RMS voltage noise of $v_{\mathrm{pd}} = 300\,\mu\mathrm{V}$, hence, this detector is more suitable for the LIDAR receiver. A second matching photodetector was later constructed to monitor fluctuations in the laser output energy, this is referred to as the 'reference' photodetector.

5.4 Local Sensitivity Estimate

In this section we detail two experiments used to estimate the photodetector contribution to the system SNR. In Section 5.4.1, I describe an investigation of the reproducibility of the pulse energy ratio. A fiber delay-line was used to generate two pulses from a single pulsed low-power laser diode. In Section 5.4.2, I measure differential absorption through a reference methane cell.

5.4.1 Pulse Energy Ratio Reproducibility

The measurement system used to estimate the reproducibility of the pulse energy ratio measured using the TIA photodetector is shown in Figure 5.12. The pulses were produced using a fiber-coupled InGaAs/InP laser diode from *Roithner Lasertechnik* (LFO-18/2-i) and a Max3669 laser driver from *Maxim Integrated*. This driver can modulate the diode current with a rise/fall time of 200 ps, enabling generation of pulses with a width of 100 ns.

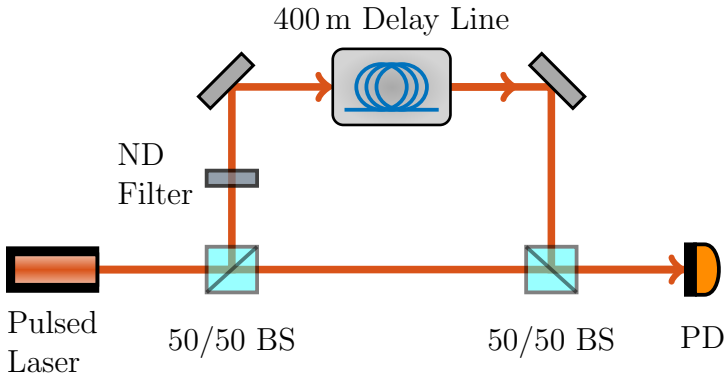

Figure 5.12: A schematic of the delay-line system used to estimate the reproducibility of the pulse energy ratio from a single pulse-pair.

The pulse is split using a 50/50 beam-splitter with half directed immediately onto the photodetector. A 400 m fiber delay-line from *AFW Technologies* (SM1-22-B-400-BX) is used to delay the other half of the pulse with a time-delay similar to that expected in the airborne system. We refer to the first and second pulse measured on

the photodetector as the 'reference' and 'signal' respectively. An ND filter is used to attenuate the signal pulse over a range of energies.

We recorded 1000 consecutive pulses at each signal attenuation using the GaGe CSE1642 ADC; a 125 MHz, 200 MS/s, 16-bit device. An example of one pulse-pair is plotted in Figure 5.13. In comparison to the reference pulse the signal pulse is delayed by 2 µs and attenuated by -1.05 dB.

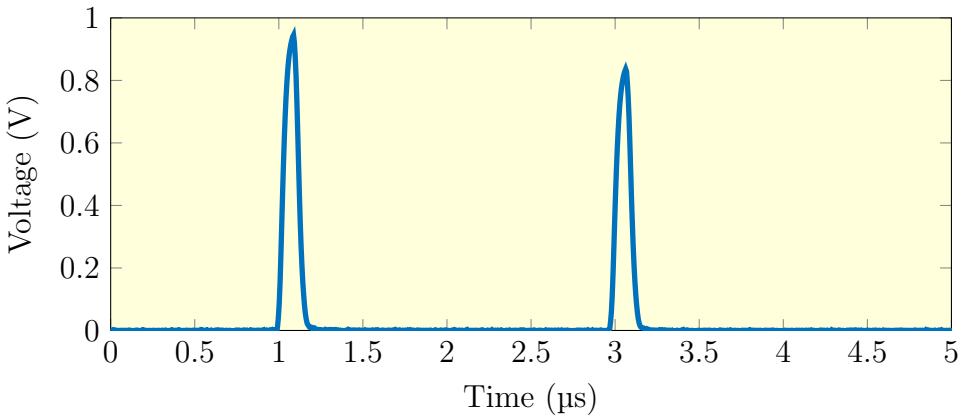

Figure 5.13: Time-trace of the pulses measured in the delay-line experiment for ND = 0.

Two signal processing algorithms were used to determine the ratio of the single-shot energies in the reference and signal pulses: integration and matched-filtering. The Matched-Filtering (MF) technique, which is commonly used to improve measurement SNR in the presence of white noise [264] is described mathematically in Appendix F. The steps used are listed below:

1. Subtract the background determined using post-trigger data.
2. Isolate the signal and reference pulses using a flat-top window of fixed width.
3. Determine the signal pulse energy (E_{sig}) and reference pulse energy (E_{ref}) using either integration or matched-filtering.

For the integration algorithm:

(a) Calculate the area under each pulse using numerical integration.

(b) Calculate the pulse energy ratio $R = E_{\text{sig}}/E_{\text{ref}}$.

For the matched-filter algorithm:

(a) Create a MF template by time-reversing the low-noise reference pulse.

(b) Apply the template to the reference and signal pulses via a convolution.

(c) Calculate the pulse energies by the maximum of the matched filtered output.

(d) Calculate the pulse energy ratio $R = E_{\text{sig}}/E_{\text{ref}}$.

For each algorithm, we calculate the mean $\langle R \rangle$, standard deviation σ_R, and the corresponding signal-to-noise ratio (SNR $\equiv \langle R \rangle / \sigma_R$), for each ND. The SNR's are plotted in Figure 5.14 for each ND as a function of the signal pulse energy.

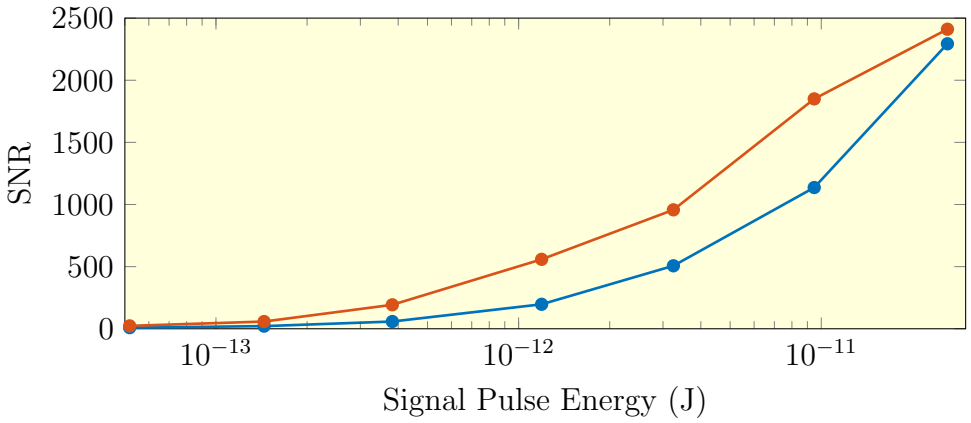

Figure 5.14: Measured SNR of the single-pulse pair as a function of pulse energy highlighting the improved performance of the matched filtering algorithm in comparison to the integration algorithm.

The analysis shows that the matched-filter algorithm provides the more reproducible measurement of the pulse energy ratio, and is thus preferred.

5.4.2 Methane Cell Experiment

The measurement system used to test the dual-wavelength transmitter is shown in Figure 5.15.

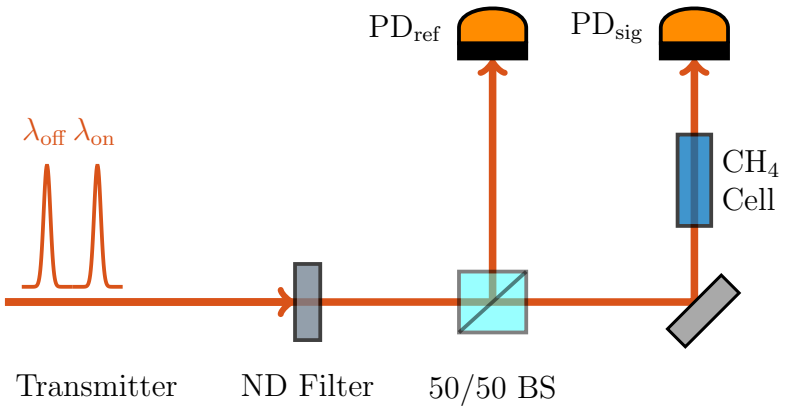

Figure 5.15: A schematic of the lab measurement system used to measure the transmission of the dual-pulsed laser through a reference gas cell.

The pulses are split using a 50/50 beam splitter, with half directed into a reference photodetector used to allow correction for pulse-to-pulse energy fluctuations. The other

half is directed through a reference methane cell into the signal photodetector. The reference cell is 5 cm long and it is filled with 740 Torr (≈1 Atm) of CH_4. The output of the laser was attenuated using an ND filter to provide a more realistic pulse incident on the photodetectors.

We recorded 2,500 consecutive pulse-pairs on the signal and reference photodetectors using the GaGe digitiser, a typical reference and signal photodetector trace is plotted in Figure 5.16.

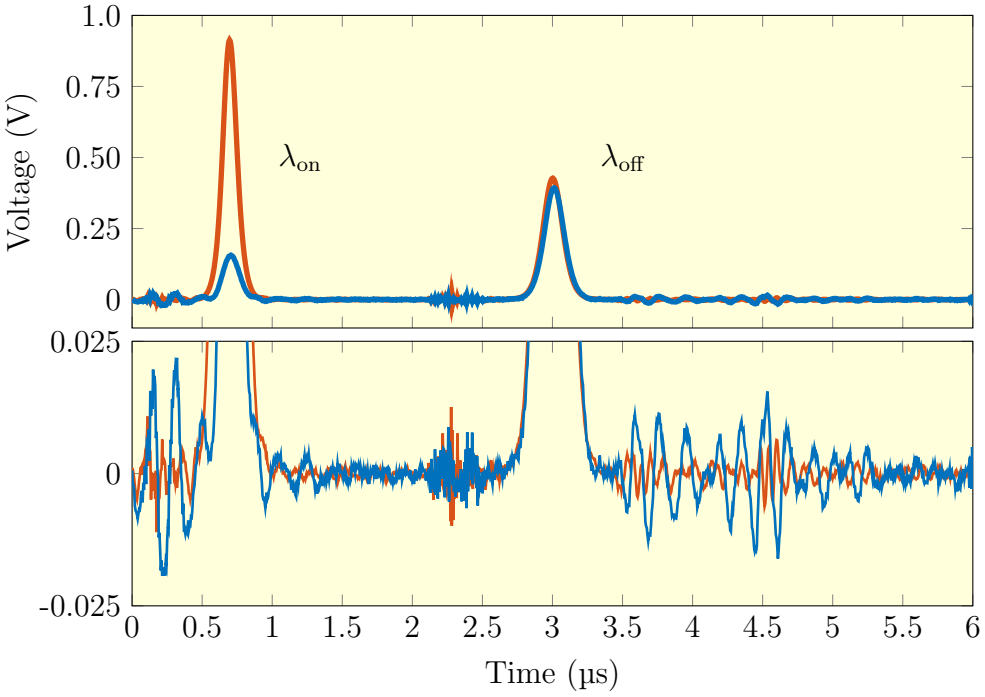

Figure 5.16: Time-trace of the reference and signal photodetectors through a methane reference gas cell. The lower axis is the photodetector baseline and is plotted to illustrate the increased noise pick-up during this measurement.

The online signal pulse is significantly attenuated relative to the online reference pulse, suggesting it was strongly absorbed by the methane in the reference cell as expected. The detector baselines, plotted in the lower axis, both exhibit a spurious non-Gaussian noise that was not present in previous measurements. The source of this noise, and its effect on the transmission measurement, is discussed later in this section.

The energy of the online and offline pulses at each detector were calculated using the matched filter algorithm described in Section 5.4.1. The signal detector pulse energies were then normalised using the reference detector pulse energies:

$$E_{\text{on,normalised}} = E_{\text{on,sig}}/E_{\text{on,ref}}$$
$$E_{\text{off,normalised}} = E_{\text{off,sig}}/E_{\text{off,ref}}$$

The measured normalised energies of the offline and online pulses are plotted in Figure 5.17. We observe outlier data points in the offline pulse normalised energy. At these points we believe the offline pulse is poorly seeded and hence lases closer to the erbium gain-centre wavelength of $\lambda = 1645.15\,\text{nm}$, resulting in an increased normalised energy. We removed these outlier points by removing the offline pulses with a build-up time exceeding $1\,\mu\text{s}$. This result suggest further work is required to increase the offline optical-phase locked loop servo bandwidth, introduced in Chapter 4, to improve offline injection-seeding.

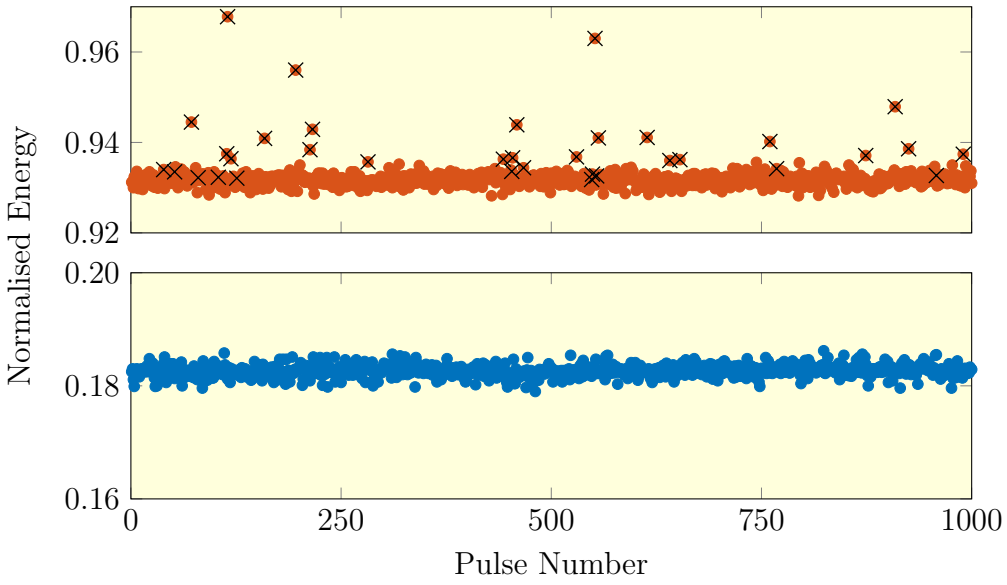

Figure 5.17: The normalised energy of the offline and online pulses. Offline pulses with an increased normalised energy are attributed to incomplete seeding, we filter all pulses with a build-up time $> 1\,\mu\text{s}$ as indicated by the crossed data points.

The mean and standard deviation of the filtered offline normalised energy are $\langle R_{\text{off}} \rangle = 0.9320$ and $\sigma_{R,\text{off}} = 0.0023$, while for the online normalised energy the mean and standard deviation are $\langle R_{\text{on}} \rangle = 0.1828$ and $\sigma_{R,\text{on}} = 0.0010$. Thus, the online and offline SNR are:

$$\text{SNR}_{\text{on}} = 402.3$$
$$\text{SNR}_{\text{off}} = 174.2$$

both are significantly lower than the SNR measured in Section 5.4.1. We attribute this SNR degradation to the increased detector baseline noise highlighted in Figure 5.16.

The high-frequency noise present before the arrival of the second pulse was caused by electrical pick-up from the Pockels Cell driver switching to a high-voltage. Thus, this noise is approximately synchronised to the pulse arrival time and its effect on the

measured energy was reduced by applying a narrow flat-top window around each pulse. The lower-frequency, higher amplitude noise present in both photodetectors is caused by pick-up from the pump diode driver. This noise was not time synchronised to the pulse arrival and hence we were not able to remove its effect. We believe this noise limits the SNR and its removal is critical in future photodetector designs.

The observed transmission through the cell was calculated using

$$T_{\text{obs}} = (E_{\text{on,normalised}}/E_{\text{off,normalised}}) \times 100$$

a frequency histogram of the measured transmission is plotted in Figure 4.34.

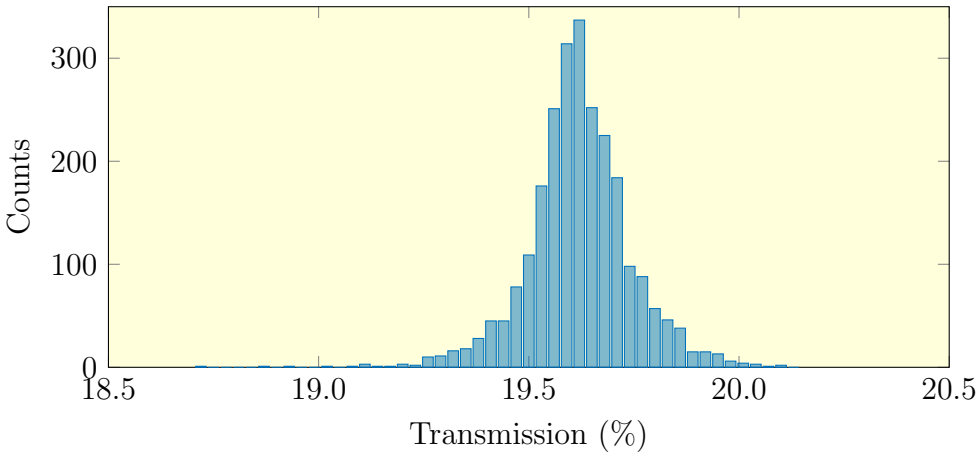

Figure 5.18: A histogram of the measured transmission of the dual-pulsed, dual-wavelength Er:YAG laser through a 5 cm reference gas cell filled with 740 Torr of methane.

The mean, standard deviation and standard error for this distribution are 0.1962, 1.25×10^{-3} and 2.5×10^{-5}. Removing the effect of absorption at λ_{off} is achieved using the correction described in Appendix G:

$$\ln(\mathrm{T_{on}}) = \ln(\mathrm{T_{obs}}) \left[\frac{1}{1-\sigma_{\text{off}}/\sigma_{\text{on}}}\right]$$
$$\Rightarrow \mathrm{T_{on}} = 0.1877$$

where we use the cross-sections described in Section 5.2.

This transmission is compared with the HITRAN prediction in Figure 5.19, which assumes that the nominal methane pressure in the cell is 740 Torr as specified. We observe a systematic offset between the measured and predicted transmission. A cell pressure of 675 Torr, rather than 740 Torr, would be required to account for this difference. Alternatively, stray light entering the reference photodetector would result in a systematic increase in the observed transmission. We attempted to minimise this effect by narrowing the entrance aperture to the photodetectors using irises.

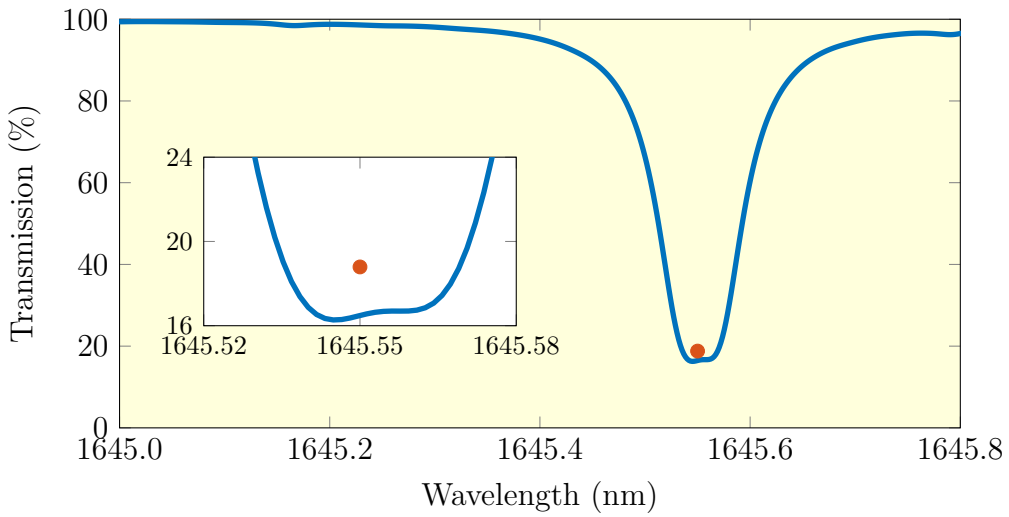

Figure 5.19: The double-pulsed transmission measurement compared to the HITRAN simulation of the reference methane cell.

5.5 Transmitting and Receiving Optical Systems

For atmospheric measurements, the transmitting optics positioned after the Q-switched laser must expand the laser mode to meet the Australian/New Zealand eye-safety regulations (AS/NZD IEC 60825.14:2011 [265]). For a pulse energy of 1.2 mJ these regulations specify the $1/e^2$ radius must exceed 11 mm at the laboratory exit, which we estimate to be 8 m from the transmitter. Using the laser mode measurements presented in Chapter 2 and the ABCD matrix formalism described in Appendix B we optimised the transmitting optics. The predicted $1/e^2$ radii in the near-field are plotted in Figure 5.20

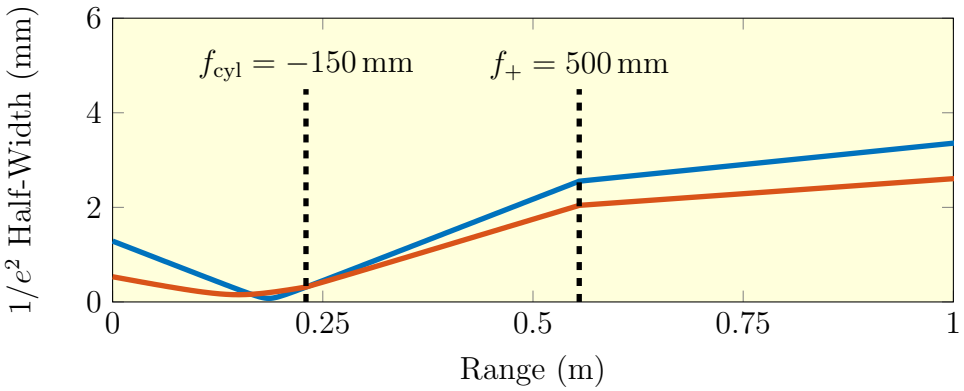

Figure 5.20: Predicted horizontal and vertical laser modes in the near-field.

A cylindrical lens f_{cyl} is positioned in the vertical plane at the circle-of-least confusion [266] to increase the divergence of the vertical mode and match it to the horizontal. Following this, a spherical lens f_+ allows the beam to diverge freely with full-angle di-

vergences of $\theta_{t,x} = 3.6\,\text{mRad}$ and $\theta_{t,y} = 2.6\,\text{mRad}$ in the horizontal and vertical planes. The average $1/e^2$ radius at the laboratory exit is predicted to be 13.9 mm, which meets the eye-safety requirements. At a range of 300 m the $1/e^2$ beam diameters are predicted to be $d_{t,x} = 1.14\,\text{m}$ and $d_{t,y} = 0.78\,\text{m}$.

To efficiently image this spot onto the photodetector described in Section 5.3 we use a *Meade* LX80 Schmidt-Cassegrain (SC) telescope. This device has a clear aperture of $D_r = 203\,\text{mm}$ and effective focal length of $f_r = 2034\,\text{mm}$. The optical efficiency of this telescope at $\lambda = 1645\,\text{nm}$ was measured to be $\eta_r = 62.04\%$.

A ray-tracing model of the receiver system, produced in ZEMAX, is illustrated in Figure 5.21. Rays from a 1 m diameter spot positioned 300 m from the telescope reflect off of the curved primary and secondary mirrors. A short focal length lens (*Thorlabs* LA1951-C) is added to tightly focus the rays at the Back Focal Plane (BFP). A virtual sensor is positioned at the BFP to mimic the photodetector, the image formed at this sensor is illustrated in the inset figure. Clearly, the hard-target scatter is efficiently focused within the 2 mm aperture with no evidence of aberrations. The effective focal length of this composite receiver design is $f_r = 480\,\text{mm}$.

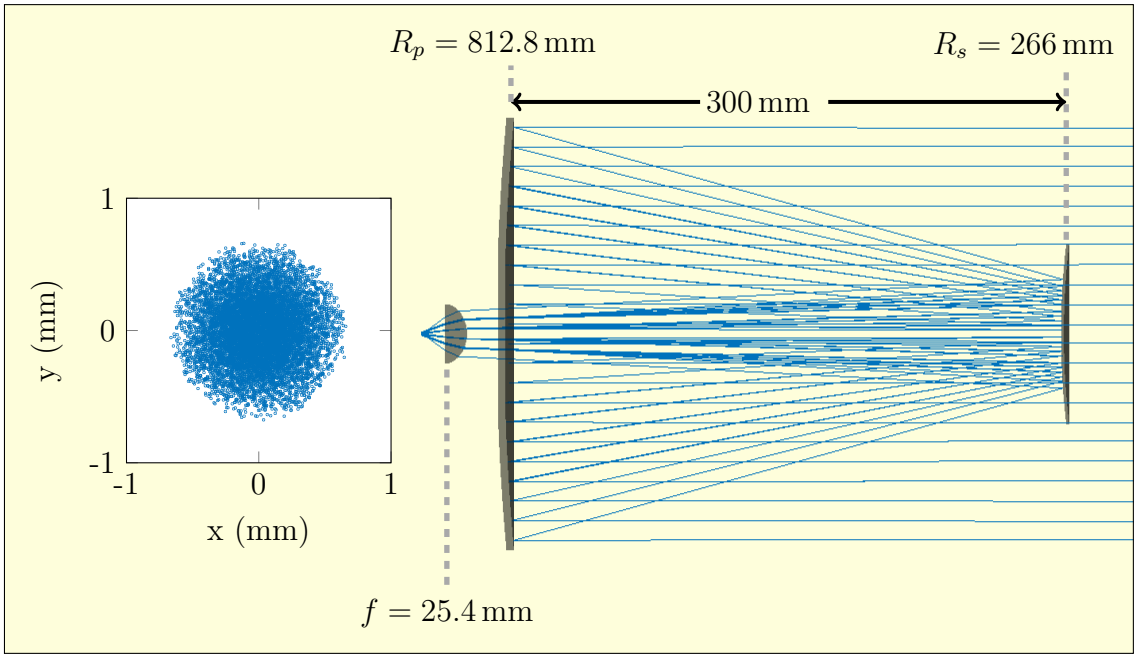

Figure 5.21: ZEMAX ray-tracing model of the SC telescope system highlighting the radius of curvature of the primary mirror R_p and secondary mirror R_s. Note that vignetted rays are not illustrated in this ray-tracing diagram.

This ray-tracing model does not account for the incomplete overlap between the laser beam and receiver Field-of-View (FOV) θ_r. We describe the overlap using the Geometric Form Factor (GFF) $G(R)$, which is uniquely determined by the transmitter-receiver configuration [267]. Using analytical expressions described in Appendix H this term is plotted for both the coaxial and biaxial configurations in Figure 5.22

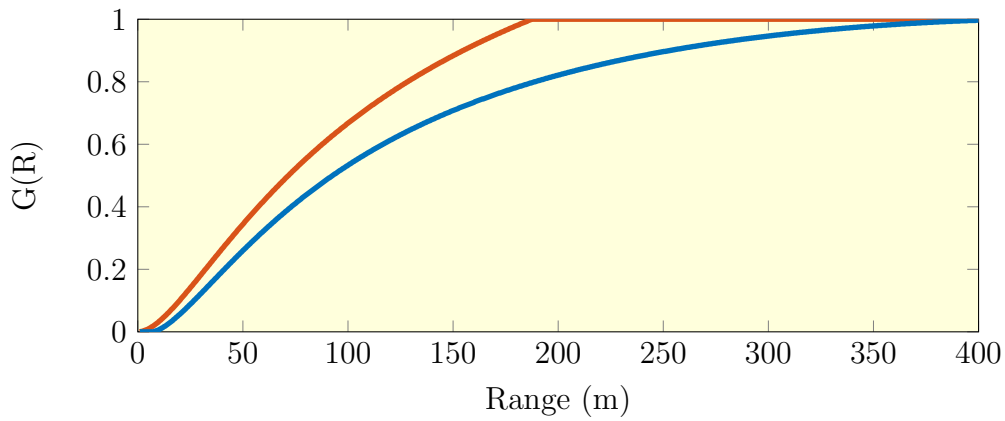

Figure 5.22: Calculated geometric form factor for a coaxial and biaxial LIDAR. An offset distance of $d_{tr} = 0.15\,\mathrm{m}$ has been assumed for the biaxial configuration.

The GFF is clearly maximised at a range of 300 m by using the coaxial configuration, hence, we employ this in the receiver system.

5.6 DIAL Sensitivity Model

Assuming similar scattering of the online and offline wavelengths with minimal interference from other atmospheric constituents the concentration of methane $\mathrm{N_{CH4}}$ measured by an airborne IPDA LIDAR system at altitude R is given by [268].

$$\mathrm{N_{CH4}} = \frac{1}{2\Delta\sigma R}\left[\ln\left(\frac{E_{\mathrm{off,normalised}}}{E_{\mathrm{on,normalised}}}\right)\right] \tag{5.6}$$

where $\Delta\sigma = \sigma_{\mathrm{on}} - \sigma_{\mathrm{off}}$ is the differential absorption cross section between the online and offline wavelengths. This expression can be written in terms of the measured transmittance T:

$$\mathrm{N_{CH4}} = \frac{-\ln(T)}{2\Delta\sigma R} \tag{5.7}$$

neglecting uncertainties in the denominator of Equation 5.7 the single-shot uncertainty in the methane concentration is given by,

$$\delta\mathrm{N_{CH4}} = \frac{\mathrm{N_{CH4}}}{-\ln(T)}\left(\frac{\delta T}{T}\right) = \frac{\mathrm{N_{CH4}}}{-\ln(T)\cdot\mathrm{SNR_{tot}}} \tag{5.8}$$

where $\mathrm{SNR_{tot}}$ describes the total signal-to-noise ratio, which is later defined in Section 5.6.7. In this section we relate $\mathrm{SNR_{tot}}$ to uncertainties introduced from instrument noise and random uncertainties in the auxiliary system parameters. For simplicity, these noise sources are also described by a signal-to-noise ratio - allowing all separate contributions to the IPDA measurement uncertainty to be estimated.

5.6.1 Photodetector Noise

For an airborne LIDAR system the measured signal is governed by the hard-target LIDAR equation [269], adapting this equation we define the collection efficiency η_f. This term describes all loss between the transmitter and the photodetector and is given by

$$\eta_f = \eta_r \cdot \rho_g \cdot G(R) \cdot \left(\frac{D_r}{2R}\right)^2 \tag{5.9}$$

where ρ_g is the ground reflectivity, $G(R)$ is the geometric form factor, R is the range to the hard-target, η_r is the receiver optical efficiency and D_r is the telescope diameter.

The voltage output of the photodetector V_{pd} is dependent on the transmitted pulse energy E_p, pulse width τ_p, photodetector responsivity $\Re$ and transimpedance gain Z_0:

$$\mathrm{V}_{pd} = \Re \cdot Z_0 \cdot \eta_f \cdot \frac{E_p}{\tau_p} \tag{5.10}$$

Thus, the photodetector SNR is calculated by the ratio of the measured photodetector voltage and the RMS output voltage noise, v_{pd}:

$$\mathrm{SNR}_{\mathrm{pd}} = \frac{\mathrm{V}_{pd}}{v_{pd}} \tag{5.11}$$

5.6.2 Shot Noise

Shot noise describes the fluctuation in the number of photons N_p counted by a photodetector. This fundamental noise limit was first observed by W. Schottky [270] and is modelled by Poisson statistics with a corresponding SNR given by.

$$\mathrm{SNR}_{\mathrm{shot}} = \sqrt{N_p} \tag{5.12}$$

Where the number of photons depends on the collection efficiency and the number of transmitted photons:

$$N_p = \eta_f \frac{E_p \lambda}{hc} \tag{5.13}$$

5.6.3 ADC Noise

An Analog-to-Digital Converter (ADC) is used to convert the analog photodetector output to a digital output for signal processing. This amplitude quantisation introduces inherent broadband noise, known as quantisation noise. For an ideal N_{bit} digitiser, the SNR in Decibel Full-Scale (dBFS) is given by [271]:

$$\mathrm{SNR}_{\mathrm{ADC}} = 6.02 N_{bit} + 1.76 \text{ dBFS} \tag{5.14}$$

In most measurement systems it is not practical to fill the full-scale of the ADC as small fluctuations can lead to signal clipping. Hence, the SNR is scaled by the fraction of the full-scale voltage V_{FS} filled by the photodetector output.

$$\mathrm{SNR_{ADC}} = \frac{V_{pd}}{V_{FS}} (6.02N_{bit} + 1.76) \ \ \mathrm{dB} \tag{5.15}$$

To maximize the SNR we use the GaGe CSE1642 ADC; a 125 MHz, 200 MS/s, 16-bit device. Ideally the quantisation noise should be approximately Gaussian with no dominant distortion products present in the spectra. The output noise was characterised by recording a 16384 point FFT of the ADC output, plotted in Figure 5.23. Clearly the ADC exhibit a white noise spectra with few distortion products above the measurement noise floor.

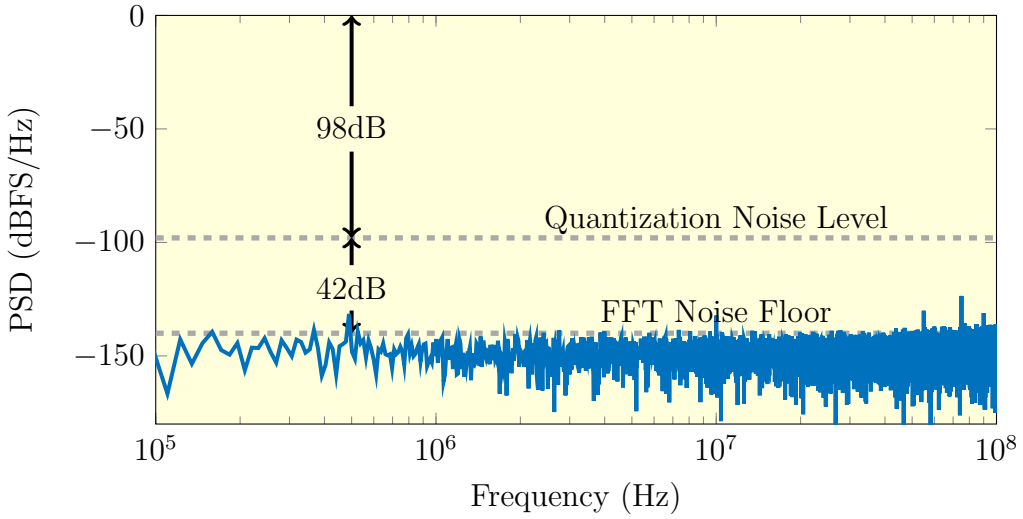

Figure 5.23: Measured digitisation noise of the GaGe low-noise ADC. The FFT noise floor is calculated using the processing gain described by W. Kester [272].

5.6.4 Speckle Noise

Speckle noise arises in the image plane of a DIAL receiver due to random phase aberrations introduced by diffuse scatter at a hard target [273,274]. The SNR of a single-shot DIAL measurement due to rough target speckle is given by [275]:

$$\mathrm{SNR_{speckle}} = \sqrt{1 + \left(\frac{\theta_t \cdot D_r}{\lambda}\right)^2} \tag{5.16}$$

where θ_t is the full-angle divergence of the transmitted beam. The speckle noise contribution is constant with range and increases for larger beam and receiver diameters. However, increasing the beam divergence will reduce the geometric form factor, degrading the photodetector, ADC and shot noise.

5.6.5 Solar Background Noise

Solar background radiation reflected from the Earths surface will introduce false readings at the photodetector, increasing the measurement uncertainty. The number of background photons N_{bg} measured over a sampling period τ_s is dependent on the optical filter bandwidth $\Delta\lambda_{BPF}$, receiver geometry and background irradiance S_{bg} and is given by [276].

$$N_{bg} = \frac{\pi^2 \lambda}{16hc} \cdot \mathrm{S}_{bg} \cdot \tau_s \cdot D_r \cdot \eta_r \cdot \Delta\lambda_{BPF} \cdot \theta_r^2 \tag{5.17}$$

To filter background solar radiation we use an optical Band-Pass Filter (BPF) manufactured by *Omega Filters* with centre wavelength $\lambda_0 = 1645.5\,\mathrm{nm}$ and FWHM bandwidth $\Delta\lambda_{BPF} = 1\,\mathrm{nm}$ positioned before the telescope BFP. The noise contribution of the solar background radiation is calculated by comparison to the number of detected photons.

$$\mathrm{SNR}_{\mathrm{solar}} = \frac{N_p}{N_{bg}} \tag{5.18}$$

5.6.6 Atmospheric Turbulence Noise

A model for describing atmospheric turbulence was proposed by Kolmogorov in 1941 [277]. His theory describes energy transfer and dissipation in complex systems of eddies. These eddies cause fluctuations in both the power and phase of an optical signal [278]. The variance in the collected power is given by [279].

$$\sigma_p^2 = P_0^2 \left(\exp\left(\sigma_{xp}^2\right) - 1\right) \tag{5.19}$$

Where P_0 is the mean collected power and σ_{xp} is given by [280]:

$$\sigma_{xp}^2 = 0.56 \left(\frac{2\pi}{\lambda}\right)^{7/6} \int_0^{2R} C_n^2(x) \left(\frac{x}{2R}\right)^{5/6} (2R - x)^{5/6}\, dx \tag{5.20}$$

Where C_n^2 is the index of refraction structure parameter, which is an altitude dependent term that describes the strength of turbulence. For atmospheric channels near the ground C_n^2 can vary from $10^{-13}\,\mathrm{m}^{-2/3}$ for strong turbulence to $10^{-17}\,\mathrm{m}^{-2/3}$ for weak turbulence [281].

Equation 5.19 can be rearranged to solve for the SNR limitation due to atmospheric turbulence.

$$\mathrm{SNR}_{\mathrm{turb}} = \frac{P_0}{\sigma_p} = \frac{1}{\sqrt{\exp\left(\sigma_{xp}^2\right) - 1}} \tag{5.21}$$

Studies of atmospheric turbulence have concluded that on a sub-millisecond time-scale

the atmosphere can be considered 'frozen' [282]. Thus, we can assume this effect can be neglected in a DIAL system with a sub-millisecond pulse separation.

5.6.7 Total Noise

Assuming all noise sources are uncorrelated and the pulse separation is small enough that turbulence induced noise can be neglected the total SNR, $\mathrm{SNR}_{\mathrm{tot}}$, is given by.

$$\mathrm{SNR}_{\mathrm{tot}} = \sqrt{\frac{1}{\frac{1}{\mathrm{SNR}_{\mathrm{pd}}^2} + \frac{1}{\mathrm{SNR}_{\mathrm{ADC}}^2} + \frac{1}{\mathrm{SNR}_{\mathrm{shot}}^2} + \frac{1}{\mathrm{SNR}_{\mathrm{speckle}}^2} + \frac{1}{\mathrm{SNR}_{\mathrm{solar}}^2}}} \tag{5.22}$$

The total SNR was estimated using the parameters in Table 5.2. The contributions to the SNR as a function of range are plotted in Figure 5.24. At a range less than 1 km the total SNR is dominated by the target speckle noise contribution. For a range of greater than 1 km the return signal significantly decreases, causing the photodetector noise to dominate. This noise model predicts an SNR of 375 at a range of 300 m.

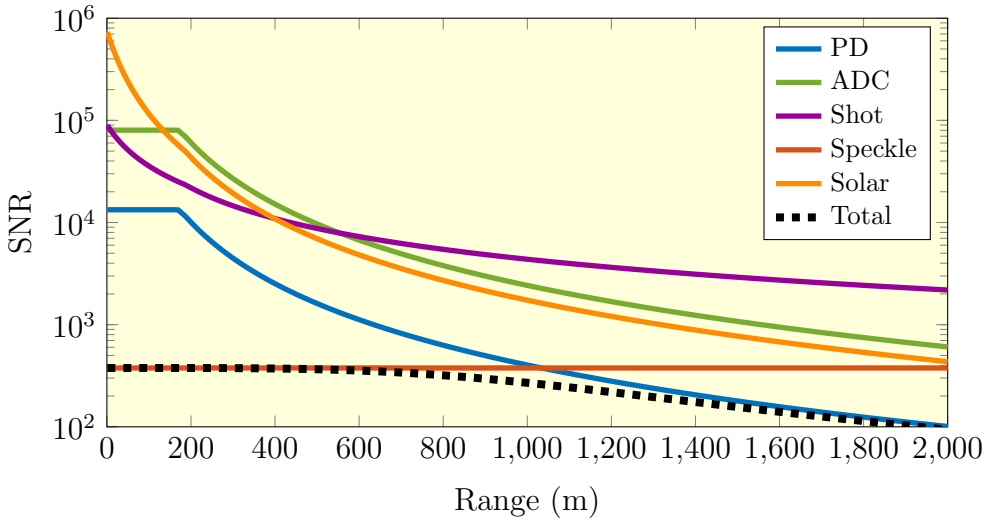

Figure 5.24: Predicted contribution of various noise sources to the IPDA LIDAR single-shot SNR. Note the PD and ADC noise is limited in the near-range due to clipping of the ADC full-scale.

Using Equations 5.8 & 5.22 we also calculate the predicted measurement sensitivity, plotted in Figure 5.25. As expected the sensitivity is limited by the instrument speckle noise in the short range with a predicted sensitivity of $\delta \mathrm{N}_{\mathrm{CH4}} = 82\,\mathrm{ppb}$ at 300 m. This improves to a sensitivity of $\delta \mathrm{N}_{\mathrm{CH4}} = 35\,\mathrm{ppb}$ at 1 km, suggesting the airborne platform should operate at a higher cruising altitude than the originally proposed 400 m.

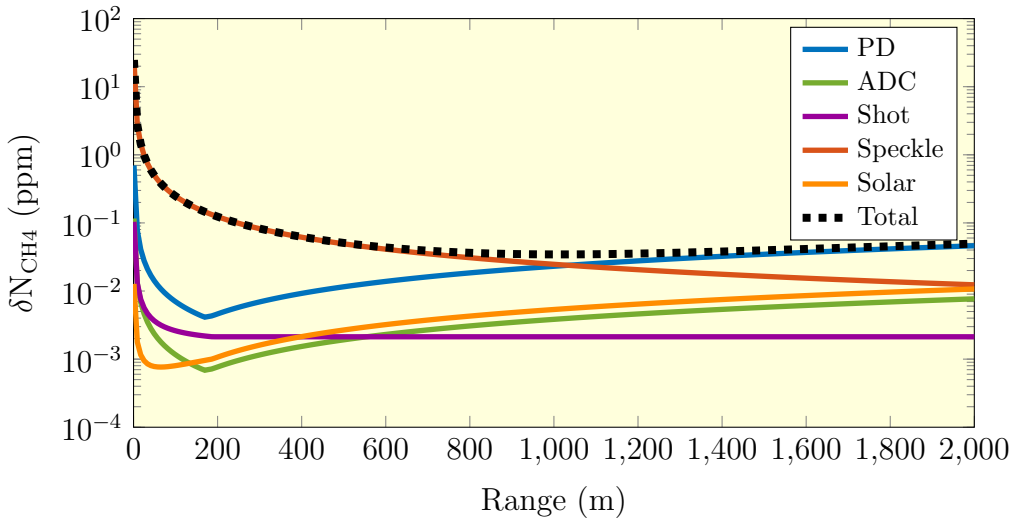

Figure 5.25: Predicted contribution of various noise sources to the IPDA LIDAR single-shot sensitivity.

Laser Transmitter		
Pulse Energy	E_p	1.2 mJ
Pulse Width	τ_p	105 ns FWHM
Average Beam Divergence	θ_l	3.1 mRad
Receiver		
Telescope Diameter	D_r	0.203 m
Telescope FOV	θ_t	4.2 mRad
Effective Focal Length	f_r	0.480 m
Optical Efficiency	η_r	62.04%
Band-Pass Filter Bandwidth	$\Delta\lambda_{BPF}$	1 nm
Detector & ADC		
Active Diameter	ϕ	2 mm
Responsivity	$\Re$	1.10
Transimpedance Gain	Z_0	10,000 V/A
RMS Voltage Noise	v_{pd}	300 µV
Number of Bits	N_{bit}	16
Voltage Full-Scale	V_{FS}	4V
Sampling Period	τ_s	1 µs
Atmosphere		
Solar Background Irradiance	S_{bg}	5.0 mW/(m^2·nm·sr) [283]
Surface Reflectivity	ρ_g	0.31 [283]
Methane Concentration	N_{CH4}	1.7 ppm [284]

Table 5.2: Instrument parameters used in the DIAL sensitivity analysis. The solar background irradiance and surface reflectivity are for a vegetative surface at 1.6 µm.

5.7 Atmospheric Sensitivity Measurement

To test the IPDA LIDAR sensitivity under realistic atmospheric conditions with a hard-target scattering surface we constructed the system illustrated in Figure 5.26.

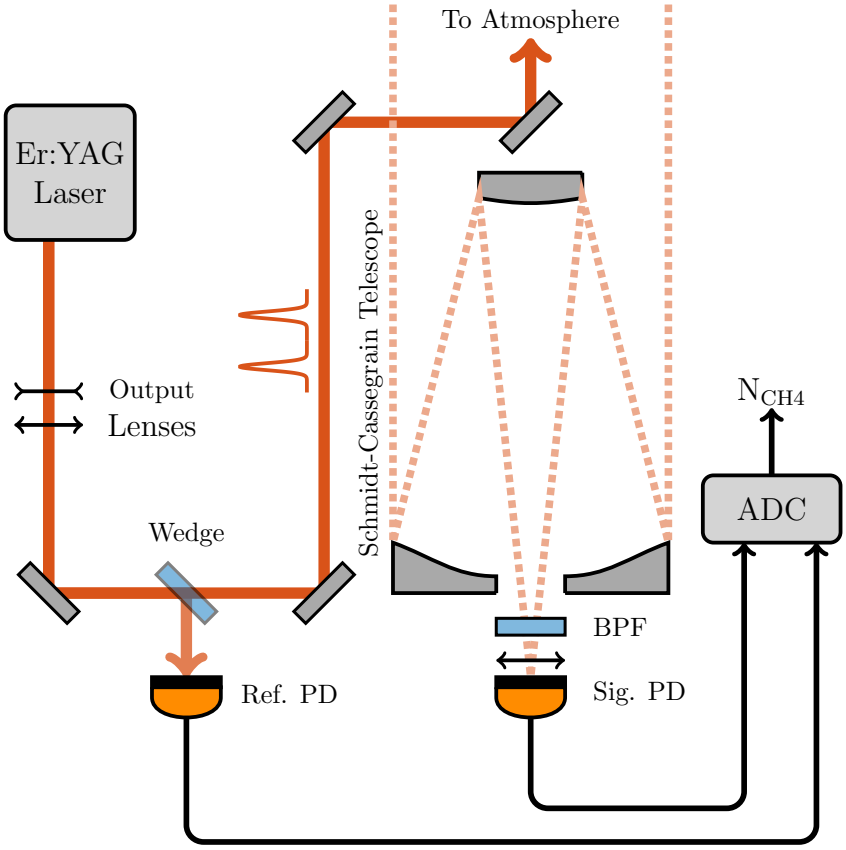

Figure 5.26: Schematic diagram of the methane DIAL system used to measure the background concentration of methane over Adelaide, Australia. The dual-pulsed, injection-seeded Er:YAG laser is passed through output lenses to ensure eye-safe operation. A small fraction of the output beam is picked-off using a wedge and monitored on the reference photodetector. A mirror mounted co-axially on the telescope transmits the beam out and two large planar mirrors (not illustrated) act as a periscope to direct the beam through a vertical roof-hatch and horizontally through the atmosphere. The return light is passed through an optical band-pass filter, collected on the signal PD and analysed using the ADC.

The atmospheric column was accessed by directing the beam through a roof-hatch located in the laboratory. To direct the beam horizontally through the atmosphere two large planar mirrors (240 mm x 300 mm) from *Edmund Optics* were mounted in a periscope configuration.

The atmospheric path for the IPDA LIDAR test is shown in Figure 5.27. A building located approximately 300 m from the roof-hatch acts as the hard-target scattering surface. This target was chosen as there is clear line-of-sight, at normal incidence and the range is close to the proposed altitude of the airborne system.

Figure 5.27: Image of the IPDA LIDAR atmospheric path courtesy of Google Earth.

The dual-pulsed, injection-seeded Er:YAG laser was operated at a pulse energy of $E_p = 1.2\,\text{mJ}$ per-pulse, a pulse-repetition frequency of 100 Hz with $\lambda_{\text{on}} = 1645.55\,\text{nm}$ and $\lambda_{\text{off}} = 1645.39\,\text{nm}$. We measured 2,500 consecutive pulse-pairs using the GaGe ADC. An example of the time-trace measured by the signal photodetector is plotted in Figure 5.28.

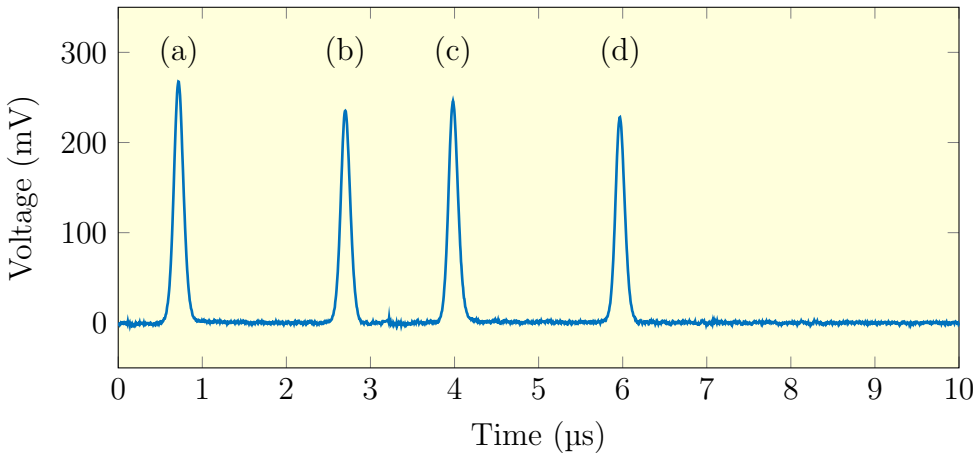

Figure 5.28: Example of the time-trace recorded on the signal photodetector. Pulses (a) and (c) are the pulses scattered into the signal photodetector before transmission into the atmosphere whilst pulses (b) and (d) are the corresponding online and offline pulses after transmission through the atmospheric column.

The source of the scattered pulses, labelled (a) and (c), was unable to be identified and removed. It is likely these arise due to multiple scattering events within the laboratory that scatter through the large aperture telescope. The on-off pulse delay was extended to 3.2 µs to ensure the online return and offline scatter (pulses labelled (b) and (c)) were sufficiently separated. Using the time-delay between the reference

photodetector and pulse (b) we calculate the range to the hard-target. The mean and standard deviation of the measured range is:

$$R = 308.48 \pm 0.43\,\text{m}$$

where the uncertainty in this measurement is due to the sampling rate of the ADC (200 MS/s). The average range is consistent with the range estimated using Google Earth and suggests we are scattering off of the hard-target.

We used the matched-filtering algorithm discussed in Section 5.4.1 to extract the online and offline pulse energies at the signal and reference photodetectors. These were then converted to a transmission and a methane concentration by applying Equation 5.7. The measured transmission and methane concentration are plotted as a function of measurement time in Figure 5.29.

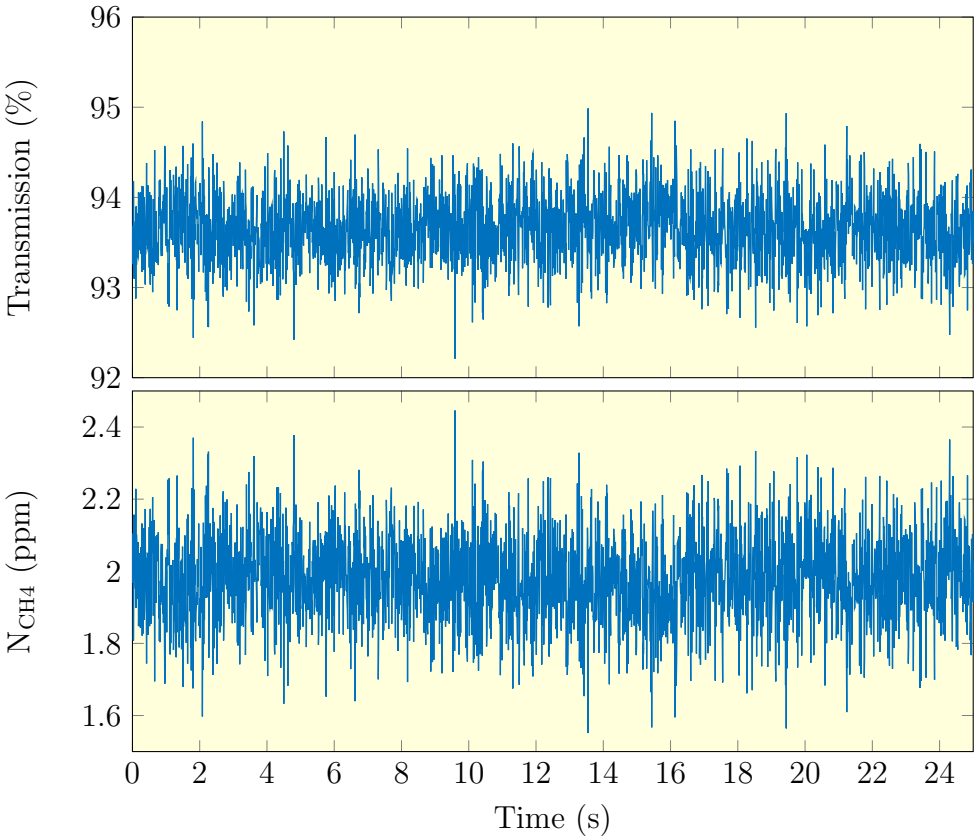

Figure 5.29: The measured transmission and corresponding methane concentration through an atmospheric column recorded on the 02/04/2019 at 10:45AM.

The corresponding frequency histogram of the measured methane concentration is plotted in Figure 5.30, indicating normally-distributed data as expected. The mean, standard deviation and standard error for this data are 1.979, 0.124 and 0.003 ppm respectively.

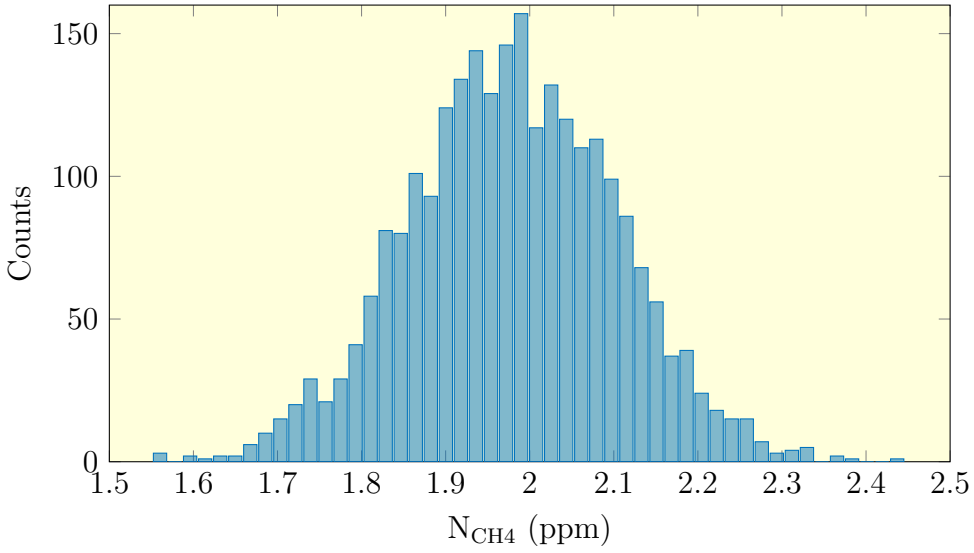

Figure 5.30: A histogram of the measured methane concentration of the dual-pulsed Er:YAG laser through an atmospheric column at a range of 308.5m.

Thus, the average methane concentration of 1.979 ± 0.003 ppm is significantly higher than the expected background methane concentration of 1.7 ppm. This may be caused by anthropogenic sources beneath the atmospheric path such as leaking gas infrastructure [285, 286] or methane production in the sewer system [287]. An Adelaide newspaper reported in 2010 that minor gas leaks in the city pipeline infrastructure are extensive [288].

Hatch *et al.* reported the measurement of methane in south-eastern Australia using the *Picarro* G2201-i portable cavity ring-down spectrometer mounted on a car [289, 290]. This device can measure local methane and carbon dioxide concentrations with a quoted sensitivity of 50 ppb. A mobile measurement was conducted in Adelaide during July 2014 for a five hour observation time during which a concentration below 3 ppm was measured for 87% of the measurement run. This result is consistent with our initial background concentration estimate.

The extremely low uncertainty in the mean required averaging over 25 s. Averaging data collected using an airborne system would degrade the spatial resolution, however. The effect of averaging on the uncertainty in the mean and the corresponding spatial resolution, assuming an airborne system mounted in a Cessna 404 Titan, which has a typical cruising speed of 75 m/s [291], in plotted in Figure 5.31. For comparison we plot the predicted $1/\sqrt{\tau}$ noise performance, this represents the averaging improvement expected for a signal with a white noise distribution. Lastly, the sensitivity predicted in Section 5.6 model is plotted for comparison to the measured sensitivity.

Figure 5.31 shows that a sensitivity of $\delta N_{CH4} = 20$ ppb can be achieved with an average time of $\tau = 0.5$ s, corresponding to a spatial resolution of 37 m. The measured sensitivity trends away from the the predicted $1/\sqrt{\tau}$ averaging improvement for

time periods $> 1\,\mathrm{s}$. We attribute this to slow changes in the atmospheric methane concentration, temperature and pressure in the beam-path.

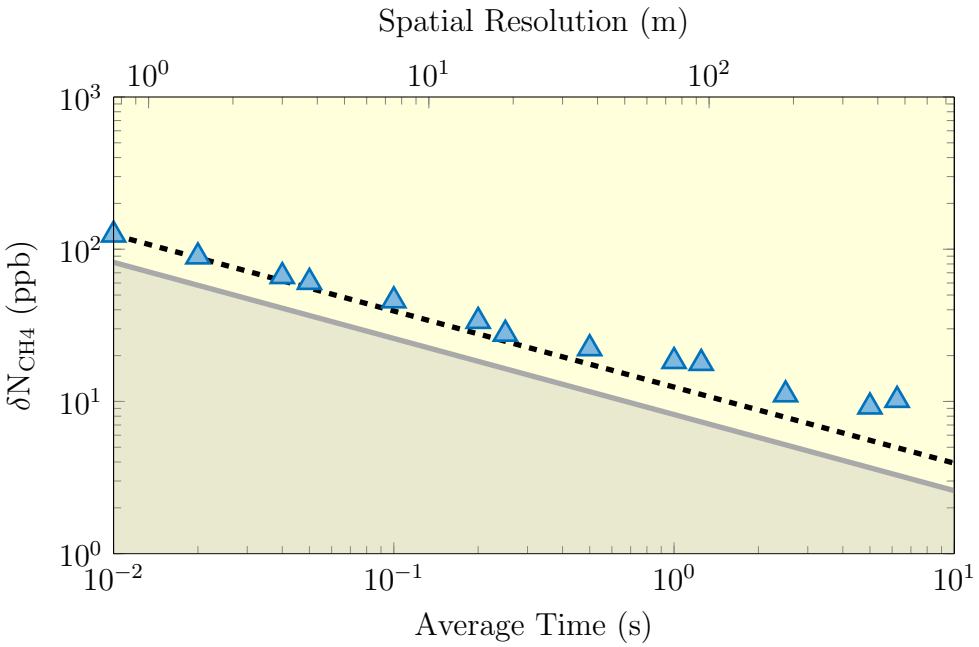

Figure 5.31: The decrease in the methane measurement standard error as a function of the average time and spatial resolution. The dashed black line represents the theoretical $1/\sqrt{\tau}$ improvement in noise performance whilst the grey shaded area is the noise floor predicted by the sensitivity model.

The measured single-shot sensitivity of $\delta N_{CH4} = 124\,\mathrm{ppb}$ is higher than the predicted single-shot sensitivity of $\delta N_{CH4} = 82\,\mathrm{ppb}$. Thus further work is required to better constrain the noise model parameters, particularly the transmitted beam-divergence which is crucial in calculating the contribution of speckle noise to the total system SNR.

We compare the sensitivity of our system to other published methane DIAL systems in Figure 5.32. The sensors presented in this figure include compact handheld systems designed for local measurements and satellite systems for global methane monitoring.

Clearly our system offers an improved methane measurement sensitivity. The two closest performing systems, described by Riris *et al.* [64–66] and Amediek *et al.* [67–69], are airborne systems that use two optical parametric generation sources to produce wavelengths near $1.6\,\mu\mathrm{m}$. This increases the instrument size and weight and thus requires a larger aircraft, increasing the operating costs and cruising altitude. By using one laser source to produce both the online and offline pulse we believe our system offers a compact, high-sensitivity, financially competitive instrument for the airborne sensing of methane leaks from gas pipelines. Additionally, optimisation of the receiver system and increase of the laser repetition rate should further improve the sensitivity.

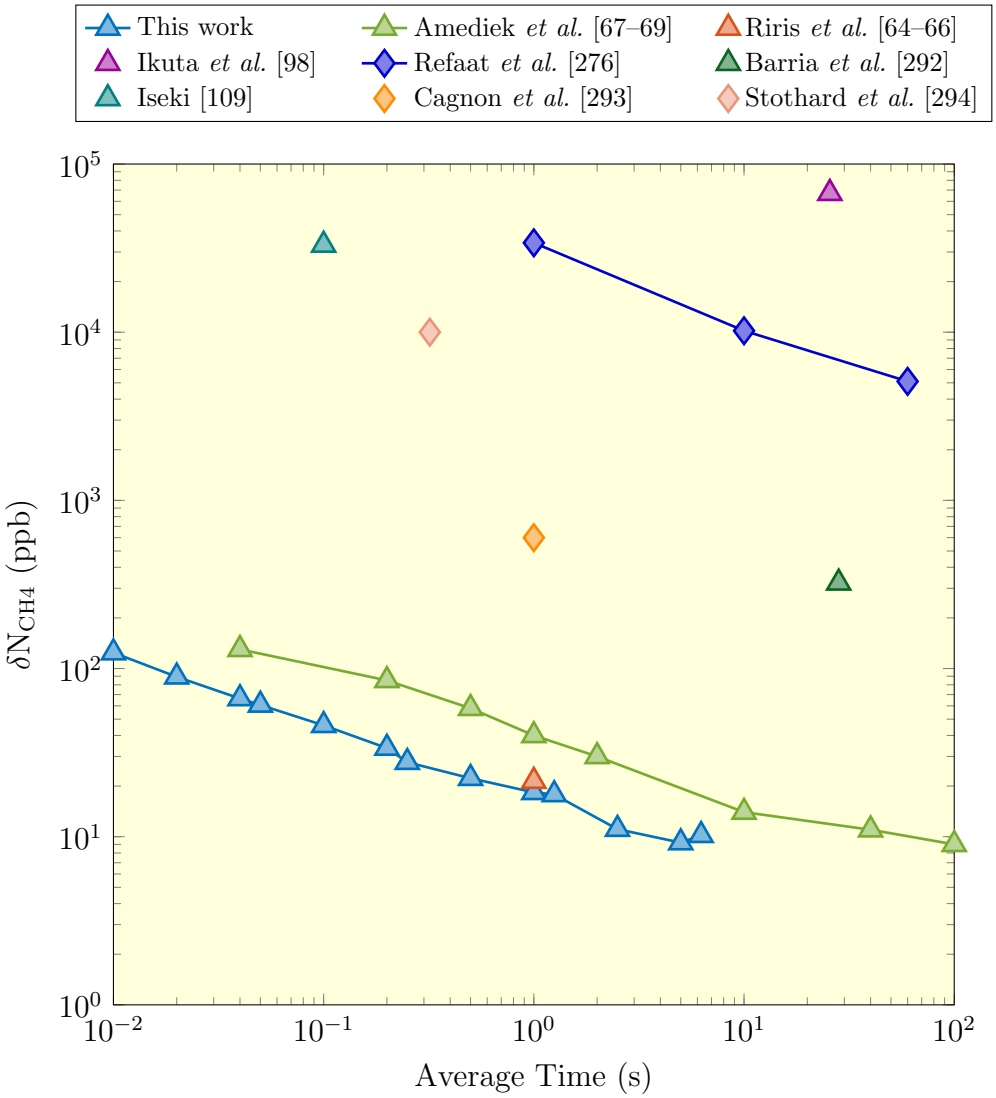

Figure 5.32: A comparison between the methane measurement sensitivity and other published DIAL systems. Data points represented by a diamond marker signify sensors which rely on scatter from atmospheric molecules whilst those represented by a triangle marker signify sensors which rely on hard-target reflection.

5.8 Conclusion

In this chapter we have described the development and testing of an IPDA LIDAR system for high-sensitivity methane sensing over a range of 300 m. A custom large-area, low-noise, high-gain, high-bandwidth photodetector was modelled, designed and constructed to measure the weak return LIDAR signal from a hard-target reflection. A commercial telescopic system was then modelled to ensure the laser footprint can be efficiently imaged onto the photodetector.

A noise model was introduced to predict the IPDA LIDAR sensitivity. This suggested a single-shot measurement sensitivity of 82 ppb, limited by hard-target speckle noise, can be achieved at a range of 300 m. Measurements of the system noise were

performed in a controlled environment to remove the contribution of speckle noise and other atmospheric variations. As predicted, the measurement noise was limited by voltage noise at the photodetector output. This noise was degraded due to pick-up from the slave lasers high-current pump-diode driver and high-voltage Q-switch driver. However, this noise is still below the speckle noise prediction and hence should not dominate.

A measurement of the background concentration of methane over the city of Adelaide was performed. We measured an elevated methane concentration of 1.979 ± 0.003 ppm along a 308.5 m atmospheric path. The measured single-shot system sensitivity was 124 ppb, which could be reduced further by averaging over longer time-periods. By comparing this result to the sensitivity of other published DIAL methane sensors we observe our system offers a higher sensitivity. This can be improved by increasing the laser repetition rate to enable increased averaging without sacrificing the spatial resolution.

Chapter 6

Conclusion

This thesis described the development of an Integrated Path Differential Absorption (IPDA) LIDAR system for the sensing of anthropogenic sources of methane in the natural gas sector. A dual-pulsed Q-switched erbium-doped YAG (Er:YAG) laser capable of reliably producing injection-seeded pulses at the methane online and offline wavelengths was developed. The dual-wavelength transmitter and a bespoke receiver system was used to measure the background concentration of methane over a 300 m atmospheric column. A summary of the key system parameters demonstrated in this Thesis are outlined in Table 6.1.

Parameter	Requirements	Results in this Thesis
Online Wavelength λ_{on}	1645.55 nm	1645.55 nm
Offline Wavelength λ_{off}	<1645.40 nm	1645.39 nm
Output Pulse Energy	> 1 mJ	1.2 mJ
Pulse Duration	100 ns	105 ns
Pulse Repetition Frequency	1 kHz	100 Hz
On/Off Pulse Delay δt_{off}	2 µs	2.3 µs
Spatial Beam Quality	$M^2 < 2$	$M_x^2 = 1.04$, $M_y^2 = 1.01$
Wall-Plug Efficiency	-	0.15%
On/Off Frequency Stability	-	435 kHz/5.19 MHz
On/Off Control Bandwidth	> 1kHz	7.35 kHz/300 kHz
Photodetector Diameter ⌀	> 1 mm	2 mm
Photodetector Bandwidth	> 10 MHz	18 MHz
Photodetector Gain	-	10,000 V/A
Photodetector Noise	-	300 μV_{rms}
Telescope Diameter	-	0.203 m
Telescope Focal Length	-	0.48 m
Range Accuracy	<1 m	0.43 m
DIAL Single-Shot Sensitivity	-	124 ppb

Table 6.1: A table of the Er:YAG methane DIAL system requirements and results achieved in this thesis.

The Q-switched Er:YAG 'slave' laser was characterised in Chapter 2. This uses a Co-Planar Folded Slab (CPFS) end-pumped by a 1470 nm diode array to achieve pulses with energy 1.2 mJ and width 105 ns. Unfortunately, the repetition rate of the laser was limited to 100 Hz to ensure stable pulse-to-pulse energy. Wavelength tuning by injection-seeding the slave laser with a low-power 'master' laser was investigated. Two master lasers were considered; a Distributed Feedback (DFB) diode laser and an External Cavity Diode Laser (ECDL), both of which are tunable around the methane absorption line of 1645.55 nm.

Light from the narrow linewidth ECDL was injected into the ring-resonator slave laser via an intra-cavity PBS and properties of the slave laser pulsed output were used to quantify the quality of injection-seeding. Unfortunately, the seeding was inefficient and there was evidence of an uncontrolled dual-pulsing, both of which would compromise reliable wavelength tuning for methane sensing.

An injection-seeded numerical model of our laser system was described in Chapter 3. Discrepancies between experiment and theory were observed and it was discovered that these were caused by unforeseen oscillations in the Pockels Cell. To mute these oscillations we reduced the resonator losses, allowing below-threshold regenerative amplification of the injected light from the master laser during the low-Q phase of the pulse cycle. This resulted in improved injection-seeding behaviour with no evidence of self-dual pulsing.

In Chapter 4 we described a control system to ensure reliable injection-seeding based upon the Pound-Drever-Hall (PDH) technique. While this technique has been used in other Q-switched systems, the control bandwidth is commonly limited by the low-Q state of the slave cavity. For our laser, however, the reduced losses increased the Q of the slave cavity between pulses, enabling the master laser to be tightly locked to a resonant mode of the slave laser.

The transmission of the master laser through the slave cavity was monitored using a custom saturating photodetector capable of resolving the PDH sidebands whilst quickly recovering from a high peak-power pulse. The ECDL master laser was locked to the slave cavity via feedback to a slave cavity PZT and the master laser current with a control bandwidth of 7.35 kHz. This enabled reliable injection-seeding at the online wavelength of 1645.55 nm. An Optical Phase Locked Loop (OPLL) was used to lock the DFB master laser at the offline wavelength of 1645.39 nm, corresponding to an integer number of slave cavity Free Spectral Ranges (FSR). An AOM switch is used to switch the injected input between the online and offline master lasers, generating two injection-seeded pulses separated by 2.3 µs. To our knowledge the smallest temporal separation of two different wavelength pulses from a single Q-switched laser source.

In Chapter 5 we described a custom receiver system for high-sensitivity ground-based atmospheric measurements of methane. A sensitivity model that predicted a

single-shot measurement sensitivity of 82 ppb at a range of 300 m was described. The limiting noise source, due to speckle from the hard-target, can be improved by increasing the target spot-size or operating at higher altitudes.

The background concentration of methane was measured for a 300 m long atmospheric column over the city of Adelaide, Australia. We obtained an average background concentration of 1.979 ± 0.003 ppm with a single-shot sensitivity of 124 ppb. To our knowledge the system sensitivity is the highest achieved by a methane IPDA LIDAR system.

6.1 Future Work

The results presented in this Thesis are a promising proof of concept, suggesting that a single laser source can be used to sense methane through an atmospheric column with a high sensitivity. However, significant work is still required to transition this technology to a commercial product capable of long-term flight trials and further improve system performance.

Slave Laser

We are currently assessing an alternative slave laser geometry in which an Er:YAG rod is end-pumped with a narrow-linewidth, high beam-quality Erbium-Doped Fiber Laser (EDFL) operating at 1532 nm. This simple design should enable an increased pumping efficiency and allow a higher Pulse Repetition Frequency (PRF) and increased pulse energy. These will provide an improved measurement sensitivity without degrading the spatial resolution via averaging. Furthermore, we believe this geometry will overcome the laser induced damage which occurred on the Total-Internal Reflection (TIR) faces of the CPFS gain medium.

Injection-Seeding Control Systems

While the control systems described in Chapter 4 enabled spectral control of the slave laser adequate for a laboratory environment, further work is required to optimise these control systems for long-term flight trials. The low-frequency and high-frequency controllers used to control the online master laser should be improved to optimise the phase at the cross-over frequency and the 0 dB frequency. This will minimise servo peaking and hence the closed-loop frequency noise. We are currently assessing a balanced Piezo-Electric Transducer (PZT) design to enhance the low-frequency control bandwidth and simplify the servo design.

As observed in Chapter 5, the offline pulse sporadically lases near the erbium line-centre wavelength, suggesting incomplete injection-seeding is occurring. While this

spectral fluctuation does not limit system sensitivity it should be removed in future work by improving the OPLL servo. As discussed previously, a higher control bandwidth could be achieved by feedback to an Electro-Optic Modulator (EOM), further suppressing the broadband frequency noise of the offline master laser.

The design and performance of the injection-seeding control systems would be simplified by using narrow linewidth master lasers that enable DC feedback. This would reduce the system complexity, size and the challenges associated with engineering a bespoke airborne system.

Advancements in Field Programmable Gate Arrays (FPGAs) have enabled digital servo controllers with complex but easily controllable transfer functions [295–297]. Such devices would allow optimisation of the closed-loop gain with a capacity for parallel input/output operations. Thus, all control systems could be operated from one low-cost, low-power digital device. These devices could also be configured to automatically acquire lock [298], thus mitigating the risk of the system losing lock during high vibration events such as take-off.

Ground-Based IPDA LIDAR System

Further work is required to better understand and overcome the speckle noise we believe limits our system sensitivity. Simple noise models predict this can be improved by increasing the divergence of the transmitted beam, however, this will degrade the return signal strength. Alternatively, the diameter of the receiving telescope could be increased but this places significant constraints on the total instrument footprint. Thus, careful optimisation of these parameters is required. Furthermore, the photodetector design should be updated to reduce the noise pick-up from both the diode driver and Q-switch driver.

A potential improvement to the IPDA LIDAR system which was considered but not explored was to use hollow-core photonic crystal fiber to deliver the slave laser output to the transmitter. This fiber offers a flexible and robust means of beam deliver with a low propagation loss and high damage threshold [299]. This would enable the slave laser to be mechanically decoupled from the transmitter system, thus simplifying the design of a vibration insensitive slave laser mount.

Long-term ground-based measurements of background methane should be established. Our results indicated a higher than expected concentration and through further testing we could infer potential environmental and anthropogenic methane sources in the city of Adelaide. In parallel, real-time temperature and pressure data should be recorded to investigate natural fluctuations in absorption cross-sections at the online and offline wavelengths.

Alternative Atmospheric Sensing Possibilities

We adapted the ground-based IPDA LIDAR system for cloud monitoring using time-of-flight, presented in Appendix A, as the 1.6 µm Er:YAG laser enabled eye-safe operation and deeper atmospheric probing [300]. Preliminary experiments showed this system could resolve multi-layered structure within low-altitude clouds. Clouds play an important role in radiative transfer processes in the Earths atmosphere [301], hence a knowledge of their variation in space and time is crucial in modern climate change studies [302]. Further work is required to optimise this system and establish whether it can be used to complement other cloud sensing platforms.

The high-frequency stability and low-frequency chirp of the injection-seeded slave laser make it well suited for a Doppler LIDAR system in wind power generation [303], as seen in Chapter 4. Our system exhibits sub-megahertz frequency stability, which appears to be the benchmark in other published systems [136,137,304]. Wind turbines are an effective means of generating renewable energy, producing an estimated 30% of Australia's renewable energy in 2016 [305]. They operate in the lower atmosphere where both wind and turbulence dynamics are poorly understood [306]. Changes in wind-speed and direction are unpredictable and ultimately limit the effectiveness of wind energy as a reliable power source. A Doppler LIDAR system that monitors long-range wind speed would enable substantial improvements in the performance of wind power in an interconnected power grid [307].

Airborne Flight Trials

The intention of future research is to transition the ground-based system to an aircraft for flight trials. This will require significant engineering to ensure the system is rugged, minimises power consumption and meets the safety requirements for mounting in an aircraft. Where possible, the dependence on commercially available components should be minimised to reduce the risk of redundancy. One could imagine a bespoke modular system that enabled components to be easily replaced and tested, minimising potential down-time.

Once the system is functional preliminary flight trials should commence immediately. This will allow the system sensitivity to be measured under realistic conditions for a range of cruising altitudes. Further upgrades to the data acquisition and processing systems would be required to handle the large data sets recorded during these flight trials. Communication between the IPDA LIDAR system and the aircraft GPS should be established for real-time concentration mapping, with the ultimate goal of rapidly mapping sources of methane produced by the natural gas sector in Australia and overseas.

Appendix A

Thesis Publications

The commercially sensitive nature of the research presented in this Thesis meant that we did not pursue publishing any work directly related to methane sensing. This is a requirement to ensure the intellectual property developed can be protected for future commercialisation and potential patents. The publication provided in this Appendix describes a cloud sensing demonstration that was undertaken during my candidature. This experiment was not dependent on any patentable techniques described in this Thesis.

PROCEEDINGS OF SPIE

SPIEDigitalLibrary.org/conference-proceedings-of-spie

High peak power, short pulse duration Er:YAG lasers and applications

Joshua Pease, Lachlan Harris, Myles Clark, Sarah Watzdorf, Richard White, et al.

Joshua Pease, Lachlan Harris, Myles Clark, Sarah Watzdorf, Richard White, Peter Veitch, David Ottaway, "High peak power, short pulse duration Er:YAG lasers and applications," Proc. SPIE 10981, Laser Technology for Defense and Security XV, 109810N (13 May 2019); doi: 10.1117/12.2524139

SPIE.

Event: SPIE Defense + Commercial Sensing, 2019, Baltimore, Maryland, United States

High peak power, short duration Er:YAG lasers and Applications

Joshua Pease[a,b], Lachlan Harris[a,b], Myles Clark[a,b], Sarah Watzdorf[a,b], Richard White[a,b], Peter Veitch[a,b], and David Ottaway[a,b]

[a]Department of Physics, School of Physical Sciences, The University of Adelaide, Adelaide, South Australia, Australia
[b]The Institute of Photonics and Advanced Sensing, The University of Adelaide, Adelaide, South Australia, Australia

ABSTRACT

We describe the development of a number of eyesafe Er:YAG laser systems. Based on the Co Planar Folded Zig Zag geometry, these lasers were primarily developed for hard target ranging at distances greater than 20 km. We also present results where these lasers have been used to explore the profiles of cloud structures over Adelaide, South Australia.

Keywords: Er:YAG, Q-Switched, Cavity Dumping, Cloud Sensing

1. INTRODUCTION

Er:YAG lasers system have undergone significant development in the last 15 years driven primarily by the fact that they offer high peak power emission that is centered in the 'eyesafe 1.5 μm and 1.8 μm band. Lasers operating at these wavelength are critically important because they allow the highest possible emission of peak power without risking damage to the human eye.[1] This is a critical feature if these lasers are to be transmitted into the atmosphere for remote sensing applications such as LIDAR. Er:YAG lasers emit primarily at two wavelengths in this regime, 1617 and 1645 nm.[2] The development of Er:YAG lasers operating in this wavelength band has often replaced more complicated Optical Parametric Oscillator (OPO) based systems[3,4] for applications including range finding and wind sensing. As noted over forty years ago by White and Schleusener[5] Er:YAG lasers can be utilized for methane detection as it emits near a methane absorption line at 1645nm, enabling these lasers to be used in methane Differential Absorption Lidar (DIAL).

These systems require a high pulse energy and short pulse duration laser source because peak power is a major determinant of the sensitivity of systems that detect return power such as hard target laser range finders. The sensitivity of coherent systems such as Doppler Lidars depends on the average power emitted, hence, high sensitivity can be obtained by implementing a low pulse energy, high repetition rate laser from a convenient source such as a fibre laser. However, range confusion can limit the use of these systems in ranges exceeding 20km thus potential improvements can be achieved in coherent systems if lower repetition high pulse energy lasers are developed.

In this paper, we describe the development of a Q-switched Er:YAG laser system based upon the Co-Planar Folded Zig-Zag Slab (CPFS) geometry capable of achieving pulses with a duration of 4.5ns and a pulse energy of 10mJ corresponding to a peak power of 2MW - the highest demonstrated from a nanosecond regime Er:YAG laser. We then demonstrate the applicability of these lasers for remote sensing by exploring the profiles of cloud structures using a LIDAR system.

2. LASER DEVELOPMENT

Er:YAG lasers can be resonantly pumped using lasers operating at bands centered at 1532 nm and 1470 nm. The 1532 nm pump band is quite narrow but has a higher absorption cross section.[6] The narrowness of this transition means that band must be pumped by narrow band sources such as fibre lasers or volume Bragg grating

Laser Technology for Defense and Security XV, edited by Mark Dubinskiy, Timothy C. Newell, Proc. of SPIE Vol. 10981, 109810N · © 2019 SPIE
CCC code: 0277-786X/19/$18 · doi: 10.1117/12.2524139

stabilized laser diodes. The 1470 nm pump transition is considerably broader but has lower absorption cross section which requires careful consideration of the gain medium design to ensure efficient pump absorption.

Most of our work has focused on the development of Er:YAG lasers that are pumped by spectrally broad diode lasers.[7,8] We have developed the first Er:YAG laser that uses the CPFS geometry that was originally pioneered by Richards and McInnes for side pumped Nd:YAG lasers.[9] A schematic of this is shown below in Figure 1. We employ an end-pumping scheme where a 1470nm diode array is coupled into the slab using a lens-duct. This diode is fast-axis collimated to maximise the pump intensity within the slab whilst the slow-axis is un-collimated and is trapped in the slab by total internal reflection. Low doping densities are required for operation in the eyesafe band to prevent excess loss due to upconversion.[2] This means that the slabs need to be quite long ranging from 2-3 cm for 0.5 at.% doped slab. The Q-switch is formed using a Rubidium Titanyl Phosphate (RTP) pockels cell and a Quarter Wave Plate (QWP).

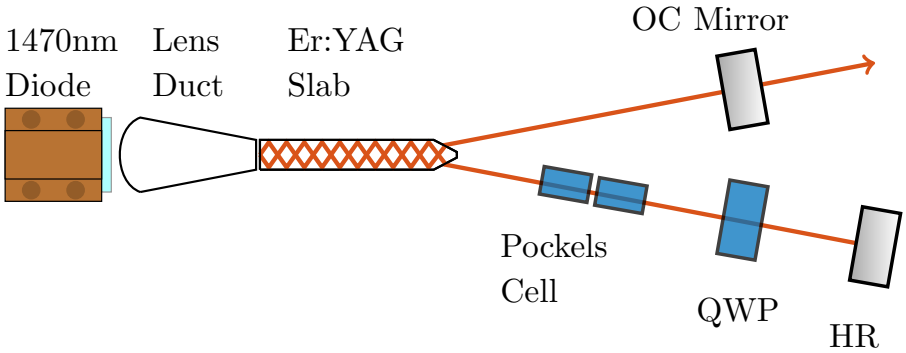

Figure 1: A schematic of the end-pumped CPFS slab geometry in standing wave Q-switched operation.

The CPFS laser geometry offers the highest gain per pump volume of any known laser geometry. Further, the higher circulating intensities in the gain medium mean that the population inversion is rapidly extracted leading to shorter duration pulses. The increased gain also allows for increased output coupler transmissions which lowers the intra-cavity intensity on critical components.

This relationship can be expressed mathematically using an equation that we derived during the development of the our Er:YAG CPFS Q-Switched laser system.[10] This relationship shows that the product of the energy of an actively Q-switched pulse and its duration is constant,

$$E \times \Delta t = \frac{8E_{photon}At_r}{B(f_1+f_2)\sigma}\frac{-ln(R)}{\delta - ln(R)} \tag{1}$$

where E_{photon} is the photon energy of the Er:YAG laser, A is the cross sectional area of the lasing mode, t_r is the round trip time of the resonator, σ is the cross section of the lasing transition, δ is the loss in the resonator and f_1 and f_2 are the Boltzmann factors for the lower lasing and upper lasing sub-levels respectively. B accounts for laser mode overlapping with itself within the gain medium which effects the laser light intensity that interacts with the population inversion. B has the following values: 1 for a non-zigzag ring resonator, 2 for a non-zigzag linear resonator, 2 for a zig-zag ring resonator and 4 for a zigzag linear resonator.

This relationship is important when assessing how to achieve short pulse durations when operating close to the damage threshold of optical materials. This demonstrates why lasers based on the CPFS geometry have an advantage in achieving short pulse durations. When compared to the non-folded geometries the CPFS slab allows for an increase of 2 of the B factor with a mild increase in the round trip cavity length. This allowed us to demonstrate a pulse duration of 14.5 ns with a pulse energy of 6 mJ. Further since optical damage prevented this energy of the pulse being increased it became necessary to explore other options for reducing the pulse duration of these pulses for higher spatial resolution time of flight measurements.

Cavity dumping is a modification of the well-established Q-Switching technique (see Stoneman et al.[11] for example). This technique has been shown to allow the generation of high peak power pulses at the cost of increased complexity and often lower efficiency. In this technique a Pockels cell and polarizer are used to form a variable reflectivity output coupler. Similar to Q-Switching the round trip cavity gain is held low during the pumping cycle by setting the transmission of the output coupler to 1. During the pulse formation stage the reflectivity of the output coupler is set to 1 allowing the fastest possible pulse formation time. When the desired peak power has been reached the transmission of the output coupler is minimized, releasing the stored light in one round trip or longer if the switching time of the Pockels cell is longer than a round trip. Cavity dumping has the advantage that circulating power inside the resonator need not be higher than of the lasing pulse that is ultimately produced.

We found that the timing of the Cavity Dump was critical. Peak power and efficiency are generally achieved when the cavity dump occurs when the circulating power is at its highest. However, in a damage threshold limited operating environment we found that we could achieve higher peak powers if we increased our pump rate and switched earlier. This is because this significantly reduced the build-up time of the pulse and the time that the energy spent in the resonator, thereby significantly reducing the risk of damage. Using this technique we were able to demonstrate pulses with a duration of 4.5 ns and pulse energy of 10 mJ resulting in a peak power of 2 MW which remains the highest peak power demonstrated from an nanosecond regime Er:YAG laser.[12]

3. CLOUD SENSING DEMONSTRATION

High-altitude thin clouds play an important role in radiative transfer processes in the Earths atmosphere,[13] so a knowledge of their variation in space and time is crucial in modern climate change studies.[14] Pulsed LIDAR systems offer a convenient method of profiling the atmosphere; however, these measurements are often limited by a lack of eye-safe laser sources capable of deep cloud probing.[15] By operating in the eye-safe 1.6μm wavelength band Er:YAG lasers enable a high-energy source capable of running in populated areas for continuous cloud sensing. Furthermore, the low atmospheric scattering coefficient at this wavelength[16] allows measurements which probe deeper into the atmosphere.

Using the Er:YAG laser described in Section 2 and the atmospheric sensing capabilities of our laboratory we performed time-of-flight measurements of overhead clouds. To ensure eye-safe operation the laser energy was reduced to 1.9mJ with a pulse duration of 95ns at a repetition rate of 1kHz. To sense the return pulses we used the detection system shown in Figure 2.

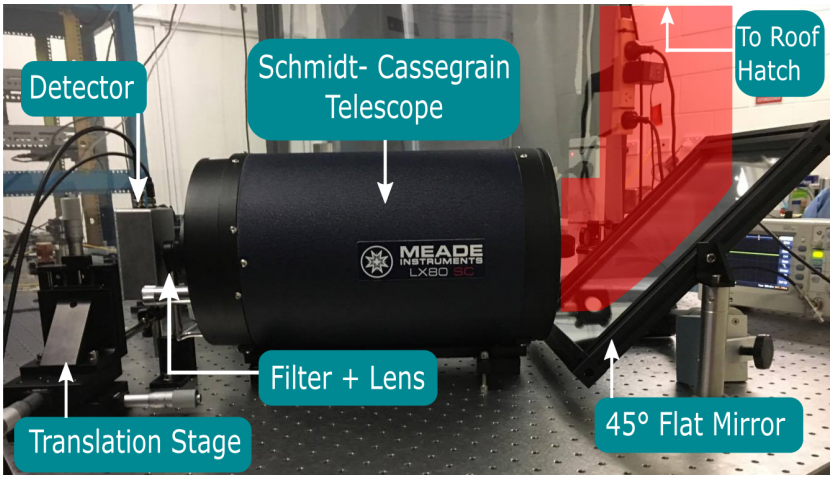

Figure 2: The detection system used in the cloud LIDAR tests highlighting the key components.

The laser source is sent vertically through a roof hatch using a 45° flat mirror, the scattered return light is then collected using a commercial Schmidt-Cassegrain telescope (Meade LX80). A custom 5MHz high-gain photodetector is placed at the back focal plane to measure the time-of-flight. Narrow-band filters are placed before this photodetector to remove any solar background radiation. A 16-bit 200MS/s ADC (GaGe Razor 16) is used to digitize the return signal, allowing long-term continuous cloud monitoring. An example of the return signals observed using this system is illustrated below in Figure 3.

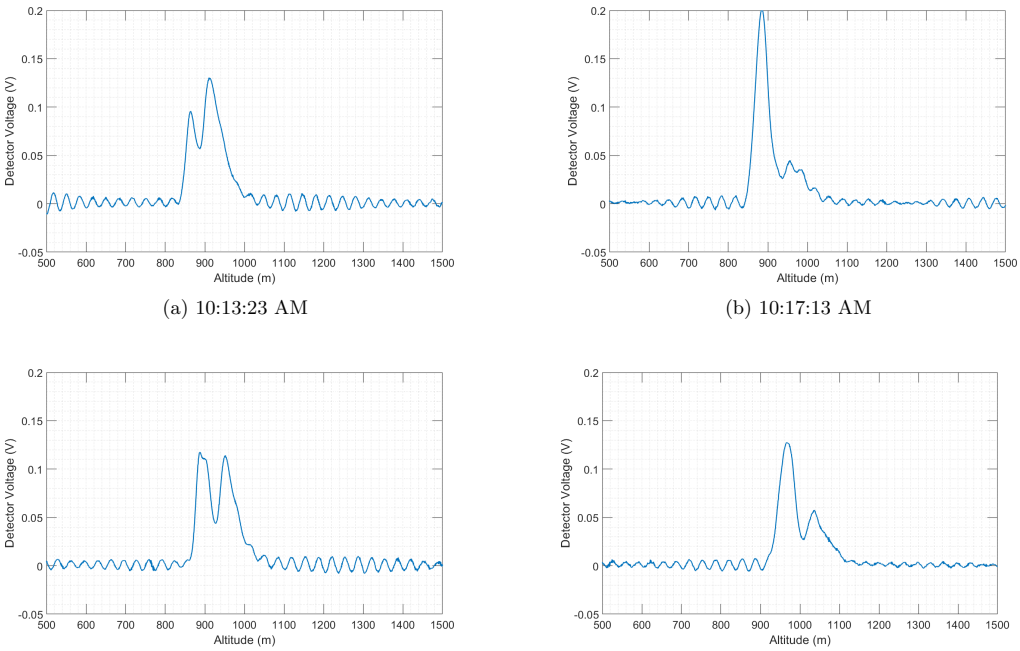

(a) 10:13:23 AM

(b) 10:17:13 AM

(c) 10:18:49 AM

(d) 10:27:52 AM

Figure 3: Example of return signals observed highlighting the multiple scattering events that are measured through the layers of the cloud

The results presented are averaged over a time of one second (corresponding to $N = 1000$ shots), allowing high signal-to-noise ratio measurements whilst not sacrificing temporal resolution. Clearly these traces highlight that we are capable of measuring multiple scattering events within a single cloud and hence resolve its multi-layered structure. This is critical in environmental modelling as a major source of uncertainty is the amount of cloud overlap in multi-layered cloud systems.[17] Experimental studies have shown that approximately half of all cloud systems are multi-layered.[18]

This ground based technology can be used to complement satellite based cloud LIDAR systems such as CALIPSO[19] which are able to resolve higher altitude cloud structure (10km) but with a significantly lower spatial resolution (>1km). This technology may enable a network of ground based cloud sensors capable of continual observations of multi-layered cloud structure in densely populated environments.

An example of the morning cloud structure measured over Adelaide, South Australia over a one hour period is illustrated in Figure 4. We observe a band of low-altitude clouds starting at 900m and rising to 1100m over the hour. It is possible that these low dense clouds may be obscuring higher altitude cloud structure.

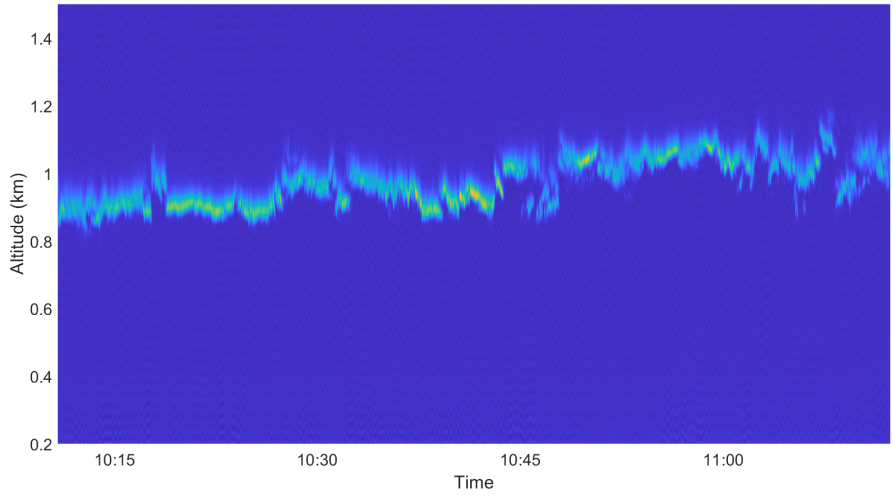

Figure 4: Cloud profile obtained by the near-IR LIDAR taken in the early morning

4. CONCLUSION

In this paper we described the development of Er:YAG lasers based on the Co-Planar Slab Geometry. These lasers were able to demonstrate very high peak power when operated in cavity dumped mode. We also described a new cloud lidar that makes use of these lasers to provide ultra high temporal resolution measurements of cloud structure.

ACKNOWLEDGMENTS

We acknowledge the support of the Australian Research Council (ARC) through grants LP110200734 and LP140100589. We also acknowledge the support of The South Australian Government, Aerometrex Pty Ltd and Venture Next.

REFERENCES

[1] Protection, A. R. et al., "ARPANSA-lasers and intense pulsed light (IPL) sources," (2011).

[2] Setzler, S. D., Francis, M. P., Young, Y. E., Konves, J. R., and Chicklis, E. P., "Resonantly pumped eyesafe erbium lasers," *IEEE Journal of Selected Topics in Quantum Electronics* **11**(3), 645–657 (2005).

[3] Riris, H., Numata, K., Li, S., Wu, S., Ramanathan, A., Dawsey, M., Mao, J., Kawa, R., and Abshire, J. B., "Airborne measurements of atmospheric methane column abundance using a pulsed integrated-path differential absorption lidar," *Applied optics* **51**(34), 8296–8305 (2012).

[4] Numata, K., Wu, S., and Riris, H., "Fast-switching methane lidar transmitter based on a seeded optical parametric oscillator," *Applied Physics B* **116**(4), 959–966 (2014).

[5] White, K. O. and Schleusener, S. A., "Coincidence of Er:YAG laser emission with methane absorption at 1645.1 nm," *Applied Physics Letters* **21**(9), 419–420 (1972).

[6] Kudryashov, I., Ter-Gabrielyan, N., and Dubinskii, M., "Resonantly diode-pumped Er:YAG laser: 1470-nm versus 1530-nm CW pumping case," in [*Laser Technology For Defense And Security V*], **7325**, 732505, International Society for Optics and Photonics (2009).

[7] Chang, N., Simakov, N., Hosken, D., Munch, J., Ottaway, D., and Veitch, P., "Resonantly diode-pumped continuous-wave and Q-switched *Er: YAG* laser at 1645 nm.," *Optics express* **18**(13), 13673–13678 (2010).

[8] Chang, N. W.-H., Hosken, D. J., Munch, J., Ottaway, D., and Veitch, P. J., "Stable, single frequency *Er:YAG* lasers at 1.6 μm," *IEEE Journal of Quantum Electronics* **46**(7), 1039–1042 (2010).

[9] Richards, J. and McInnes, A., "Versatile, efficient, diode-pumped miniature slab laser," *Optics letters* **20**(4), 371–373 (1995).

[10] Ottaway, D. J., Harris, L., and Veitch, P. J., "Short-pulse actively *Q*-switched *Er:YAG* lasers," *Optics express* **24**(14), 15341–15350 (2016).

[11] Stoneman, R. C., Hartman, R., Schneider, E. A., Garvin, C. G., and Henderson, S. W., "Eyesafe diffraction-limited single-frequency 1-ns pulsewidth *Er:YAG* laser transmitter," in [*Laser Source Technology for Defense and Security III*], **6552**, 65520H, International Society for Optics and Photonics (2007).

[12] Harris, L., Clark, M., Veitch, P., and Ottaway, D., "Compact cavity-dumped Q-switched *Er:YAG* laser," *Optics letters* **41**(18), 4309–4311 (2016).

[13] Hartmann, D. L., Holton, J. R., and Fu, Q., "The heat balance of the tropical tropopause, cirrus, and stratospheric dehydration," *Geophysical research letters* **28**(10), 1969–1972 (2001).

[14] Nakajima, T. and King, M. D., "Determination of the optical thickness and effective particle radius of clouds from reflected solar radiation measurements. part i: Theory," *Journal of the atmospheric sciences* **47**(15), 1878–1893 (1990).

[15] Spinhirne, J. D., "Micro pulse lidar," *IEEE Transactions on Geoscience and Remote Sensing* **31**(1), 48–55 (1993).

[16] Bucholtz, A., "Rayleigh-scattering calculations for the terrestrial atmosphere," *Applied Optics* **34**(15), 2765–2773 (1995).

[17] Charlock, T., Rose, F., Alberta, T., Smith, G., Rutan, D., Manalo-Smith, N., Minnis, P., and Wielicki, B., "Cloud profiling radar requirements: Perspective from retrievals of the surface and atmospheric radiation budget and studies of atmospheric energetics," *Appendix B in Utility and Feasibility of a Cloud Profiling Radar* , 46 (1994).

[18] Winker, D. M., "Cloud distribution statistics from lite," (1998).

[19] Winker, D. M., Pelon, J. R., and McCormick, M. P., "The calipso mission: Spaceborne lidar for observation of aerosols and clouds," in [*Lidar Remote Sensing for Industry and Environment Monitoring III*], **4893**, 1–12, International Society for Optics and Photonics (2003).

Appendix B

Slave Cavity ABCD Matrices

As a Gaussian beam propagates through an optical element both the radius ω and wavefront curvature R are modified - mathematically this is described by the ABCD matrix formalism [308]. This matrix formalisation will form the basis of a theoretical calculation of the slave laser cavity mode. To begin we introduce the complex beam parameter q, which describes a Gaussian beam at a position z along the Optical Axis (OA).

$$\frac{1}{q\left(z\right)} = \frac{1}{R\left(z\right)} - i\frac{\lambda}{\pi\omega^2\left(z\right)} \tag{B.1}$$

Optical elements which alter this Gaussian beam are uniquely defined by an ABCD matrix; a 2×2 matrix with a normalised determinant. This definition allows complex optical systems, such as our slave cavity, to be decomposed into a set of individual matrices which when concatenated describes the complete system. The complex beam parameter at the output (q_{out}) of this system can be calculated by operating on the input complex beam parameter (q_{in}) with the ABCD matrix.

$$q_{\text{out}} = \frac{Aq_{\text{in}} + B}{Cq_{\text{in}} + D} \tag{B.2}$$

For a stable optical resonator the Gaussian mode must be self-consistent after one round-trip (i.e. $q_{\text{in}} = q_{\text{out}}$), imposing this restriction on equation B.2 gives equation B.3. This is only a valid solution if the square-root term is real, this restriction is commonly referred to as the half-trace inequality [309] and is crucial in the design of stable optical resonators.

$$\frac{1}{q} = \frac{D - A}{2B} + \frac{i}{2B}\sqrt{4 - \left(A + D\right)^2} \tag{B.3}$$

Solving this expression gives the complex beam parameter at the start of the resonator q_0 and both the waist size ω_0 and position z_0 can be calculated. By propagating this initial value through the individual components within the resonator the mode

profile can be mapped out. This method was applied to the slave resonator and the fundamental mode is plotted in Figure B.1. Due to the astigmatic nature of the fundamental mode the horizontal and vertical eigen-modes are plotted separately.

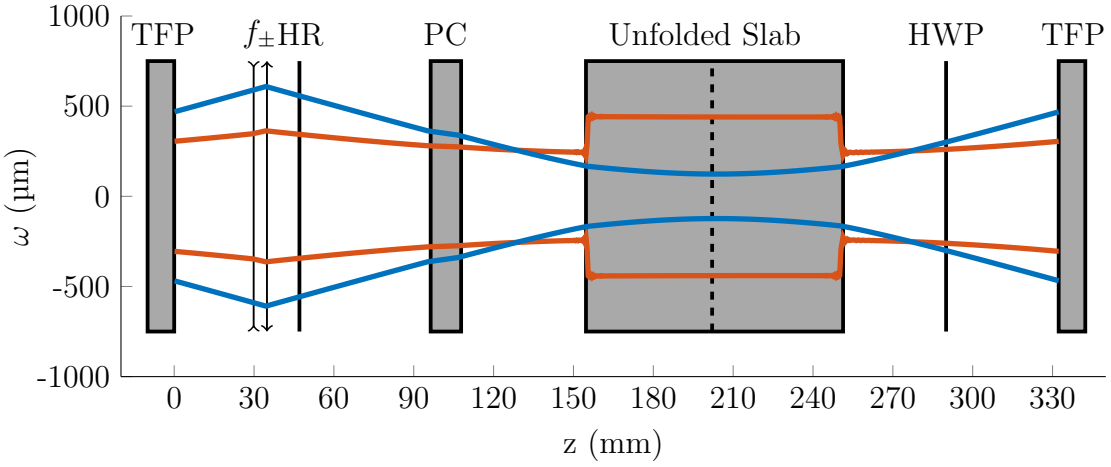

Figure B.1: The unfolded slave cavity resonator, highlighting the solved horizontal and vertical eigen-modes where $f_+ = 100\,\text{mm}$ and $f_- = -200\,\text{mm}$ in the horizontal plane. Note that the TFP appears twice as it is used as the starting position for this simulation.

The telescopic arrangement of the lenses is used to adjust the mode size within the slab so that it best overlaps with the pumped region. Clearly, the negative cylindrical lens acts to expand the horizontal mode whilst still clearing the hard-edge aperture at the entrance and exit faces of the CPFS gain medium. This mode-size is used in the numerical model presented in Chapter 3.

Appendix C

Jones Calculus

The polarisation state of a monochromatic plane wave can be described by a 2 x 1 vector known as the Jones vector, mathematically this is given by

$$\vec{E} = \begin{pmatrix} E_{0x}e^{i\phi_x} \\ E_{0y}e^{i\phi_y} \end{pmatrix} \tag{C.1}$$

where the first term represents the horizontally polarised (π) component and the second term represents the vertically polarised (σ) component. Optical elements which alter the polarisation state of this light are described by a 2 x 2 matrix known as the Jones matrix. The change in polarisation as it propagates through this element is calculated via operating on the Jones vector with the Jones matrix. This matrix formalisation of polarisation, known as Jones calculus [310], will form the basis of a theoretical calculation of the slave laser output coupling. A schematic of the polarisation states of the counter-clockwise slave laser mode is illustrated in Figure C.1.

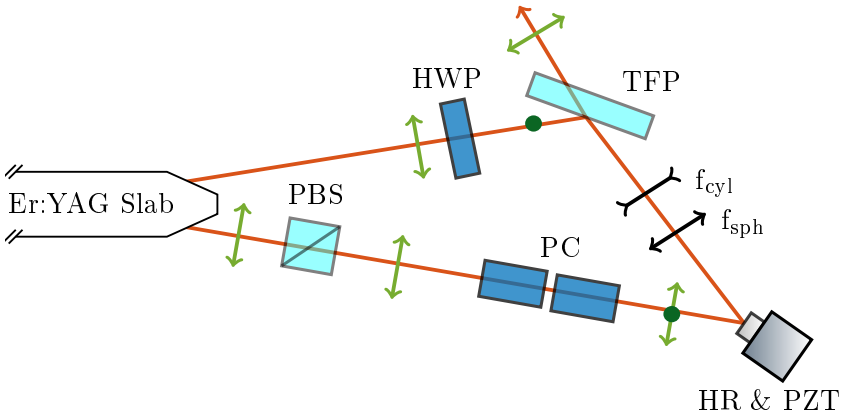

Figure C.1: Schematic of the slave laser mode highlighting the horizontal and vertical polarisation states

The laser mode following the Polarising Beam Splitter (PBS) is purely π polarised, applying a voltage to the Pockels Cell (PC) then rotates the polarisation of the light

that is incident on the Thin-Film Polariser (TFP), thus providing a means of dynamically tuning the output coupling. This is described by the following Jones matrix calculation.

$$\vec{E_{out}} = J_{PC}\vec{E_{in}} \tag{C.2}$$

Where $\vec{E_{in}}$ is the Jones vector of the π polarised light incident on the PC, J_{PC} is the Jones matrix of the PC and $\vec{E_{out}}$ is the Jones vector of the light incident on the TFP. The fraction of this vector that is π polarised is used to calculate the effective output coupling.

The Jones matrix of the PC is calculated by first considering the Jones matrix of a linear phase retarder with phase retardation δ.

$$J_r(\delta) = \begin{pmatrix} e^{-j\delta/2} & 0 \\ 0 & e^{-j\delta/2} \end{pmatrix} \tag{C.3}$$

In general, the PC is axially rotated relative to the optical axis at angle θ. This is accounted for by applying the rotation matrix

$$R(\theta) = \begin{pmatrix} \cos(\theta) & \sin(\theta) \\ -\sin(\theta) & \cos(\theta) \end{pmatrix} \tag{C.4}$$

to the Jones matrix for a linear phase retarder, giving the following Jones matrix.

$$\begin{aligned} J_{pc} &= R(-\theta)J_r(\delta)R(\theta) \\ &= \begin{pmatrix} \cos(\delta/2) + j\cos(2\theta)\sin(\delta/2) & j\sin(2\theta)\sin(\delta/2) \\ j\sin(2\theta)\sin(\delta/2) & \cos(\delta/2) - j\cos(2\theta)\sin(\delta/2) \end{pmatrix} \end{aligned} \tag{C.5}$$

The phase retardation δ through the electro-optic crystal of length l_{pc} is related to the voltage applied V by the following expression.

$$\delta = \frac{2\pi l_{pc} n_0^3 r V}{\lambda d_{pc}} \tag{C.6}$$

Where d_{pc} is the electrode separation, n_0 is the nominal refractive index, r is the electro-optic coefficient and λ is the incident wavelength. Our system uses a PC made from Rubidium Titanyl Phosphate (RTP) manufactured by Raicol Crystals. This has a matched pair of 5 mm long crystals axially rotated by 45° with an electrode separation of 4 mm. RTP has a nominal refractive index of $n_0 = 1.57$ at $\lambda = 1645$ nm and the electro-optic coefficient is $r_{c2} = 23.6$ pm/V [311].

Appendix D

The Pound-Drever-Hall Technique

The Pound-Drever-Hall (PDH) technique is a powerful tool for stabilising the frequency of an existing laser - since it was first described in 1983, this technique has become ubiquitous in many applied fields where a narrow-linewidth source is required including gravitational wave interferometry [312] and quantum optics [313].

Consider a laser source with natural frequency jitter, we require an accurate means of measuring this jitter to correct for it. A convenient means to discriminate frequency changes is by monitoring the transmission (or reflection) of the beam as it propagates through a Fabry-Perot cavity. The intensity at the reflected output is given by [314]

$$I_R(\omega) = \frac{\left(\sqrt{R_1} - \sqrt{R_2}\omega\right)^2 + 4\sqrt{R_1 R_2}\omega \sin^2(kL)}{\left(1 - \sqrt{R_1 R_2}\omega\right)^2 + 4\sqrt{R_1 R_2}\omega \sin^2(kL)} \tag{D.1}$$

where R_i is the reflectivity of output port i and ν describes the round-trip cavity loss. If the frequency of the light is scanned the resonator output will show sharp resonance features as plotted in Figure D.1.

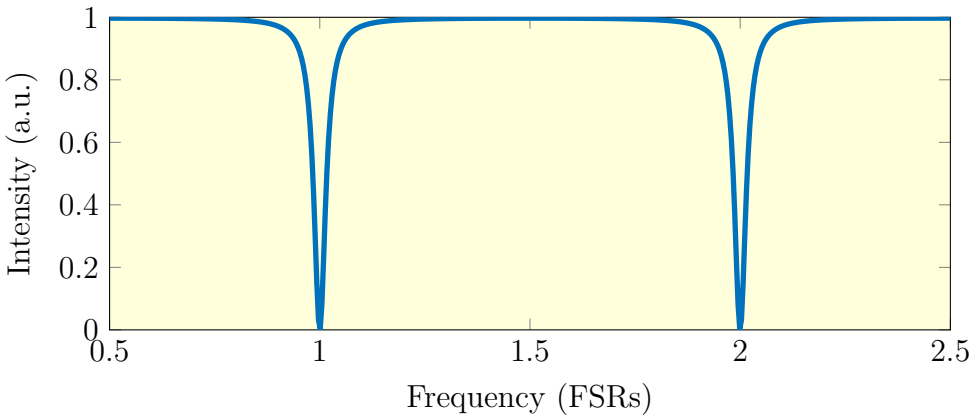

Figure D.1: Predicted reflection of a lossless Fabry-Perot cavity as the frequency is swept for $R_1 = R_2 = 90\%$

These resonant frequencies have a resonance width denoted Δ_s and are separated by a Free Spectral Range (FSR) denoted Δ_ν, for a cavity of length L this is given by.

$$\Delta_\nu = \frac{c}{2L} \tag{D.2}$$

Using these fundamental properties of the Fabry-Perot cavity we can generate the reflection coefficient $F(\omega)$, which is the ratio of the reflected and incident electric field, for a symmetric lossless cavity this is given by [315].

$$F(\omega) = \frac{E_{\text{ref}}}{E_{\text{inc}}} = \frac{R\left(\exp\left(\frac{i\omega}{\Delta_\nu}\right) - 1\right)}{1 - R^2\exp\left(\frac{i\omega}{\Delta_\nu}\right)} \tag{D.3}$$

This is plotted in Figure D.2.

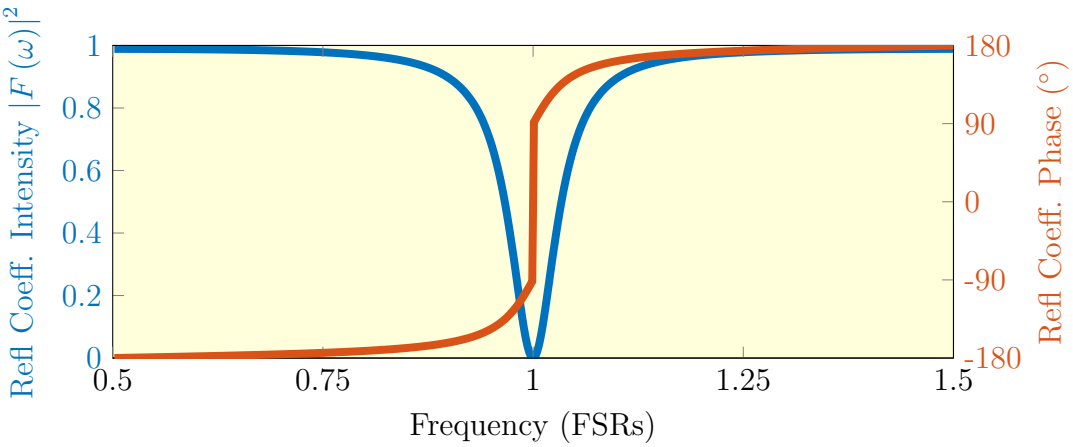

Figure D.2: Fabry-Perot cavity predicted reflection coefficient; magnitude and phase for $R = 90\%$

Clearly the reflected optical intensity is symmetric about resonance, an effective control system cannot be designed to stay at this minima as the Fabry-Perot cannot discriminate what side of resonance the laser is positioned on. Instead, we must rely on the asymmetric phase of this feature, the key to the Pound-Drever-Hall technique is that it provides a means of indirectly measuring this phase. This is achieved by modulating the laser frequency (or alternatively phase) at frequency Ω to generate sidebands with a defined phase relationship to the carrier frequency ω. Mathematically, the incident electric field is given by

$$\begin{aligned} E_{\text{inc}} &= E_0 e^{i(\omega t + \beta \sin\Omega t)} \\ &\approx E_0\left[e^{i\omega t} + (\beta/2)\left(e^{i(\omega+\Omega)t} - e^{i(\omega-\Omega)t}\right)\right] \end{aligned} \tag{D.4}$$

where β is the modulation depth, this is typically set such that the power is contained

within the carrier and first order sidebands. To calculate the reflected field we can scale each term independently by the reflection coefficient at the corresponding frequency.

$$E_{\text{ref}} = E_0 \left[F(\omega)\, e^{i\omega t} + (\beta/2) \left(F(\omega+\Omega)\, e^{i(\omega+\Omega)t} - F(\omega-\Omega)\, e^{i(\omega-\Omega)t} \right) \right] \tag{D.5}$$

We are interested in the power of the reflected beam, since that is the quantity ultimately measured with a photodetector. This is given by $P_{\text{ref}} = |E_{\text{ref}}|^2$,

$$\begin{aligned} P_{\text{ref}} =& P_0 |F(\omega)|^2 + P_0 \frac{\beta^2}{4} \left[|F(\omega+\Omega)|^2 + |F(\omega-\Omega)|^2 \right] \\ &+ P_0 \beta \left[\text{Re}\{Y(\omega)\} \cos(\Omega t) + \text{Im}\{Y(\omega)\} \sin(\Omega t) \right] + \mathcal{O}(\Omega^2) \end{aligned} \tag{D.6}$$

where we have introduced the following term for simplicity.

$$Y(\omega) = F(\omega)\, F^*(\omega+\Omega) - F^*(\omega)\, F(\omega-\Omega) \tag{D.7}$$

We are interested in the two sinusoidal terms that are dependent on the modulation frequency Ω because they contain the phase information. By setting the modulation frequency Ω to be sufficiently large, it is clear from Figure D.2 that the sidebands will experience a $\pm 180°$ phase shift relative to the carrier frequency and as such the real component of $Y(\omega)$ is zero, leaving only the term proportional to $\sin(\Omega t)$ in equation D.6. By demodulating the electrical signal, an error signal of the following form is generated.

$$\epsilon \propto \text{Im}\{F(\omega)\, F^*(\omega+\Omega) - F^*(\omega)\, F(\omega-\Omega)\} \tag{D.8}$$

This is plotted in Figure D.3.

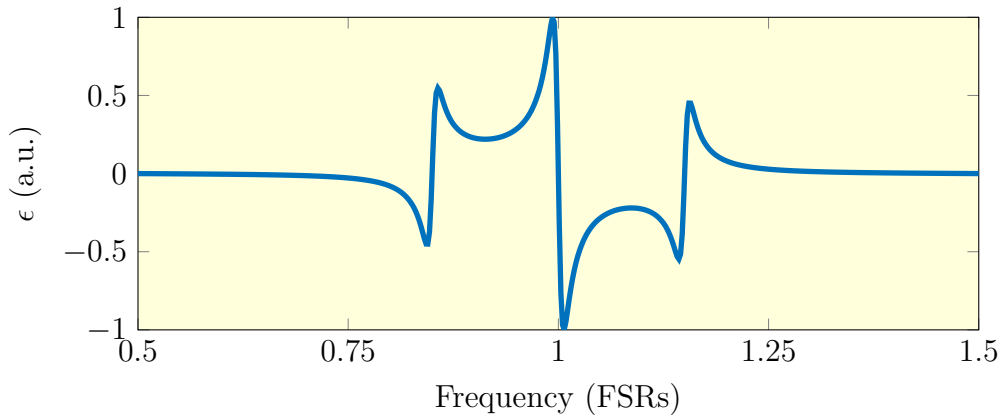

Figure D.3: Predicted Pound-Drever-Hall error signal for a symmetrical Fabry-Perot cavity with $R = 98\%$ and $\Omega > \Delta\nu$

An effective feedback system can be designed to operate in the asymmetric steep linear region in the centre of this error signal. Experimentally this is commonly achieved using the system illustrated in Figure D.4.

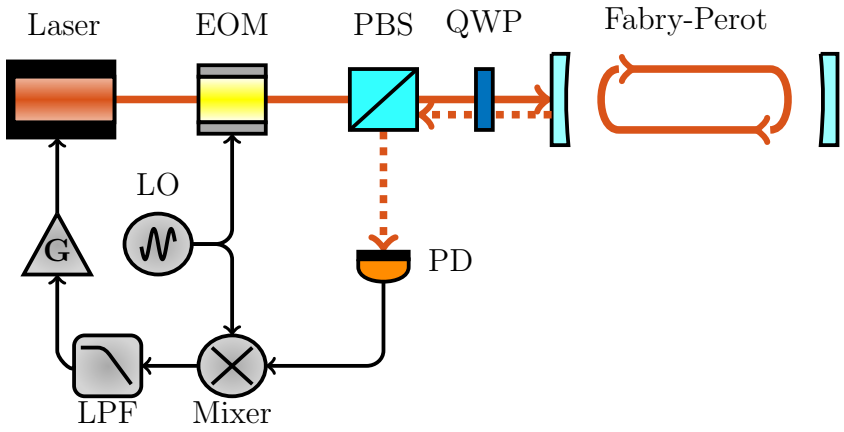

Figure D.4: The Pound-Drever-Hall locking schematic - a local oscillator (LO) imposes high-frequency side-bands on a laser through an electro-optic modulator (EOM). A polarising beam splitter (PBS) and quarter-wave plate (QWP) form a free-space isolator, allowing the Fabry-Perot reflection to be monitored on a photodiode (PD). The corresponding electrical signal is demodulated using a mixer and a low-pass filter (LPF) and is fedback to the laser through a gain stage.

Appendix E

TIA Design Considerations

The layout of a Printed Circuit Board (PCB) for high speed applications is a critical step in ensuring the circuit meets design requirements. The choice of physical characteristics such as track spacing, track width, component packaging, etc. can affect the integrity of the signal. There is a range of publicly available design guides that describe the techniques used to overcome these physical limitations, however, these guides are often conflicting and the techniques described can change on a case-by-case basis. Even key textbooks in the field refer to the art of PCB design as a 'black magic' [316] [317]. In this Appendix I will condense some of the key design techniques discussed by *Analog Dialogue* [318] and *Texas Instruments* [319] that were used in the design of the TIA illustrated in Figure E.1.

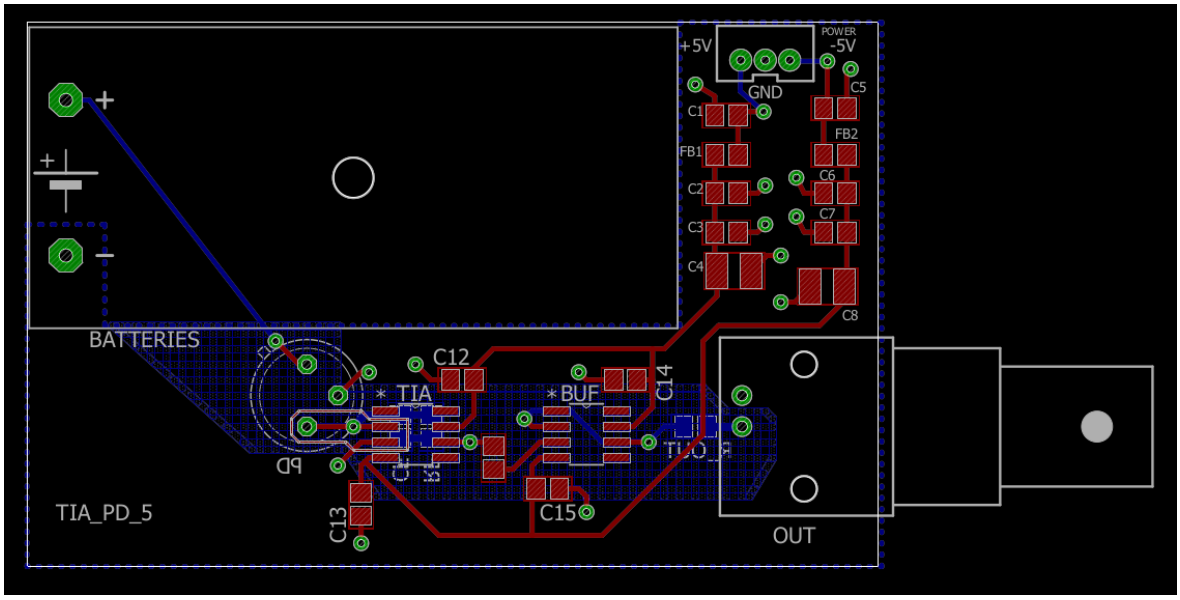

Figure E.1: Printed circuit board layout of the transimpedance amplifier.

In this board the top layer components and tracks are drawn in red whilst the bottom layer components and tracks are drawn in blue. Vias, drawn in green, allow routing of signals between board layers. Despite their convenience it is important to

limit the use of them where possible, particularly in sensitive board areas, as they have an inherent capacitance and inductance that can introduce parasitic affects. The dashed blue line surrounding the board edge shows the ground plane, by keeping this unbroken it ensures all components see a common ground and removes the issue of ground loops. This ground plane is removed from the sensitive feedback path (as signified by the blue hatching) as it can introduce stray capacitance.

It is necessary to pay special care when positioning the sensitive path that takes the photocurrent to the inverting input of the operational amplifier. Here the track length is kept as short as possible, with the feedback path routed underneath the op-amp to minimise parasitic capacitance and inductance. Furthermore, a guard ring tied to the non-inverting op-amp input surrounds the inverting input. This acts to absorb leakage current from other points on the board, significantly reducing the chance of it reaching the sensitive input path. A unity gain buffer formed with the OPA820 amplifier is placed at the output stage to isolate the sensitive feedback path from the output.

To ensure high-frequency voltage noise from the power supply does not dominate the output voltage noise a pi-filter formed using a ferrite bead and capacitors is applied. The ferrite bead (TDK MMZ2012Y152BT000) is a passive element that has resistive, inductive and capacitive properties; these are typically used in power supply filters as they are compact and can ensure there are no anti-resonance peaks in the frequency response [320]. The capacitors are staggered to overcome their equivalent series inductance (ESL) which ultimately can limit their effectiveness at high frequencies [321]. The predicted transfer function, plotted in Figure E.2, illustrates a filter with high insertion loss and no anti-resonance peaking.

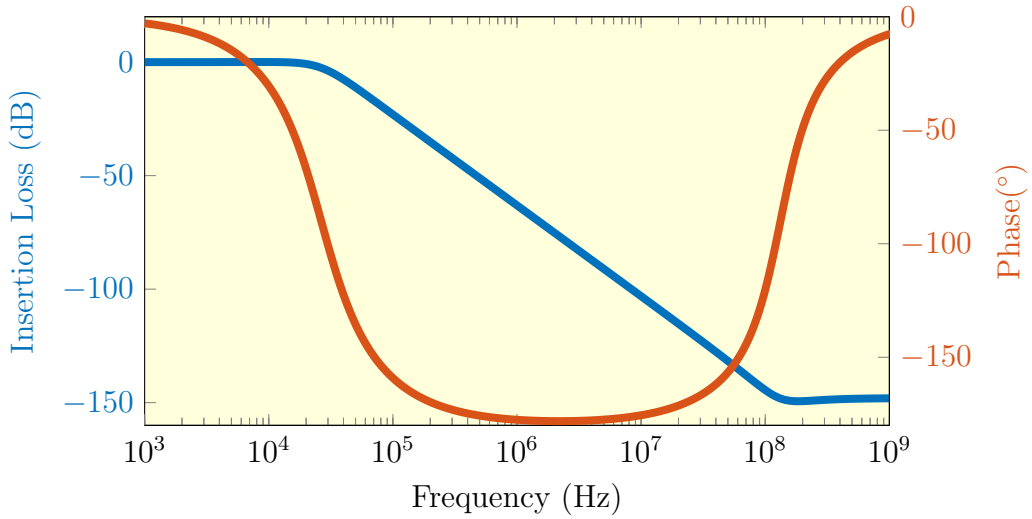

Figure E.2: Predicted transfer function of the pi-filter used in the TIA circuit to filter power supply noise from the operational amplifiers.

Appendix F

The Matched Filter

Matched filtering is a signal processing technique used to maximise the Signal-to-Noise Ratio (SNR) in the presence of additive white noise. A rigorous introduction to the theory of matched filtering is not necessary for this application, instead a simplified version of the theory presented by George Turin [264] will be introduced. Consider receiving a waveform $x(t)$ which consists of the signal of interest $s(t)$ plus an additive white noise $n(t)$ with a power density $N_0/2$, we can write.

$$x(t) = s(t) + n(t) \tag{F.1}$$

Operating on this waveform with a linear filter produces an output $y(t)$ which consists of a component due to the noise $y_n(t)$ and a component due to the signal $y_s(t)$. We wish to find which filter will maximise the output when $s(t)$ is present, to quantify this we require the instantaneous power in $y_s(t)$ to be maximum in comparison to the average power in $n(t)$. If $Y(j\omega)$ is the transfer function of the filter then the output noise power is.

$$P_n = \frac{N_0}{2} \int_{-\infty}^{\infty} |Y(j\omega)|^2 \, d\omega \tag{F.2}$$

Similarly, if $S(j\omega)$ is the output signal spectrum then the instantaneous power evaluated at time $t = t_0$ is.

$$P_s = \left[\int_{-\infty}^{\infty} S(j\omega) Y(j\omega) e^{j\omega t_0} d\omega \right]^2 \tag{F.3}$$

We wish to maximise the ratio of equation F.3 to equation F.2, our signal to noise ratio.

$$SNR_{\text{mf}} = \frac{2 \left[\int_{-\infty}^{\infty} S(j\omega) Y(j\omega) e^{j\omega t_0} d\omega \right]^2}{N_0 \int_{-\infty}^{\infty} |Y(j\omega)|^2 \, d\omega} \tag{F.4}$$

The numerator can be simplified by recognising $Y(j\omega)$ and $S(j\omega)e^{j\omega t_0}$ can be substituted for $f(x)$ and $g(x)$ into the Schwarz inequality.

$$\left| \int f(x)g(x)dx \right|^2 \leq \int |f(x)|^2 \, dx \int |g(x)|^2 \, dx \tag{F.5}$$

By inspection, the equality in this expression holds when $f(x) = kg^*(x)$, so equation F.4 is maximised when.

$$Y(j\omega) = kS^*(j\omega)e^{-j\omega t_0} \tag{F.6}$$

Applying the inverse Fourier transform we can find the form for the optimum filter in the time domain.

$$y(t) = ks(t_0 - t) \tag{F.7}$$

Hence, the optimum filter template is the time-reversed signal of interest with a time shift t_0 and scaling factor k. The matched filter is applied through multiplication in the frequency domain, or alternatively, via a convolution in the time domain. The effectiveness of matched filtering can be visualised clearly be generating an arbitrary Gaussian pulse with additive white noise and applying a convolution with the noiseless Gaussian, as plotted in Figure F.1.

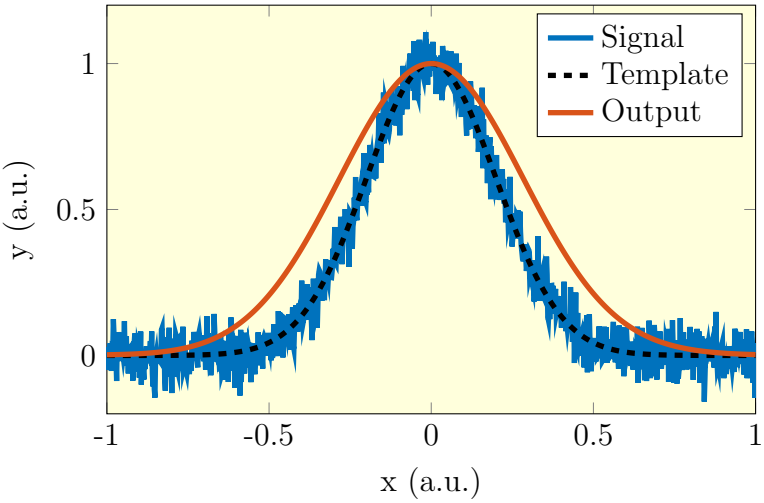

Figure F.1: The effect of a matched filter on a synthesised Gaussian pulse with white noise.

Appendix G

IPDA LIDAR Analysis for Non-Negligible Offline Absorption

For an Integrated Path Differential Absorption (IPDA) LIDAR system the offline wavelength should be carefully chosen to avoid absorption from the gas species probed by the online wavelength. However, limitations in the laser transmitter may cause the offline wavelength to be positioned on the 'tail' of the absorption line, leading to a systematic offset in the measured concentration. In this Appendix we derive the mathematical correction used to adjust for non-negligible offline absorption.

The total transmittance through the atmospheric column at the online and offline wavelengths are given by:

$$\mathrm{T_{total,on}} = \mathrm{T_{transmit,on}} \mathrm{T_{gas,on}} \tag{G.1}$$

$$\mathrm{T_{total,off}} = \mathrm{T_{transmit,off}} \mathrm{T_{gas,off}} \tag{G.2}$$

where $\mathrm{T_{gas,on}}$ and $\mathrm{T_{gas,off}}$ are the transmittance through the gas species at the online and offline wavelengths respectively. Whilst $\mathrm{T_{transmit,on}}$ and $\mathrm{T_{transmit,off}}$ describe all other losses at the online and offline wavelengths respectively.

Thus, the observed transmittance is given by:

$$\begin{aligned} \mathrm{T_{obs}} &= \mathrm{T_{total,on}} / \mathrm{T_{total,off}} \\ &= \mathrm{T_{gas,on}} / \mathrm{T_{gas,off}} \end{aligned} \tag{G.3}$$

where it has been assumed that the separation between the online and offline wavelengths is small enough that $\mathrm{T_{transmit,on}} = \mathrm{T_{transmit,off}}$. Equation G.3 can be written in terms of the on/off absorption cross-sections ($\sigma_{\mathrm{on/off}}$) the gas concentration (N) and the path length L.

$$\begin{aligned} \mathrm{T_{obs}} &= \mathrm{e}^{\sigma_{\mathrm{on}}\mathrm{NL}}/\mathrm{e}^{\sigma_{\mathrm{off}}\mathrm{NL}} \\ &= \mathrm{e}^{-(\sigma_{\mathrm{on}}-\sigma_{\mathrm{off}})\mathrm{NL}} \end{aligned}$$

Which we rearrange to calculate the column integrated gas concentration:

$$\mathrm{NL} = \frac{-\ln\left(\mathrm{T_{obs}}\right)}{(\sigma_{\mathrm{on}} - \sigma_{\mathrm{off}})} \tag{G.4}$$

Thus, the online transmittance can be written in terms of the observed transmittance and offline transmittance:

$$\begin{aligned} \mathrm{T_{on}} &= \mathrm{T_{obs}}\mathrm{T_{off}} \\ &= \mathrm{T_{obs}}\mathrm{e}^{\sigma_{\mathrm{off}}\mathrm{NL}} \end{aligned}$$

Substituting Equation G.4 yields:

$$\begin{aligned} \ln\left(\mathrm{T_{on}}\right) &= \ln\left(\mathrm{T_{obs}}\right) - \sigma_{\mathrm{off}}\left[\frac{\ln\left(\mathrm{T_{obs}}\right)}{\sigma_{\mathrm{on}} - \sigma_{\mathrm{off}}}\right] \\ &= \ln\left(\mathrm{T_{obs}}\right)\left[1 + \frac{\sigma_{\mathrm{off}}}{\sigma_{\mathrm{on}} - \sigma_{\mathrm{off}}}\right] \\ &= \ln\left(\mathrm{T_{obs}}\right)\left[\frac{\sigma_{\mathrm{on}}}{\sigma_{\mathrm{on}} - \sigma_{\mathrm{off}}}\right] \\ &= \ln\left(\mathrm{T_{obs}}\right)\left[\frac{1}{1 - \sigma_{\mathrm{off}}/\sigma_{\mathrm{on}}}\right] \end{aligned} \tag{G.5}$$

In the limit where $\sigma_{\mathrm{off}} \ll \sigma_{\mathrm{on}}$ it is clear that the online transmittance will be equal to the observed transmittance, as expected. We apply Equation G.5 to adjust for absorption at the offline wavelength.

Appendix H

The Geometric Form Factor

The Geometric Form Factor (GFF) describes the overlap between the laser beam's optical intensity distribution and the receiver's active detection Field-of-View (FOV) at range R. The analytical expressions of the GFF described by Hao *et al.* [322] are introduced in this Appendix. The parameters used in this calculation are illustrated in Figure H.1.

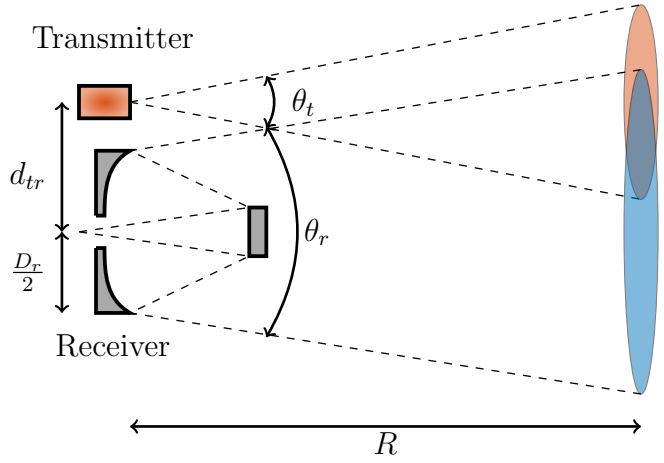

Figure H.1: Key optical parameters of the transmitter and receiver used in the calculation of the geometric form factor.

A laser transmitter with full-angle divergence θ_t forms a spot at range R. This is imaged by a receiver with full-angle divergence θ_r, diameter D_r, focal length f_r to an aperture with a diameter ϕ. We define the image at the focal plane to have a diameter $e(R)$ which is given by.

$$e(R) = f_r \left[\theta_l + \frac{D_r}{R}\right] \tag{H.1}$$

This illustrated configuration is referred to as a biaxial system, in which the transmitter and receiver are separated by distance d_{tr}. In this Appendix we also consider the coaxial case in which $d_{tr} = 0$.

Biaxial LIDAR Configuration

First we define the distance between the image spot centre and telescope aperture centre, this is given by.

$$\nu(R) = \frac{f_r d_{tr}}{R} \tag{H.2}$$

The geometric form factor takes a different value depending on the relative position of these two spots, this is described by the following analytical function.

$$G(R) = \begin{cases} 0 & \text{if } \nu(R) > \frac{\phi + e(R)}{2}; \\ \dfrac{[\psi_1(R) - \sin(\psi_1(R))]\,\phi^2 + [\psi_2(R) - \sin(\psi_2(R))]\,e^2(R)}{2\pi e^2(R)} & \text{if } \nu(R) > \dfrac{|\phi - e(R)|}{2} \\ & \quad \& \ \nu(R) < \dfrac{\phi + e(R)}{2}; \\ \dfrac{\phi^2}{e^2(R)} & \text{if } \nu(R) < \dfrac{e(R) - \phi}{2} \\ & \quad \& \ e(R) > \phi; \\ 1 & \text{if } \nu(R) < \dfrac{e(R) - \phi}{2} \\ & \quad \& \ e(R) \leq \phi; \end{cases} \tag{H.3}$$

Where the following two terms have been introduced for simplicity.

$$\psi_1(R) = 2\arccos\left[\frac{\phi^2 + 4\nu^2(R) - e^2(R)}{4\nu(R)\phi}\right] \tag{H.4}$$

$$\psi_2(R) = 2\arccos\left[\frac{e^2(R) + 4\nu^2(R) - \phi^2}{4\nu(R)e(R)}\right] \tag{H.5}$$

Coaxial LIDAR Configuration

The calculation of the geometric form factor for a coaxial system is significantly simpler, it is given by the following analytical function.

$$G(R) = \begin{cases} \dfrac{\phi^2}{e^2(R)} & \text{if } e(R) > \phi; \\ 1 & \text{otherwise;} \end{cases} \tag{H.6}$$

Bibliography

[1] J Hansen, Mki Sato, and R Ruedy. Radiative forcing and climate response. *Journal of Geophysical Research: Atmospheres*, 102(D6):6831–6864, 1997.

[2] Jos Lelieveld and Paul J Crutzen. Indirect chemical effects of methane on climate warming. *Nature*, 355(6358):339–342, 1992.

[3] Piers Forster, Venkatachalam Ramaswamy, Paulo Artaxo, Terje Berntsen, Richard Betts, David W Fahey, James Haywood, Judith Lean, David C Lowe, Gunnar Myhre, et al. Changes in atmospheric constituents and in radiative forcing. chapter 2. In *Climate Change 2007. The Physical Science Basis*. 2007.

[4] C MacFarling Meure, D Etheridge, C Trudinger, P Steele, R Langenfelds, T Van Ommen, A Smith, and J Elkins. Law dome CO2, CH4 and N2O ice core records extended to 2000 years BP. *Geophysical Research Letters*, 33(14), 2006.

[5] Ed Dlugokencky. *NOAA/ESRL*. `www.esrl.noaa.gov/gmd/ccgg/trends_ch4/`.

[6] Jean-Robert Petit, Jean Jouzel, Dominique Raynaud, Narcisse I Barkov, J-M Barnola, Isabelle Basile, Michael Bender, J Chappellaz, M Davis, G Delaygue, et al. Climate and atmospheric history of the past 420,000 years from the Vostok ice core, Antarctica. *Nature*, 399(6735):429, 1999.

[7] Jonathan A Patz, Diarmid Campbell-Lendrum, Tracey Holloway, and Jonathan A Foley. Impact of regional climate change on human health. *Nature*, 438(7066):310, 2005.

[8] David B Lobell, Marshall B Burke, Claudia Tebaldi, Michael D Mastrandrea, Walter P Falcon, and Rosamond L Naylor. Prioritizing climate change adaptation needs for food security in 2030. *Science*, 319(5863):607–610, 2008.

[9] Robert McLeman and Barry Smit. Migration as an adaptation to climate change. *Climatic change*, 76(1-2):31–53, 2006.

[10] Joel E Cohen, Christopher Small, Andrew Mellinger, John Gallup, and Jeffrey Sachs. Estimates of coastal populations. *Science*, 278(5341):1209–1213, 1997.

[11] Nathan P Myhrvold and Ken Caldeira. Greenhouse gases, climate change and the transition from coal to low-carbon electricity. *Environmental Research Letters*, 7(1):014019, 2012.

[12] Stabilization Wedges. Solving the climate problem for the next 50 years with current technologies pacala, s.; socolow, r. *Science (Washington, DC, United States)*, 305(5686):968–972, 2004.

[13] Aranya Venkatesh, Paulina Jaramillo, W Michael Griffin, and H Scott Matthews. Uncertainty in life cycle greenhouse gas emissions from united states natural gas end-uses and its effects on policy. *Environmental science & technology*, 45(19):8182–8189, 2011.

[14] April EPA. Inventory of us greenhouse gas emissions and sinks: 1990-2009. *Environmental Protection Agency2012*, 2011.

[15] Ramón A Alvarez, Stephen W Pacala, James J Winebrake, William L Chameides, and Steven P Hamburg. Greater focus needed on methane leakage from natural gas infrastructure. *Proceedings of the National Academy of Sciences*, 109(17):6435–6440, 2012.

[16] Robert W Howarth, Renee Santoro, and Anthony Ingraffea. Methane and the greenhouse-gas footprint of natural gas from shale formations. *Climatic change*, 106(4):679, 2011.

[17] U.S. Energy Information Administration. *EIA*. `https://www.eia.gov/state/maps.php`.

[18] S Basu and PK Basu. Nanocrystalline metal oxides for methane sensors: role of noble metals. *Journal of Sensors*, 2009, 2009.

[19] Yijiang Lu, Jing Li, Jie Han, H-T Ng, Christie Binder, Christina Partridge, and M Meyyappan. Room temperature methane detection using palladium loaded single-walled carbon nanotube sensors. *Chemical Physics Letters*, 391(4-6):344–348, 2004.

[20] V Zeninari, B Parvitte, D Courtois, VA Kapitanov, and Yu N Ponomarev. Methane detection on the sub-ppm level with a near-infrared diode laser photoacoustic sensor. *Infrared physics & technology*, 44(4):253–261, 2003.

[21] Xiao Liu, Sitian Cheng, Hong Liu, Sha Hu, Daqiang Zhang, and Huansheng Ning. A survey on gas sensing technology. *Sensors*, 12(7):9635–9665, 2012.

[22] Byard W Mosher, Peter M Czepiel, Robert C Harriss, Joanne H Shorter, Charles E Kolb, J Barry McManus, Eugene Allwine, and Brian K Lamb. Methane emissions at nine landfill sites in the northeastern united states. *Environmental science & technology*, 33(12):2088–2094, 1999.

[23] Gunnar BÖrjesson, Åsa Danielsson, and Bo H Svensson. Methane fluxes from a swedish landfill determined by geostatistical treatment of static chamber measurements. *Environmental Science & Technology*, 34(18):4044–4050, 2000.

[24] PM Czepiel, JH Shorter, B Mosher, E Allwine, JB McManus, RC Harriss, CE Kolb, and BK Lamb. The influence of atmospheric pressure on landfill methane emissions. *Waste Management*, 23(7):593–598, 2003.

[25] A Tregoures, A Beneito, P Berne, MA Gonze, JC Sabroux, D Savanne, Z Pokryszka, C Tauziede, P Cellier, P Laville, et al. Comparison of seven methods for measuring methane flux at a municipal solid waste landfill site. *Waste Management & Research*, 17(6):453–458, 1999.

[26] PM Czepiel, B Mosher, RC Harriss, JH Shorter, JB McManus, CE Kolb, E Allwine, and BK Lamb. Landfill methane emissions measured by enclosure and atmospheric tracer methods. *Journal of Geophysical Research: Atmospheres*, 101(D11):16711–16719, 1996.

[27] J Bogner, M Meadows, and P Czepiel. Fluxes of methane between landfills and the atmosphere: natural and engineered controls. *Soil Use and Management*, 13(s4):268–277, 1997.

[28] Jacob Mønster, Jerker Samuelsson, Peter Kjeldsen, and Charlotte Scheutz. Quantification of methane emissions from 15 danish landfills using the mobile tracer dispersion method. *Waste Management*, 35:177–186, 2015.

[29] Tara I Yacovitch, Scott C Herndon, Gabrielle Petron, Jonathan Kofler, David Lyon, Mark S Zahniser, and Charles E Kolb. Mobile laboratory observations of methane emissions in the barnett shale region. *Environmental science & technology*, 49(13):7889–7895, 2015.

[30] Bo Galle, Jerker Samuelsson, Bo H Svensson, and Gunnar Börjesson. Measurements of methane emissions from landfills using a time correlation tracer method based on ftir absorption spectroscopy. *Environmental Science & Technology*, 35(1):21–25, 2001.

[31] Charlotte Scheutz, Jerker Samuelsson, Anders Michael Fredenslund, and Peter Kjeldsen. Quantification of multiple methane emission sources at landfills using a double tracer technique. *Waste Management*, 31(5):1009–1017, 2011.

[32] Jacob G Mønster, Jerker Samuelsson, Peter Kjeldsen, Chris W Rella, and Charlotte Scheutz. Quantifying methane emission from fugitive sources by combining tracer release and downwind measurements–a sensitivity analysis based on multiple field surveys. *Waste Management*, 34(8):1416–1428, 2014.

[33] ED Thoma, BC Squier, D Olson, AP Eisele, JM DeWees, RR Segall, MS Amin, and M Modrak. Assessment of methane and voc emissions from select upstream oil and gas production operations using remote measurements, interim report on recent survey studies. In *Proceedings of 105th Annual Conference of the Air & Waste Management Association, Control*, number 2012-A, pages 298–312, 2012.

[34] Eben D Thoma, Tracey L Footer, William R Stevens, Jason M DeWees, Roger B Green, Gary R Hater, Nathan D Swan, and Jeff Chanton. Development of the mobile tracer correlation method for quantification of emissions from landfills and other large area sources. In *Global Waste Management Symposium, September 30th–October 3rd*, 2012.

[35] Veronica K Figueroa, Kevin R Mackie, Nick Guarriello, and C David Cooper. A robust method for estimating landfill methane emissions. *Journal of the Air & Waste Management Association*, 59(8):925–935, 2009.

[36] Jane Hodgkinson and Ralph P Tatam. Optical gas sensing: a review. *Measurement Science and Technology*, 24(1):012004, 2012.

[37] New Source Performance Standards; Oil and Natural Gas Sector: Emission Standards for New, Reconstructed, and Modified Sources. Standard, Environmental Protection Agency, 2016.

[38] Arvind P Ravikumar, Jingfan Wang, and Adam R Brandt. Are optical gas imaging technologies effective for methane leak detection? *Environmental science & technology*, 51(1):718–724, 2016.

[39] Prachi Patel. Monitoring methane, 2017.

[40] Halley L Brantley, Eben D Thoma, William C Squier, Birnur B Guven, and David Lyon. Assessment of methane emissions from oil and gas production pads using mobile measurements. *Environmental science & technology*, 48(24):14508–14515, 2014.

[41] Thomas G McRae and Thomas J Kulp. Backscatter absorption gas imaging: a new technique for gas visualization. *Applied optics*, 32(21):4037–4050, 1993.

[42] Peter E Powers, Thomas J Kulp, and Randall Kennedy. Demonstration of differential backscatter absorption gas imaging. *Applied optics*, 39(9):1440–1448, 2000.

[43] David Richard Lyon. *Quantifying, Assessing, and Mitigating Methane Emissions from Super-emitters in the Oil and Gas Supply Chain*. PhD thesis, University of Arkansas, 2016.

[44] MG Villani, P Bergamaschi, M Krol, JF Meirink, and F Dentener. Inverse modeling of european CH4 emissions: sensitivity to the observational network. *Atmospheric chemistry and physics*, 10(3):1249–1267, 2010.

[45] H Bovensmann, JP Burrows, M Buchwitz, J Frerick, S Noël, VV Rozanov, KV Chance, and APH Goede. SCIAMACHY: Mission objectives and measurement modes. *Journal of the atmospheric sciences*, 56(2):127–150, 1999.

[46] Akihiko Kuze, Hiroshi Suto, Masakatsu Nakajima, and Takashi Hamazaki. Thermal and near infrared sensor for carbon observation fourier-transform spectrometer on the greenhouse gases observing satellite for greenhouse gases monitoring. *Applied optics*, 48(35):6716–6733, 2009.

[47] David W Griffith, GC Toon, B Connor, R Sussmann, Thorsten Warneke, Nicholas M Deutscher, Paul O Wennberg, Justus Notholt, V Sherlock, J Robinson, et al. Preliminary validation of column-averaged volume mixing ratios of carbon dioxide and methane retrieved from GOSAT short-wavelength infrared spectra. 2011.

[48] RJ Engelen and GL Stephens. Information content of infrared satellite sounding measurements with respect to CO2. *Journal of Applied Meteorology*, 43(2):373–378, 2004.

[49] Xiaozhen Xiong, Chris Barnet, Eric Maddy, Colm Sweeney, Xingpin Liu, Lihang Zhou, and Mitch Goldberg. Characterization and validation of methane products from the atmospheric infrared sounder (airs). *Journal of Geophysical Research: Biogeosciences*, 113(G3), 2008.

[50] K Minschwaner and GL Manney. Derived methane in the stratosphere and lower mesosphere from aura microwave limb sounder measurements of nitrous oxide, water vapor, and carbon monoxide. *Journal of Atmospheric Chemistry*, 71(4):253–267, 2014.

[51] JW Waters. Microwave limb-sounding of earth's upper atmosphere. *Atmospheric research*, 23(3-4):391–410, 1989.

[52] Joe W Waters, Lucien Froidevaux, Robert S Harwood, Robert F Jarnot, Herbert M Pickett, William G Read, Peter H Siegel, Richard E Cofield, Mark J Filipiak, Dennis A Flower, et al. The earth observing system microwave limb sounder (eos mls) on the aura satellite. *IEEE Transactions on Geoscience and Remote Sensing*, 44(5):1075–1092, 2006.

[53] FT Barath, MC Chavez, RE Cofield, DA Flower, MA Frerking, MB Gram, WM Harris, JR Holden, RF Jarnot, WG Kloezeman, et al. The upper atmosphere research satellite microwave limb sounder instrument. *Journal of Geophysical Research: Atmospheres*, 98(D6):10751–10762, 1993.

[54] Dan Slater, Paul Stek, Rick Cofield, Robert Dengler, Jack Hardy, Robert Jarnot, and Ray Swindlehurst. A large aperture 650 ghz near-field measurement system for the earth observing system microwave limb sounder. In *Antenna Measurement Techniques Association Conference*, 2001.

[55] Robert T Menzies and David M Tratt. Differential laser absorption spectrometry for global profiling of tropospheric carbon dioxide: selection of optimum sounding frequencies for high-precision measurements. *Applied Optics*, 42(33):6569–6577, 2003.

[56] C Stephan, M Alpers, B Millet, G Ehret, P Flamant, and C Deniel. MERLIN: a space-based methane monitor. In *Lidar Remote Sensing for Environmental Monitoring XII*, volume 8159, page 815908. International Society for Optics and Photonics, 2011.

[57] Chandler E Kemp, Arvind P Ravikumar, and Adam R Brandt. Comparing natural gas leakage detection technologies using an open-source virtual gas field simulator. *Environmental science & technology*, 50(8):4546–4553, 2016.

[58] David M Tratt, Kerry N Buckland, Jeffrey L Hall, Patrick D Johnson, Eric R Keim, Ira Leifer, Karl Westberg, and Stephen J Young. Airborne visualization and quantification of discrete methane sources in the environment. *Remote sensing of environment*, 154:74–88, 2014.

[59] Andrew K Thorpe, Dar A Roberts, Eliza S Bradley, Christopher C Funk, Philip E Dennison, and Ira Leifer. High resolution mapping of methane emissions from marine and terrestrial sources using a cluster-tuned matched filter technique and imaging spectrometry. *Remote Sensing of Environment*, 134:305–318, 2013.

[60] Magnus Gålfalk, Göran Olofsson, Patrick Crill, and David Bastviken. Making methane visible. *Nature Climate Change*, 6(4):426, 2016.

[61] Glynn C Hulley, Riley M Duren, Francesca M Hopkins, Simon J Hook, William R Johnson, Bjorn T Eng, Jonathan M Mihaly, Veljko M Jovanovic, Seth L Chazanoff, Zak K Staniszewski, et al. High spatial resolution imaging of methane and other trace gases with the airborne Hyperspectral Thermal Emission Spectrometer (HyTES). *Atmospheric Measurement Techniques*, 9(5):2393, 2016.

[62] Le Kuai, John R Worden, King-Fai Li, Glynn C Hulley, Francesca M Hopkins, Charles E Miller, Simon J Hook, Riley M Duren, and Andrew D Aubrey. Characterization of anthropogenic methane plumes with the hyperspectral thermal emission spectrometer (hytes): A retrieval method and error analysis. 2016.

[63] Edwin Thornton and Nick Bowmar. The application of a laser based open-path spectrometer for the measurement of fugitive emissions and process control. In *AWMA Annual Symposium*, 1999.

[64] Haris Riris, Kenji Numata, Steve Li, Stewart Wu, Anand Ramanathan, Martha Dawsey, Jianping Mao, Randolph Kawa, and James B Abshire. Airborne measurements of atmospheric methane column abundance using a pulsed integrated-path differential absorption lidar. *Applied optics*, 51(34):8296–8305, 2012.

[65] Anand Ramanathan, Kenji Numata, Stewart T Wu, Steven X Li, Martha W Dawsey, Jianping Mao, Stephan R Kawa, and Haris Riris. Airborne measurement of atmospheric methane concentration using pulsed lidar. In *Infrared Remote Sensing and Instrumentation XX*, volume 8511, page 85110E. International Society for Optics and Photonics, 2012.

[66] Haris Riris, Kenji Numata, Stewart Wu, Brayler Gonzalez, Michael Rodriguez, Stan Scott, Stephan Kawa, and Jianping Mao. Methane optical density measurements with an integrated path differential absorption lidar from an airborne platform. *Journal of applied remote sensing*, 11(3):034001, 2017.

[67] Axel Amediek, Gerhard Ehret, Andreas Fix, Martin Wirth, Christian Büdenbender, Mathieu Quatrevalet, Christoph Kiemle, and Christoph Gerbig. CHARM-F A new airborne integrated-path differential-absorption lidar for carbon dioxide and methane observations: measurement performance and quantification of strong point source emissions. *Applied optics*, 56(18):5182–5197, 2017.

[68] Axel Amediek, Gerhard Ehret, Andreas Fix, Martin Wirth, Christian Büdenbender, Mathieu Quatrevalet, and Christoph Kiemle. Performance of Charm-F–the airborne demonstrator for Merlin. In *EPJ Web of Conferences*, volume 176, page 01002. EDP Sciences, 2018.

[69] Andreas Fix, Axel Amediek, Heinrich Bovensmann, Gerhard Ehret, Christoph Gerbig, Konstantin Gerilowski, Klaus Pfeilsticker, Anke Roiger, and Martin Zöger. CoMet: An airborne mission to simultaneously measure CO2 and CH4 using lidar, passive remote sensing, and in-situ techniques. In *EPJ Web of Conferences*, volume 176, page 02003. EDP Sciences, 2018.

[70] Jarett Bartholomew, Philip Lyman, Carl Weimer, and William Tandy. Wide area methane emissions mapping with airborne ipda lidar. In *Lidar Remote Sensing for Environmental Monitoring 2017*, volume 10406, page 1040607. International Society for Optics and Photonics, 2017.

[71] Tom Burr and Nicolas Hengartner. Overview of physical models and statistical approaches for weak gaseous plume detection using passive infrared hyperspectral imagery. *Sensors*, 6(12):1721–1750, 2006.

[72] Tom Burr, Bernie Foy, Herb Fry, and Brian McVey. Characterizing clutter in the context of detecting weak gaseous plumes in hyperspectral imagery. *Sensors*, 6(11):1587–1615, 2006.

[73] SR Kawa, J Mao, JB Abshire, GJ Collatz, X Sun, and CJ Weaver. Simulation studies for a space-based co2 lidar mission. *Tellus B: Chemical and Physical Meteorology*, 62(5):759–769, 2010.

[74] Guy G Goyer and Robert Watson. The laser and its application to meteorology. *Bulletin of the American Meteorological Society*, 44(9):564–570, 1963.

[75] Brent Schwarz. Lidar: Mapping the world in 3d. *Nature Photonics*, 4(7):429, 2010.

[76] Yasser Y Hassebo. *Lidar signal-to-noise ratio improvements: Considerations and techniques*. City University of New York, 2007.

[77] RM Schotland. Some observations of the vertical profile of water vapor by means of a laser optical radar(measurement and theory, including signal to noise and transfer function calculations, of atmospheric water vapor using ruby laser optical radar). *1966.*, pages 273–283, 1966.

[78] Gérard Megie. Laser remote sensing: fundamentals and applications. *Eos, Transactions American Geophysical Union*, 66(40):686–686, 1985.

[79] Eugenio Zanzottera. Differential absorption lidar techniques in the determination of trace pollutants and physical parameters of the atmosphere. *Critical reviews in analytical chemistry*, 21(4):279–319, 1990.

[80] Jeremy T Dobler, F Wallace Harrison, Edward V Browell, Bing Lin, Doug McGregor, Susan Kooi, Yonghoon Choi, and Syed Ismail. Atmospheric co 2 column measurements with an airborne intensity-modulated continuous wave 1.57 μm fiber laser lidar. *Applied optics*, 52(12):2874–2892, 2013.

[81] James B Abshire, Haris Riris, Clark J Weaver, Jianping Mao, Graham R Allan, William E Hasselbrack, and Edward V Browell. Airborne measurements of co 2 column absorption and range using a pulsed direct-detection integrated path differential absorption lidar. *Applied Optics*, 52(19):4446–4461, 2013.

[82] A Amediek, A Fix, M Wirth, and G Ehret. Development of an opo system at 1.57 μm for integrated path dial measurement of atmospheric carbon dioxide. *Applied Physics B*, 92(2):295–302, 2008.

[83] Daisuke Sakaizawa, Chikao Nagasawa, Tomohiro Nagai, Makoto Abo, Yasukuni Shibata, Masahisa Nakazato, and Tetsu Sakai. Development of a 1.6 μm differential absorption lidar with a quasi-phase-matching optical parametric oscillator and photon-counting detector for the vertical co 2 profile. *Applied optics*, 48(4):748–757, 2009.

[84] William Johnson, Kevin S Repasky, and John L Carlsten. Micropulse differential absorption lidar for identification of carbon sequestration site leakage. *Applied optics*, 52(13):2994–3003, 2013.

[85] RA Robinson, TD Gardiner, F Innocenti, A Finlayson, PT Woods, and JFM Few. First measurements of a carbon dioxide plume from an industrial source using a ground based mobile differential absorption lidar. *Environmental Science: Processes & Impacts*, 16(8):1957–1966, 2014.

[86] Gary D Spiers, Robert T Menzies, Joseph Jacob, Lance E Christensen, Mark W Phillips, Yonghoon Choi, and Edward V Browell. Atmospheric co 2 measurements with a 2 μm airborne laser absorption spectrometer employing coherent detection. *Applied optics*, 50(14):2098–2111, 2011.

[87] Ti Chuang, Brooke Walters, Tim Shuman, Andrew Losee, Tom Schum, Kent Puffenberger, and Ralph Burnham. Single frequency and wavelength stabilized near infrared laser source for water vapor dial remote sensing application. In *Solid State Lasers XXIV: Technology and Devices*, volume 9342, page 93420J. International Society for Optics and Photonics, 2015.

[88] SM Spuler, KS Repasky, B Morley, D Moen, Matthew Hayman, and AR Nehrir. Field-deployable diode-laser-based differential absorption lidar (dial) for profiling water vapor. *Atmospheric Measurement Techniques*, 8(3):1073–1087, 2015.

[89] R Michael Hardesty. Coherent dial measurement of range-resolved water vapor concentration. *Applied optics*, 23(15):2545–2553, 1984.

[90] Gerhard Ehret, Klaus P Hoinka, Joël Stein, Andreas Fix, Christoph Kiemle, and Gorazd Poberaj. Low stratospheric water vapor measured by an airborne dial. *Journal of Geophysical Research: Atmospheres*, 104(D24):31351–31359, 1999.

[91] Tammy M Weckwerth, Kristy J Weber, David D Turner, and Scott M Spuler. Validation of a water vapor micropulse differential absorption lidar (dial). *Journal of Atmospheric and Oceanic Technology*, 33(11):2353–2372, 2016.

[92] HJ Kölsch, P Rairoux, JP Wolf, and L Wöste. Comparative study of nitric oxide immission in the cities of lyon, geneva, and stuttgart using a mobile differential absorption lidar system. *Applied Physics B*, 54(1):89–94, 1992.

[93] N Menyuk, DK Killinger, and WE DeFeo. Remote sensing of no using a differential absorption lidar. *Applied optics*, 19(19):3282–3286, 1980.

[94] Takuya Nayuki, Tetsuo Fukuchi, Nianwen Cao, Hideto Mori, Takashi Fujii, Koshichi Nemoto, and Nobuo Takeuchi. Sum-frequency-generation system for differential absorption lidar measurement of atmospheric nitrogen dioxide. *Applied optics*, 41(18):3659–3664, 2002.

[95] Ryoichi Toriumi, Hideo Tai, and Nobuo Takeuchi. Tunable solid-state blue laser differential absorption lidar system for no2 monitoring. *Optical Engineering*, 35(8):2371–2376, 1996.

[96] Kenji Numata, Stewart Wu, and Haris Riris. Fast-switching methane lidar transmitter based on a seeded optical parametric oscillator. *Applied Physics B*, 116(4):959–966, 2014.

[97] Narasimha S Prasad and Allen R Geiger. Remote sensing of propane and methane by means of a differential absorption lidar by topographic reflection. *Optical Engineering*, 35(4):1105–1112, 1996.

[98] Kouki Ikuta, Noboru Yoshikane, Nilesh Vasa, Yuji Oki, Mitsuo Maeda, Michihiro Uchiumi, Youichirou Tsumura, Jun Nakagawa, and Noriyuki Kawada. Differential absorption lidar at 1.67 μm for remote sensing of methane leakage. *Japanese journal of applied physics*, 38(1R):110, 1999.

[99] Claus Weitkamp. *Lidar: range-resolved optical remote sensing of the atmosphere*, volume 102. Springer Science & Business, 2006.

[100] Kent A Fredriksson and Hans M Hertz. Evaluation of the DIAL technique for studies on NO2 using a mobile lidar system. *Applied optics*, 23(9):1403–1411, 1984.

[101] M Uchiumi, O Choo Chee, K Muraoka, M Maeda, and O Uchino. Dial measurement of ch4, co2, co and n2o using a tunable ir source based on the ti: sapphire laser. *17th ILRC*, 1994.

[102] Jens Bösenberg and David J Brassington. *Instrument development for atmospheric research and monitoring: lidar profiling, DOAS and tunable diode laser spectroscopy*, volume 8. Springer Science & Business Media, 1997.

[103] Syed Ismail and Edward V Browell. Airborne and spaceborne lidar measurements of water vapor profiles: a sensitivity analysis. *Applied Optics*, 28(17):3603–3615, 1989.

[104] Edward V Browell, Syed Ismail, and Benoist E Grossmann. Temperature sensitivity of differential absorption lidar measurements of water vapor in the 720-nm region. *Applied optics*, 30(12):1517–1524, 1991.

[105] G Megie and RT Menzies. Complementarity of uv and ir differential absorption lidar for global measurements of atmospheric species. *Applied optics*, 19(7):1173–1183, 1980.

[106] Gerd A Wagner and David F Plusquellic. Ground-based, integrated path differential absorption lidar measurement of co 2, ch 4, and h 2 o near 1.6 μm. *Applied optics*, 55(23):6292–6310, 2016.

[107] Axel Amediek, Andreas Fix, Gerdhard Ehret, J Caron, and Y Durand. Airborne lidar reflectance measurements at 1.57 μm in support of the A-SCOPE mission for atmospheric CO2. *Atmospheric Measurement Techniques*, 2(2):755–772, 2009.

[108] P Vujkovic-Cvijin, DE Cooper, JE van der Laan, RE Warren, and KK Krist. Mobile remote sensor for leak detection in natural gas pipelines. *Proc. of IGRC 2001*, 2001.

[109] Takaya Iseki. Lasermethane tma portable remote methane detector. In *Int. Gas Research Conference*, 2004.

[110] Moran Chen, Patrick M Burns, Viatcheslav Litvinovitch, Mark Storm, and Nicholas W Sawruk. Er: Yag laser technology for remote sensing applications. In *Lidar Technologies, Techniques, and Measurements for Atmospheric Remote Sensing XII*, volume 10006, page 1000603. International Society for Optics and Photonics, 2016.

[111] Patrick M Burns, Moran Chen, David Pachowicz, Slava Litvinovitch, Fran Fitzpatrick, and Nicholas W Sawruk. Single frequency er: Yag methane/water vapor dial source. In *Applications of Lasers for Sensing and Free Space Communications*, pages SW3H–2. Optical Society of America, 2018.

[112] Kenneth O White and Stuart A Schleusener. Coincidence of Er:YAG laser emission with methane absorption at 1645.1 nm. *Applied Physics Letters*, 21(9):419–420, 1972.

[113] Nikita Simakov, David J Hosken, Murray W Hamilton, Jesper Munch, and Peter J Veitch. Injection mode-locked, q-switched nd: Yag laser at 1319 nm. *IEEE Journal of Quantum Electronics*, 46(7):1086–1090, 2010.

[114] Thomas P Rutten, Peter J Veitch, Céline dOrgeville, and Jesper Munch. Injection mode-locked guide star laser concept and design verification experiments. *Optics express*, 15(5):2369–2374, 2007.

[115] Matthew C Heintze, Nick WH Chang, Francois Jeanneret, Jesper Munch, David J Ottaway, and Peter J Veitch. Single-pulse measurement of wind velocities using an er: Yb: glass coherent laser radar. *Applied optics*, 50(21):4017–4023, 2011.

[116] J Richards and A McInnes. Versatile, efficient, diode-pumped miniature slab laser. *Optics letters*, 20(4):371–373, 1995.

[117] Alasdair McInnes and James Richards. Thermal effects in a coplanar-pumped folded-zigzag slab laser. *IEEE journal of quantum electronics*, 32(7):1243–1252, 1996.

[118] Tso Fan and ROBERTL Byer. Modeling and cw operation of a quasi-three-level 946 nm nd: Yag laser. *IEEE Journal of Quantum Electronics*, 23(5):605–612, 1987.

[119] M Dubinskii, N Ter-Gabrielyan, GA Newburgh, and LD Merkle. Ultra-low photon defect diode-pumped cryo-cooled er: Yag laser. In *Laser Source Technology for Defense and Security III*, volume 6552, page 65520M. International Society for Optics and Photonics, 2007.

[120] Scott D Setzler, Michael J Shaw, Mark J Kukla, Josef R Unternahrer, Kenneth M Dinndorf, James A Beattie, and Evan P Chicklis. A 400w cryogenic er: Yag laser at 1645 nm. In *Laser Technology for Defense and Security VI*, volume 7686, page 76860C. International Society for Optics and Photonics, 2010.

[121] JW Kim, DY Shen, Jayanta K Sahu, and W Andrew Clarkson. Fiber-laser-pumped Er:YAG lasers. *IEEE Journal of Selected Topics in Quantum Electronics*, 15(2):361–371, 2009.

[122] Igor Kudryashov, Nikolai Ter-Gabrielyan, and Mark Dubinskii. Resonantly diode-pumped Er:YAG laser: 1470-nm versus 1530-nm CW pumping case. In *Laser Technology For Defense And Security V*, volume 7325, page 732505. International Society for Optics and Photonics, 2009.

[123] Dmitri Garbuzov, Igor Kudryashov, and Mark Dubinskii. 110 w (0.9 j) pulsed power from resonantly diode-laser-pumped 1.6-μ m er: Yag laser. *Applied Physics Letters*, 87(12):121101, 2005.

[124] Daniel O Hogenboom, Minh Nguyen, and Hsian P Chou. Good beam quality from a diamond-cooled er: Yag laser. In *Laser Source and System Technology for Defense and Security II*, volume 6216, page 62160F. International Society for Optics and Photonics, 2006.

[125] Ji Won Kim, JK Sahu, and WA Clarkson. Impact of energy-transfer-upconversion on the performance of hybrid er: Yag lasers. In *Solid State Lasers XVII: Technology and Devices*, volume 6871, page 68710W. International Society for Optics and Photonics, 2008.

[126] Igor Kudryashov, Dmitri Garbuzov, and Mark Dubinskii. Volume bragg grating improves characteristic of resonantly diode-pumped er: Yag, 1.65-μm dpssl. In *Solid State Lasers XVI: Technology and Devices*, volume 6451, page 64510P. International Society for Optics and Photonics, 2007.

[127] K Spariosu, V Leyva, RA Reeder, and M Klotz. All-solid-state 12-watt CW and actively Q-switched Er:YAG laser operating at 1645 nm. In *Solid State Lasers XIV: Technology and Devices*, volume 5707, pages 150–165. International Society for Optics and Photonics, 2005.

[128] DY Shen, PJ Jander, JK Sahu, and WA Clarkson. High-power and ultra-efficient operation of 1645 nm Er:YAG laser pumped by a 100w tunable Er, Yb fiber laser. In *Advanced Solid-State Photonics*, page 618. Optical Society of America, 2005.

[129] DY Shen, JK Sahu, and WA Clarkson. Electro-optically q-switched er: Yag laser in-band pumped by an er, yb fiber laser. In *Advanced Solid-State Photonics*, page WD4. Optical Society of America, 2006.

[130] Rulian Fu, Guangjun Wang, Zhaoqi Wang, Enxu Ba, Guoguang Mu, and Xin-Hua Hu. Design of efficient lens ducts. *Applied optics*, 37(18):4000–4003, 1998.

[131] Walter Koechner. *Solid-state laser engineering*, volume 1. Springer, 2013.

[132] Javier Alda, Daniel Vazquez, and Eusebio Bernabeu. Wavefront and amplitude profile for astigmatic beams in semiconductor lasers: analytical and graphical treatment. *Journal of optics*, 19(5-6):201, 1988.

[133] Evgenia Kochkina. *Stigmatic and Astigmatic Gaussian Beams in Fundamental Mode: Impact of Beam Model Choice on Interferometric Pathlength Signal Estimates*. PhD thesis, Technische Informationsbibliothek und Universitätsbibliothek Hannover (TIB) Hannover, 2013.

[134] Michale S Fee, Karsten Danzmann, and Steven Chu. Optical heterodyne measurement of pulsed lasers: toward high-precision pulsed spectroscopy. *Physical Review A*, 45(7):4911, 1992.

[135] Norman P Barnes and James C Barnes. Injection seeding. i. theory. *IEEE Journal of Quantum Electronics*, 29(10):2670–2683, 1993.

[136] T Schröder, C Lemmerz, O Reitebuch, M Wirth, C Wührer, and R Treichel. Frequency jitter and spectral width of an injection-seeded q-switched nd: Yag laser for a doppler wind lidar. *Applied Physics B*, 87(3):437–444, 2007.

[137] Haiyun Xia, Xiankang Dou, Dongsong Sun, Zhifeng Shu, Xianghui Xue, Yan Han, Dongdong Hu, Yuli Han, and Tingdi Cheng. Mid-altitude wind measurements with mobile rayleigh doppler lidar incorporating system-level optical frequency control method. *Optics express*, 20(14):15286–15300, 2012.

[138] Jun Zhou, Ting Yu, Jinzi Bi, Xiaolei Zhu, and Weibiao Chen. Diode pumped injection seeded nd: Yag laser. *Chinese Optics Letters*, 4(5):292–293, 2006.

[139] Klaus Ertel, Holger Linné, and Jens Bösenberg. Injection-seeded pulsed ti: sapphire laser with novel stabilization scheme and capability of dual-wavelength operation. *Applied optics*, 44(24):5120–5126, 2005.

[140] AQ Liu and XM Zhang. A review of mems external-cavity tunable lasers. *Journal of Micromechanics and Microengineering*, 17(1):R1, 2006.

[141] Vijaysekhar Jayaraman, Z-M Chuang, and Larry A Coldren. Theory, design, and performance of extended tuning range semiconductor lasers with sampled gratings. *IEEE Journal of Quantum Electronics*, 29(6):1824–1834, 1993.

[142] Yuichi Tohmori, Yuzo Yoshikuni, Hiroyuki Ishii, Fumiyoshi Kano, Toshiaki Tamamura, Yasuhiro Kondo, and Mitsuo Yamamoto. Broad-range wavelength-tunable superstructure grating (ssg) dbr lasers. *IEEE journal of quantum electronics*, 29(6):1817–1823, 1993.

[143] John E Carroll, James Whiteaway, Dick Plumb, and RGS Plumb. *Distributed feedback semiconductor lasers*, volume 10. IET, 1998.

[144] Fabien Kéfélian, Haifeng Jiang, Pierre Lemonde, and Giorgio Santarelli. Ultralow-frequency-noise stabilization of a laser by locking to an optical fiber-delay line. *Optics letters*, 34(7):914–916, 2009.

[145] Qian Zhou, Jie Qin, Weilin Xie, Zhangweiyi Liu, Yitian Tong, Yi Dong, and Weisheng Hu. Dynamic frequency-noise spectrum measurement for a frequency-swept dfb laser with short-delayed self-heterodyne method. *Optics express*, 23(22):29245–29257, 2015.

[146] Charles Henry. Theory of the linewidth of semiconductor lasers. *IEEE Journal of Quantum Electronics*, 18(2):259–264, 1982.

[147] AR Newbery. A method for producing controllable double pulses from a q-switched laser. *Opto-electronics*, 1(3):134–137, 1969.

[148] D Bruneau, H Cazeneuve, C Loth, and J Pelon. Double-pulse dual-wavelength alexandrite laser for atmospheric water vapor measurement. *Applied optics*, 30(27):3930–3937, 1991.

[149] Chen Chang-Shui, Zhang Yi-Shi, Yu Jin-Wang, Fang Jian, and Liu Song-Hao. Experimental study on dual wavelength and dual pulse q-switched frequency doubling on a tunable cr: Lisaf laser. *Chinese Physics Letters*, 26(9):094206, 2009.

[150] Tamer F Refaat, Upendra N Singh, Jirong Yu, Mulugeta Petros, Ruben Remus, and Syed Ismail. Double-pulse 2-μm integrated path differential absorption lidar airborne validation for atmospheric carbon dioxide measurement. *Applied Optics*, 55(15):4232–4246, 2016.

[151] F Gibert, D Edouart, C Cénac, F Le Mounier, and A Dumas. New advances in 2-? m high-power dual-frequency single-mode q-switched ho: Ylf laser for dial and ipda application. In *International Conference on Space OpticsICSO 2014*, volume 10563, page 105630S. International Society for Optics and Photonics, 2017.

[152] Jirong Yu, Alain Braud, and Mulugeta Petros. 600-mj, double-pulse 2-microm laser. *Optics letters*, 28(7):540–542, 2003.

[153] Didier Bruneau, Stephane Delmonte, and Jacques Pelon. Modeling of tm, ho: Yag and tm, ho: Ylf 2-μm lasers and calculation of extractable energies. *Applied optics*, 37(36):8406–8419, 1998.

[154] AN Bondarenko, GV Krivoshchekov, and VA Smirnov. Single-frequency ruby laser with active q-switch. *ZhETF Pisma Redaktsiiu*, 9:100, 1969.

[155] Renjie Zhou, Wei Shi, Eliot Petersen, Arturo Chavez-Pirson, Mark Stephen, and Nasser Peyghambarian. Transform-limited, injection seeded, q-switched, ring cavity fiber laser. *Journal of Lightwave Technology*, 30(16):2589–2595, 2012.

[156] NJ Vasa, M Tanaka, T Okada, M Maeda, and O Uchino. Comparative study of spectral narrowing of a pulsed ti: Sapphire laser using pulsed and cw injection seeding. *Applied Physics B*, 62(1):51–57, 1996.

[157] Irving Bigio and Michael Slatkine. Injection-locking unstable resonator excimer lasers. *IEEE journal of quantum electronics*, 19(9):1426–1436, 1983.

[158] OL Bourne and AJ Alcock. A high-power, narrow linewidth xecl* oscillator. *Applied Physics Letters*, 42(9):777–779, 1983.

[159] J-L Lachambre, Pierre Lavigne, Gabriel Otis, and Michel Noel. Injection locking and mode selection in tea-co 2 laser oscillators. *IEEE Journal of Quantum Electronics*, 12(12):756–764, 1976.

[160] Y Park, G Giuliani, and R Byer. Single axial mode operation of a q-switched nd: Yag oscillator by injection seeding. *IEEE Journal of Quantum Electronics*, 20(2):117–125, 1984.

[161] HIDE Tashiro, TSUTOMU Shimada, KOICHI Toyoda, and SUSUMU Namba. Studies on injection locking of a tea-co 2 laser for stable high-power operation. *IEEE journal of quantum electronics*, 20(2):159–165, 1984.

[162] U Ganiel, A Hardy, and D Treves. Analysis of injection locking in pulsed dye laser systems. *IEEE Journal of Quantum Electronics*, 12(11):704–716, 1976.

[163] John B Gruber, John R Quagliano, Michael F Reid, Frederick S Richardson, Marian E Hills, Michael D Seltzer, Sally B Stevens, Clyde A Morrison, and Toomas H Allik. Energy levels and correlation crystal-field effects in Er 3+-doped garnets. *Physical Review B*, 48(21):15561, 1993.

[164] JW Kim, DY Shen, JK Sahu, and WA Clarkson. High-power in-band pumped Er:YAG laser at 1617 nm. *Optics express*, 16(8):5807–5812, 2008.

[165] Yan Zheng, Chunqing Gao, Ran Wang, Mingwei Gao, and Qing Ye. Single frequency 1645 nm Er:YAG nonplanar ring oscillator resonantly pumped by a 1470 nm laser diode. *Optics letters*, 38(5):784–786, 2013.

[166] DENNIS K KILLINGER. Phonon-assisted upconversion in 1.64 μm er: Yag lasers. In *Conference on Lasers and Electro-Optics*, page THJ4. Optical Society of America, 1987.

[167] WP Risk. Modeling of longitudinally pumped solid-state lasers exhibiting reabsorption losses. *JOSA B*, 5(7):1412–1423, 1988.

[168] P Peterson, A Gavrielides, and PM Sharma. Cw theory of a laser diode-pumped two-manifold solid state laser. *Optics communications*, 109(3-4):282–287, 1994.

[169] Nick W. Chang. *Eye-safe Er:YAG Lasers for Coherent Remote Sensing*. PhD thesis, School of Chemistry and Physics, The University of Adelaide, 2012.

[170] Raymond J Beach. Cw theory of quasi-three level end-pumped laser oscillators. *Optics Communications*, 123(1-3):385–393, 1996.

[171] Frédérica Augé, Frédéric Druon, François Balembois, Patrick Georges, Alain Brun, Frédéric Mougel, Gérard Aka, and D Vivien. Theoretical and experimental investigations of a diode-pumped quasi-three-level laser: the yb/sup 3+/-doped ca/sub 4/gdo (bo/sub 3/)/sub 3/(yb: Gdcob) laser. *IEEE Journal of quantum electronics*, 36(5):598–606, 2000.

[172] Marc Eichhorn. Numerical modeling of diode-end-pumped high-power Er^{3+}:YAG lasers. *IEEE Journal of Quantum Electronics*, 44(9):803–810, 2008.

[173] Jeffrey O White, Mark Dubinskii, Larry D Merkle, Igor Kudryashov, and Dmitri Garbuzov. Resonant pumping and upconversion in 1.6 μm er 3+ lasers. *JOSA B*, 24(9):2454–2460, 2007.

[174] Jeffrey O White and Carl E Mungan. Measurement of upconversion in er: Yag via z-scan. *JOSA B*, 28(10):2358–2361, 2011.

[175] Zeev Burshtein. Radiative, nonradiative, and mixed-decay transitions of rare-earth ions in dielectric media. *Optical Engineering*, 49(9):091005, 2010.

[176] Nikolay Ter-Gabrielyan, Mark Dubinskii, G Alex Newburgh, Arockiasamy Michael, and Larry D Merkle. Temperature dependence of a diode-pumped cryogenic er: Yag laser. *Optics express*, 17(9):7159–7169, 2009.

[177] Dhiraj K Sardar, Charles C Russell III, John B Gruber, and Toomas H Allik. Absorption intensities and emission cross sections of principal intermanifold and inter-stark transitions of er 3+(4 f 11) in polycrystalline ceramic garnet y 3 al 5 o 12. *Journal of applied physics*, 97(12):123501, 2005.

[178] MO Iskandarov, AA Nikitichev, and AI Stepanov. Quasi-two-level er3+: Y3 al5 o12 laser for the 1.6-micrometer range. *Journal of Optical Technology*, 68(12):885, 2001.

[179] Dhiraj K Sardar, William M Bradley, John J Perez, John B Gruber, Bahram Zandi, J Andrew Hutchinson, C Ward Trussell, and Milan R Kokta. Judd–ofelt analysis of the er3+ (4f11) absorption intensities in er3+- doped garnets. *Journal of applied physics*, 93(5):2602–2607, 2003.

[180] B Simondi-Teisseire, B Viana, D Vivien, and AM Lejus. Yb3+ to er3+ energy transfer and rate-equations formalism in the eye safe laser material yb: Er: Ca2al2sio7. *Optical Materials*, 6(4):267–274, 1996.

[181] Lawrence F Shampine and Mark W Reichelt. The matlab ode suite. *SIAM journal on scientific computing*, 18(1):1–22, 1997.

[182] Marc Eichhorn, ST Fredrich-Thornton, E Heumann, and G Huber. Spectroscopic properties of er 3+: Yag at 300–550 k and their effects on the 1.6 μm laser transitions. *Applied Physics B*, 91(2):249–256, 2008.

[183] York E Young, Scott D Setzler, Kevin J Snell, Peter A Budni, Thomas M Pollak, and EP Chicklis. Efficient 1645-nm Er:YAG laser. *Optics letters*, 29(10):1075–1077, 2004.

[184] Scott D Setzler, York E Young, Kevin J Snell, Peter A Budni, Thomas M Pollak, and Evan P Chicklis. High-peak-power erbium lasers resonantly pumped by fiber lasers. In *Solid State Lasers XIII: Technology and Devices*, volume 5332, pages 85–97. International Society for Optics and Photonics, 2004.

[185] William G Wagner and Bela A Lengyel. Evolution of the giant pulse in a laser. *Journal of Applied Physics*, 34(7):2040–2046, 1963.

[186] John J Degnan. Theory of the optimally coupled q-switched laser. *IEEE Journal of Quantum Electronics*, 25(2):214–220, 1989.

[187] Toshihiko Baba, Tetsuko Hamano, Fumio Koyama, and Kenichi Iga. Spontaneous emission factor of a microcavity dbr surface-emitting laser. *IEEE Journal of Quantum Electronics*, 27(6):1347–1358, 1991.

[188] Gunnar Björk, Susumu Machida, Yoshihisa Yamamoto, and Kazuhiro Igeta. Modification of spontaneous emission rate in planar dielectric microcavity structures. *Physical Review A*, 44(1):669, 1991.

[189] MP Van Exter, G Nienhuis, and JP Woerdman. Two simple expressions for the spontaneous emission factor β. *Physical Review A*, 54(4):3553, 1996.

[190] Gijs van Soest and Ad Lagendijk. β factor in a random laser. *Physical Review E*, 65(4):047601, 2002.

[191] David J Ottaway, Lachlan Harris, and Peter J Veitch. Short-pulse actively Q-switched Er:YAG lasers. *Optics Express*, 24(14):15341–15350, 2016.

[192] Nick Wei-Han Chang, David J Hosken, Jesper Munch, David Ottaway, and Peter J Veitch. Stable, single frequency er: Yag lasers at 1.6um. *IEEE Journal of Quantum Electronics*, 46(7):1039–1042, 2010.

[193] Markus Pollnau, Th Graf, JE Balmer, W Lüthy, and HP Weber. Explanation of the cw operation of the er 3+ 3-μm crystal laser. *Physical Review A*, 49(5):3990, 1994.

[194] S Hannemann, E-J Van Duijn, and W Ubachs. A narrow-band injection-seeded pulsed titanium: sapphire oscillator-amplifier system with on-line chirp analysis for high-resolution spectroscopy. *Review of Scientific Instruments*, 78(10):103102, 2007.

[195] Mark S Bowers and Stephen E Moody. Cavity equations for a laser with an externally injected signal. *JOSA B*, 11(11):2266–2275, 1994.

[196] Richard T White, Yabai He, Brian J Orr, Mitsuhiko Kono, and KGH Baldwin. Control of frequency chirp in nanosecond-pulsed laser spectroscopy. 1. optical-heterodyne chirp analysis techniques. *JOSA B*, 21(9):1577–1585, 2004.

[197] S Gangopadhyay, N Melikechi, and EE Eyler. Optical phase perturbations in nanosecond pulsed amplification and second-harmonic generation. *JOSA B*, 11(1):231–241, 1994.

[198] P Bakule, PEG Baird, MG Boshier, SL Cornish, DF Heller, K Jungmann, IC Lane, V Meyer, PHG Sandars, WT Toner, et al. A chirp-compensated, injection-seeded alexandrite laser. *Applied Physics B*, 71(1):11–17, 2000.

[199] Richard T. White. *Quasi-Phase-Matched Nonlinear-Optical Devices*. PhD thesis, Macquarie University, Sydney, 2004.

[200] Larry A Rahn. Feedback stabilization of an injection-seeded nd: Yag laser. *Applied optics*, 24(7):940–942, 1985.

[201] Isa Servan Uzun, Abbes Amira, and Ahmed Bouridane. Fpga implementations of fast fourier transforms for real-time signal and image processing. *IEE Proceedings-Vision, Image and Signal Processing*, 152(3):283–296, 2005.

[202] Daiki Hirabayashi, Yusuke Osawa, Naohiro Harigai, Haruo Kobayashi, Osamu Kobayashi, Kiichi Niitsu, Takahiro J Yamaguchi, and Nobukazu Takai. Phase noise measurement with sigma-delta tdc. In *IEEE International Test Conference, Poster Session, Anaheim, CA (Sept. 2013)*, 2013.

[203] SW Henderson, EH Yuen, and ES Fry. Fast resonance-detection technique for single-frequency operation of injection-seeded nd: Yag lasers. *Optics letters*, 11(11):715–717, 1986.

[204] Ran Wang, Qing Ye, Yan Zheng, Mingwei Gao, and Chunqing Gao. Single-frequency operation of a resonantly pumped 1.645 μm er: Yag q-switched laser. In *Solid State Lasers XXIII: Technology and Devices*, volume 8959, page 89590F. International Society for Optics and Photonics, 2014.

[205] CQ Gao, Y Shi, Q Ye, S Wang, QX Na, Q Wang, and MW Gao. 10 mj single-frequency, injection-seeded Q-switched Er:YAG laser pumped by a 1470 nm fiber-coupled LD. *Laser Physics Letters*, 15(2):025003, 2018.

[206] Shuo Wang, Chunqing Gao, Yang Shi, Rui Song, Quanxin Na, Mingwei Gao, and Qing Wang. 1645-nm single-frequency, injection-seeded q-switched er: Yag master oscillator and power amplifier. *Optical Engineering*, 57(2):026120, 2018.

[207] BQ Yao, X Yu, XL Liu, XM Duan, YL Ju, and YZ Wang. Room temperature single longitudinal mode laser output at 1645 nm from a laser-diode pumped Er:YAG nonplanar ring oscillator. *Optics express*, 21(7):8916–8921, 2013.

[208] BQ Yao, Yu Deng, TY Dai, XM Duan, Ju You-Lun, and Yue-Zhu Wang. Single-frequency, injection-seeded Er:YAG laser based on a bow-tie ring slave resonator. *Quantum Electronics*, 45(8):709, 2015.

[209] RWP Drever, John L Hall, FV Kowalski, J_ Hough, GM Ford, AJ Munley, and H Ward. Laser phase and frequency stabilization using an optical resonator. *Applied Physics B*, 31(2):97–105, 1983.

[210] V Wulfmeyer, M Randall, A Brewer, and RM Hardesty. 2-μm doppler lidar transmitter with high frequency stability and low chirp. *Optics letters*, 25(17):1228–1230, 2000.

[211] Eric Black. Notes on pound-drever-hall technique. *LIGO Technical notes*, 1998.

[212] Alexander Sträßer, Thomas Waltinger, and Martin Ostermeyer. Injection seeded frequency stabilized nd: Yag ring oscillator following a pound-drever-hall scheme. *Applied optics*, 46(34):8358–8363, 2007.

[213] Martin Ostermeyer and Alexander Strasser. Pound-drever-hall frequency stabilization of q-switched solid state laser oscillators in the sub-mhz range. In *2008 Conference on Lasers and Electro-Optics and 2008 Conference on Quantum Electronics and Laser Science*, pages 1–2. IEEE, 2008.

[214] Martin Ostermeyer, Thomas Waltinger, and Markus Gregor. Frequency stabilization of a q-switched nd: Yag laser oscillator with stability better 300 khz following an rf-sideband scheme. *Optics Communications*, 282(16):3302–3307, 2009.

[215] K Nicklaus, V Morasch, M Hoefer, J Luttmann, M Vierkötter, M Ostermeyer, J Höffner, Christian Lemmerz, and D Hoffmann. Frequency stabilization of q-switched nd: Yag oscillators for airborne and spaceborne lidar systems. In *Solid State Lasers XVI: Technology and Devices*, volume 6451, page 64511L. International Society for Optics and Photonics, 2007.

[216] S Eckel, AO Sushkov, and SK Lamoreaux. Note: A high dynamic range, linear response transimpedance amplifier. *Review of Scientific Instruments*, 83(2):026106, 2012.

[217] Hong-Soo Cho, Chung-Hwan Kim, and Sang-Gug Lee. A high-sensitivity and low-walk error ladar receiver for military application. *IEEE Transactions on Circuits and Systems I: Regular Papers*, 61(10):3007–3015, 2014.

[218] Mohamed Atef. Transimpedance amplifier with a compression stage for wide dynamic range optical applications. *Microelectronics Journal*, 46(7):593–597, 2015.

[219] Hao Zheng, Rui Ma, and Zhangming Zhu. A linear and wide dynamic range transimpedance amplifier with adaptive gain control technique. *Analog Integrated Circuits and Signal Processing*, 90(1):217–226, 2017.

[220] R Ahrenkiel. Wide-bandwidth logarithmic amplifier for analyzing decay kinetics. *Review of Scientific Instruments*, 40(1):78–81, 1969.

[221] CA Grimbergen and GHP Köhnke. Fast-response apparatus for 11-decade logarithmic current–voltage measurements. *Review of Scientific Instruments*, 47(7):854–858, 1976.

[222] U Dürig, L Novotny, B Michel, and A Stalder. Logarithmic current-to-voltage converter for local probe microscopy. *Review of scientific instruments*, 68(10):3814–3816, 1997.

[223] Menachem Abraham. Bootstrap-transimpedance preamplifier for a fiber optic receiver, August 13 1985. US Patent 4,535,233.

[224] Haijun Zhou, Wenhai Yang, Zhixiu Li, Xuefeng Li, and Yaohui Zheng. A bootstrapped, low-noise, and high-gain photodetector for shot noise measurement. *Review of Scientific Instruments*, 85(1):013111, 2014.

[225] Haijun Zhou, Wenzhe Wang, Chaoyong Chen, and Yaohui Zheng. A low-noise, large-dynamic-range-enhanced amplifier based on jfet buffering input and jfet bootstrap structure. *IEEE Sensors Journal*, 15(4):2101–2105, 2015.

[226] Andre Vladimirescu. *The SPICE book*. John Wiley & Sons, Inc., 1994.

[227] Paul W Tuinenga. *SPICE: a guide to circuit simulation and analysis using PSpice*, volume 1. Prentice Hall Englewood Cliffs, 1995.

[228] Alejandro G Yepes, Francisco D Freijedo, Óscar Lopez, and Jesús Doval-Gandoy. Analysis and design of resonant current controllers for voltage-source converters by means of nyquist diagrams and sensitivity function. *IEEE Transactions on Industrial Electronics*, 58(11):5231–5250, 2011.

[229] Harry Nyquist. Regeneration theory. *Bell system technical journal*, 11(1):126–147, 1932.

[230] Gene F Franklin, J David Powell, Abbas Emami-Naeini, and J David Powell. *Feedback control of dynamic systems*, volume 3. Addison-Wesley Reading, MA, 1994.

[231] A Dandridge and L Goldberg. Current-induced frequency modulation in diode lasers. *Electronics Letters*, 18(7):302–304, 1982.

[232] Masaaki Imai and Koji Kawakita. Measurement of direct frequency modulation characteristics of laser diodes by michelson interferometry. *Applied optics*, 29(3):348–353, 1990.

[233] Soichi Kobayashi, Yoshihisa Yamamoto, Minoru Ito, and Tatsuya Kimura. Direct frequency modulation in algaas semiconductor lasers. *IEEE Transactions on Microwave Theory and Techniques*, 30(4):428–441, 1982.

[234] HENNING Olesen and GUNNAR Jacobsen. A theoretical and experimental analysis of modulated laser fields and power spectra. *IEEE Journal of Quantum Electronics*, 18(12):2069–2080, 1982.

[235] Travis C Briles, Dylan C Yost, Arman Cingöz, Jun Ye, and Thomas R Schibli. Simple piezoelectric-actuated mirror with 180 khz servo bandwidth. *Optics express*, 18(10):9739–9746, 2010.

[236] David Goldovsky, Valery Jouravsky, and Avi Peer. Simple and robust phase-locking of optical cavities with¿ 200 khz servo-bandwidth using a piezo-actuated mirror mounted in soft materials. *Optics express*, 24(25):28239–28246, 2016.

[237] Ralf Kohlhaas, Thomas Vanderbruggen, Simon Bernon, Andrea Bertoldi, Arnaud Landragin, and Philippe Bouyer. Robust laser frequency stabilization by serrodyne modulation. *Optics letters*, 37(6):1005–1007, 2012.

[238] Patrick Kwee, C Bogan, K Danzmann, M Frede, H Kim, P King, J Pöld, O Puncken, Rick L Savage, F Seifert, et al. Stabilized high-power laser system for the gravitational wave detector advanced ligo. *Optics express*, 20(10):10617–10634, 2012.

[239] Philippe Cassard and J-M Lourtioz. Injection locking of high-power pulsed lasers. i. monochromatic injection. *IEEE journal of quantum electronics*, 24(11):2321–2337, 1988.

[240] LH Enloe and JL Rodda. Laser phase-locked loop. *Proceedings of the IEEE*, 53(2):165–166, 1965.

[241] David Marpaung, Chris Roeloffzen, René Heideman, Arne Leinse, Salvador Sales, and José Capmany. Integrated microwave photonics. *Laser & Photonics Reviews*, 7(4):506–538, 2013.

[242] Katarzyna Balakier, Martyn J Fice, Lalitha Ponnampalam, Alwyn J Seeds, and Cyril C Renaud. Monolithically integrated optical phase lock loop for microwave photonics. *Journal of Lightwave Technology*, 32(20):3893–3900, 2014.

[243] Shintaro Hisatake, Jae-Young Kim, Katsuhiro Ajito, and Tadao Nagatsuma. Self-heterodyne spectrometer using uni-traveling-carrier photodiodes for terahertz-wave generators and optoelectronic mixers. *Journal of Lightwave Technology*, 32(20):3683–3689, 2014.

[244] John Payne, Bill Shillue, and Andrea Vaccari. Photonic techniques for use on the atacama large millimeter array. In *Microwave Photonics, 1999. MWP'99. International Topical Meeting on*, pages 105–108. IEEE, 1999.

[245] Fabien Gibert, Jessica Pellegrino, Dimitri Edouart, Claire Cénac, Laurent Lombard, Julien Le Gouët, Thierry Nuns, Alberto Cosentino, Paolo Spano, and Gior-

gia Di Nepi. 2-μm double-pulse single-frequency tm: fiber laser pumped ho: Ylf laser for a space-borne co 2 lidar. *Applied Optics*, 57(36):10370–10379, 2018.

[246] Murray Hamilton, Roger Atkinson, Alex Dinovitser, Eva Peters, and Robert A Vincent. Toward low-cost water-vapour differential absorption lidar. In *Lidar Remote Sensing for Environmental Monitoring IX*, volume 7153, page 71530C. International Society for Optics and Photonics, 2008.

[247] Alex Dinovitser, Murray Hamilton, and RA Vincent. Transmitter design for differential absorption water vapour lidar. In *Proceedings of 8th International Symposium on Tropospheric Profiling*, 2009.

[248] Alex Dinovitser, Murray W Hamilton, and Robert A Vincent. Stabilized master laser system for differential absorption lidar. *Applied optics*, 49(17):3274–3281, 2010.

[249] U Gliese, Torben Nørskov Nielsen, Marlene Bruun, E Lintz Christensen, KE Stubkjaer, S Lindgren, and B Broberg. A wideband heterodyne optical phase-locked loop for generation of 3-18 ghz microwave carriers. *IEEE Photonics Technology Letters*, 4(8):936–938, 1992.

[250] U Gliese, T Nielsen, Marlene Bruun, Erik Lintz Christensen, and KE Stubkjaer. A 3-18 ghz microwave signal generator based on optical phase locked semiconductor dfb lasers. In *Proc. Digest LEOS Summer Topical Meeting*, pages 5–6, 1993.

[251] LN Langley, MD Elkin, C Edge, MJ Wale, U Gliese, X Huang, and AJ Seeds. Packaged semiconductor laser optical phase-locked loop (opll) for photonic generation, processing and transmission of microwave signals. *IEEE Transactions on Microwave Theory and Techniques*, 47(7):1257–1264, 1999.

[252] M Grant, W Michie, and M Fletcher. The performance of optical phase-locked loops in the presence of nonnegligible loop propagation delay. *Journal of lightwave technology*, 5(4):592–597, 1987.

[253] Katarzyna Balakier, Lalitha Ponnampalam, Martyn J Fice, Cyril C Renaud, and Alwyn J Seeds. Integrated semiconductor laser optical phase lock loops. *IEEE Journal of Selected Topics in Quantum Electronics*, 24(1):1–12, 2018.

[254] L Kazovsky. Balanced phase-locked loops for optical homodyne receivers: performance analysis, design considerations, and laser linewidth requirements. *Journal of Lightwave Technology*, 4(2):182–195, 1986.

[255] RT Ramos and AJ Seeds. Delay, linewidth and bandwidth limitations in optical phase-locked loop design. *Electronics Letters*, 26(6):389–391, 1990.

[256] Floyd M Gardner. *Phaselock techniques*. John Wiley & Sons, 2005.

[257] Laurence S Rothman, Iouli E Gordon, Alain Barbe, D Chris Benner, Peter F Bernath, Manfred Birk, Vincent Boudon, Linda R Brown, Alain Campargue, J-P Champion, et al. The hitran 2008 molecular spectroscopic database. *Journal of Quantitative Spectroscopy and Radiative Transfer*, 110(9-10):533–572, 2009.

[258] Richard M Schotland. Errors in the lidar measurement of atmospheric gases by differential absorption. *Journal of Applied Meteorology (1962-1982)*, pages 71–77, 1974.

[259] Eduard Säckinger. *Analysis and Design of Transimpedance Amplifiers for Optical Receivers*. John Wiley & Sons, 2017.

[260] João Pedro Leal Abalada De Carvalho et al. *Design of a Transimpedance Amplifier for an Optical Receiver*. PhD thesis, 2017.

[261] TP Pearsall, RA Logan, and CG Bethea. Gainas/inp large bandwidth (¿ 2 ghz) pin detectors. *Electronics Letters*, 19(16):611–612, 1983.

[262] Philip CD Hobbs. *Building electro-optical systems: making it all work*, volume 71. John Wiley & Sons, 2011.

[263] AV Masalov, A Kuzhamuratov, and AI Lvovsky. Noise spectra in balanced optical detectors based on transimpedance amplifiers. *Review of Scientific Instruments*, 88(11):113109, 2017.

[264] George Turin. An introduction to matched filters. *IRE transactions on Information theory*, 6(3):311–329, 1960.

[265] Australian Radiation Protection et al. ARPANSA-lasers and intense pulsed light (IPL) sources. 2011.

[266] Hans R Bilger and Taufiq Habib. Knife-edge scanning of an astigmatic gaussian beam. *Applied optics*, 24(5):686–690, 1985.

[267] Jürgen Harms. Lidar return signals for coaxial and noncoaxial systems with central obstruction. *Applied Optics*, 18(10):1559–1566, 1979.

[268] Ellis E Remsberg and Larry L Gordley. Analysis of differential absorption lidar from the space shuttle. *Applied optics*, 17(4):624–630, 1978.

[269] Michael J Kavaya, Robert T Menzies, David A Haner, Uri P Oppenheim, and Pierre H Flamant. Target reflectance measurements for calibration of lidar atmospheric backscatter data. *Applied optics*, 22(17):2619–2628, 1983.

[270] Walter Schottky. Über spontane stromschwankungen in verschiedenen elektrizitätsleitern. *Annalen der physik*, 362(23):541–567, 1918.

[271] William Ralph Bennett. Spectra of quantized signals. *The Bell System Technical Journal*, 27(3):446–472, 1948.

[272] Walt Kester. Taking the mystery out of the infamous formula," snr= 6.02 n+ 1.76 db," and why you should care. *Analog Devices Tutorial, MT-001 Rev. A*, 10(08), 2009.

[273] Joseph W Goodman. Some fundamental properties of speckle. *JOSA*, 66(11):1145–1150, 1976.

[274] David L Fried. Statistics of the laser radar cross section of a randomly rough target. *JOSA*, 66(11):1150–1160, 1976.

[275] Bradly J Cooke, Bryan E Laubscher, Maureen M Cafferty, Nicholas L Olivas, Mark J Schmitt, Kenneth R Fuller, Roy M Goeller, Donald E Mietz, Joseph J Tiee, Robert K Sander, et al. Analysis and design methodology for the development of optimized direct detection co 2 dial receivers. In *Infrared Spaceborne Remote Sensing V*, volume 3122, pages 128–162. International Society for Optics and Photonics, 1997.

[276] Tamer F Refaat, Syed Ismail, Amin R Nehrir, John W Hair, James H Crawford, Ira Leifer, and Timothy Shuman. Performance evaluation of a 1.6-μm methane dial system from ground, aircraft and uav platforms. *Optics express*, 21(25):30415–30432, 2013.

[277] Andrey Nikolaevich Kolmogorov. Dissipation of energy in locally isotropic turbulence. In *Dokl. Akad. Nauk SSSR*, volume 32, pages 16–18, 1941.

[278] Xiaoming Zhu and Joseph M Kahn. Free-space optical communication through atmospheric turbulence channels. *IEEE Transactions on communications*, 50(8):1293–1300, 2002.

[279] Aniceto Belmonte, A Comerón, Juan Antonio Rubio, J Bará, and E Fernández. Atmospheric-turbulence-induced power-fade statistics for a multiaperture optical receiver. *Applied optics*, 36(33):8632–8638, 1997.

[280] Sherman Karp, Robert M Gagliardi, Steven E Moran, and Lawrence B Stotts. Optical channels: Fibers, clouds, water, and the atmosphere (applications of communications theory), 1988.

[281] JW Goodman. Statistical optics. 1985. *Google Scholar*, 1988.

[282] HT Yura. Signal-to-noise ratio of heterodyne lidar systems in the presence of atmospheric turbulence. *Optica Acta: International Journal of Optics*, 26(5):627–644, 1979.

[283] G Ehret, C Kiemle, M Wirth, A Amediek, A Fix, and S Houweling. Space-borne remote sensing of CO2, CH4, and N2O by integrated path differential absorption lidar: a sensitivity analysis. *Applied Physics B*, 90(3-4):593–608, 2008.

[284] Leon Clarke, James Edmonds, Henry Jacoby, Hugh Pitcher, John Reilly, and Richard Richels. Scenarios of greenhouse gas emissions and atmospheric concentrations. 2007.

[285] Nathan G Phillips, Robert Ackley, Eric R Crosson, Adrian Down, Lucy R Hutyra, Max Brondfield, Jonathan D Karr, Kaiguang Zhao, and Robert B Jackson. Mapping urban pipeline leaks: Methane leaks across boston. *Environmental pollution*, 173:1–4, 2013.

[286] Joseph C von Fischer, Daniel Cooley, Sam Chamberlain, Adam Gaylord, Claire J Griebenow, Steven P Hamburg, Jessica Salo, Russ Schumacher, David Theobald, and Jay Ham. Rapid, vehicle-based identification of location and magnitude of urban natural gas pipeline leaks. *Environmental science & technology*, 51(7):4091–4099, 2017.

[287] Albert Guisasola, David de Haas, Jurg Keller, and Zhiguo Yuan. Methane formation in sewer systems. *Water Research*, 42(6-7):1421–1430, 2008.

[288] David Nankervis. Gas leaks prompt blast fear. *The Advertiser*, 2010.

[289] Mike Hatch. Environmental geophysics: Gas spectrometry: very shallow surface geophysics. *Preview*, 2016(180):32–33, 2016.

[290] MA Hatch, MJ Kennedy, MW Hamilton, and RA Vincent. Methane variability associated with natural and anthropogenic sources in an australian context. *Australian Journal of Earth Sciences*, 65(5):683–690, 2018.

[291] Robin E Bell, Bernard J Coakley, and Robert W Stemp. Airborne gravimetry from a small twin engine aircraft over the long island sound. *Geophysics*, 56(9):1486–1493, 1991.

[292] Jessica Barrientos Barria, Alexandre Dobroc, Hélène Coudert-Alteirac, Myriam Raybaut, Nicolas Cézard, Jean-Baptiste Dherbecourt, Thomas Schmid, Basile Faure, Grégoire Souhaité, Jacques Pelon, et al. Simultaneous remote monitoring of atmospheric methane and water vapor using an integrated path dial instrument based on a widely tunable optical parametric source. *Applied Physics B*, 117(1):509–518, 2014.

[293] François CAGNON, Frédérique BOURNAZAUD, A Hoffstaedt, and M Ulbricht. Laser based natural gas remote detection. *Proc. of 22 nd WGC*.

[294] David JM Stothard, Malcolm H Dunn, and Cameron F Rae. Hyperspectral imaging of gases with a continuous-wave pump-enhanced optical parametric oscillator. *Optics express*, 12(5):947–955, 2004.

[295] Yuen Fong Chan, M Moallem, and Wei Wang. Efficient implementation of pid control algorithm using fpga technology. In *2004 43rd IEEE Conference on Decision and Control (CDC)(IEEE Cat. No. 04CH37601)*, volume 5, pages 4885–4890. IEEE, 2004.

[296] Yuen Fong Chan, M Moallem, and Wei Wang. Design and implementation of modular fpga-based pid controllers. *IEEE transactions on Industrial Electronics*, 54(4):1898–1906, 2007.

[297] Michal Kocur, Stefan Kozak, and Branislav Dvorscak. Design and implementation of fpga-digital based pid controller. In *Proceedings of the 2014 15th International Carpathian Control Conference (ICCC)*, pages 233–236. IEEE, 2014.

[298] K Huang, H Le Jeannic, J Ruaudel, O Morin, and J Laurat. Microcontroller-based locking in optics experiments. *Review of Scientific Instruments*, 85(12):123112, 2014.

[299] YY Wang, Xiang Peng, Meshaal Alharbi, C Fourcade Dutin, Thomas D Bradley, Frédéric Gérôme, Michael Mielke, Timothy Booth, and F Benabid. Design and fabrication of hollow-core photonic crystal fibers for high-power ultrashort pulse transportation and pulse compression. *Optics letters*, 37(15):3111–3113, 2012.

[300] Anthony Bucholtz. Rayleigh-scattering calculations for the terrestrial atmosphere. *Applied Optics*, 34(15):2765–2773, 1995.

[301] Dennis L Hartmann, James R Holton, and Qiang Fu. The heat balance of the tropical tropopause, cirrus, and stratospheric dehydration. *Geophysical research letters*, 28(10):1969–1972, 2001.

[302] Teruyuki Nakajima and Michael D King. Determination of the optical thickness and effective particle radius of clouds from reflected solar radiation measurements. part i: Theory. *Journal of the atmospheric sciences*, 47(15):1878–1893, 1990.

[303] Thomas J Kane, Bingkun Zhou, and Robert L Byer. Potential for coherent doppler wind velocity lidar using neodymium lasers. *Applied optics*, 23(15):2477–2481, 1984.

[304] Zhishen Liu, Songhua Wu, and Bingyi Liu. Seed injection and frequency-locked nd: Yag laser for direct detection wind lidar. *Optics & Laser Technology*, 39(3):541–545, 2007.

[305] CEC Clean Energy Council. Clean energy australia report 2016. *CEC Publication, Melbourne*, 2016.

[306] Torben Mikkelsen. Remote sensing of wind. *Remote sensing for wind energy*, pages 7–20, 2010.

[307] Cristina L Archer and Mark Z Jacobson. Supplying baseload power and reducing transmission requirements by interconnecting wind farms. *Journal of Applied Meteorology and Climatology*, 46(11):1701–1717, 2007.

[308] Anthony Gerrard and James M Burch. *Introduction to matrix methods in optics*. Courier Corporation, 1994.

[309] Herwig Kogelnik and Tingye Li. Laser beams and resonators. *Applied optics*, 5(10):1550–1567, 1966.

[310] R Clark Jones. A new calculus for the treatment of optical systems. iv. *Josa*, 32(8):486–493, 1942.

[311] M Roth, M Tseitlin, and N Angert. Oxide crystals for electro-optic q-switching of lasers. *Glass physics and chemistry*, 31(1):86–95, 2005.

[312] Alex Abramovici, William E Althouse, Ronald WP Drever, Yekta Gürsel, Seiji Kawamura, Frederick J Raab, David Shoemaker, Lisa Sievers, Robert E Spero, Kip S Thorne, et al. Ligo: The laser interferometer gravitational-wave observatory. *Science*, 256(5055):325–333, 1992.

[313] Miao Zhu and John L Hall. Short and long term stability of optical oscillators. In *Frequency Control Symposium, 1992. 46th., Proceedings of the 1992 IEEE*, pages 44–55. IEEE, 1992.

[314] Norman Hodgson and Horst Weber. The fabry perot resonator. In *Optical Resonators*, pages 137–162. Springer, 1997.

[315] Eric D Black. An introduction to pound–drever–hall laser frequency stabilization. *American journal of physics*, 69(1):79–87, 2001.

[316] Howard W Johnson, Martin Graham, et al. *High-speed digital design: a handbook of black magic*, volume 1. Prentice Hall Upper Saddle River, NJ, 1993.

[317] Howard W Johnson and Martin Graham. *High-speed signal propagation: advanced black magic*. Prentice Hall Professional, 2003.

[318] J Ardizzoni. *A Practical Guide to High-Speed Printed-Circuit-Board Layout*. Analog Dialogue, September 2005.

[319] R Schmid, S Baier, R Stephens, X Ramus, J Karki, and M Steffes. *High Speed Analog Design and Application Seminar*. Texas Instruments, 2004.

[320] Altera. *Designing Power Isolation Filters with Ferrite Beads for Altera FPGAs*, July 2009. Rev. 1.

[321] Timothy C Neugebauer, Joshua W Phinney, and David J Perreault. Filters and components with inductance cancellation. *IEEE Transactions on Industry Applications*, 40(2):483–491, 2004.

[322] Cong-hui Hao, Pan Guo, He Chen, Yin-chao Zhang, and Si-ying Chen. Determination of geometrical form factor in coaxial lidar system. In *International Symposium on Photoelectronic Detection and Imaging 2013: Laser Sensing and Imaging and Applications*, volume 8905, page 89051V. International Society for Optics and Photonics, 2013.